ALMA MATER STUDIORUM - UNIVERSITÀ DI BOLOGNA

FACOLTÀ DI CHIMICA INDUSTRIALE

Dipartimento di Chimica Fisica ed Inorganica

Master of Science in Advanced Spectroscopy in Chemistry

Classe LM/71 - Scienze e Tecnologie della Chimica Industriale

N-Heterocyclic carbene complexes of silver, rhodium and iron: structures, dynamics and catalysis

EXPERIMENTAL THESIS

Presented by

Marta Brucka

Supervisor:

Prof. **Maria Cristina Cassani**

Co-Supervisors:

Dr. **Michele Mancinelli**

Dr. **Rita Mazzoni**

Mr. **Gavino Solinas**

First Session

Academic Year 2011-2012

Table of contents

Summary

The research performed in the framework of this Master Thesis has been directly inspired by the recent work of an organometallic research group led by Professor Maria Cristina Cassani on a topic related to the structures, dynamics and catalytic activity of N-heterocyclic carbene-amide rhodium(I) complexes[1]. A series of [BocNHCH$_2$CH$_2$ImR]X (R = Me, X = I, **1a'**; R = Bz, X = Br, **1b'**; R = trityl, X = Cl, **1c'**) amide-functionalized imidazolium salts bearing increasingly bulky N-alkyl substituents were synthetized and characterized. Subsequently, these organic precursors were employed in the synthesis of silver(I) complexes as intermediate compounds on a way to rhodium(I) complexes [Rh(NBD)X(NHC)] (NHC = 1-(2-NHBoc-ethyl)-3-R-imidazolin-2-ylidene; X = Cl, R = Me (**3a'**), R = Bz (**3b'**), R = trityl (**3c'**); X = I, R = Me (**4a'**)), Scheme 1.

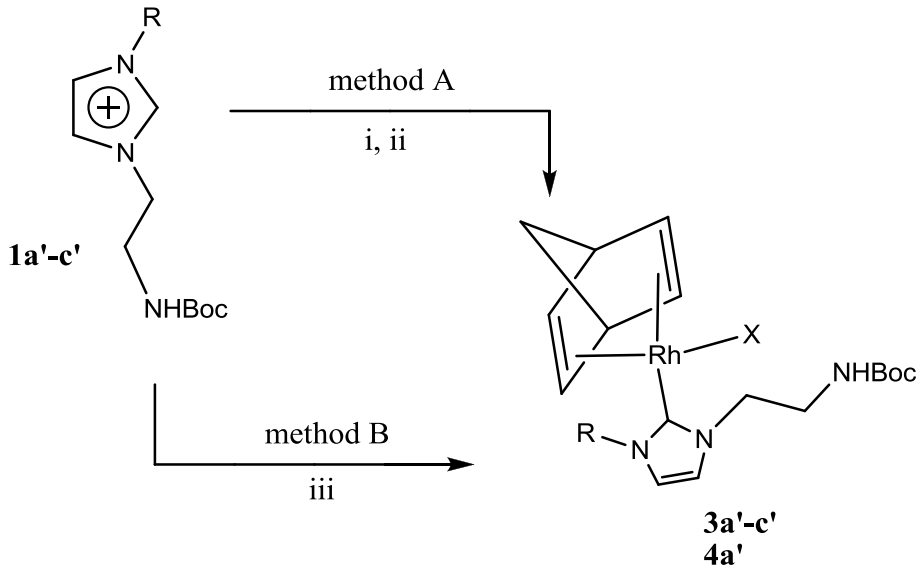

X = Cl; R = Me (**3a'**), Bz (**3b'**), trityl (**3c'**)
X = I; R = Me (**4a'**)

Scheme 1. Synthesis of amide-functionalized rhodium(I) complexes 3a'-c' and 4a'.

Reactions and conditions for **3a'-c'**: (i) Ag_2O, CH_2Cl_2, r.t.; (ii) $[Rh(NBD)Cl]_2$, CH_2Cl_2, r.t., 2 h. Reaction and conditions for **4a'**: (iii) $[Rh(NBD)(O^tBu)]_2$, THF, r.t., 3 h.

VT NMR studies of these complexes revealed a restricted rotation barriers about the metal-carbene bond. However, while the rotation barriers calculated for the complexes in which R = Me, Bz (**3a'**,**b'** and **4a**) matched the experimental values, this was not true in the trityl case **3c'**, where the experimental value was very similar to that obtained for compound **3b'** and much smaller with respect to the calculated one. In addition, the energy barrier

derived for **3c'** from line shape simulation showed a strong dependence on the temperature, while the barriers measured for **3a',b'** did not show this effect.

In view of these results and in order to establish the reasons for the previously found inconsistency between calculated and experimental thermodynamic data, the first objective of this master thesis was the preparation of a series of rhodium(I) complexes [Rh(NBD)X(NHC)] (NHC = 1-benzyl-3-R-imidazolin-2-ylidene; X = Cl, R = Me, Bz, trityl, ^{t}Bu), containing the benzyl substituent as a chiral probe, followed by full characterization.

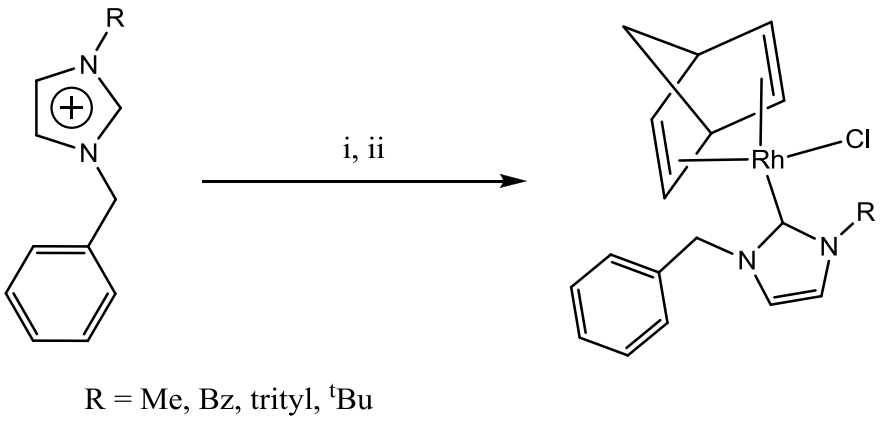

R = Me, Bz, trityl, ^{t}Bu

Scheme 2. Synthesis of rhodium(I) complexes presented in this thesis.
Reactions and conditions: (i) Ag_2O, CH_2Cl_2, r.t.; (ii) $[Rh(NBD)Cl]_2$, CH_2Cl_2, r.t., 2h

The second objective of this work was to investigate the catalytic activity of the new rhodium compounds in the hydrosilylation of terminal alkynes for comparison purposes with the reported complexes[1].

Another purpose of this work was to employ the prepared N-heterocyclic ligands in the synthesis of iron(II)-NHC complexes.

1 INTRODUCTION

1.1 Carbenes – general introduction

Carbenes are uncharged compounds featuring a dicoordinate carbon atom with two valence shell electrons which do not participate in any bonding interactions. The carbon atom contains six electrons, which occupy *1s*, *2s* and partially *2p* orbitals. Depending on the degree of the hybridization of these orbitals, carbenes adopt different geometries: either nonlinear (bent), emerging from the sp^2 hybridization or linear in case of the *sp* hybridization (Figure 1.1).

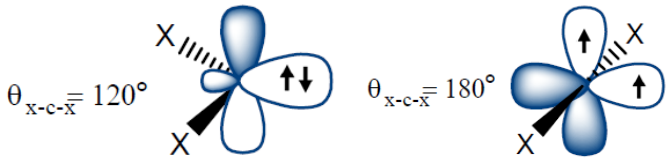

Figure 1.1 sp^2 and *sp*–hybridized orbitals of a carbon atom.

sp-type hybridization leads to mixing of *2s* and $2p_z$ orbitals, whereas the two nonbonding $2p_x$ and $2p_y$ stay degenerate. The degeneracy is broken when a carbon atom adopts the sp^2 hybridization which involves the additional contribution of the p_x orbital. The latter one becomes energetically stabilized since obtaining some *s* character and conventionally, after Bertrand[2], is called σ, whereas the unchanged p_y is called p_π. Figure 1.2 presents the break of the degeneracy of the *p* orbitals after adopting the sp^2 hybridization.

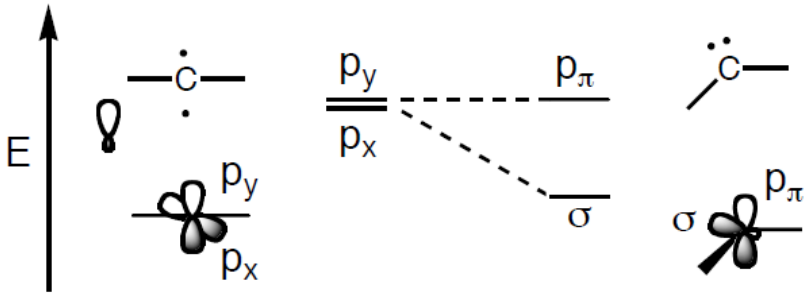

Figure 1.2 Break of the degeneracy of carbon's p orbitals when adopting the sp^2 hybridization.

1.1.1 Triplet vs. singlet carbenes

The two lone electrons of a carbene can be assigned to the two empty *p* orbitals of carbon atom in different ways. Four different electronic configurations are then possible for the sp^2-hybridized carbon atom (Figure 1.3). According to the rule for determination of multiplicity of electronic states: 2S+1, where S corresponds to the total spin, triplet and singlet carbenes can be specified. Triplet state results from two singly occupied nonbonding *p* orbitals by two electrons with parallel spins, whereas an excited singlet state is attributed to two singly occupied nonbonding *p* orbitals by two electrons with opposite spins. Finally, there are two alternative configurations for a ground singlet state: one with the lone electron pair placed in the σ orbital leaving the p_π orbital vacant and the second one with an opposite configuration (p_π filled and σ vacant). Due to the electrostatic interactions between the two electrons, triplet state is usually lower in energy than the singlet states.

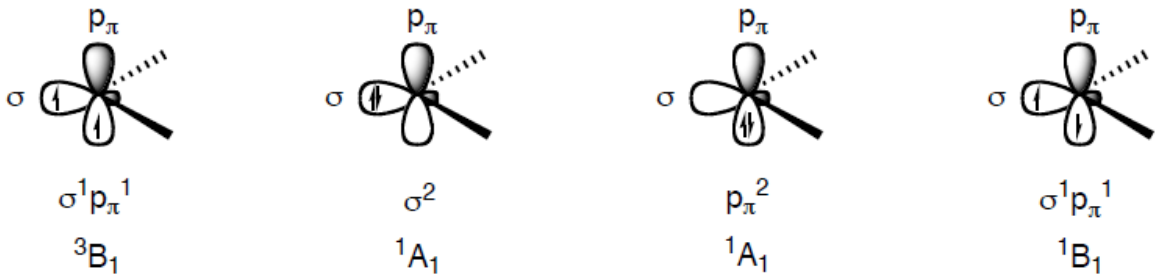

a) triplet state b) singlet state c) singlet state d) excited singlet state

Figure 1.3 sp^2 hybrid structure of carbon atom with different assignment of the two nonbonding electrons.

The carbene ground-state multiplicity is related to the relative energy of the σ and p_π orbitals. When the separation between these two levels is large, it is hardly likely for an electron to occupy the upper level, thus singlet state is favored. As a contrary, when these two levels become close to each other on the energy scale, one of the nonbonding electrons can easily 'jump' to the higher p_π level. Gleiter and Hoffman[3] determined the limit of energy difference to be at least 2 eV to make the ground state of a carbene to be a singlet. Due to the fact that the nature of a substituent on carbon atom can tune the energy of the singlet–triplet splitting, the ground state spin multiplicity and subsequently the reactivity of a particular carbene depends both on electronic and steric effects supplied by the substituent groups.

1.1.2 Electronic effects

Electronic effects can be either inductive or mesomeric.

a) Inductive effects

Inductive influence of the substituents is related to their electronegativity. Electronegative atoms or groups are σ–electron withdrawing substituents, hence they inductively stabilize the σ nonbonding orbital by increasing its *s* character, leading to lowering its energy in the energy diagram. As a result, since p_π is unchanged, the gap is increased, favoring the singlet ground state. In case of σ–electron donating substituents (electropositive), the σ - p_π is small and therefore the triplet ground state is favored. Figure 1.4 shows the influence of electronegativity of a carbon substituents on the energy gap between p_π and σ orbitals.

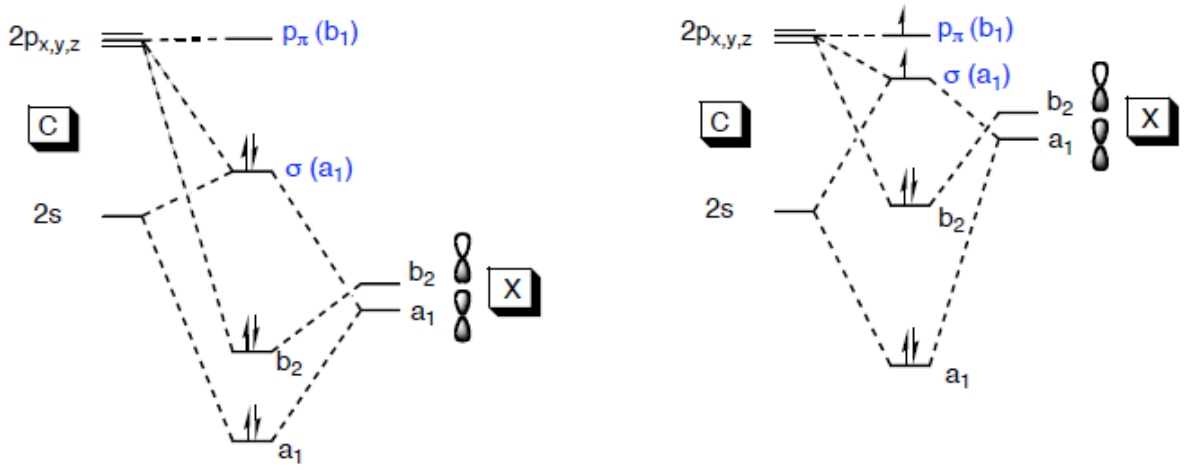

a) σ – electron withdrawing substituents b) σ – electron donating substituents

Figure 1.4 Perturbation orbital diagrams showing the influence of the inductive effects.

Table 1.1 shows different substituents grouped accordingly to their electronic properties.

Table 1.1 Different types of substituents of a carbene center.

σ-withdrawing	σ-donating	π-withdrawing (Z)	π –donating (X)
-F	-Li	-COR	-F
-O		-CN	-Cl
-Cl		$-CF_3$	-Br
-N		$-BR_2$	-I
-Br		$-SiR_3$	$-NR_2$
		$-PR_3^+$, ...	$-PR_2$
			-OR
			-SR
			$-SR_3$, …

b) Mesomeric effects

Mesomeric effects refer to the ability of carbene substituents to donate or withdraw electrons via π-type overlapping with the orbitals of a carbon; depending on the type of the substituents, three groups of singlet carbenes with different characteristics can be thus specified, after Bertrand terminology, the highly bent (X,X)-carbenes and linear or quasi-linear (Z,Z)- and (X,Z)-carbenes[2], where Z refers to π-withdrawing substituents and X to π-donating ones. (Figure 1.5).

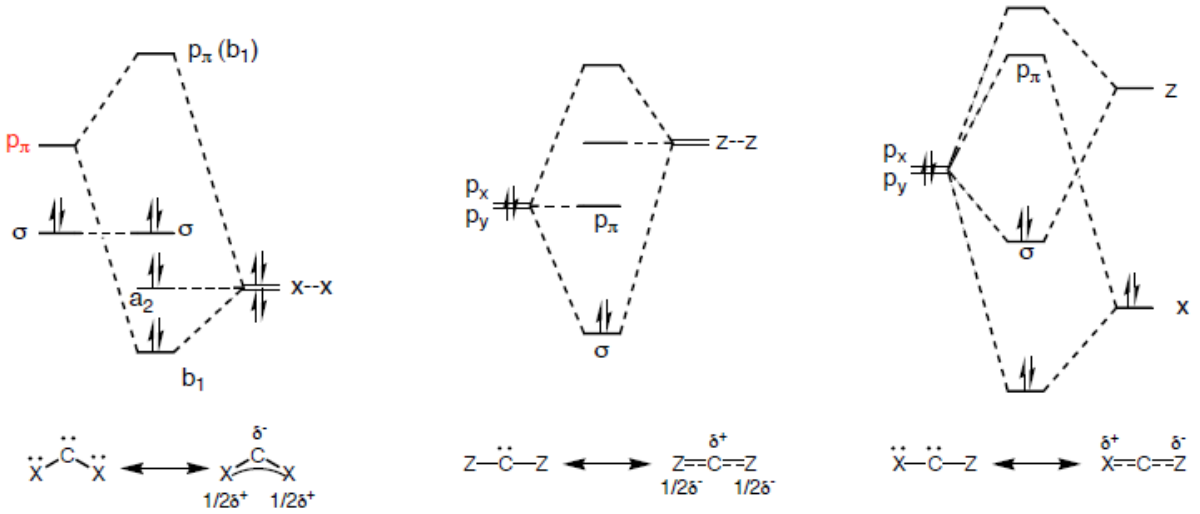

Figure 1.5 Perturbation orbital diagrams showing the influence of the mesomeric effects.

(X,X)-carbenes are built from two π-donor groups being at the same time σ-attractors (electronegative) attached to a carbon atom. This way of substitution is called: push, push mesomeric-pull, pull inductive pattern. An interaction between the substituent lone pairs with

the vacant carbon p_π orbital leads to a significant increase of the energy of the latter which means a break of the degeneracy between p_π and σ, which in turn support the bent geometry of the carbenes. The most representative examples of these carbenes are diaminocarbenes together with the group of NHC (N-heterocyclic carbenes). The stability of these species relies on a preservation of the electroneutrality of the carbene center. Lone electron pair on a carbon is stabilized by inductive effect of electronegative nitrogen atoms, which on the other hand donate electrons to the nonbonding orbitals of the carbene center (Figure 1.6), imposing some multiple bond character; accordingly, the formal structure of carbenes can be written as a superposition of two zwitterionic structures, shown in Figure 1.7.

The π donation induces the nucleophilicity of the carbenes.

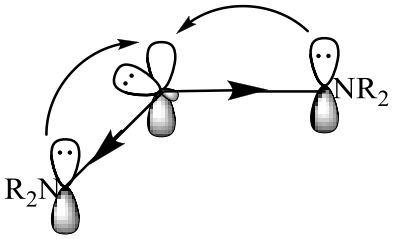

Figure 1.6 Electronic effects of the substituents for diaminocarbenes.

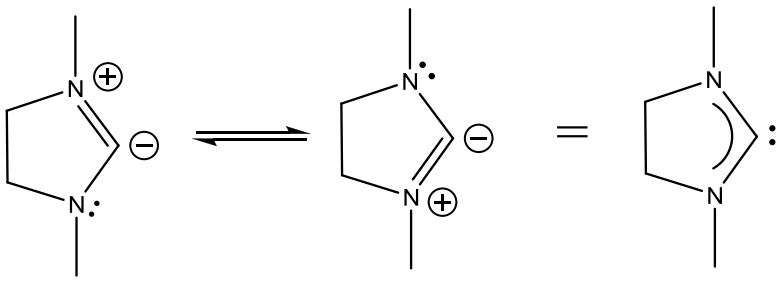

Figure 1.7 Resonance structures of NHCs.

(Z,Z)-carbenes possess two substituents both of them being π-attractors σ-donors, which means an electron deficiency in one of the nonbonding *p* orbitals, compensated by the σ-donation of the electropositive substituents. Diborylcarbenes are examples of this group. Due to the withdrawal effect, the carbenes will act as electrophilic agents.

(X,Z)-carbenes possess two different substituents (π-donor and π-acceptor) which exert an opposite influence. Each of them interact with different *p* carbon orbitals (p_y and p_x, respectively). The destabilization of p_y and stabilization of p_x breaks the degeneracy, favoring the singlet ground state, even though the geometry is linear due to the *sp* hybridization. Examples of the push, pull mesomeric substituted carbenes are

phosphinophosphoniocarbenes. The last two groups of carbenes will not be discussed in details in the following thesis.

Finally, steric effects are related to the bulkiness of carbon substituents. Bulky substituents kinetically stabilize all types of carbenes. Due to steric interactions, two big substituents will stabilize linear geometry of carbenes, thereby the degeneracy of carbon orbitals and in turn the triplet ground state.

1.1.3 Reactivity

The ground-state spin multiplicity of carbenes is directly related to their reactivity. A carbene in its singlet ground state, possessing a lone electron pair and a vacant *p* orbital shows an ambiphilic properties and is usually compared to that of carbenium ions $(CR_3)^+$; on the other hand, a carbene in its triplet state with two singly occupied *p* orbitals is often compared to the diradicals $:CR_3$. These differences in electronic properties have a direct impact on the mechanisms, which these species react through.

The illustrative example of the difference in the reactivity of singlet and triplet carbenes is an addition to alkenes (discussed in details in section 1.2.5). Carbenes with a triplet ground state participate in stepwise radical additions, which go through an intermediate with two unpaired electrons (stereoselective reaction), whereas singlet carbene can react in a single step (stereospecific reaction), Figure 1.8.

a)

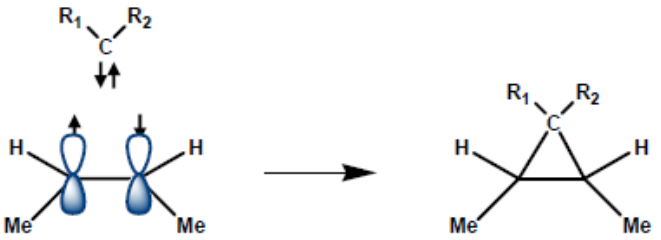

b)

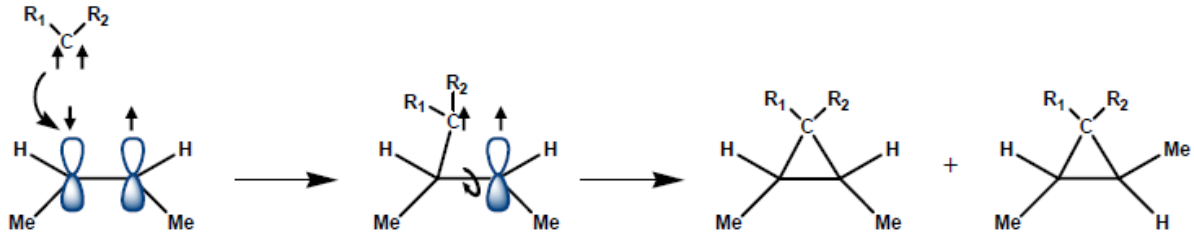

Figure 1.8 Addition reaction of a carbene to but-2-ene. The reaction is direct for a singlet carbene (a) and multistep for a triplet carbene (b).

1.2 N-Heterocyclic Singlet Carbenes

N-heterocyclic carbenes belong to a wider group of diaminocarbenes; they form complexes with any type of main group and transition metal elements of the periodic table; they are characterized by a great diversity of structural motifs and thus offer a wide range of possibilities for fine-tuning the steric pressure on both the carbene and the coordinated metal, modulating the catalytic properties.

1.2.1 Synthesis

The first efforts to isolate a carbene were put in the early 1960s by Wanzlick, shortly after the discovery of the first metal-carbene complexes (See section 1.2.6). *N*-heterocyclic organic salts were considered already at that time to be the most prominent precursors for stable carbenes, since some presumptions were employed with regard to an enhanced stability of carbenes possessing amino substituents. The proposed method relied on an extrusion of chloroform from the imidazolidene adduct by a thermal α-elimination as depicted in Scheme 1.1 Reaction carried out by Wanzlick in order to isolate a first stable carbene., but the reaction led directly to the dimeric electron rich olefin instead of the desired monomeric carbene[4].

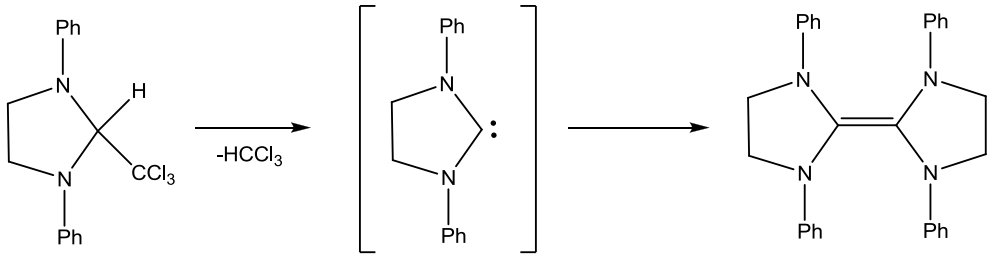

Scheme 1.1 Reaction carried out by Wanzlick in order to isolate a first stable carbene.

Subsequent work of Wanzlick brought an idea that imidazolium salts with enough bulky substituents on nitrogen atoms could be deprotonated by a base, for example potassium *tert*-butoxide. The idea was realized by Arduengo, when in 1991 he obtained 1,3-diadamantyl-2,3-dihydro-1*H*-imidazol-2-ylidene as a crystalline and thermally stable compound, by deprotonation of the 1,3-di-adamantylimidazoulium chloride with sodium or potassium hydride in the presence of catalytic amounts of either ^{t}BuOK or the dimethyl sulfoxide anion (Scheme 1.2).

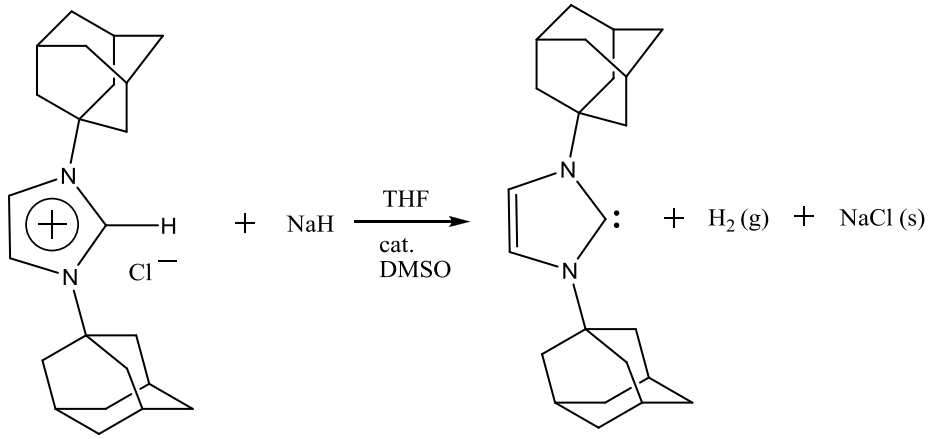

Scheme 1.2 Arduengo's synthesis of the first stable N-heterocyclic carbene.

Starting from the first preparation method, few routes to stable singlet *N*-heterocyclic carbenes can be listed.

1. Deprotonation of imidazolium salts with a base (NaH, KH) in the presence of *t*-BuOK (or DMSO) anions either in liquid ammonia or in non-protic solvents such as THF or ethers. The deprotonation requires anyhydrous conditions and the use of strong bases, with pK_a values above 14. Apart from KH and NaH, the following bases were also successfully employed for the deprotonation: tert-butoxide (*t*-BuOK), lithium aluminum hydride (LAH), n-butyllithium (*n*-BuLi), potassium hexamethyldisilazide (KHMDS) and 1,8-diazabicyclo[5.4.0]undec-7-ene (DBU). Moreover, Nolan in his review[5] referes to the

protocol proposed by Astruc et al. to deprotonate a series of imidazolium salts, using a radical anion superoxide as a base. The radical was formed in situ by reduction of ambient dioxygen with a 19-electron sandwich complex of Fe^{I} (Scheme 1.3).

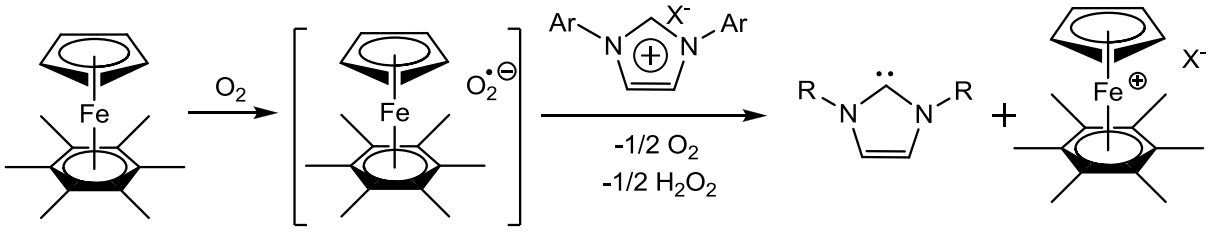

Scheme 1.3 Deprotonation of imidazolium salts, using a radical anion superoxide as a base.

2. Electrochemical or chemical reduction of imidazolium salts. A negative potential as low as −2.28 V and an excess of potassium in boiling THF is required to obtain the desired carbenes via the chemical reduction. The mechanism of a reduction process involves a formation of a radical imidazole intermediate, followed by a further loss of a hydrogen radical (Scheme 1.4).

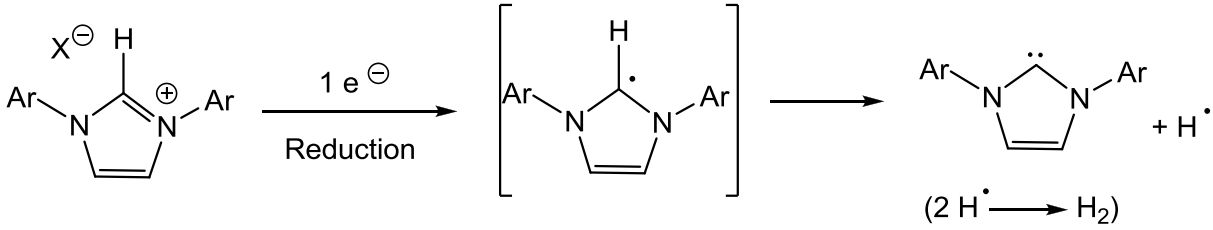

Scheme 1.4 Reduction of imidazolium salts.

3. Reduction of imidazole-2(3*H*)-thiones with potassium in boiling THF (Scheme 1.5).

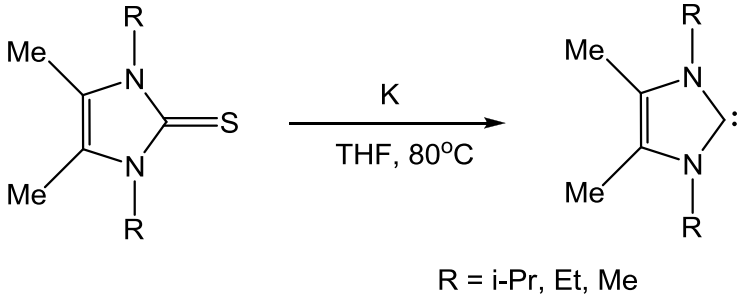

Scheme 1.5 Reduction of imidazole-2(3H)-thiones.

4. Thermal elimination (80°C) of methanol in vacuo from 5-methoxy-1,3,4-triphenyl-4,5-dihydro-1H-1,2,4-triazole affords 1,2,4-triazol-5-ylidene (Scheme 1.6).

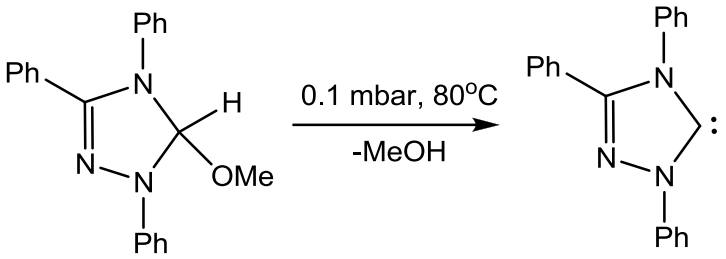

Scheme 1.6 Thermal elimination.

1.2.2 Imidazolium precursors

As already mentioned, the most versatile method to obtain stable carbenes but also to synthesize complexes of NHCs with metals (See section 1.2.6) consists of using the corresponding imidazolium salts.

Generally, imidazolium salts are room-temperature non-aqueous ionic liquids ("NAIL"), commonly used as solvents in organic syntheses, which thanks to their unique physical-chemical and recently also widely studied biochemical properties hold applications in variety of scientific fields, such as: organometallic syntheses and catalysis, as electrolytes in electrochemistry, in fuel and solar cells, as a stationary phase for chromatography, as matrices for mass spectrometry, supports for the immobilization of enzymes, as liquid crystals, templates for the synthesis of nanomaterials[6], etc.

The first reported room temperature ionic liquids were 1-n-butyl-3-methylimidazolium tetrafluoroborate ($BMI.BF_4$), hexafluorophosphate ($BMI.PF_6$) and their analogues. The subsequently synthesized imidazolium salts contained alkyl groups on both N-sides of the imidazole fragment and particularly these types of the salts have been widely studied. These species are liquids in a broad range of temperatures (down to -80°C) and are characterized to have high thermal and chemical stability, large electrochemical window (up to 7 V), high density, relatively low viscosity, and very small vapor pressure. The listed characteristics of the imidazolium salts render them an excellent media for various transformations in solution. Since the ionic liquid effect on catalytic performance of organometallic species has been discovered by Calò[7], it is presumed that the beneficial activity can result from the facile conversion of the ILs into NHC-metal complexes[8]; moreover, their use as immobilizing agents for transition metal catalyst precursors, is justified by an ease of product separation and catalyst recycling[9]. Recently, the diverse array of applications of the ionic liquids based on the imidazolium moiety is expanded by fuctionalisation of the cation or anion of these species[10].

1.2.2.1 Synthesis of imidazolium salts

Synthesis of imidazolium salts can be roughly devided into two methods:

1. Alkylation of an existing imidazoles with appropriate electrophiles (Scheme 1.7).

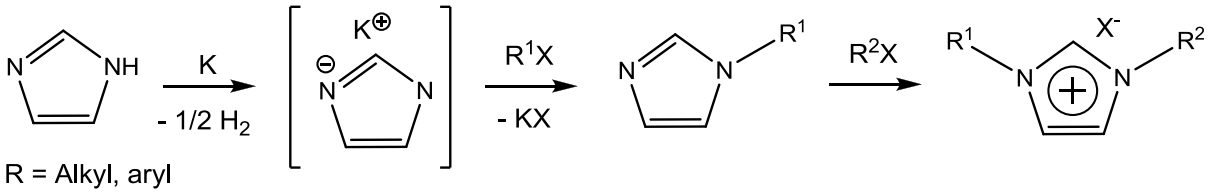

Scheme 1.7 Reaction between imidazole and potassium to generate an imidazolide anion and subsequent stepwise alkylation.

2. Ring formation.

"There are no really general ways of synthesizing imidazoles and it is invariably necessary to consider a number of divergent methods whenever a synthesis is contemplated."[11]

In the literature indeed there are few synthetic procedures reported to afford heterocycles based on imidazole structure. However, the most commonly cited are derived from a general procedure, proposed by Debus in 1858 and developed by Radziszewski up to 1882. This reaction relies on a condensation of an α-dicarbonyl compound, an aldehyde and two equivalents of ammonia to afford the imidazole (or an 1 equivalent of ammonia together with an 1 equivalent of an amine, to obtain the 1-substituted imidazoles), Scheme 1.8. A variety of α-dicarbonyl compounds including glyoxal (a), pyruvaldehyde (b), porphyrin-2,3-diones (c) and benzyl (d) have been already used to successfully afford the corresponding imidazole derivatives.

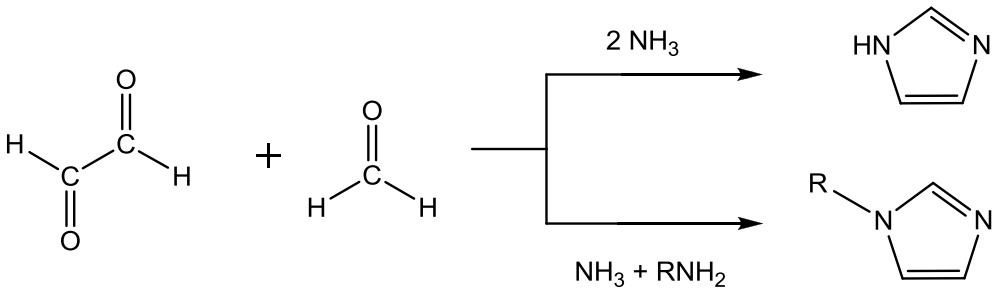

Scheme 1.8 General scheme of Debus-Radziszewski reaction.

The general mechanism of this reaction has not been established, but the most likely route would be initiated by a successive nucleophilic attack of the two molecules of ammonia (alternatively ammonia and an amine) lone pairs towards the carbonyl carbon atom of the α-

dicarbonyl compound, coupled with an elimination of water molecules to afford the corresponding Shiff base (α-diimine). The subsequent condensation with an aldehyde leads to a formation of the desired imidazole derivative. Figure 1.9 shows the proposed mechanism to obtain a substituted imidazole ring at position 2 and a side reaction leading to formation of oxazole.

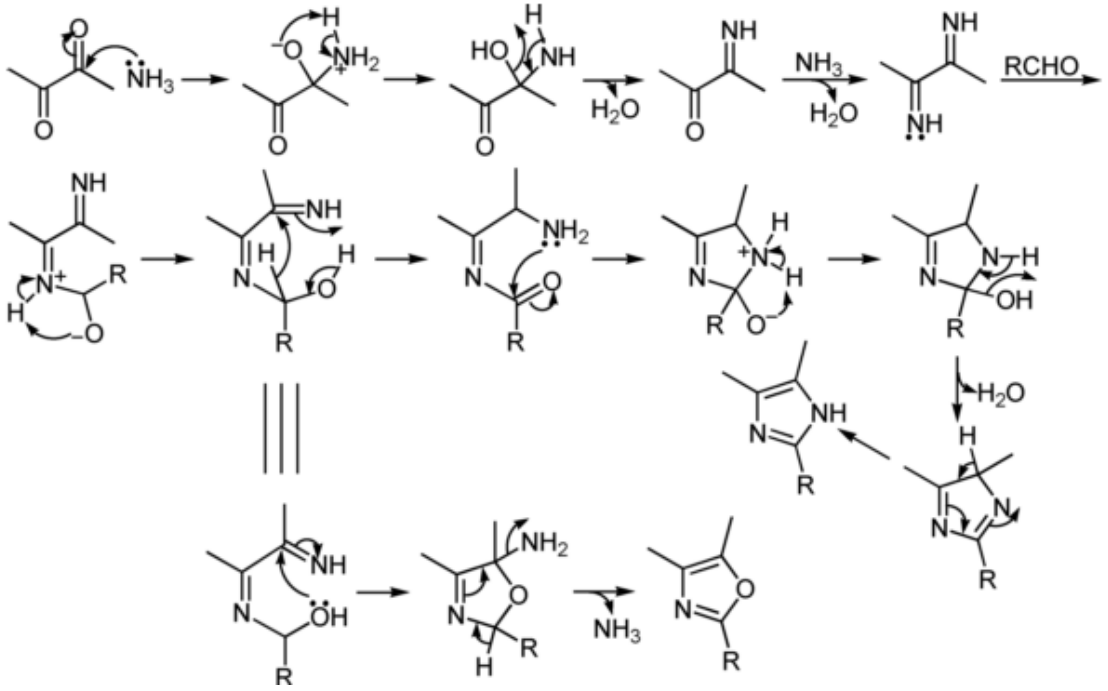

Figure 1.9 Proposed mechanism of Debus-Radziszewksi reaction of synthesis of an imidazole derivative.

Specifically, the ring formation leading to the imidazolium salts can be realized in four ways, illustrated by the following schemes:

a) symmetric synthesis

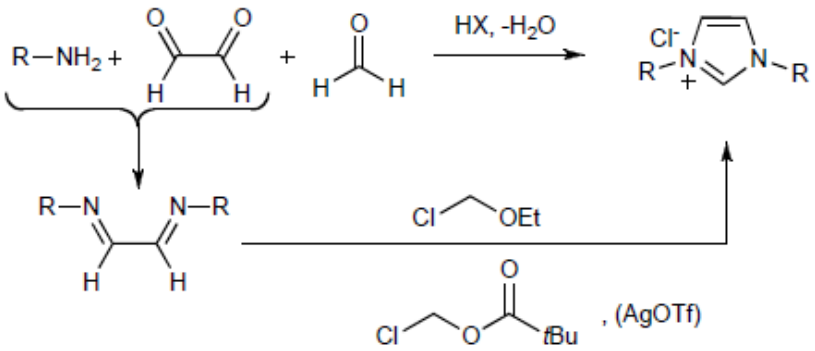

Scheme 1.9 Symmetric synthesis of an imidazolium salt.

The above reaction (Scheme 1.9) proceeds under acidic conditions through a coupling between the amine and the glyoxal to afford the corresponding Schiff base. Condensation with formaldehyde leads to the imidazolium salt[12]. This one-pot reaction has been successively applied for a formation of a symmetric N,N'-substituted imidazolium salts with various, bulky aryl- and alkyl- groups. An even more versatile modification of this method, proposed by Glorius et al.[13] relies on the use of silver triflate with chloromethyl pivalate to generate in situ an alkylating reagent, which in a second step leads to an efficient cyclisation of different types of diimines. The described procedure consists of distinct steps with the previous isolation of the Schiff base.

b) unsymmetrical synthesis

An asymmetric mono N-substituted imidazoles, which can be subsequently N-alkylated, are synthesized by one-pot reaction between glyoxal, ammonia (or ammonium chloride), formaldehyde (or paraformaldehyde), and only one equivalent of primary amine (Scheme 1.10).

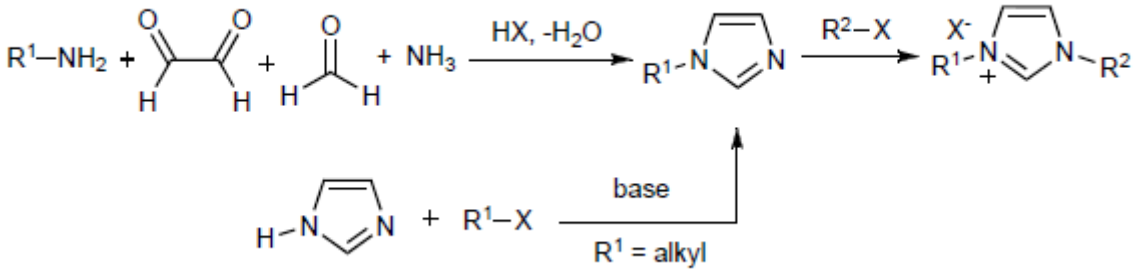

Scheme 1.10 Asymmetric synthesis of an imidazolium salt.

c) unsymmetrical synthesis of imidazolidinium salts

d) unsymmetrical synthesis of imidazolium salts

1.2.3 NMR and X-Ray diffraction of N-heterocyclic carbenes and imidazolium salts

The carbon atom placed between the two nitrogen atoms (or other X-type substituents like sulfur S) of the imidazolium cationic salts, resonates at the chemical shift in the range: 135 – 180 ppm. The signal deriving from the carbon atom of the corresponding stable carbenes is much more deshielded – chemical shift in the range 205 – 220 ppm for the

unsaturated heterocyclic carbenes, and 235 – 245 ppm for the saturated equivalents and a very low field resonances: 235 – 300 ppm appear for acyclic aminocarbenes.

The bond angle NCN in a singlet cyclic carbenes is found to lay in the range 100 - 110°. Expectedly, the angle is bigger in structures of acyclic carbenes (around 120°) due to steric effects. The observed N-$C_{carbene}$ bond lengths are between 1.32 and 1.37 Å, whereas the respective N-C bond in their organic ionic precursors is only a little shorter (1.28 – 1.33 Å). This increase in bond length could be attributed to a decrease in π-delocalization or $p\pi$-$p\pi$ interaction in the carbene relative to the carbenium ion, however, the change in a hybridization at the carbene center between carbenium ion and carbene is an important factor which must be taken into account while considering the change in the bond distances[14]. It is said that in the case of a free carbene, the in-plane lone pair of electrons at the carbene center is stabilized by more s-orbital character. As a consequence, the N-C σ-bonds take on more *p*-character at the carbene center; this lead to the observed increase in the N-C distances upon deprotonation of the imidazolium salts[14]. To sum up, the discussed structural changes (decrease in C-N distances and increase in the N-C-N angle) appear to be typical for protonation of all singlet carbenes.

1.2.4 Electronic structure of N-Heterocyclic carbenes

Two theories contribute to the establishment of the electronic structure and stability of NHCs.

1. The statement of Dixon and Arduengo[14] that stability of five-membered ring carbenes (Figure 1.10a) comes from the inductive effect of nitrogen atoms bonded to the carbene center. The theory is based on the results obtained from neutron and X-ray diffraction studies and fortified by a perfectly matching results from DFT calculations. Figure 1.10b shows a contour line diagrams of the electron density, which indicates high electron density in the plane of the molecule (blue cloud) and electron deficiency below and above the molecular plane (yellow cloud). Moreover, contour plots 70 pm above the molecular plane show maxima of electron density localized on nitrogen atoms and C=C double bond (Figure 1.10c).

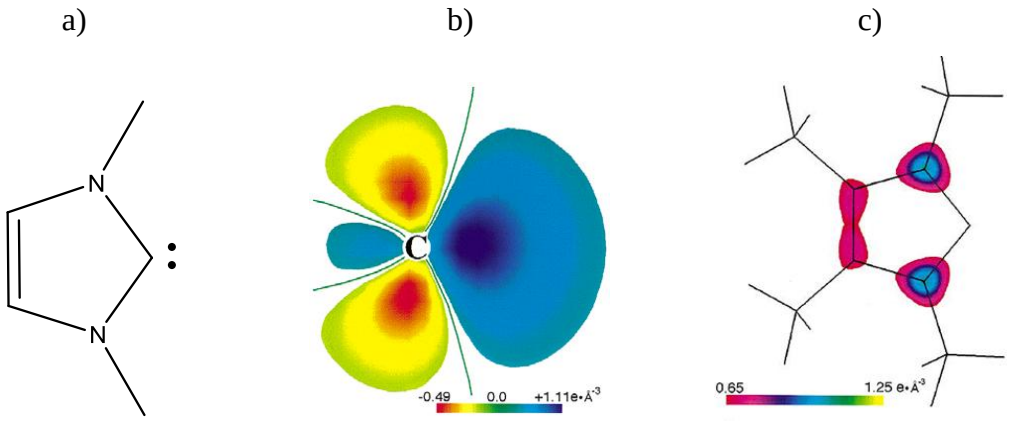

Figure 1.10 Valence electron density determined for 1,3,4,5-tetramethylimidazol-2-ylidene.

2. Theory confirming the presence of cyclic electron delocalization introduced independently by Apeloig and Frenking, derived from structural, thermodynamic and magnetic data and ionization potentials. Although this aromatic character is less pronounced than in the imidazolium salt precursors (as it has been confirmed by X-ray diffraction data, See section 1.2.3), it provides an additional stabilization of ca. 20 kcal/mol (Figure 1.11).

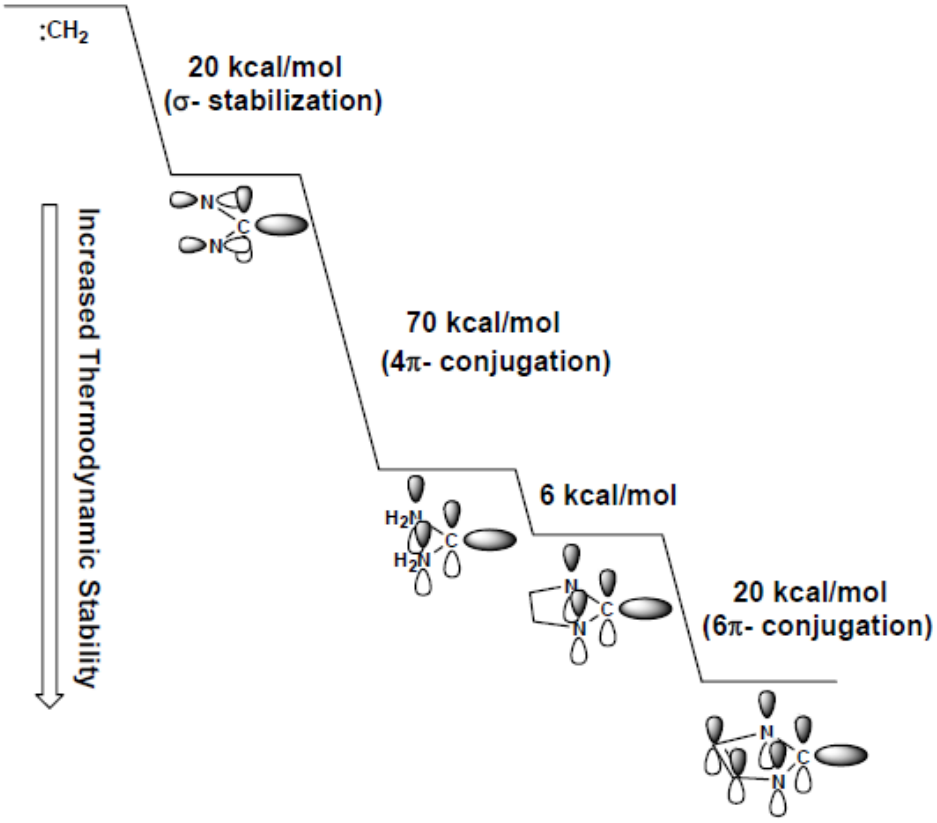

Figure 1.11 Diagram of thermodynamic stability of different carbenes obtained from DFT calculations.

Combining the two foregoing arguments, it can be concluded, that electron delocalization indeed occurs, nevertheless the major stabilizing effect is ascribed to the influence of the π-donors σ-attractors nitrogen atoms bonded to the carbene center. This statement is in agreement with the fact that non-aromatic aminocarbenes have also been isolated.

1.2.5 Reactivity

As it was briefly mentioned in the general introduction, the reactivity of singlet carbenes is determined by the potential of acting as both electrophilic and nucleophilic agents and these species can be used for a preparation of carbene-Lewis base and carbene-Lewis acid adducts, respectively.

The following description of reactions of N-heterocyclic carbenes only covers the cases related to the transient species.

1.2.5.1 1,2-Migration Reactions

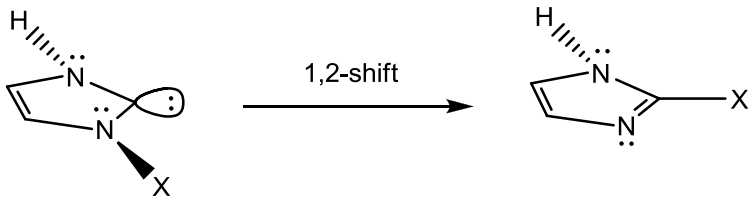

Scheme 1.11 1,2-Migration reaction.

For aromatic NHCs the reaction occurs strictly via intermolecular process, because an intramolecular reaction in the plane of the ring is forbidden with regard to the non-crossing rule (two orbitals with the same symmetry cannot cross) formulated by von Neumann and Wigner[15]. For this reason, the migration requires a carbene and an electrophilic agent.

1.2.5.2 Carbene dimerization

The dimerization reaction leading to the corresponding enetetramines makes a major limitation in synthesis of a stable diaminocarbenes. Two different mechanisms are proposed for the discussed reaction. The first one postulates the attack of the lone electron pair placed in the in-plane σ orbital of one carbene molecule toward the unoccupied out-of-plane p_π orbital of the other carbene (Figure 1.12). Since the carbene vacant orbital has a high energy

resulting from the interaction with lone electron pairs of neighboring nitrogen atoms, the energy of the formed double bond should be high, which is in agreement with experimental data (dimerization energy 19-45 kcal/mol).

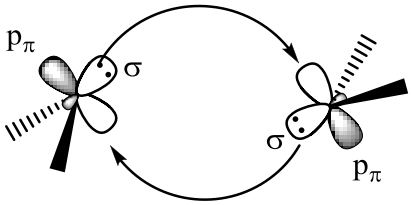

Figure 1.12 Schematic representation of the dimerization of singlet carbenes via interaction of lone electron pairs.

The second proposed mechanism relies on the nucleophilic attack of a carbene upon its conjugate acid (imidazolium salt) and a subsequent proton elimination.

The imidazolidinylidenes (saturated ring systems) and imidazolylidenes (systems containing one double bond) reveal an opposite stability with respect to the dimerization. In the case of the formers, the equilibrium is shifted towards the formation of the dimeric tetraazafulvalenes; in order to prevent the dimerization, the carbenes can be stabilized with sterically demanding substituents. On the other hand, the dimers of the imidazolylidenes are unlikely to form, even in a case of the molecules with small substituents such as methyl group, (Figure 1.13).

a) b)

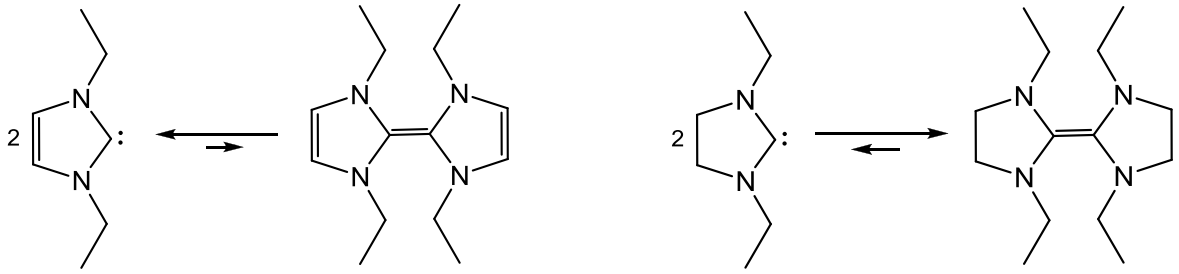

Figure 1.13 Stability toward dimerization of imidazolidinylidenes (a) and imidazolylidenes (b).

1.2.5.3 Addition to multiple bonds

As it was shown in the general introduction, both singlet and triplet transient carbenes, plying the role of electrophiles, react with multiple bonds of a variety of compounds, but by a totally different mechanism; the addition reactions involve olefins, carbonyl derivatives and carbon-heteroatom triple bonds.

In the reaction with alkenes, transient singlet carbenes, in contrast to those with the triplet ground state, react in a single concerted step, leading to cycloalkanes in a stereospecific manner, (Scheme 1.12).

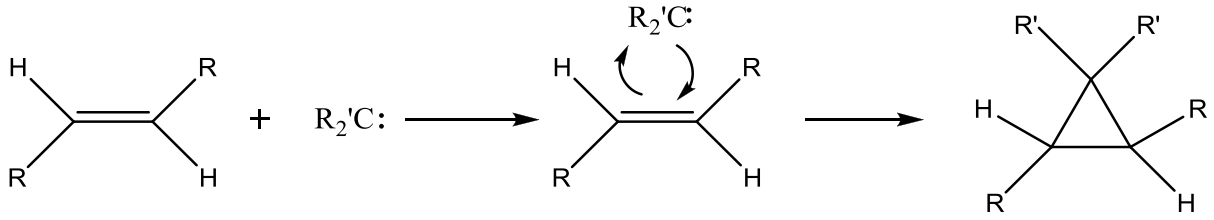

Scheme 1.12 One-step addition of a singlet carbene to carbon-carbon double bond.

The reaction with carbonyl derivatives goes through the donation of the oxygen lone pair toward the empty orbital of an electrophilic carbene, leading to carbonyl ylides which immediately react with unsaturated species via [3+2]-cycloaddition, Scheme 1.13.

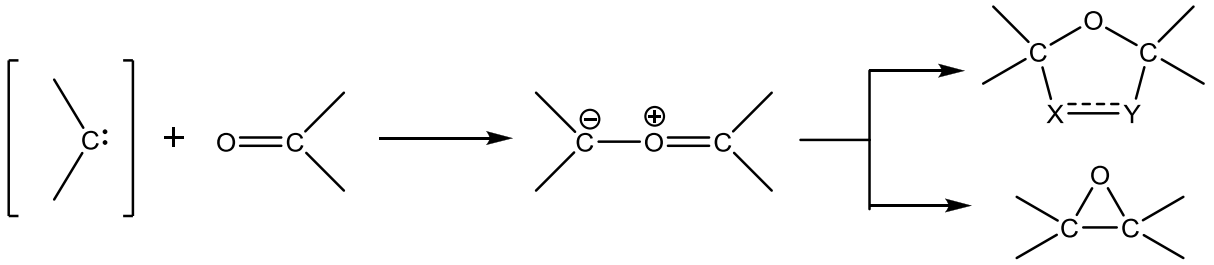

Scheme 1.13 Addition to carbonyl derivatives.

Similarly, transient electrophilic carbenes are known to react with nitriles to afford nitrile ylides, Scheme 1.14.

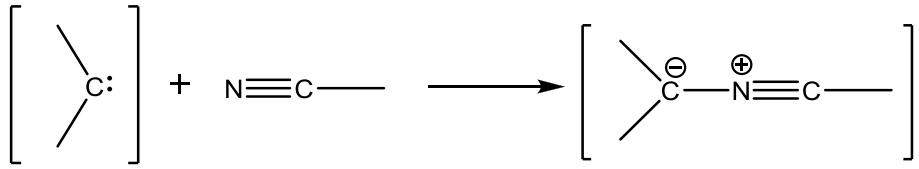

Scheme 1.14 Addition to carbon-heteroatom triple bonds.

1.2.5.4 Insertion reactions

Insertion into C-H bonds is a well established reaction of transient singlet and triplet carbenes. However, singlet carbenes, as opposite to the others, react in a one-step process, according the spin conservation rule, involving a three-center cyclic transition state as shown in Scheme 1.15.

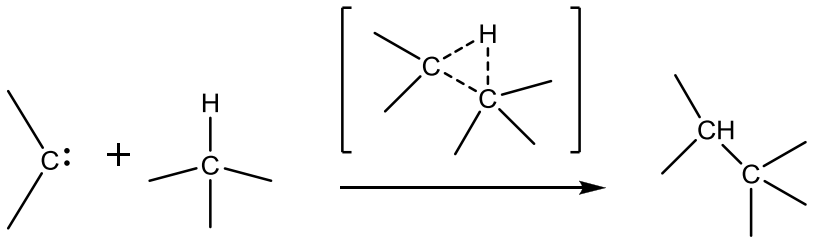

Scheme 1.15 Insertion into unpolarized C-H bonds.

1.2.5.5 Carbene-Lewis acid and carbene-Lewis base adducts.

a) The carbene-Lewis acid adducts (reverse ylides) result from the reaction between a nucleophilic carbene and an acid possessing an empty orbital, according the Scheme 1.16;

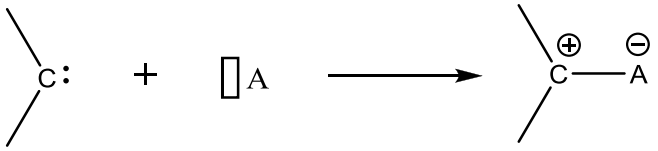

Scheme 1.16 Formation of reverse ylide from a free carbene and Lewis acid.

for instance adducts of carbenes with elements of groups 13, 14, 15, 16 and 17 of the periodic table. Another interesting example of this kind of reaction is the protonation of a carbene. Particularly, the imdazol-2-ylidenes, being strong bases can go through the proton exchange between the free carbene and its conjugate acid as shown in Scheme 1.17; it is worth mentioning that the bis(carbene)-proton complex bearing significantly bulky mesityl substituents, has been isolated by Arduengo[16].

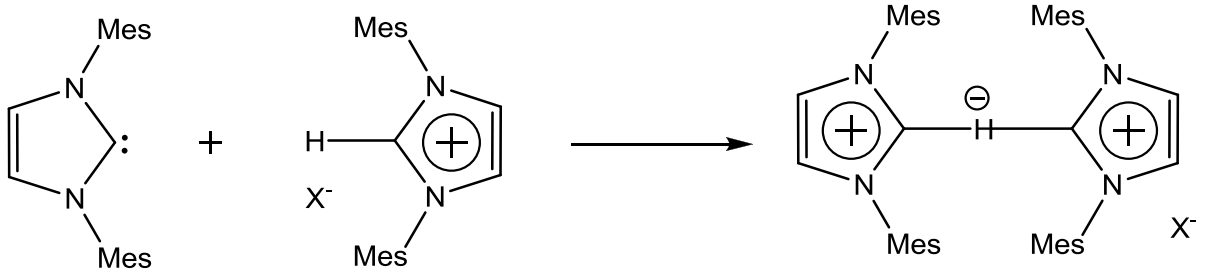

Scheme 1.17 Protonation of a free carbene leading to unusual 3-center 4-electron biscarbene system.

b) On the other hand, the reaction between electrophilic carbenes with a lone electron pair of a donor leads to the formation of normal ylides, as reported in Scheme 1.18, for instance the carbene-pyridine adducts.

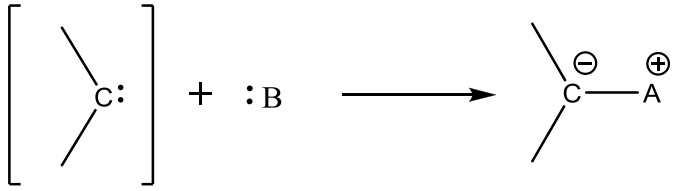

Scheme 1.18 Formation of a normal ylide from a free carbene and Lewis base.

1.2.6 N-heterocyclic carbenes–transition metal adducts

The first two metal (Cr, Hg) complexes with N-heterocyclic carbenes as ligands (Figure 1.14) were reported in the literature by Wanzlick[17] and Öfele[18] in 1968. Both of them were synthesized from the corresponding imidazolium salts and metal precursors containing a sufficiently basic group to deprotonate the salts.

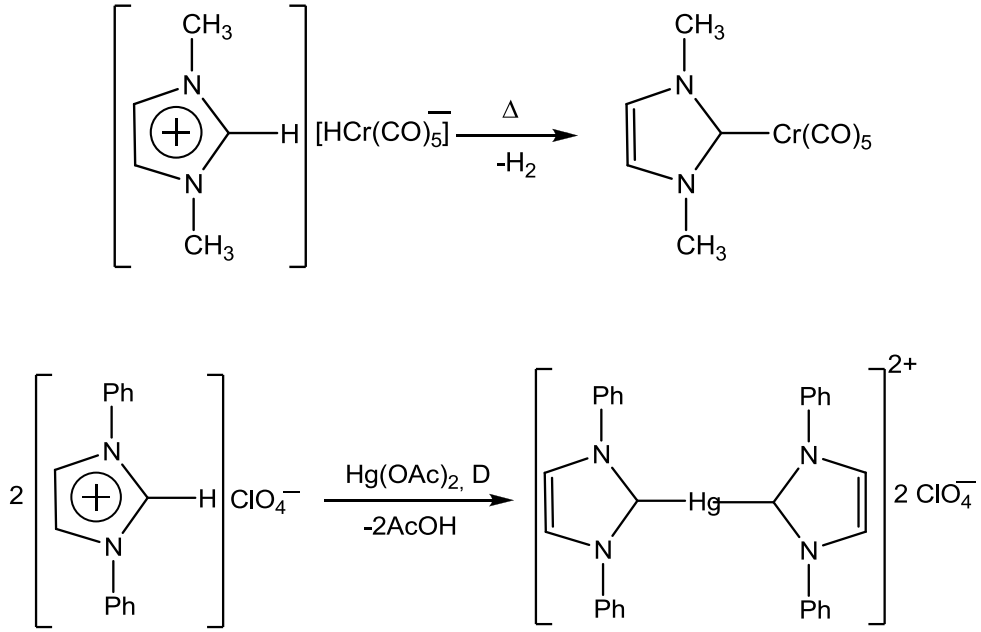

Figure 1.14 Two first metal complexes with N-heterocyclic carbenes as ligands.

1.2.6.1 Synthesis

There are several routes leading to the transition metal complexes with NHCs, shown in Figure 1.15 and described below.

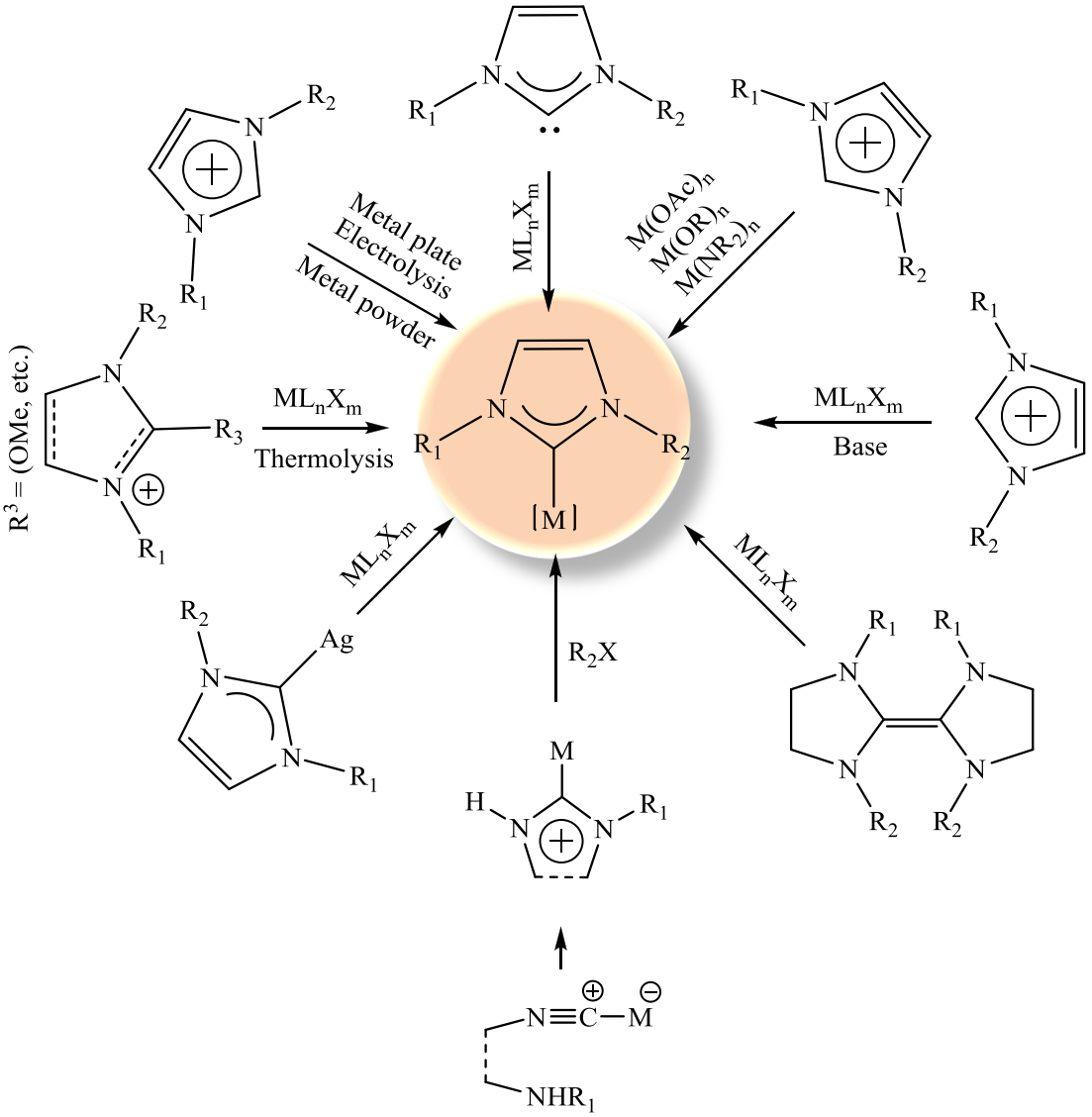

Figure 1.15 Synthetic routes to metal-NHC complexes.

1. The reaction between free carbenes and metal precursors possessing easily replaceable two-electron donor ligands, such as tetrahydrofuran, carbon monoxide, nitriles, phosphines or pyridine. The reaction can involve multiple substitution, affording bis- or even triscarbene complexes. The obvious difficulty and the resulting limitation of this synthetic method relies on the isolation of the free carbene[19].

2. Deprotonation of the azolium salts in the reaction with suitable transition metal salts, containing a basic ligand such as hydride, alkoxide or acetate. This method is commonly

applied for synthetizing metal-carbene complexes due to its versatility with comparison to the first described route[18].

3. In situ deprotonation reaction of an imidazolium salt with a transition metal precursor in the presence of a base (K_2CO_3, NEt_3, etc.)[20].

4. Reaction of the corresponding electron-rich olefin dimers with metal precursors leads to a imidazolidin-2-ylidene complexes[21].

5. Transformation of other C-bound ligands, for example inter- or intramolecular addition of N-nucleophiles to coordinated isocyanides[22].

6. Transfer of a carbene between different transition metal centers. The most commonly used NHC transfer reagents are Ag(I) complexes[23,24,2]. This method is very well established for the preparation of a broad veriety of transition metal-NHCs complexes such as: Au(I), Pd(II), Rh(I), Rh(III), Ir(I), Ir(III), Cu(I), Cu(II), Ru(II), Ru(III), Ru(IV), Ni(II), Pt(II)[24].

7. Thermal decomposition of carbene adducts of alcohol, chloroform, pentafluorobenzene, CO_2, CS_2, cyanide and phosphenium in the presence of metal precursor[23].

8. Reaction of imidazolium salts and metal powders in air[25].

1.2.6.2 Electronic properties

Since the unique bonding properties of NHCs as ligands in transition metal chemistry determine the activity of the coordinated metal center, which in turn has an impact on catalytic properties of these systems, the electronic properties of the metal-carbene complexes were profoundly studied.

Two types of complexes can be distinguished according to the nature of bonding between a carbene and a metal.

1. **Fischer-type** complexes with the carbene-metal bond originating from the carbene to metal σ donation and the metal to carbene π-backdonation (donor-acceptor bond), Figure 1.16a.

2. **Schrock-type** complexes with the metal-carbene bond having covalent nature, resulting from the overlapping of singly occupied orbitals of triplet carbenes and triplet metal fragments, Figure 1.16b.

a) b)

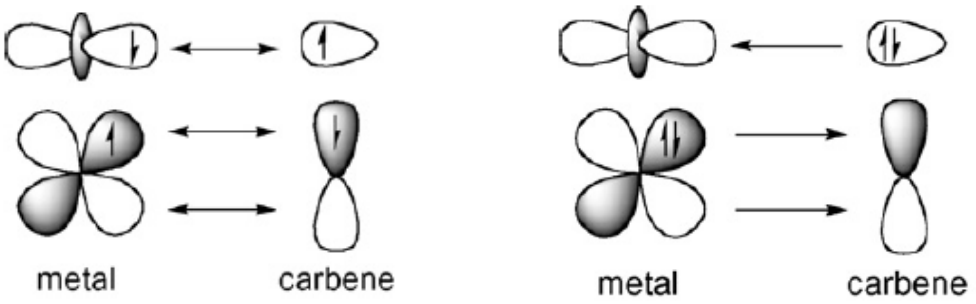

Figure 1.16 Metal–carbon bonding in Schrock (a) and Fischer (b) carbene complexes.

Fischer complexes are formed with electron-rich (low valent) metal atoms/cations and carbene centers stabilized by electron donation from the π-donor substituents. In contrast, Schrock complexes are formed with electron-poor metal centers (in high oxidation states) and π-withdrawing substituents.

In 2000, Bertrand in his comprehensive review on stable carbenes highlighted the superiority of carbene to metal σ-donation over the metal to carbene π-donation in case of N-heterocyclic carbenes, describing the latter as negligible. The NHCs should be then considered as a non-classical Fischer complexes according to the definition given above. Bertrand at this point refers to the results obtained by photoelectron spectroscopy and DFT calculations presented by Arnold et al.[26] However, this point of view is not free from controversies and has been recently quaestioned[27] (See section 1.5); particularly, the π-back bonding component is reported to be significant for group 11 metals, copper, silver and gold[5,28]. The general consensus in this affair can be formulated in a way that the π-back-donation to NHCs exists but is smaller than the π-back-donation of Fisher carbenes.

1.2.6.3 Comparison between phosphines and NHCs as ligands

For a long time, NHCs were considered to be so-called "mimics" of phosphines due to significant similarities in electronic properties.

In metal complexes, both of these two groups of compounds play the same role of monodendate two-electron donor ligands. The ability of phosphines and NHCs to accept electrons from orbitals of a metal was studied by the use of IR spectroscopy in a series of nickel, rhodium, iridium[29,30] and iron[27] complexes containing carbenes, phosphines and CO ligands. In a totally symmetric vibrational mode of CO specie, more basic ligands (better σ-

donors) induce lower vibrational frequencies (See section 1.5). These studies showed that NHCs surpass even most basic phosphines in the electron donating ability and for this reason the bonds formed by NHCs with metals are considered to be stronger that the metal-phosphines, Scheme 1.19.

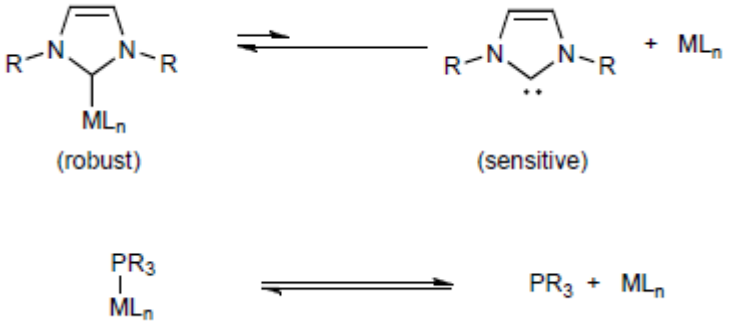

Scheme 1.19 Shift of equilibrium towards the formation of carbene-metal complexes from the free carbenes and comparison with the equilibrium for phosphines.

Another aspect differing phosphines and NHCs is the ability of the latters to form complexes with alkaline, lanthanides and high oxidation state metals in which the π-back-donation does not occur. The stability of NHCs toward oxidation will be discussed in the section devoted to the catalytic properties of transition metal-NHCs complexes (Section 1.6).

1.3 N-Heterocyclic carbene silver(I) complexes

The high interest in studying Ag(I)-NHCs emerges mainly from the ease of their preparation and the transmetallation efficiency to obtain other important metal-NHCs. In addition, the silver(I) complexes hold potential applications in medicine, nanomaterials, liquid crystals and organic synthesis.

1.3.1 Synthesis

There are two general synthetic ways to obtain Ag(I)-NHCs: (1) the silver base method and (2) the free carbene method; additionally, Garrision and Youngs[28] distinguish (3) the in-situ reaction of imidazolium salts with a base in a presence of silver salt and (4) the transmetallation between a complex of tungsten-NHC and silver precursor.

In spite of the fact that the first structurally characterized Ag(I)-NHC complex was synthesized via the free carbene and silver salt route, the use of Ag_2O both as a base and silver source in the complexes syntheses is most common among the other possibilities for few following reasons: (1) Ag_2O is relatively stable and readily accessible, (2) the reactions can be carried out in mild conditions, (3) special preparation of the solvents is not required, (4) chirality can be retained.

The free carbene route is not favorable due to the requirement of using strong bases such as KH or KO^tBu; the main risk is that the base can attack other acidic protons in the ligand. This argument is especially significant for ligands containing methylene groups in α position with respect to the nitrogen atom, where the deprotonation usually leads to the products of decomposition instead to the free carbene[28] (Scheme 1.20).

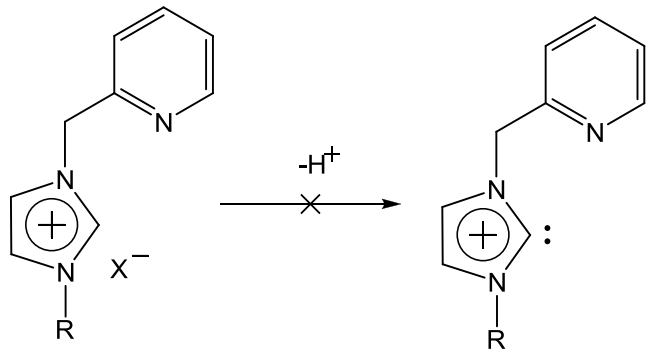

Scheme 1.20 Unsuccessful deprotonation of methylene-linked imidazolium salt.

1.3.2 Structures.

The Ag(I)-NHC complexes reveal a great structural diversity in the solid state. Whereas the imidazolium ligands in the presence of silver source and non-coordinating anions form invariably a structural motif with two carbene moieties bound to the silver cation, the silver complexes with coordinating anions like halides, are found to form five different bonding motifs, presented in Figure 1.17.

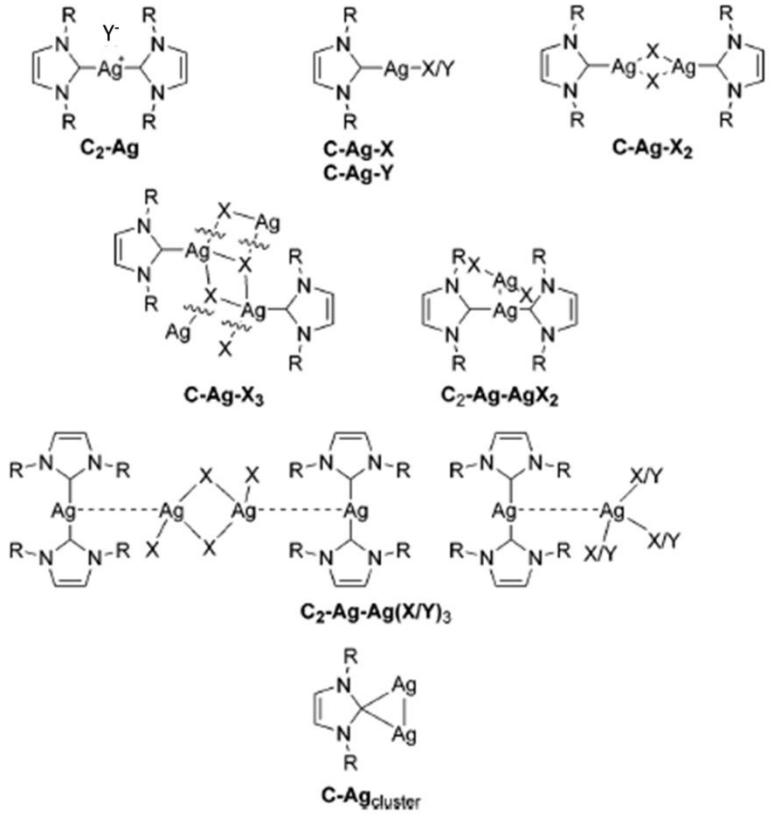

Figure 1.17 Bonding motifs of silver N-heterocyclic carbenes. X = halide and Y = non-halide.

These structures are described as: coordinating (C-Ag-X/Y), bridging (C-Ag-X_2), staircase (C-Ag-X_3), halogeno counterion of type $[AgX_2]^-$ (C_2-Ag-AgX_2), halogeno counterions of type $[Ag_2X_4]^{2-}$, and silver NHCs with silver-silver interactions that are stabilized by three donor groups.

1.3.3 NMR

One of the most common techniques, used for a characterization of the Ag(I)-NHCs, is ^{1}H and ^{13}C NMR spectroscopy, which is justified by the experimental difficulty to obtain single crystals suitable for the X-Ray diffraction. In fact, the information about the presence of the silver complexes gained from the NMR experiments is immediate. The characteristic feature of ^{13}C NMR spectrum is the resonance of the carbon atom of carbene coordinated to silver, appearing over a wide range of chemical shift: 213.7 – 163.2 ppm[28]. The observed signal appears as a singlet, or a doublet due to the coupling to the magnetically active silver nucleus, with a spin of 1/2. Silver has two naturally occurring isotopes, ^{107}Ag and ^{109}Ag, with

a percent abundance of 51.839(7)% and 48.161(7)%, respectively. The ^{1}J coupling constants range from 180 to 234 Hz and 204 to 270 Hz[28], respectively for the two isotopes. Therefore in theory, the expected splitting pattern in the cases where the coupling is observed, should be consisted of a doublet of doublets due to the presence of the two isotopes. However, in majority of cases the splitting is not observed. This interesting property of the spectra was attributed by Lin and coworkers[31] to the fluxionality of silver NHC complexes on the NMR time scale. The presence of the singlet is explained by the increase of the velocity of the exchange of the ligands, resulting in the averaged picture in ^{13}C NMR spectrum. On the other hand, the presence of the doublet (or doublet of doublets) indicate either a static conformation of the complex in question, or a process which is very slow on NMR time scale.

1.4 Rhodium(I)-NHC complexes

Most of the rhodium(I) complexes with NHCs described in the literature were synthesized via transmetalation from corresponding silver(I)-NHC complexes in the presence of adequate rhodium precursor; this method has the advantage of avoiding the harsh reaction conditions provided by the use of a strong base to form the free carbene; consequently, the syntheses from silver complexes afford the rhodium compounds in high yields (70-90%). This protocol has been used for the first time in 2003[30].

As it was mentioned before, some rhodium-NHC complexes containing carbonyl derivatives as ligands, likewise few other transition metal complexes (Ni, Ir and Fe) have been employed as probes for the basicity of the N-heterocyclic ligand, by means of IR spectroscopy; this method allows for the determination of Tolman electronic parameters for NHCs.

Moreover, rhodium (and iridium and iron[32])-NHC complexes reveal unique properties (never observed before in the NHC chemistry, neither for other phosphine-related complexes[33]), namely aliphatic and aromatic C-H activation[33,34]; these (mostly) intramolecular processes lead to corresponding cyclometalated species. Specifically, a very interesting, highly unusual behavior has been reported by Nolan et al. for a rhodium dimer $[Rh(COE)_2Cl]_2$ (COE–cyclooctene) reacting with I^tBu = N,N-di(tert-butyl)imidazole-2-ylidene, shown in Scheme 1.21.

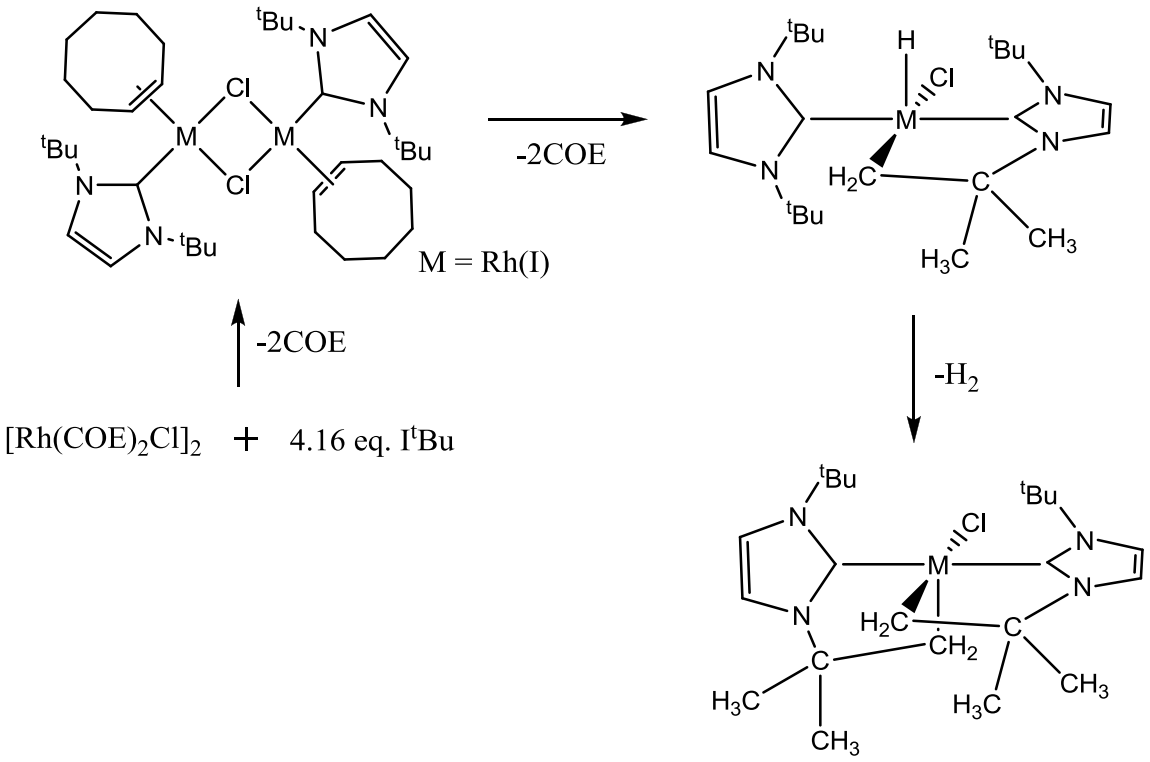

Scheme 1.21 Unprecedented reactivity between I^{t}Bu and Rh(I) dimer leading to doubly cyclometalated complex.

Furthermore, some rhodium-NHC (NHC = imidazolin-2-ylidene) complexes, bearing a sterically demanding ligand such as COD (1,5-Cyclooctadiene) or NBD (norbornadiene), display restricted rotation about the metal-carbene bond (which is essentially single), the rate of which can be controlled by altering the steric bulk of the auxilliary ligands. For instance, a study related to the stereodynamics of the series of rhodium(I) complexes [Rh(NBD)X(NHC)] (NHC = 1-(2-NHBoc-ethyl)-3-R-imidazolin-2-ylidene; X = Cl, R = Me, Bz, trityl; X = I, R = Me) has been recently reported[1]; the steric hindrance of these complexes has been examined by means of VT NMR, which can provide kinetic and thermodynamic information and moreover determine the possibility to separate the two enantiomers, resulting from the dynamic behavior (Figure 1.18)

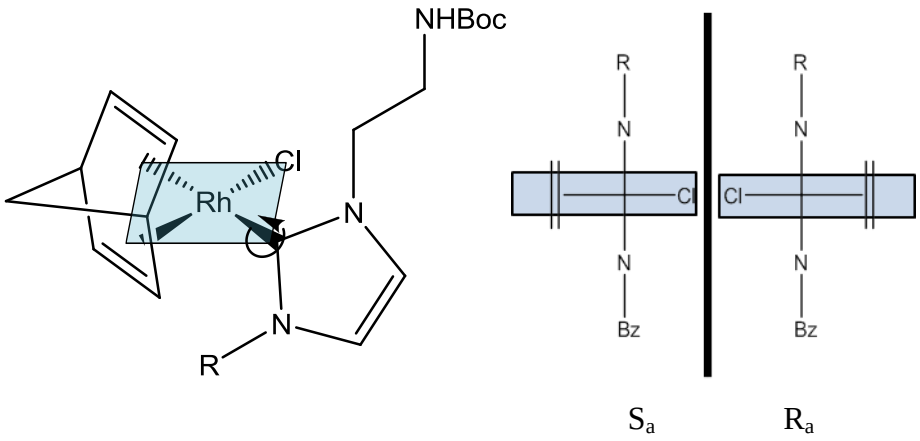

Figure 1.18 Enantiomers resulting from the hindered rotation about rhodium-carbene bond.

1.4.1 Atropoisomers

Atropisomers are stereoisomers resulting from hindered rotation about single bonds where the steric strain barrier to rotation is high enough to allow for the isolation of the conformers[35]; they display an axial chirality which generates enantiomers in the absence of stereogenic centers. This class of compounds has attracted considerable attention due to its potential in asymmetric syntheses and catalysis.

Formally, atropisomers are conformers that interconvert with a half-life of more than 1000 seconds at a given temperature. Atropoismerism was first time detected in biaryl compound 6,6'-dinitro-2,2'-diphenic acid in 1922 (Figure 1.19);

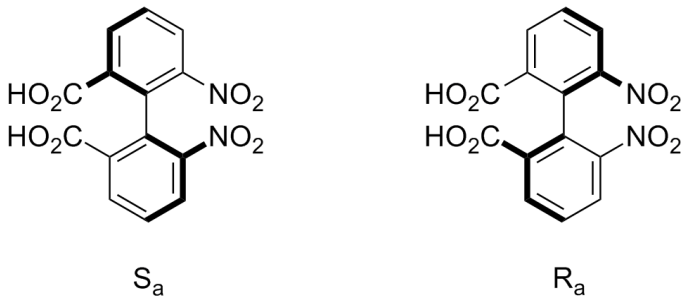

Figure 1.19 Atropisomers of 6,6'-dinitro-2,2'-diphenic acid.

The equilibrium between atropoisomers can be reached thermally, as opposite to other chiral compounds, which must be treated chemically.

1.5 Iron(II)-NHCs complexes

The inquiry into *N*-heterocyclic carbene piano-stool iron(II) complexes within the framework of this thesis arises from the fact that these systems reveal particular properties. First of all they have been already investigated as a probes for the bonding of *N*-heterocyclic carbenes to transition metal complexes[27] and this study opened a new perspectives for the interpretation of the acceptor properties of the carbenes. Additionally, the iron is an interesting alternative to other transition metals used in homogeneous catalysis, because it is cheap, non-toxic, environmentally friendly and abundant[32]; specifically, the iron complexes display the catalytic activity in hydrosilylation of carbonyl derivatives and hydrogen transfer reactions. However, despite the interesting chemistry behind, iron is still one of the rare transition metals which has not been intensively studied in the context of NHCs.

The particular constitution of piano-stool iron(II) complexes, which possess both the redox active Fe^{II} center and CO ligand(s), makes them to be an attractive probes for measuring the carbene basicity in a quantitative way (Figure 1.20).

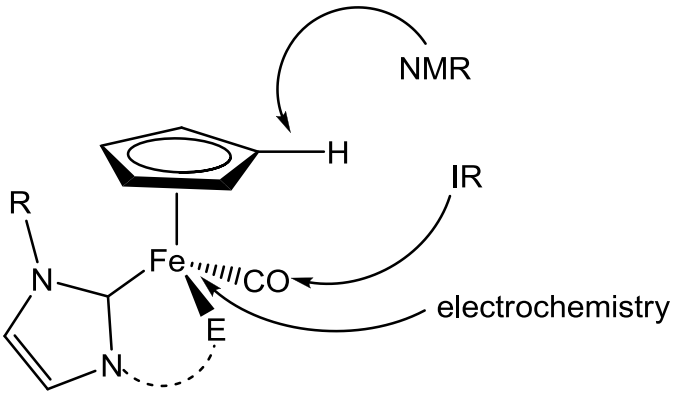

Figure 1.20 Direct and indirect probes for ligand tuning in Fe(II) carbene complexes.

1.5.1 CO as a ligand.

Carbon monoxide bonds to transition metals using its HOMO and LUMO orbitals (Figure 1.21). The σ-bond results from an overlap of the occupied, nonbonding orbital of the carbon with an empty d orbital of a metal. A pair of π bonds arises from an overlap of filled d orbitals of a metal with the two degenerate π* antibonding LUMO orbitals of the carbon. This bonding has a synergic mechanism. The displacement of the electrons of the metal towards the empty orbitals of CO in the π bonding, increases the basicity of CO in the σ bonding. On the other hand, the partial shift of the electrons of the carbon toward the metal center, induces

a local electron deficiency on the CO ligand, which increases its ability as an π acceptor. In simple words, formation of the σ bond strengthens the π bond and the opposite.

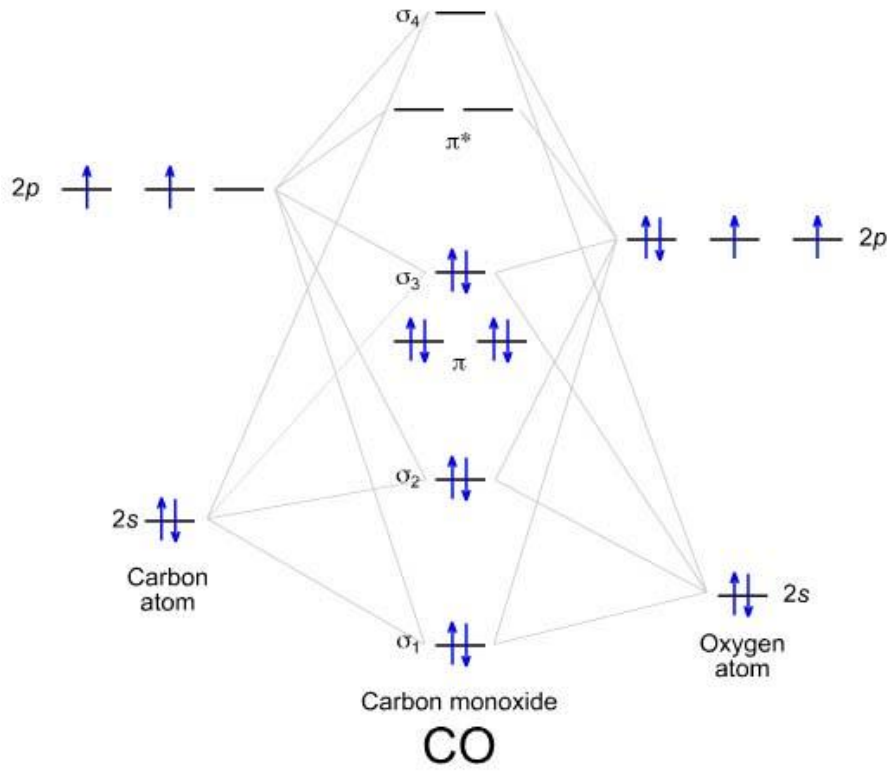

Figure 1.21 Molecular orbitals (MO) diagram of carbon monoxide.

The electron density on a metal center in complexes containing CO as a ligand can be monitored by IR spectroscopy. The increase of the electron density on a metal is delocalized on the CO ligands by occupying the π* antibonding orbitals, which leads to a weakening of the C≡O triple bond. This in turn causes the shift of the CO stretching band in IR spectrum to lower frequencies.

1.5.2 Electrochemical measurements

The possibility of using electrochemical analysis for the ligand basicity determination, relies on the fact that ligands being strong *σ* donors can easily saturate the metal center with the electron density, which leads to the facilitated oxidation of iron(II) to iron(III). As a consequence, the Fe^{III}/Fe^{II} redox potential can be used as a probe of the ligand basicity[27].

The oxidation potential is much lower in case of the neutral iron(II) complexes than in the cationic forms. Moreover, the electronic parameters which can be derived from the

electrochemical analysis indicate only a minor differences between the basicity of carbenes, pyridines and most basic phosphines.

1.5.3 Nature of bonding of NHCs to iron

The information derived from the electrochemical measurements are in accordance with the ^{1}H NMR data, which show similar chemical shift for the cyclopentadienyl ring protons in iron complexes bearing pyridine and the ones bearing carbenes as a ligands. This suggests that there must be a significant contribution of π back-bonding from metal to carbene in order to balance the stronger effect of σ donation of carbenes when compared to pyridine. This indication is eventually confirmed by DFT and calculations of a transferred charge from metal to ligand in three iron complexes containing CO, pyridine and NHC, respectively. These results may be extrapolated for other metal-NHCs.

Finally, the orbitals which are involved in π back-bonding in the Fe-NHCs have been determined as the HOMO of the $[Fe(cp)(CO)_2]^+$ fragment as a donor and the NHC's π* antibonding orbital LUMO+1.

1.5.4 Synthesis

These complexes are attainable by synthetic route starting from corresponding imidazolium salts and followed by deprotonation with a strong base like KO^{t}Bu and subsequent in situ metalation with iron(II) precursor $[FeI(cp)(CO)_2]$ to form a cationic compound with a halide as a counter ion (Figure 1.22). Interestingly, under UV irradiation, the complexes lose CO, which place is filled by the halide atom to afford neutral iron compounds[27].

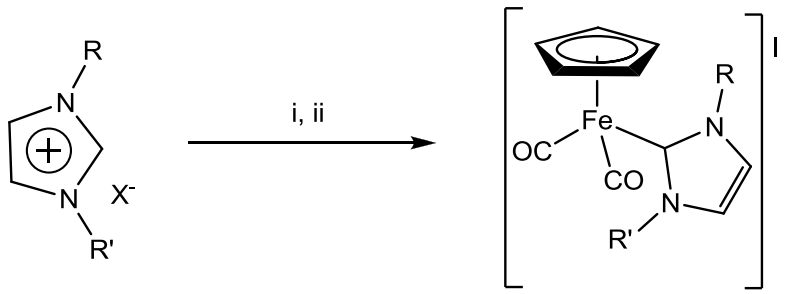

(i) [FeI(cp)(CO)2], toluene, r.t., 20 h
(ii) KO^{t}Bu, THF, r.t., 1.5 h

Scheme 1.22 Synthetic protocol leading to piano-stool iron(II) complexes.

Another very interesting, unprecedented protocol has been proposed by Royo et al.[32] consisting in oxidative addition of the C–H bond of imidazolium to Fe(0), followed by elimination of the Fe–H intermediate and the cyclopentadienyl proton, as shown in Scheme 1.23

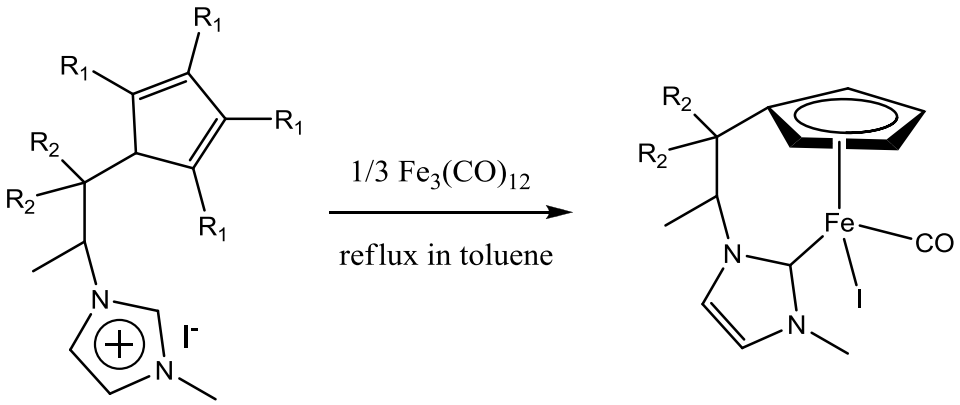

Scheme 1.23 Synthesis of piano-stool iron(II)-NHC complexes under mild conditions.

It is noteworthy that this type of C–H activation is unique in Fe–NHC chemistry. The big advantage of this method is the lack of necessity to use a base, which can lead to the decomposition of imidazolium salts as precursors for the complexes synthesis. According to the report of Royo, the synthesis affords only one diastereoisomer in spite of the fact that the aliphatic linker between the NHC and the cyclopentadienyl ring and the metal center both possess a stereogenic centers.

1.6 Catalytic properties of transition metal-NHCs complexes.

N-heterocyclic carbenes, due to their particular coordination chemistry, became recently "broadly catalytically useful ligands"[36] with the potential to supplement and in part, replace the ubiquitous class of organophosphanes in a number of organometallic catalytic reactions. NHCs both stabilize and activate metal centers in different catalytic steps of organic syntheses, for example, C-H activation, C-C, C-H, C-O and C-N bond formation[8]. Nowadays, the most common NHCs used in catalysis are five-membered ring imidazolylidenes and imidazolinylidenes, whose impressive versatility has been proven in many types of catalytic reactions[37]. Their outstanding potential as supporting ligands in metal-mediated catalytic reactions arises mainly from the remarkable stability of the formers, especially in an oxidation conditions. An illustrative example can be the formation of a rhenium-NHC complex in the

course of the reaction of methylrhenium trioxide (MTO) with a free carbene, in THF at 60 °C[38] (Scheme 1.24).

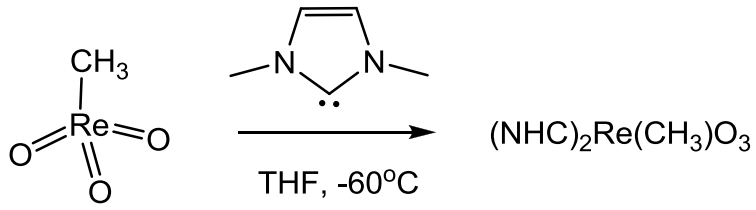

Scheme 1.24 Reaction between MTO and a free carbene leading to a Re-NHC complex.

The used NHC was shown to be stable toward oxidation at -60°C, whereas phosphines are rapidly oxidized with MTO. The formed complex is stable below -20°C.

Moreover, the strong σ-electron-donating properties of NHC, making the carbene-metal bond so strong, prevent the dissociation of the carbene from the metal center, hence no ligand excess is required.

Additionally, N-heterocyclic carbenes have been found to be active in asymmetric catalysis. The preparation and use of enantiomerically pure complexes with a chirality introduced to different parts of the carbene molecules has been reported; the complexes can feature either chiral substituents at the nitrogen atoms, a chiral ring framework, a chiral metal center or a chiral backbone (Figure 1.22).

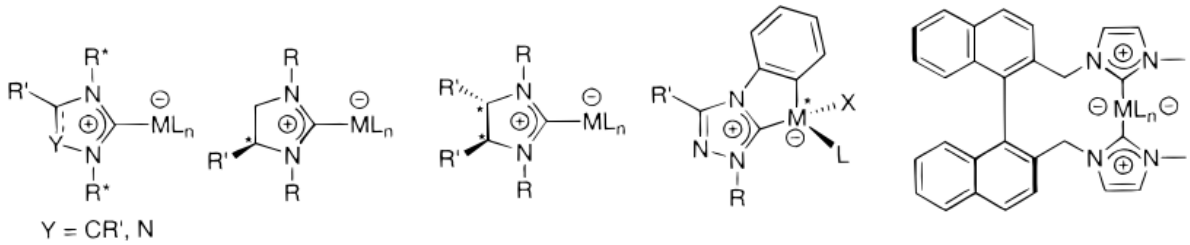

Figure 1.22 Different types of chiral NHCs.

Overview of the most investigated catalytic reactions employing transition metals-NHCs as the catalysts:

1. Heck-type reactions.

Heck-type reactions lead to products of coupling between halide-substituted aromatic species and unsaturated compounds such as alkenes, alkynes and aromatic rings, shown in Scheme 1.25.

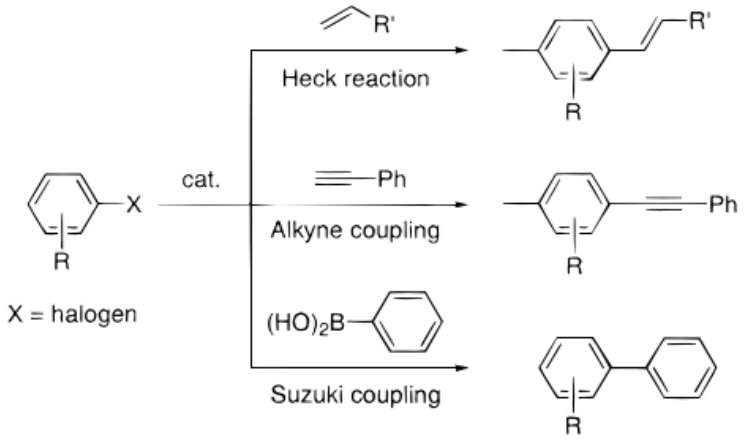

Scheme 1.25 Heck-type reactions.

Catalysts used for these reactions are palladium complexes with the general formula $[PdL_2I_2]$ adopting the usual square-planar geometry and bearing two NHC (namely 1,3-dimethylimidazole-2-ylidene) and two iodides as ligands (Figure 1.23).

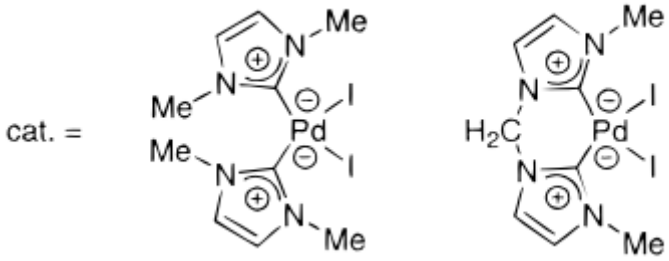

Figure 1.23 Palladium(II) catalysts for the Heck-type reactions.

2. Hydrogenation of olefins.

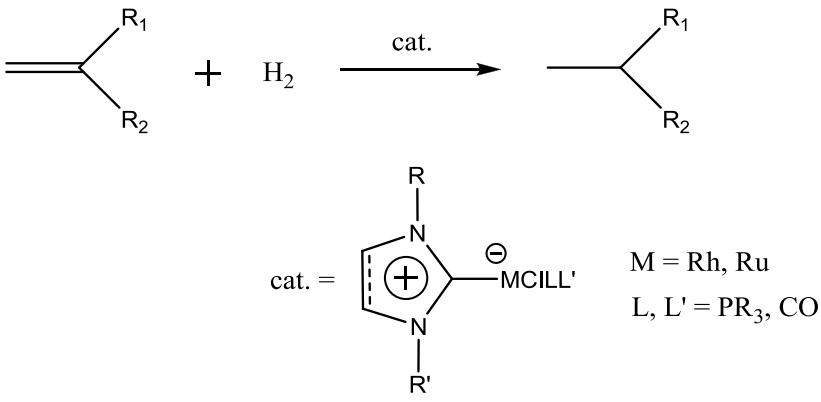

Scheme 1.26 Hydrogenation of olefins.

The reactions between olefins and hydrogen, shown in Scheme 1.26 are catalyzed by rhodium(I) and ruthenium(II) complexes possessing both N-heterocyclic carbene and phosphine as ligands. The use of the mixed systems is justified by the difference in electronic properties of these ligands; due to the fact that phosphines are weaker σ-donors and stronger π-acceptors than carbenes, the electron density at the metal center is decreased when comparing with biscarbene complexes, which facilitates the reaction of the reagent with H_2.

3. Hydroformylation of olefins.

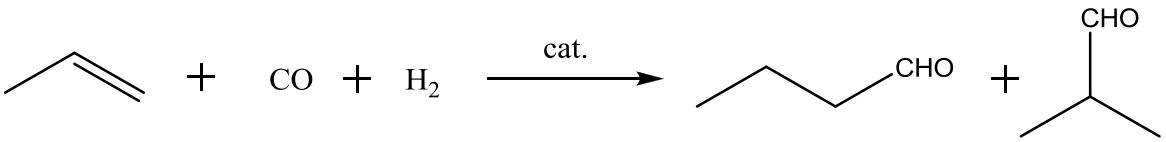

Scheme 1.27 Hydroformylation of olefins.

Hydroformylation of olefins relies on a reaction of an alkene with carbon oxide and hydrogen to afford corresponding aldehydes, Scheme 1.27. Rhodium(I)-NHC complexes have been successfully employed as catalysts in this reaction, although their activity has been found as slightly lower than with the use of triphenylphosphine complex $RhH(CO)(PPh_3)_3$, due to the increase of the electron density on metal center by the carbene. Nevertheless, the rhodium(I)-NHC complexes such as [RhCl(COD)(carbene)], $[RhCl(PPh_3)_2$-(carbene)], [RhCl(CO)(PPh3)(carbene)] or [RhCl(CO)(carbene)2] are still considered as a promising alternatives for the phosphines due to the long-term stability of the N-heterocyclic carbenes.

4. Hydrosilylation reactions.

Various rhodium- and ruthenium-carbene complexes have been investigated in the hydrosilylation reactions, which involve the addition of inorganic or organic silicon hydrides to multiple bonds such as alkyne, alkene and carbonyl groups[39] (Scheme 1.28).

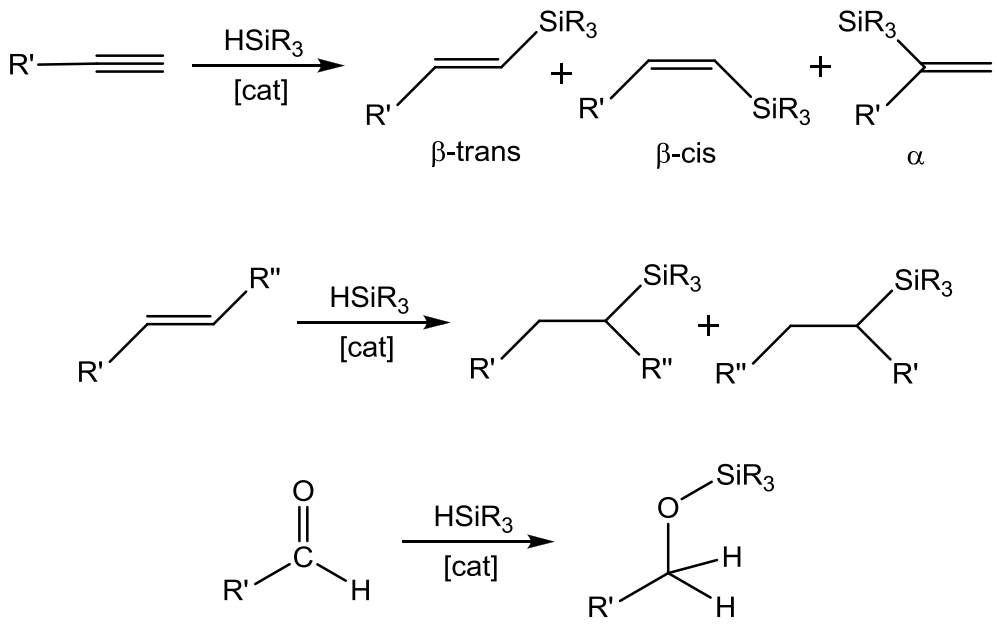

Scheme 1.28 Hydrosilylation reactions.

Regarding the hydrosilylation reactions of terminal alkenes, rhodium-NHC complexes (both the complexes possessing only NHCs and systems combining NHCs with phosphines) have been proved to be better catalysts in the anti-Markovnikov addition that complexes of a type $[RhCl(PPh_3)_3]$, bearing only the phosphines ligands, due to the increase of the electron density at the metal center in case of the NHC complexes, thanks to the remarkable donating ability of carbenes[39].

With alkynes, mixture of α-2-silyl-1-alkyl and cis and trans silylated alkenes are generally obtained but cis to trans isomerization is completely achieved by the elongation of the reaction time or alternatively by heating. The drawback of this reaction is the difficulty to obtain the desired products in good yields in a selective way; usually the increase in the yield induces a drop in the selectivity and the opposite; for instance, the rhodium complex shown in Figure 1.24a, synthesized by Buchmeiser[39], was examined in the hydrosilylation of ketones, alkenes and alkynes; the reaction employing the alkynes afforded products in moderate yields but was found to be selective, even with the low catalyst loadings (i.e., as low as 0.05 mol %). On the other hand, the complex shown in Figure 1.24b, has been tested in the hydrosilylation reactions by Oro et al.[40], where good yields and fair to good selectivity have been found.

a) b)

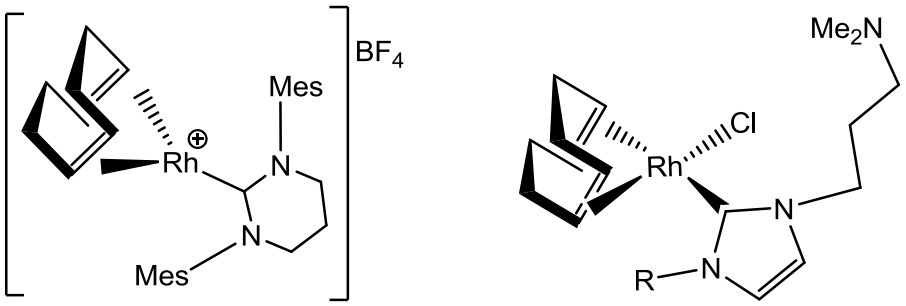

Figure 1.24 Structures of Rh(I)-NHC complexes active in alkyne hydrosilylation.

Recently in the laboratory, where this thesis was prepared, the catalytic activity of a series of neutral N-heterocyclic carbene-amide rhodium(I) complexes of the type [Rh(NBD)X(NHC)], bearing increasingly bulky N-alkyl substituents (Figure 1.25) has been investigated in the hydrosilylation of terminal alkynes, differing in the substituent size.

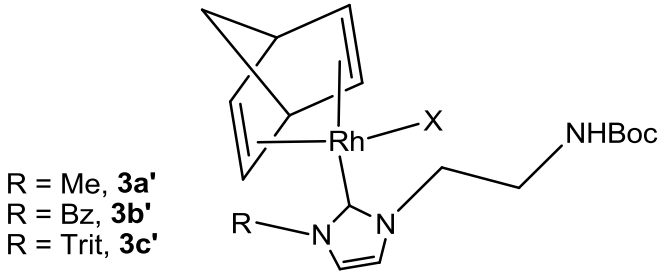

Figure 1.25 Amide-functionalized rhodium complexes 3a', 3b' and 3c'.

It has been found that the steric hindrance on the N-Heterocyclic ligand and on the alkyne substrates affect both conversion and selectivity of these reactions. The catalyzed hydrosilylation reactions employing less encumbered alkynes like tolylacetylene and phenylacetylene led to the formation of the mixture of the three possible isomeric vinylsilane derivatives: β-(Z)- or β-(E)-1-silyl-1-alkenes from the anti-Markovnikov addition and α-2-silyl-1-alkene from the Markovnikov addition and alkene as the fourth product. As reported[39,37], the β-(Z) vinylsilane is the major product until the substrate completely disappears; however, once complete conversion is reached, β-(Z) isomerizes to β-(E) vinylsilane, which, at the end of the reaction, is always the major product. On the other hand, when more hindered acetylenes have been used as substrates, only the formation of two products: β-(E) and α has been observed.

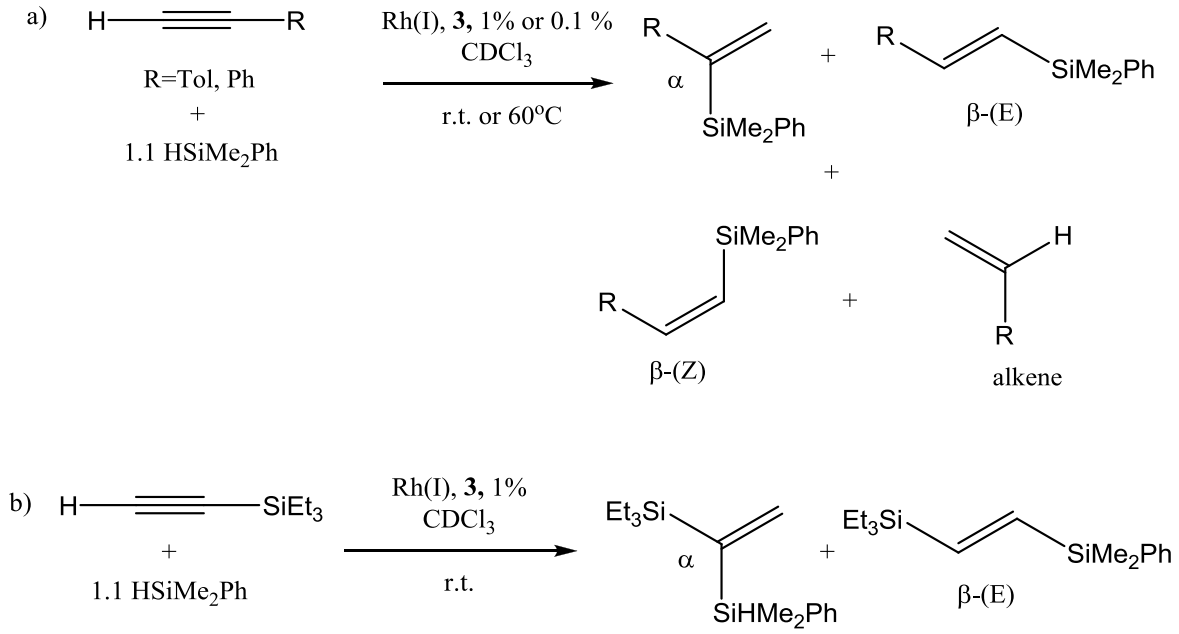

Scheme 1.29 Hydrosilylation reactions of PhC≡CH, TolC≡CH (a) and Et3SiC≡CH (b) catalyzed by 3a'-c' complexes.

Regarding the influence of the steric encumbrance of the alkynes on the conversion rate, an illustrative example is the use of the tertiary propargyl alcohol (CPh_2OH)C≡CH which slowed down the reaction (144 h, Conv. > 99%) more than 20 times when compared to the phenyl-, tolylacetyene and 1-hexyne (6 h, Conv. > 99%).

Similarly, the speed of the conversion can be increased by the decrease of the steric hindrance of the rhodium catalysts. For instance, Figure 4 shows the influence of the bulkiness of the rhodium ligands on the conversion of phenylacetylene, where the catalyst loading was 1 mol % with respect to the alkyne; as can be seen, the complex **3c'** possessing NHC with trityl group on one N-side of the imidazolium moiety, extended the time needed for the total conversion up to 145 h with comparison to the reaction catalyzed by the N-methyl substituted **3a'**, where the complete conversion was reached after 6h.

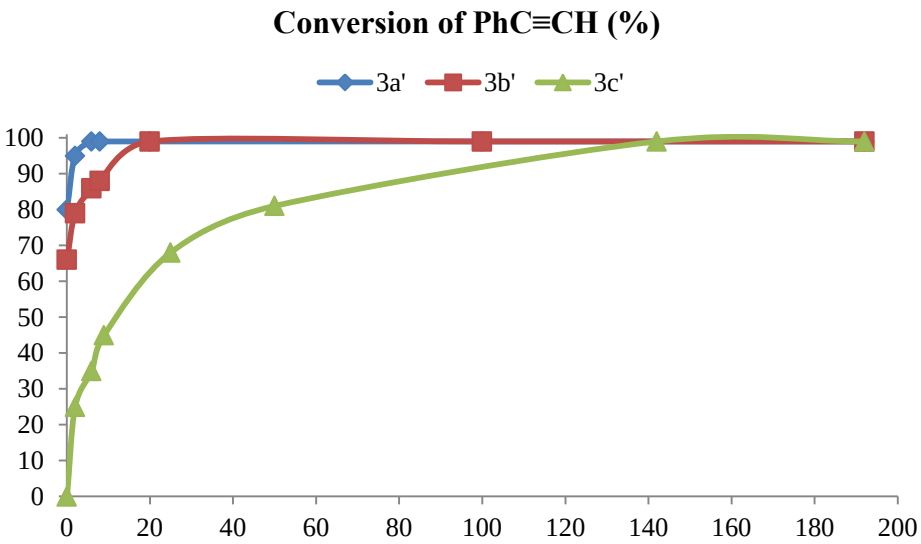

Figure 1.26 Reaction profile of conversion vs time for the hydrosilylation of PhC≡CH with complexes 3a', 3b', and 3c'.

Nevertheless, the neutral amide-functionalized rhodium(I) complexes **3a'-c'** have been shown to be efficient catalysts for the hydrosilylation of terminal alkynes, providing good yields (with the reservation to highly encumbered complexes) and high selectivity.

The presented above short list of catalytic reactions mediated by transition metal complexes bearing NHCs gives just a flavor of the ever-increasing catalytic potential of these species as chelating, functionalized chiral and immobilized ligands in a variety of reactions.

1.7 Methods and techniques

1.7.1 Dynamic NMR

NMR is an important tool for studying molecular structures and molecular dynamics for both organic and inorganic compounds. In contrast to most of the spectroscopic techniques, which give just the averaged picture of the investigated systems due to the high energy (frequency) radiation which they are based on, the low barrier of activation energy of majority of the molecular dynamic processes matches the range of frequency used in NMR thus the time-dependent processes can significantly affect the NMR spectra; consequently, dynamic NMR is used to study species that undergo physical or chemical changes with time and can be used to determine the equilibrium and the rate constants, which can subsequently serve for calculation of the thermodynamic parameters of the system.

There are generally two ways to investigate the molecular dynamics by NMR. The first one relies on lineshape analysis performed on the NMR spectra aquired in the range of temperature sufficient to cover both the low and fast exchange limits (See section 1.7.1.1). This method is called variable temperature NMR (VT NMR). The second method is based on saturation transfer phenomenon, which is a principal of a few experimental techniques, among which two are discussed in this thesis: NOESY (Nuclear Overhauser Enhancement Spectroscopy) and 1D EXSY (Exchange Spectroscopy). Both these methods with an aid of computer simulations of the band shape allow the determination of rate constants (*k*) and subsequently, using Eyring equation, a derivation of activation energies ($\Delta G^{\ddagger}$ in kcal mol^{-1}) and with a much smaller accuracy, the values of activation enthalpy and entropy $\Delta H^{\ddagger}$ and $\Delta S^{\ddagger}$. For processes, which are sufficiently slow to be monitored by the dynamic NMR technique, *k* constants in a range of a few to a few thousands reciprocal seconds (s^{-1}) can be determined, which corresponds to the reliable values of $\Delta G^{\ddagger}$ between 4.5 and 23 kcal mol^{-1}(18.8 - 96.2 kJ mol^{-1}).

1.7.1.1 VT NMR

The formal condition which must be fulfilled in order to detect a dynamic behavior by NMR is related to the kinetic constant by the following formula:

$$k \ll \frac{\pi \Delta \nu}{2} \qquad \text{Eq. 1.1}$$

where *k* is the kinetic constant, and $\Delta\nu$ is the difference between the separate resonances in the absence of an exchange.

In the series of spectra required at different temperatures, generally three situations can be distinguished and described according to the shape of the spectral lines.

1. At low temperature, when a dynamic phenomena are significantly slowed down, the exchanging nuclei spend a relatively long time in a given location in the molecule. In this framework, it is likely that the nuclei present in a sample will have different magnetic environment or in other words they will experience not averaged influence from the surrounding nuclei. Consequently, the spectrum should reveal more complex pattern than at

higher temperature. In this **slow exchange limit**, for a quasi-static situation, the linewidth is inversely proportional to the T_2 relaxation process:

$$\left(\boldsymbol{W_{1/2}}\right)_{\mathbf{0}} = \frac{\mathbf{1}}{\boldsymbol{\pi T_2}} \qquad \text{Eq. 1.2}$$

When the temperature is increased, and the exchange starts to take place, the nuclei spend some time in one or the other location. This leads to a broadening of the signals, which is a direct consequence of the Heisenberg uncertainty principle. When the lifetime in a given location becomes shorter, the energy and the linewidth gets less defined. In this case, the linewidth is given by the following formula, containing the factor related to the exchange:

$$\left(\boldsymbol{W_{1/2}}\right)_{\boldsymbol{ex}} = \frac{\mathbf{1}}{\boldsymbol{\pi T_2}} + \frac{\mathbf{1}}{\boldsymbol{\tau_{ex}}} \qquad \text{Eq. 1.3}$$

The kinetic constant can be easily derived, knowing that:

$$\boldsymbol{k} = \frac{\mathbf{1}}{\boldsymbol{\tau_{ex}}} \qquad \text{Eq. 1.4}$$

and one obtains:

$$\left(\boldsymbol{W_{1/2}}\right)_{\boldsymbol{ex}} = \frac{\mathbf{1}}{\boldsymbol{\pi T_2}} + \frac{\boldsymbol{k}}{\boldsymbol{\pi}} \qquad \text{Eq. 1.5}$$

Which eventually gives:

$$\boldsymbol{k} = \boldsymbol{\pi}\left\{\left(\boldsymbol{W_{1/2}}\right)_{\boldsymbol{ex}} - \frac{\mathbf{1}}{\boldsymbol{\pi T_2}}\right\} = \boldsymbol{\pi}\left\{\left(\boldsymbol{W_{1/2}}\right)_{\boldsymbol{ex}} - \left(\boldsymbol{W_{1/2}}\right)_{\mathbf{0}}\right\} \qquad \text{Eq. 1.6}$$

This formula (Eq. 1.6) to calculate kinetic constant is valid in the slow exchange limit, where the line broadening is not that significant.

2. When the temperature is increased even more, the exchange processes become faster, the broadening of the spectral lines is continuing and at a particular temperature, called **coalescence temperature**, the two signals coming from the two exchanging nuclei merge to form a very broad, top-flat signal. At the coalescence, the lifetime at particular exchange site, (so that the kinetic constant) can be very accurately related to the temperature. The kinetic constant is thus given by:

$$\boldsymbol{k = \frac{\pi|\nu_A - \nu_B|}{\sqrt{2}}} \qquad \text{Eq. 1.7}$$

where ν_A and ν_B are the resonant frequencies (expressed in Hz) of nuclei A and B in the absence of the exchange. The coalescence temperature is not a constant value for a given compound, but changes with the magnetic field strength and the solvent.

3. With a further increase of the temperature, the dynamics of a studied system becomes fast on the NMR time scale, and only an averaged signals are observed. Generally, the spectrum is simplified and the higher the temperature, the narrower the averaged peaks. This situation is called a **fast exchange limit** and the kinetic constant at this point is expressed as:

$$\boldsymbol{k = \frac{(\nu_A - \nu_B)^2}{2\left\{(W_{1/2})_{ex} - (W_{1/2})_0\right\}}} \qquad \text{Eq. 1.8}$$

As can be seen from the above discussion, the kinetic constant calculations are easiest at the coalescence temperature and in practice, only for this particular temperature the kinetic constant is calculated from the formula. For other temperatures, the complete lineshape simulation and fitting is done in a computer program and kinetic constants are derived.

In order to obtain a thermodynamic information from the NMR spectra, an Eyring equation is applied, which can be expressed in the form of the following formula:

$$\boldsymbol{\Delta G^{\ddagger} = RT\left\{23.759 + ln\left(\frac{k}{T}\right)\right\}} \qquad \text{Eq. 1.9}$$

where the rate constant is calculated at coalescence temperature.

By combining the above formula with the relationship:

$$\boldsymbol{\Delta G^{\ddagger} = \Delta H^{\ddagger} - T\Delta S^{\ddagger}} \qquad \text{Eq. 1.10}$$

one obtains

$$\boldsymbol{RT\left\{23.759 + ln\left(\frac{k}{T}\right)\right\} = \Delta H^{\ddagger} - T\Delta S^{\ddagger}} \qquad \text{Eq. 1.11}$$

and after a simple mathematical transformation, the following formula (Eq. 1.12) is established:

$$\boldsymbol{ln\left(\frac{k}{T}\right) = \frac{\Delta H^{\ddagger}}{R}\frac{1}{T} - \left(\frac{\Delta S^{\ddagger}}{R} + 23.759\right)} \qquad \text{Eq. 1.12}$$

which can be expressed as a linear function:

$$y = ax - b \qquad \text{Eq. 1.13}$$

where: $ln\left(\frac{k}{T}\right) = y, \frac{\Delta H^{\ddagger}}{R} = a, \frac{1}{T} = x, \left(\frac{\Delta S^{\ddagger}}{R} + 23.759\right) = b.$

A plot of $ln\left(\frac{k}{T}\right)$ against $\frac{1}{T}$ gives a straight line with gradient $\frac{\Delta H^{\ddagger}}{R}$ and intercept $\frac{\Delta S^{\ddagger}}{R} + 23.759$, as shown in the Figure 1.27.

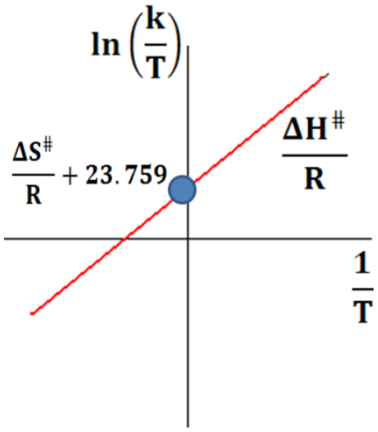

Figure 1.27 Eyring plot.

1.7.1.2 Nuclear Overhauser Enhancement Spectroscopy (NOESY) and Exchange Spectroscopy (EXSY)

NOESY and EXSY are the same experiment, based on the same pulse sequence with a difference in the duration of a mixing time (Figure 1.28); whereas it is usually in the range 0.025-0.1 s for the latter, in NOESY can be more than ten times longer ~1.5 s. The two modes of the experiment are used for different purposes. The NOESY experiment provides an information about the proximity of two nuclei in space, even if they are not bonded, whereas the EXSY experiment detects a chemical or conformational exchange.

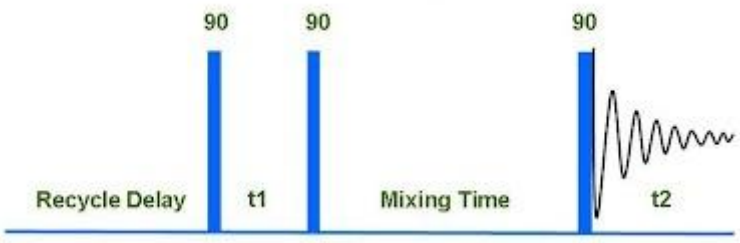

Figure 1.28 Pulse sequence for NOESY and EXSY spectroscopy.

The term Exchange Spectroscopy (EXSY) usually refers to 2D technique, which allows for a simple assignment of exchanging nuclei from diagonal spots in the 2D plot. However, it can be used also in a 1D mode as a selective experiment that uses shaped pulses to selectively excite specific resonances, producing either their saturation or inversion, followed by examination of the effects of the perturbation on the remaining sites in order to determine the pathways and rate constants of chemical exchange.

The pulse sequence presented in Figure 1.28 affects the two slowly exchanging spins as follows; the first 90° pulse places the magnetization, initially oriented along the z direction, in the xy plane. The two spins, magnetically inequivalent due to the different environment, precess at their individual frequencies for a time t_1. After this period, each of them has a particular orientation, with x, y and z (the latter due to relaxation) components of magnetization vector. The second pulse then turns this magnetization into the xz plane. Following this pulse, a short mixing time (around 0.05 s) is applied for an exchange of magnetization to occur. A FID is produced by moving the z magnetization back into the xy plane at the end of the mixing time.

In order to present a procedure allowing for the determination of the kinetic constants from the 1D EXSY experiment, one should consider the example of a two geminal nuclei, which exchange due to a rotation around a chiral axis present in a molecule, which results in the lost of the magnetic equivalency and generation of the two enantiomers (Figure 1.29).

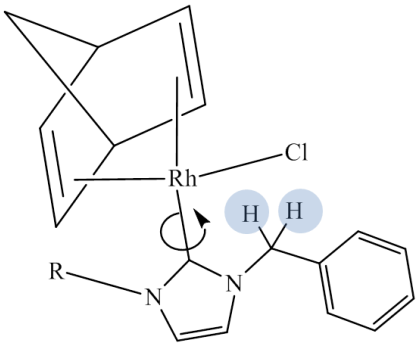

Figure 1.29 Geminal benzylic protons as a chiral probe.

Specifically in this situation, the relative intensity of the two signals coming from the two exchanging geminal protons corresponds to the proportion of the two enantiomers in the mixture. Consequently, the procedure to determine the kinetic constant for the enantiomerization is as follows; the intensity of the two signals is compared for few different mixing times. It is clear, that in case of a longer mixing time, when there is more time given for the irradiated nucleus to transfer the saturation to its geminal neighbor, the difference in

the intensity will be bigger. The below formula allows for the calculation of the enantiomeric excess with respect to the equilibrium situation, for each of the mixing times in an array.

$$\boldsymbol{ln}([\boldsymbol{A}]_{\boldsymbol{eq}} - [\boldsymbol{A}]_{\boldsymbol{t}}) \qquad \text{Eq. 1.14}$$

where $[A]_{eq}$ denotes a mole fraction of one enantiomer with respect to the other at equilibrium and $[A]_t$ expresses the mole fraction for a particular mixing time. In the case when at equilibrium there is the 50:50 proportion of the enantiomers, the above formula becomes:

$$\boldsymbol{ln}(\boldsymbol{^1/_2} - [\boldsymbol{A}]_{\boldsymbol{t}}) \qquad \text{Eq. 1.15}$$

The plot of the values calculated from the Eq.1.14 against the mixing times gives a straight line in the form of:

$$\boldsymbol{ln}\big([\boldsymbol{A}]_{\boldsymbol{eq}} - [\boldsymbol{A}]_{\boldsymbol{t}}\big) = -\boldsymbol{k} \cdot \boldsymbol{t} + \boldsymbol{ln}([\boldsymbol{A}]_{\boldsymbol{eq}}) \qquad \text{Eq. 1.16}$$

with a gradient corresponding to a kinetic constant and an intercept corresponding to $ln([A]_{eq})$ (Figure 1.30).

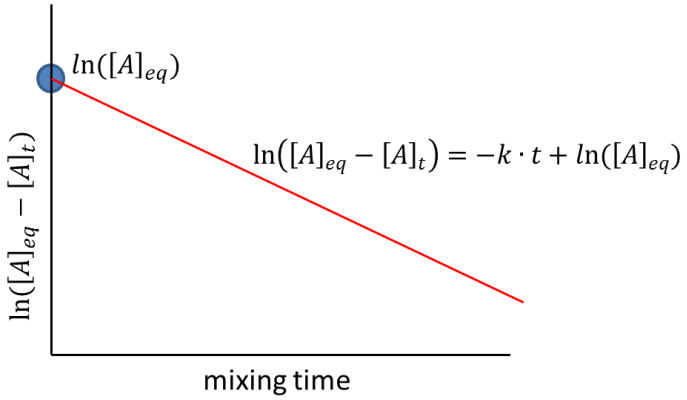

Figure 1.30 The plot of $\ln([A]_{eq} - [A]_t)$ vs. mixing time.

Since $k = k_1 + k_2$, where k_1 and k_2 refer to the kinetic constants for the isomerization for enantiomer 1 and enantiomer 2 respectively, and $k_1 = k_2$, consequently: $k_1 = k/2$.

1.7.2 Density functional theory(DFT)

DFT is a quantum mechanical method used to study the ground state electronic structures of atoms, molecules and condensed phases.

DFT theory was developed in ’60 by Walter Kohn and coworkers, who shared The Noble Prize in Physics and Chemistry in 1998 for this achievement. DFT theory arose from a brilliant idea, which is now established in the principal theorems of DFT, which say that the ground state energy E_0 is directly proportional, or in other words is completely determined by the ***one electron probability density ρ(r)***, which is the total electron density at position r. The energy E is defined in these theorems as a so-called functional of the electron density, which means that for a given density function $\rho(r)$, there is a single corresponding energy $E[\rho]$. This definition has been made with an analogy to the definition of a mathematical function, which send a number x to a number $f(x)$, whereas a functional F sends a function f to a number $F[f]$.

This theory, which is now ubiquitously used in chemistry due to its efficiency and relatively low cost has been developed as an ingenious alternative for “traditional” quantum theories based on a global wavefunction. In contrast to the complexity of the latter one, the mentioned density function $\rho(r) = \rho(x,y,z)$ is a real positive function of only the three variables.

The mentioned one electron probability density $\rho(r)$ is expressed as a multiple integral of a wavefunction, over the coordinates of all electrons except one:

$$\boldsymbol{\rho(r_1) = N \int \dots \int |\Psi(r_1, r_2, \dots, r_N)|^2 \, dr_2 \dots dr_N} \qquad \text{Eq. 1.17}$$

and it determines the probability of finding any of the N electrons within the volume element dr_1 while the other $N-1$ electrons have arbitrary positions. One of the Kohn’s theorem proves, that the above relation is reversible, i.e. for a given ground state density $\rho(r)$ it is possible to find the corresponding ground state wavefunction $\Psi_0(r_1, \dots, r_N)$ and consequently the ground-state energy can be derived as a functional of ρ. In the above equation, the factor N comes from the fact, that electrons are indistinguishable in the framework of quantum theory. Hence, the one electron which can be labeled as 1 and is supposed to be found in the dr_1 volume, can be in fact every of the electrons in a system.

1.8 References

(1) Busetto, L.; Cassani, M. C.; Femoni, C.; Mancinelli, M.; Mazzanti, A.; Mazzoni, R.; Solinas, G. *Organometallics* **2011**, *30*, 5258.

(2) Bourissou, D.; Guerret, O.; Gabbaı, P.; Bertrand, G. *Chem. Rev.* **2000**, *100*, 39.

(3) Hoffmann, R. *J. Am. Chem. Soc.* **1968**, *90*, 1475.

(4) Wanzlick, H. W.; Kleiner, H. J. *Angew. Chem.* **1961**, *73*, 493-493.

(5) de Frémont, P.; Marion, N.; Nolan, S. P. *Coord. Chem. Rev.* **2009**, *253*, 862-892.

(6) Dupont, J. *J. Braz. Chem. Soc.* **2004**, *15*, 341-350.

(7) Caló, V.; Del Sole, R.; Nacci, A.; Schingaro, E.; Scordari, F. *Eur. J. Org. Chem. 2010* **2000**, *2000*, 869-871.

(8) Herrmann, W. a. *Angew. Chem., Int. Ed.* **2002**, *41*, 1290-1309.

(9) Scholten, J. D.; Leal, B. C.; Dupont, J. *ACS Catalysis* **2012**, *2*, 184-200.

(10) Ballarin, B.; Busetto, L.; Cristina Cassani, M.; Femoni, C. *Inorg. Chim. Acta* **2010**, *363*, 2055-2064.

(11) http://www.scripps.edu/baran/images/grpmtgpdf/Zografos_Feb_04.pdf.

(12) Gridnev, A. A.; Mihaltseva, I. M. *Synth. Commun.* **1994**, *24*, 1547-1555.

(13) Glorius, F.; Spielkamp, N.; Holle, S.; Goddard, R.; Lehmann, C. W. *Angew. Chem., Int. Ed.* **2004**, *43*, 2850-2852.

(14) Arduengo, A. J. *Acc. Chem. Res.* **1999**, *32*, 913.

(15) http://www.chm.bris.ac.uk/webprojects2002/grant/webcomp/non-crossing.html.

(16) Arduengo, A. J.; Gamper, S. F.; Tamm, M.; Calabrese, J. C.; Davidson, F.; Craig, H. A. *Structure* **1995**, *117*, 572-573.

(17) Wanzlick, H. W.; Schönherr, H. J. *Angew. Chem.* **1968**, *80*, 154-154.

(18) Ofele, K. *Angew. Chem., Int. Ed.* **1968**, *12*, 950.

(19) Arduengo III, A. J.; Dias, H. V. R.; Harlow, R. L.; Kline, M. *J. Am. Chem. Soc.* **1992**, *114*, 5530-5534.

(20) Jean-Baptiste Dit Dominique, F.; Gornitzka, H.; Hemmert, C. *Organometallics* **2010**, *29*, 2868-2873.

(21) Lappert, M. F. *J. Organomet. Chem.* **1988**, *358*, 185-213.

(22) Lin, T.-S.; Luo, M.-Z.; Liu, M.-C. *Tetrahedron* **1995**, *51*, 1055-1068.

(23) Liu, B.; Liu, X.; Chen, C.; Chen, C.; Chen, W. *Organometallics* **2012**, *31*, 282-288.

(24) Lin, I. J. B.; Vasam, C. S. *Coord. Chem. Rev.* **2007**, *251*, 642-670.

(25) Liu, B.; Xia, Q.; Chen, W. *Angew. Chem., Int. Ed.* **2009**, *48*, 5513-6.

(26) Green, J. C.; Scurr, R. G.; Arnold, P. L.; Cloke, G. N. *Chem. Commun.* **1997**, 1963-1964.

(27) Mercs, L.; Labat, G.; Neels, A.; Ehlers, A.; Albrecht, M. *Organometallics* **2006**, *25*, 5648-5656.

(28) Garrison, J. C.; Youngs, W. J. *Chem. Rev.* **2005**, *105*, 3978-4008.

(29) Kandepi, V. V. K. M.; Cardoso, J. M. S.; Peris, E.; Royo, B. *Organometallics* **2010**, *29*, 2777-2782.

(30) Chianese, A. R.; Li, X.; Janzen, M. C.; Faller, J. W.; Crabtree, R. H.; Organomet, W. A. J. *Organometallics* **2003**, *22*, 1663-1667.

(31) Wang, H. M. J.; Lin, I. J. B. *Organometallics* **1998**, *17*, 972-975.

(32) Cardoso, J. M. S.; Royo, B. *Chem. Commun.* **2012**, *48*, 4944-4946.

(33) Corbera, R.; Sanau, M.; Peris, E. *Organometallics* **2006**, *25*, 4002-4008.

(34) Scott, N. M.; Dorta, R.; Stevens, E. D.; Correa, A.; Cavallo, L.; Nolan, S. P. *J. Am. Chem. Soc.* **2005**, *127*, 3516-26.

(35) Bringmann, G.; Price Mortimer, A. J.; Keller, P. A.; Gresser, M. J.; Garner, J.; Breuning, M. *Angew. Chem., Int. Ed.* **2005**, *44*, 5384-5427.

(36) Crabtree, R. *J. Organomet. Chem.* **2005**, *690*, 5451-5457.

(37) Díez-González, S.; Marion, N.; Nolan, S. P. *Chem. Rev.* **2009**, *109*, 3612-76.

(38) Herrmann, W. A.; Öfele, K.; Elison, M.; Kuhn, F. E.; Roesky, P. W. *J. Organomet. Chem. 480*, C7-C9.

(39) Imlinger, N.; Wurst, K.; Buchmeiser, M. R. *J. Organomet. Chem.* **2005**, *690*, 4433-4440.

(40) Jiménez, M. V.; Pérez-Torrente, J. J.; Bartolomé, M. I.; Gierz, V.; Lahoz, F. J.; Oro, L. A. *Organometallics* **2008**, *27*, 224-234.

(41) Patil, S.; Deally, A.; Gleeson, B.; Helge, M.; Paradisi, F.; Tacke, M. *Appl.Organometal.Chem.* **2010**, *24*, 781-793.

(42) Moret, M.-etienne; Chaplin, A. B.; Lawrence, A. K.; Scopelliti, R.; Dyson, P. J. *Organometallics* **2005**, *24*, 4039-4048.

(43) Patil, S.; Claffey, J.; Deally, A.; Hogan, M.; Gleeson, B.; Miguel, L.; Méndez, M.; Müller-bunz, H.; Paradisi, F.; Tacke, M. *Eur. J. Inorg. Chem.* **2010**, 1020-1031.

(44) http://www.personal.psu.edu/the1/sn1ande.htm.

(45) Elango, K.; Srirambalaji, R.; Anantharaman, G. *Tetrahedron Lett.* **2007**, *48*, 9059-9062.

(46) Sauerbrey, S.; Majhi, P. K.; Daniels, J.; Schnakenburg, G.; Brändle, G. M.; Scherer, K.; Streubel, R. *Inorg. Chem.* **2011**, *50*, 793-9.

(47) Fre, P. D.; Scott, N. M.; Stevens, E. D.; Ramnial, T.; Lightbody, O. C.; Macdonald, C. L. B.; Clyburne, J. A. C.; Abernethy, C. D.; Nolan, S. P. *Organometallics* **2005**, *24*, 6301-6309.

(48) Busetto, L.; Cristina Cassani, M.; Femoni, C.; Macchioni, A.; Mazzoni, R.; Zuccaccia, D. *J. Organomet. Chem.* **2008**, *693*, 2579-2591.

(49) Abraham, R. J.; Byrne, J. J.; Griffiths, L.; Perez, M. *Magn. Reson. Chem.* **2006**, *44*, 491-509.

(50) Newman, C. P.; Clarkson, G. J.; Rourke, J. P. *J. Organomet. Chem.* **2007**, *692*, 4962-4968.

(51) Kline, M.; Harlow, R. L. *J. Am. Chem. Soc.* **1991**, *113*, 363-365.

(52) Kuhn, H.; Woodgate, G. K. *Nature* **1950**, *166*, 906.

(53) Gaillard, S.; Slawin, A. M. Z.; Nolan, S. P. *Chem. Commun.* **2010**, *46*, 2742-2744.

(54) Casarini, D.; Lunazzi, L.; Mazzanti, A. *Eur. J. Org. Chem.* **2010**, *2010*, 2035-2056.

(55) Enders, D.; Gielen, H.; Runsink, J.; Breuer, K.; Brode, S.; Boehn, K. *Eur. J. Inorg. Chem.* **1998**, 913-919.

(56) Enders, D.; Gielen, H. *J. Organomet. Chem.* **2001**, *618*, 70-80.

(57) Sabbah, M.; Soulère, L.; Reverchon, S.; Queneau, Y.; Doutheau, A. *Bioorg. Med. Chem.* **2011**, *19*, 4868-75.

(58) Hirtenlehner, C.; Krims, C.; Hölbling, J.; List, M.; Zabel, M.; Fleck, M.; Berger, R. J. F.; Schoefberger, W.; Monkowius, U. *Dalton Trans.* **2011**, *40*, 9899-9910.

(59) Sheldrick, G. M. *SADABS Program for Absorption Correction Using Area Detector Data* **1996**.

2 RESULTS AND DISCUSSION

2.1 Synthesis of Imidazolium Ligand Precursors and NHC-Silver Complexes

During the work on this thesis, the imidazolium salts reported in Scheme 2.1 were prepared.

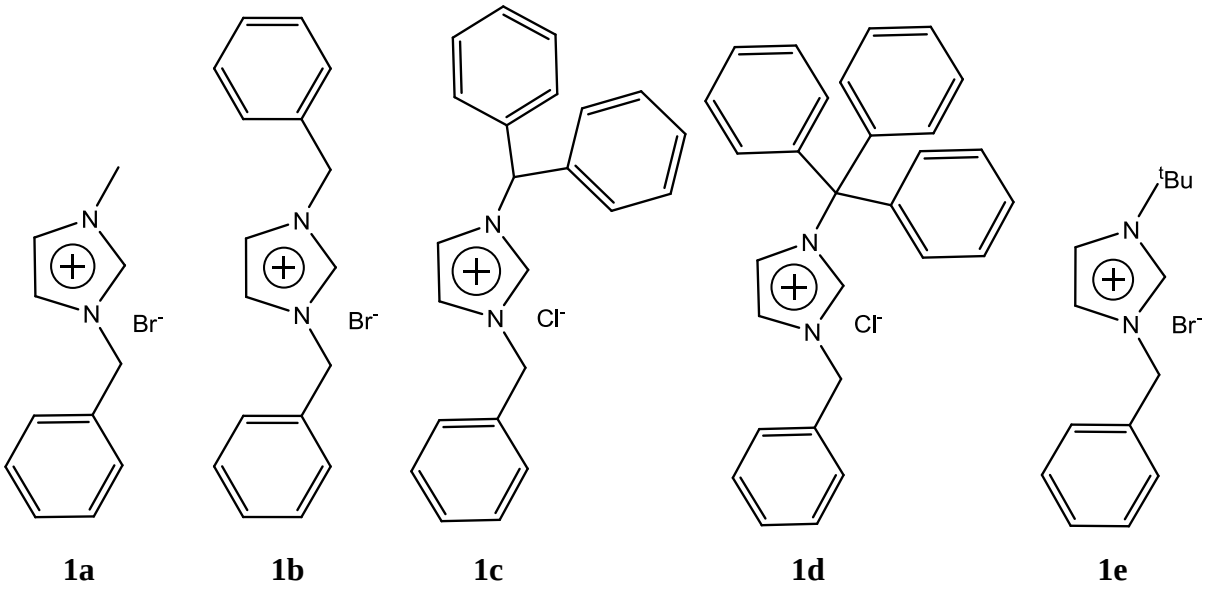

1a **1b** **1c** **1d** **1e**

Scheme 2.1 The imidazolium salts [BzImR]X 1a-e, bearing increasingly bulky N-alkyl substituents.

The imidazolium salts [BzImR]X (**1a**, R = methyl, X = Br; **1b**, R = benzyl, X = Br; **1b**) were prepared in quantitative yields following published procedures[41,42,43] by alkylation of 1-benzylimidazole with the pertinent alkyl halide in dichloromethane or/and acetonitrile at room temperature.

A similar synthetic procedure was also employed for the preparation of the novel imidazolium salts **1c, 1d** and **1e.** However, while in the case of **1d** this procedure led to the desired product in a straightforward way, in case of **1c** the product was obtained but the purification proved to be a lengthy and time-consuming process and for **1d** the alkylation of 1-benzylimidazole with 1-*tert*-butyl bromide did not afford the desired product. The most likely explanation of this failure is the occurrence of a E1 elimination reaction, in which the *tert*-butyl bromide in the presence of 1-benzylimidazole, which is a weak base (pK_a = 7.3) releases a molecule of HBr (with evolution of isobutene gas) which further reacts with benzylimidazole to form the corresponding imidazolium bromide salt. This hypothesis has been confirmed by the ^{1}H NMR analysis of the crude material, which showed the presence of

2-methylpropene with chemical shifts at 4.58 and 1.56 ppm, in perfect agreement with simulated spectra[44]; in contrast, for the 1-benzylimidazolium bromide salt a full peak assignment was not possible to be made[45]; furthermore, the most intense signal appearing in the spectrum in a low field with the chemical shift δ = 1.73 ppm was attributed to unreacted *tert*-butyl bromide. Eventually, the salt **1e** was obtained by an alkylation of *tert*-butylimidazole (prepared using the Debus-Radziszewski reaction[46] shown in Scheme 2.2) with benzyl bromide[33] (Scheme 2.3).

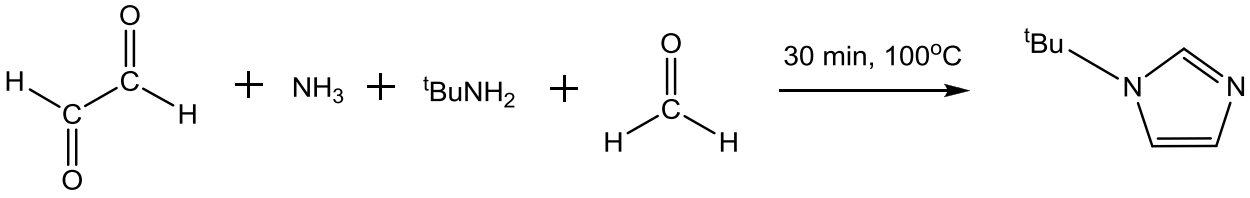

Scheme 2.2 The Debus-Radziszewski reaction employed in the synthesis of tert-butylimidazole.

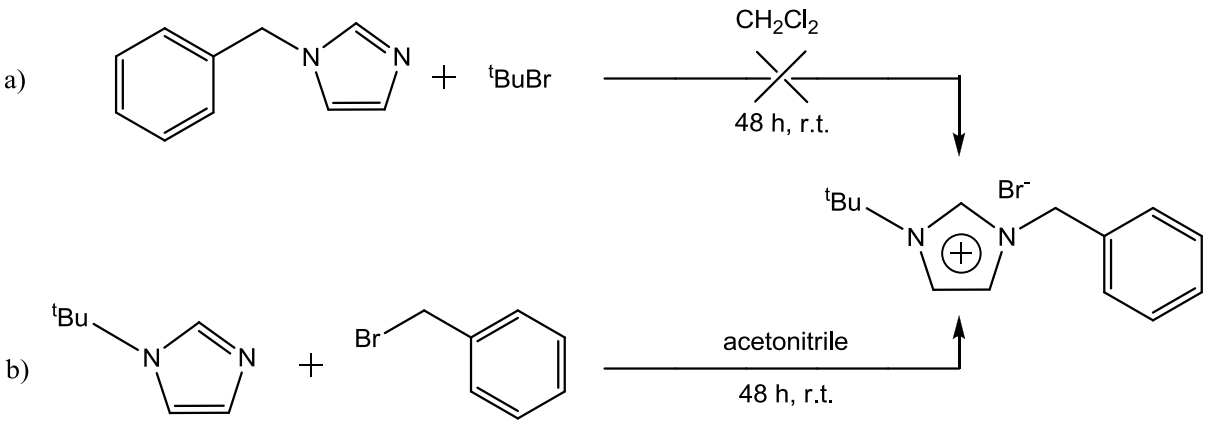

Scheme 2.3 (a) The unsuccessful synthesis of 1e by alkylation of 1-benzylimidazole with tert-butyl bromide, thwarted by the E1 elimination and (b) the alkylation of tert-butylimidazole with benzyl bromide leading to the desired product.

The imidazolium salt **1a** was isolated as a pale yellow viscous liquid, whereas the salts **1b-e** are very hygroscopic crystalline solids. Moreover, it has been observed, that the use of acetonitrile as a solvent favored the formation of crystalline solid products, whereas the syntheses carried out in dichloromethane usually led to the formation of viscous liquids. This behavior can be explained either by the different physical properties of these two solvents (much bigger dipole moment and lower density of acetonitrile with respect to DCM), which can cause different intermolecular interactions; or the difference can derive from the presence

of some impurities often present in the dichloromethane, such as hydrogen chloride or methanol. All the salts **1a-e** are soluble in chlorinated solvents and were fully characterized by elemental analysis, NMR spectroscopy and electrospray ionization mass spectrometry (ESI-MS). The NMR resonances of the imidazolium salts were observed at chemical shifts typical for compounds of this kind. The most significant chemical shifts and coupling constants in ^{1}H and ^{13}C NMR spectra of the **1a-e** compounds are presented in Table 2.1. As regards the ^{1}H NMR spectra, the acidic protons NC*H*N of the imidazole fragment were found in the range 10.66 – 9.92 ppm; the resonances of the imidazole backbone protons were observed in the aromatic region of the spectra for all of the salts, as two singlets in the spectra of **1a**, **1c** and **1d**, as a doublet with a coupling constant $^{2}J_{H,H}$ = 1.5 Hz in case of the symmetric **1b** (Figure 2.1), and as two multiplets (namely two not resolved doublet of doublets) with a coupling constant $^{1}J_{H,H}$ = 1.8 Hz and $^{2}J_{H,H} \approx {}^{1}J_{H,H}$ for **1e** (Figure 2.2). In case of **1d** the two signals were significantly shifted one from the other ($\Delta\delta$ = 0.72 ppm); the benzylic protons resonate in the range 5.36-5.21 ppm and appear as a singlet.

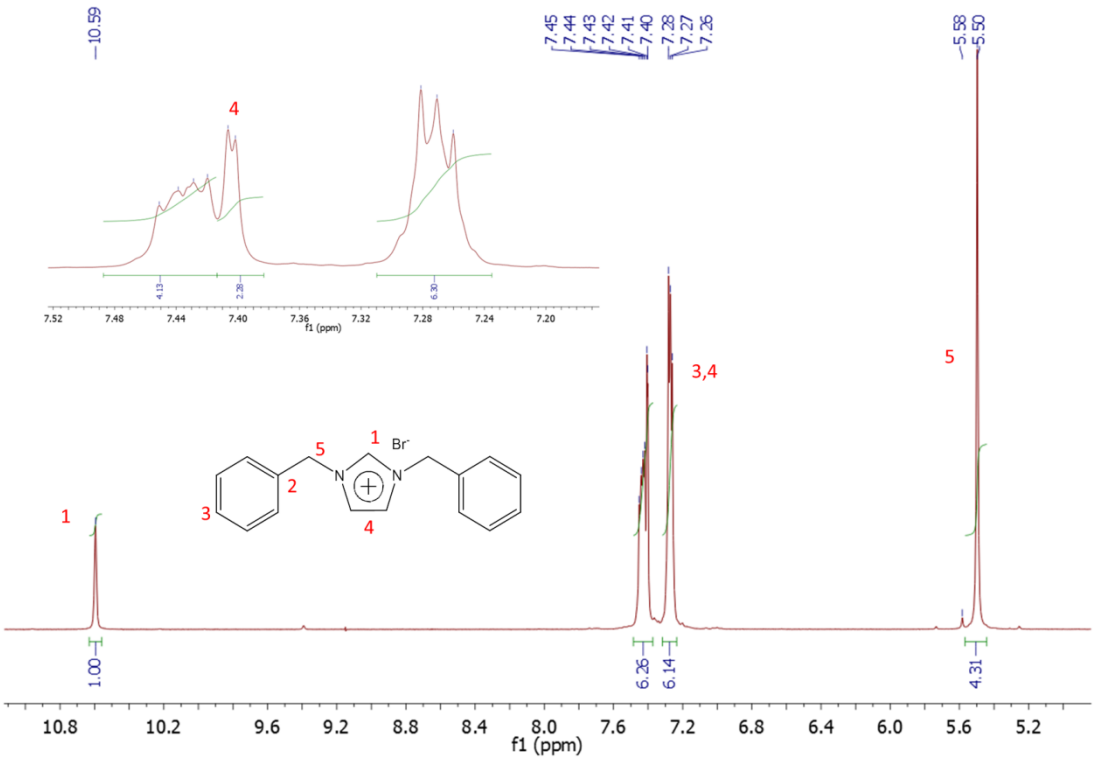

Figure 2.1 ^{1}H NMR spectrum of 1b with the inset showing signals deriving from imidazole backbone protons.

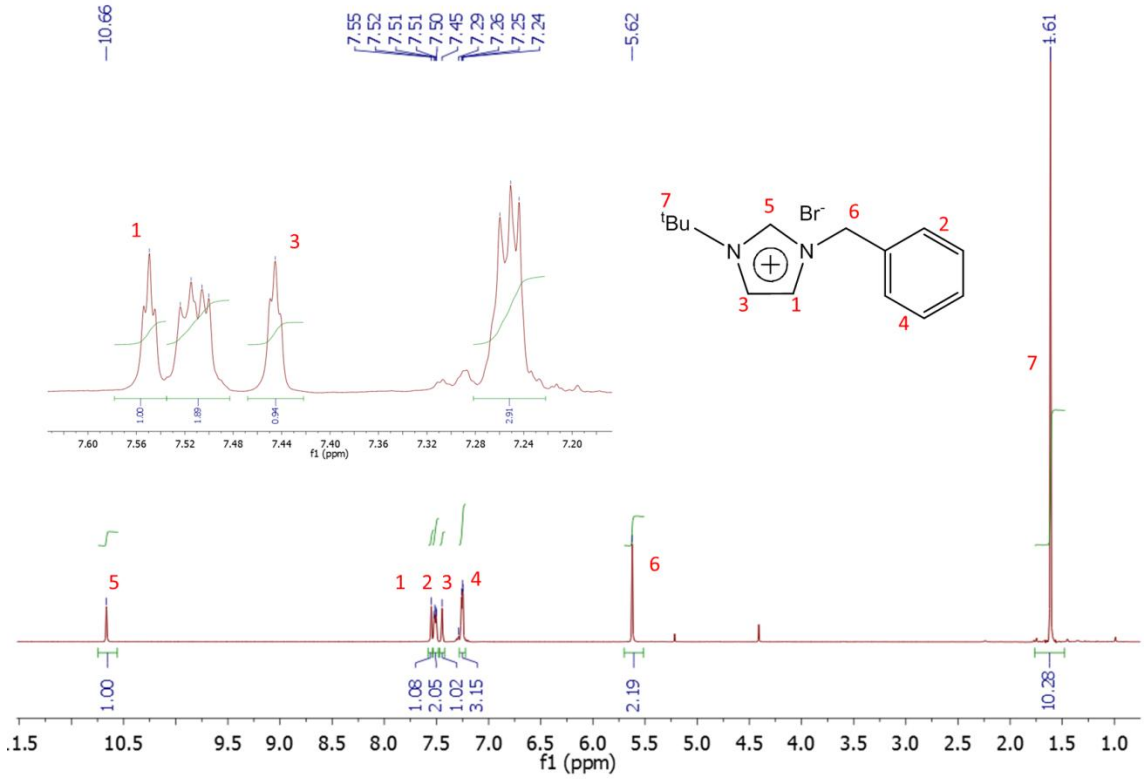

Figure 2.2 ^{1}H NMR spectrum of 1d with the inset showing signals deriving from imidazole backbone protons.

Due to the difficulties in the purification of **1c** mentioned before, the work related to the synthesis of the corresponding silver and rhodium complexes is currently in progress and will not be described in the thesis.

Table 2.1 The most significant chemical shifts in 13C and 1H NMR spectra of the 1a-e and 2a-d compounds.

Compounds	NC*H*N δ (ppm)	δ (ppm) CH_{im}	δ (ppm) NCHN	δ (ppm) CH_{im}
1a	10.58	7.48 (s)	137.9	123.2 121.6
1b	10.59	7.41 d, $J_{H,H}$ = 1.5 Hz	136.3	122.0
1c	10.74	*	140.8	122.0 121.1
1d	9.92	7.65 (s)	146.8	123.7 121.8
1e	10.66	7.55 m, $^1J_{H,H}$ = 1.82 Hz ≈ $^2J_{H,H}$ 7.45 m, $^1J_{H,H}$ = 1.88 Hz ≈ $^2J_{H,H}$	137.4	121.9 119.7
2a		6.98 d, $J_{H,H}$ = 1.79 Hz 6.93 d, $J_{H,H}$ = 1.80 Hz	s 181.8	122.5 121.1
2b		s 6.99 (s)	s 180.6	121.6
2d		7.03 d, $J_{H,H}$ = 1.90 Hz 6.91 d, $J_{H,H}$ = 1.90 Hz	185.0 d, $^1J_{C\text{-}Ag}$ = 236 Hz	123.8 118.8
2e		7.16 d, $J_{H,H}$ = 1.87 Hz 6.90 d, $J_{H,H}$ = 1.87 Hz	s 177.4 (s)	119.3

* Characterization in progress.

Silver(I)-NHC complexes **2a-d** were obtained in quantitative yields via the most common silver base route[31], by the reaction of the corresponding imidazolium salts with a small excess of Ag_2O in a 2:1.3 stoichiometric ratio (Scheme 2.4).

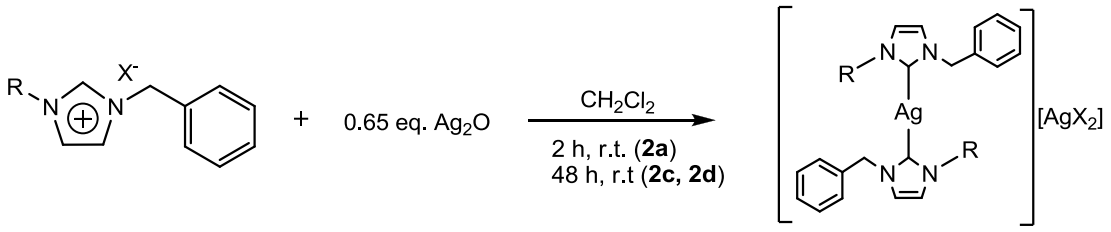

2a, 2d, 2e

R =Me (a), R = Trit (d), R = ^{t}Bu (e)

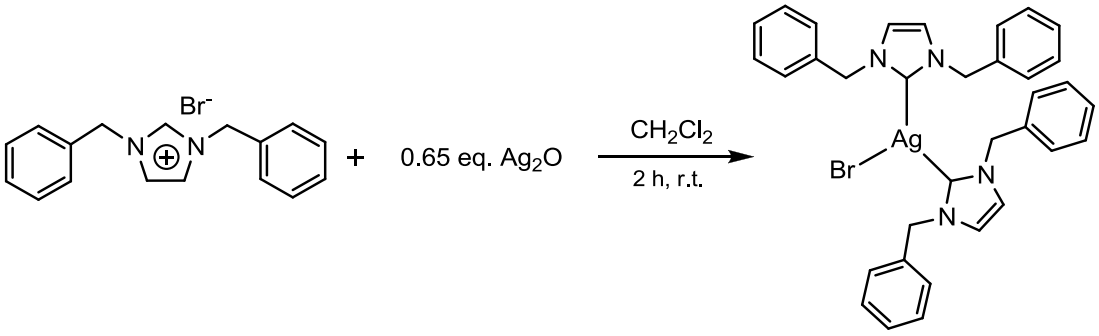

2b

R = Bz (b)

Scheme 2.4 Synthesis of silver(I)-NHC complexes 2a-d.

All the four reactions were carried out in dichloromethane at room temperature with the exclusion of light and afforded the less bulky **2a** and **2b** complexes after 2 h and the **2d** and **2e** after 48 h. The silver complexes **2a**-**e** are soluble in dichloromethane; in the end of reaction, a colorless solution and a small amount of a grey precipitate (due to the excess of Ag_2O) was found, in accordance with the reported observations[31].

The formation of **2a**, **2b**, **2d** and **2e** was unambiguously confirmed by elemental analysis, NMR spectroscopy, electrospray ionization mass spectrometry (ESI-MS) and in case of **2b** also by X-ray diffraction.

As regards the NMR data, the common features in the spectra for all of the complexes were the disappearance of the acidic imidazolium NC*H*N proton resonance in the ^{1}H NMR spectra, coupled with appearance of a highly deshielded singlet (doublet in case of **2d**, deriving from the silver-bonded $C_{carbene}$) in the ^{13} C NMR spectra (Figure 2.3). The most significant chemical shifts and coupling constants in ^{13}C and ^{1}H NMR spectra of the **2a-e** compounds are presented in Table 2.1.

As can be seen from these data, the chemical shift δ for the Ag-C resonance for the different Ag(I) complexes is found between 185.0 and 177.5 ppm. Only in the case of the complex **2d**, the coupling of the carbon nucleus to the silver one was observed as a doublet with a coupling constant $^{1}J(^{13}C\text{-}^{107/109}Ag)$ = 236 Hz, which expresses the average of coupling to the two naturally occurring isotopes of silver ^{107}Ag and ^{109}Ag (both isotopes with I=1/2). This value of the ^{1}J(C-Ag) constant lies in the range reported[28] for silver(I)-NHC complexes, specifically, the $C_{carbene}$ couples to ^{107}Ag with a coupling constant in the range 180 to 234 Hz, whereas this constant ranges from 204 to 270 Hz when $C_{carbene}$ couples to ^{109}Ag. Particularly Nolan[47] and colleagues observed for a 1,3-diisopropyl-imidazolin-2-ylidene silver chloride (IPr)AgCl and **a** 1,3-dimesityl-imidazolin-2-ylidene silver chloride (IMes)AgCl a downfield signal of carbonic carbon resonating at 184.6 ppm as a doublet of doublets with an observable coupling between carbon and silver of $^{1}J(^{13}C\text{-}^{109}Ag)$ = 253 Hz and $^{1}J(^{13}C\text{-}^{107}Ag)$ = 219 Hz.

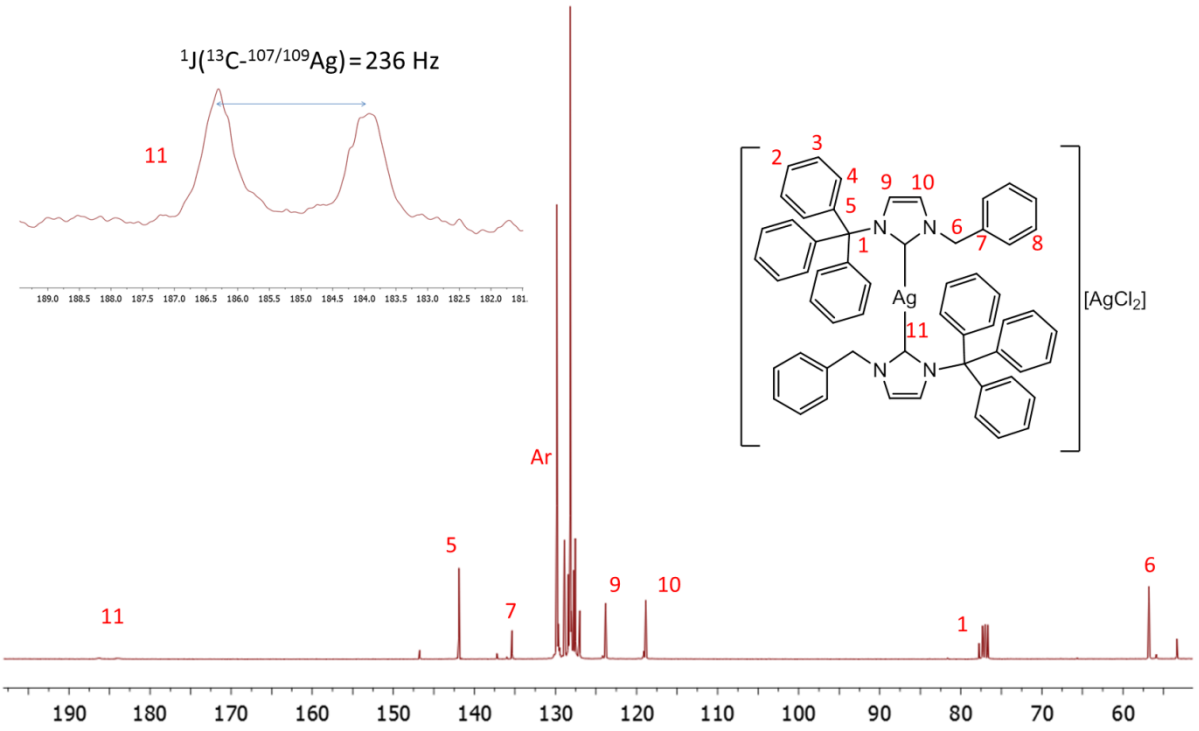

Figure 2.3 ^{13}C NMR spectrum of 2c with the inset showing the downfield doublet.

The observation of the doublet at 185 ppm in the ^{13}C NMR spectrum of **2d** indicates that the bulkiness of the substituent at the imidazolium nitrogen atom influences the dynamic behavior within the structure of the silver complex. The absence of the doublet of doublets splitting pattern in the case of **2d** suggests that the steric hindrance caused by the trityl group

on the one N-side of the imidazole is not enough high to consider its quasi-static behavior as it can be done for the mentioned examples of (IPr)AgCl and (IMes)AgCl. Nevertheless, the presumable exchange process[31] between the ligands and the metal center is slower on the NMR time scale for the **2d** than for the other three characterized complexes. The dynamic behavior in silver(I)-NHC complexes has been also investigated and reported[48] within the research group, where this thesis was prepared; the dynamics has been examined by making an advantage of PGSE NMR technique. Since the pulsed-gradient spin-echo sequence permits the measurement of the diffusion coefficients of cationic and anionic moieties of the silver salts in solution, a movement of ligands within the structure of the complexes can be determined. And indeed, in case of a biscarbene salt $[(NHC–NHBoc)_2Ag][AgI_2]$ (NHC–NHBoc = 1-(2-BocNH-ethyl)-3-methylimidazolin-2-ylidene) reported there, NHC/I exchange between two silver centers has been revealed. Due to the steric similarity of this complex and **2a**, a dynamic behavior shown in Scheme 2.5 can be proposed for the latter. Furthermore, also in the case of the reported silver complex, no ^{13}C-$^{107/109}Ag$ coupling was observed, exactly as in the cases of complexes **2a**, **2b** and **2e**, indicating similar dynamic behavior.

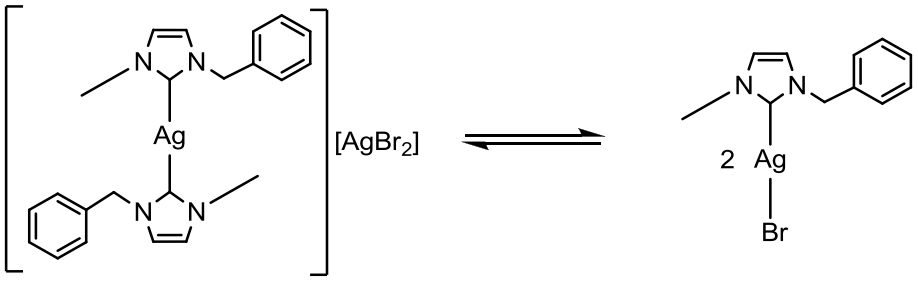

2a

Scheme 2.5 Proposed dynamic behavior within the structure of 2a.

Moreover, according to Nolan[47], the highly deshielded proton at δ = 185.0 ppm may indicate a stronger donation to the silver, which means a stronger Ag-C bond. This in turn leads to the decrease of the lability of the carbene ligands with respect to the metal center. Indeed, the carbenic carbene resonance in the group of all the silver complexes **2a-e** is most deshielded in the case of the complex **2d**.

In keeping with previous observations[48], in the ^1H NMR spectra, the resonances of imidazole backbone protons CH_{im} in the silver complexes are shifted upfield with respect to the corresponding imidazolium precursors, whereas no significant shift has been observed in the ^{13}C NMR spectra. Additionally, the chemical shift of these CH_{im} protons is solvent-

dependent. The use of DMSO-d_6 caused the downfield shift of the signals with comparison to their position in spectra acquired for the sample in $CDCl_3$, namely the signals were shifted from 7.16 and 6.90 ppm to 7.62 and 7.53 ppm. This behavior can be explained by the fact that DMSO is a H-bonding solvent, and some electrostatic interactions between the analyzed compound and the solvent are likely to form[49].

The discussed above resonances of the imidazolium backbone protons have been observed as two doublets (AB system) in case of the complexes **2a**, **2d** and **2e** with coupling constants $^1J_{H,H}$ = 1.80 Hz, $^1J_{H,H}$ = 1.90 Hz and $^1J_{H,H}$ = 1.87 Hz, respectively. In case of the complex **2b**, the protons appear as a singlet.

Crystals of **2b** suitable for single crystal X-ray diffraction were grown from a double layer of dichloromethane and petroleum ether (1:4). The molecular structure with selected bond distances and angles is presented in Figure 2.4, whereas the crystal data and the experimental details are reported in the Experimental part. Complex **2b** exists as a biscarbene compound with the two neutral carbene moieties bound to the silver cation in the presence of the anion to balance the charge.

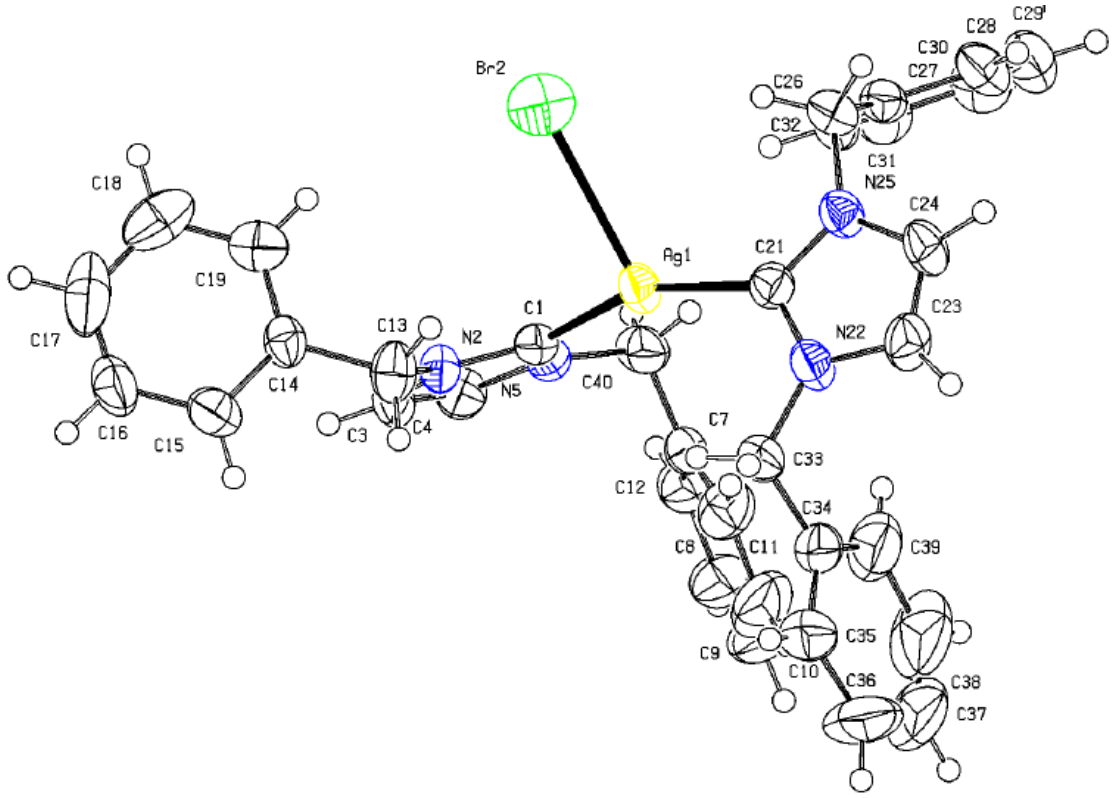

Figure 2.4 ORTEP diagram of 2b depicted with thermal elipsoids at 50% probability. Selected bond distances (Å) and bond angles (deg): Ag(1)-C(21) 2.118(7); Ag(1)-C(1) 2.125(7); Ag(1)-Br(2) 2.8609(12); C(21)-Ag(1)-C(1) 156.7(3); C(21)-Ag(1)-Br(2) 104.84(18); C(1)-Ag(1)-Br(2) 98.43(17).

The compound **2b** crystallizes in the $P2_1/n$ space group of the monoclinic crystal system (Z = 4). This particular structure for a Ag(I)-NHC complex was reported for a first time in 2007 by Newman and co-workers[50]; this finding was quite surprising at that time, since most of the silver products resulting from the reaction of imidazolium halide and Ag_2O exist in one of the two structural motifs shown in Figure 2.5, with formulas: (NHC)AgX and $(NHC)_2Ag^+/AgX_2^-$, both of them having a stoichiometry of 1 NHC:1 Ag:1 halide. The formation of one of these two structures depends mainly on the degree of polarity of a solvent used in the synthesis; the more polar solvents favor the latter, cationic silver salt. For Newman, unexpectedly, a reaction of 1,3-dibenzyl-imidazolium bromide with 5 equivalents of Ag_2O in dichloromethane afforded, in a reproducible manner, the new structure of stoichiometry 2 NHC:1 Ag:1 halide.

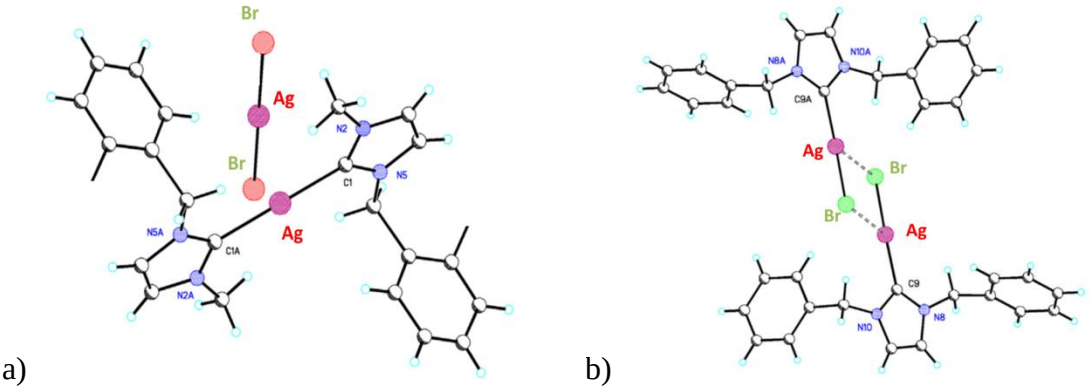

a) b)

Figure 2.5 Two most commonly formed structures of biscarbene silver(I) complexes with a stoichiometry of 1 NHC:1 Ag:1 halide.

The X-ray data obtained for **2b** synthesized in our laboratory from the reaction of 1,3-dibenzyl-imidazolium bromide **1b** with 0.65 molar equivalents of the Ag_2O in dichloromethane are in a perfect agreement (within the experimental error) with the reported ones[50].

As can be seen from the ORTEP diagram shown in Figure 4, the structure shows almost planar geometry formed by the two coordinating carbons, the bromide and the silver with the C–Ag–C angle being 156.7°. The distance between Ag and Br atoms is quite long (2.86 Å), longer than for the usual structure shown in the Figure 5b.

The reason for which the unusual bonding motif is formed is not yet explained. The same synthetic reaction was also tried[50] with different proportions of silver oxide and dibenzylimidazolium bromide affording invariably crystals with the same structure.

The complexes **2a**, **2d** and **2e**, although structurally authenticated, are reported in this thesis as a biscarbene salts of the type: $[Ag(carbene)_2][AgX_2]$, for the sake of simplicity.

Moreover, the electrospray ionization mass spectrometry analysis in methanol indicated the presence in solution of the cations $[(NHC)_2Ag]^+$ with the observed isotopic distributions in perfect agreement with the calculated ones (See experimental part for more details).

2.2 Reaction of 1a with KO^{t}Bu

One objective of this work was a preparation of a free carbene from the imidazolium salts **1a** and **1b**. Since it has been already reported by Arduengo[51], that the deprotonation of the corresponding imidazolium salt affords the corresponding free carbene without side reactions, this procedure has been repeated in our laboratory, but without a success. The deprotonation reactions were carried out under strictly anhydrous conditions in a variety of dry solvents, including acetonitrile, THF and toluene, using 1.2 molar equivalent of the base KO^{t}Bu with respect to the imidazolium salt. In most of the cases, after the addition of the base, the reaction mixture turned bright yellow, but the NMR analysis indicated only the presence of unidentified decomposition products. The difficulty of obtaining a free carbene from the imidazolium prescursors containing the methylene group on one of the N-sides was pointed out in the review of Youngs et al.[28] Eventually, we succeeded in deprotonating the salts **1a** and **1b**, without decomposition, in the reaction of the respective imidazolium salt with only 0.9 molar equivalent of the KO^{t}Bu. The choice of this proportion salt/base seems to be rational in a light of the risk to deprotonate other acidic sites in a molecule by a strong base; however, since the reaction was carried out in $CDCl_3$, an immediate deuteration occurred, which was unambiguously confirmed by the ^{13}C NMR experiment; in this spectrum, a downfield triplet deriving from the carbenic carbon coupling to the deuterium atom appeared at 135.94 ppm with coupling constant $^1J(^{13}C\text{-}D) = 33.0$ Hz (Figure 2.6).

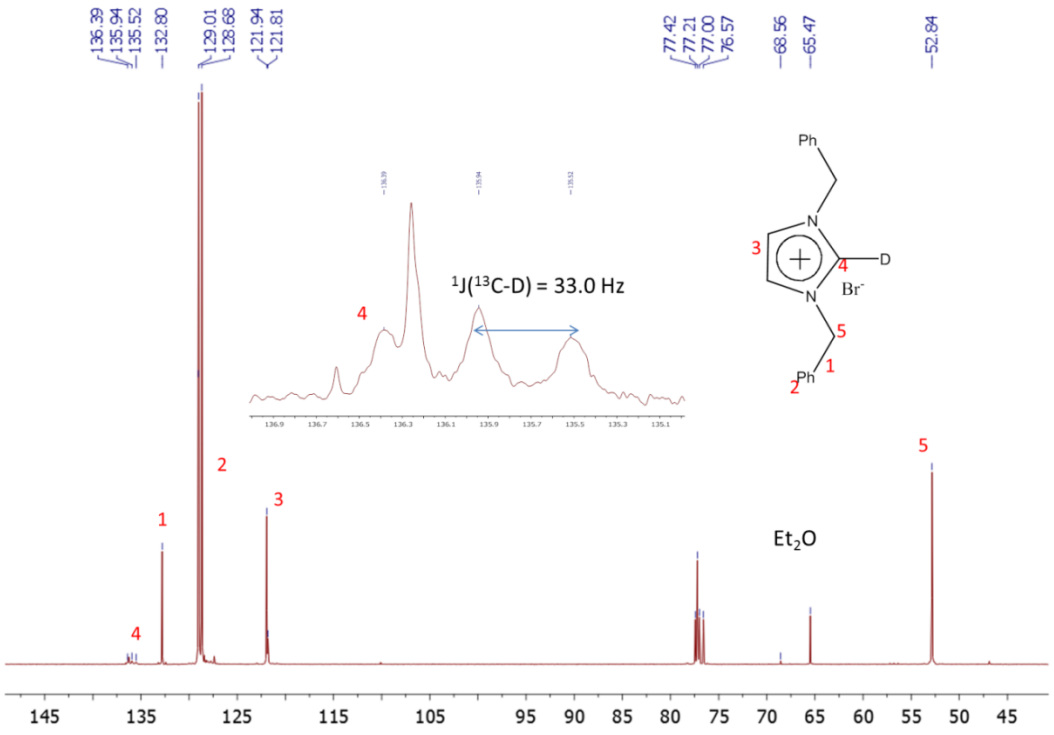

Figure 2.6 ^{13}C NMR spectrum of deuterated 1b with the inset showing the 1:1:1 triplet at 135.94 ppm.

These results indicate that the deprotonation reaction leads to the immediate formation of the desired NHC carbene, but due to its high reactivity, it can be used only *in situ* reactions.

2.3 Synthesis of Rhodium(I) Complexes and Solution NMR Studies

The rhodium complexes [Rh(NBD)Cl(NHC)] (NBD = 2,5-norbornadiene; NHC = 1-benzyl-3-R-imidazolin-2-ylidene; **3a**, R = Me; **3b**, R = benzyl; **3d**, R = trityl; **3e**, R = *tert*-butyl) were synthesized in high yields (70–95%) by transmetalation from the Ag(I)-NHC complexes **2a-e** in dichloromethane (Scheme 1.1).

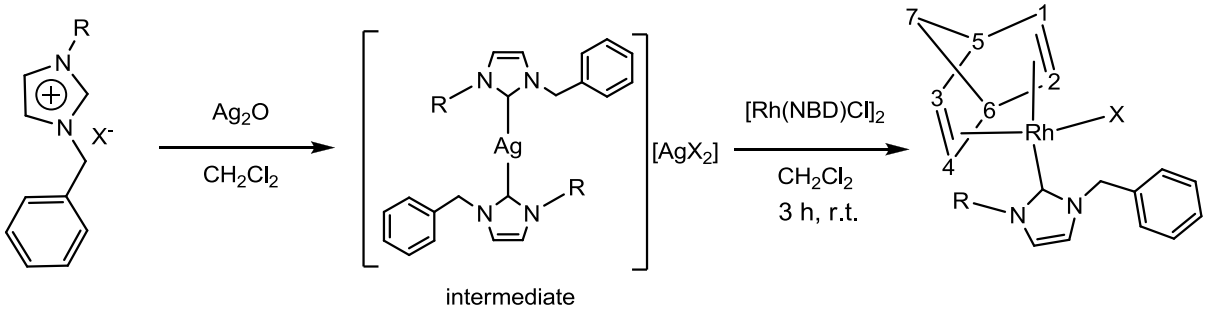

1a-e **2a-e** **3a-e**

Scheme 2.6 Synthesis of rhodium(I)-NHC complexes 3a-e.

Complexes **3a-e** were isolated as yellow microcrystalline solids, after filtering off any unreacted Ag_2O or any formed AgX by gradient column chromatography under argon on anhydrous silica gel. They are completely soluble in chlorinated solvents and acetonitrile, partially soluble in diethyl ether, and completely insoluble in petroleum ether. Complexes **3a-d** are air stable in the solid state and in solution confirmed by continuous monitoring of the NMR samples in $CDCl_3$ over 2 weeks, in opposite to the structurally similar but amide-functionalizedrhodium(I)-NHC complexes containing a Boc-protected 1-(2-aminoethyl) group on a side chain, reported in the literature[1]. The melting point has been determined only for the complex **3a** (m.p. = 142 °C) due to the fact that in the case of **3b**, a thermal decomposition occurred before the melting has been observed (at 210 °C) and the complex **3d** is hygroscopic, which made impossible the measurement of the melting temperature.

Complexes **3a-e** have been fully characterized by ESI-MS mass spectrometry, and ^{1}H and ^{13}C NMR using gCOSY, gHSQC, and gHMBC experiments for full resonance assignments. The most significant chemical shifts and coupling constants in ^{1}H and ^{13}C NMR spectra of the complexes **3a-e** are presented in Table 2.2 and Table 2.3, respectively.

Table 2.2 The most significant chemical shifts in ^{1}H NMR spectra of the rhodium(I)-NHC complexes 3a-e, acquired at room temperature.

Compounds	C*H*$_2$Ph δ (ppm)	C*H*$_{NBD}$ δ (ppm)	*C*^{7}H$_2$ δ (ppm)	*C*H$_{im}$ δ (ppm)
3a (Me)	5.73 (s)	4.84 (s) 3.73 (s) 3.36 (br s)	1.30 (m)	6.76 (s) 6.65 (s)
3b (Bz)	5.73 (br s)	4.78 (s) 3.60 (s) 3.20 (br s)	1.20 (br d, $J_{H,H}$ = 1.4 Hz)	6.61 (s)
3d (Trit.)	6.84 (d, $J_{H,H}$ = 15.06 Hz) 6.17 (d, $J_{H,H}$ = 14.79 Hz)	4.61 (s) 3.59 (s) 3.44 (s) 3.10 (s) 2.87 (s) 1.94 (s)	0.95 (m)	6.76 (d, $J_{H,H}$ = 2.06 Hz) 6.56 (d, $J_{H,H}$ = 1.97 Hz)
3e (^{t}Bu)	6.41 (d, $J_{H,H}$ = 15.09 Hz) 6.27 (d, $J_{H,H}$ = 15.09 Hz)	4.84 (m) 4.70 (m) 3.81 (br s) 3.78 (br s) 3.47 (m)	1.36 (d, $J_{H,H}$ = 8 Hz) 1.31 (d, $J_{H,H}$ = 7.99 Hz)	7.06 (d, $J_{H,H}$ = 1.97 Hz) 6.72 (d, $J_{H,H}$ = 2.03 Hz

The general trend which can be observed for all of the compounds **3a-e** is the increasing complexity of their ^{1}H NMR spectra (acquired at room temperature) with the increasing bulkiness of the N-substituents. The bigger is the steric hindrance, the higher the activation energy of the rotation about the Rh-carbene bond and the less symmetric is the specie in terms of the magnetic equivalency of the nuclei. As an example, the signals attributed to the imidazole backbone protons appear as two singlets at 6.76 and 6.65 ppm for **3a** and one singlet at 6.61 ppm for the symmetric **3b**, but in case of the more hindered **3d** and **3e** the discussed protons appear as two doublets with the $^{3}J_{H,H} \approx 2$ Hz. A similar behavior was observed at room temperature for the benzylic CH_2 protons; they are found as singlets for the complexes **3a** and **3b**, whereas in cases of **3d** and **3e** the CH_2 decoalesces into AB system, showing two doublets with the $^{2}J_{H,H} \approx 15$ Hz (Figure 2.7 and Figure 2.8). Moreover, the imidazole backbone protons resonate in a slightly lower field with respect to the corresponding imidazolium salts and the silver complexes.

The olefinic protons of the norbornadiene ligand in cases of **3a** and **3b** complexes feature three resonances (2 protons each), whereas the C^7H_2 (CH_2NBD) appears as a multiplet (**3a**) or a doublet (**3b**) in a low field at 1.30 and 1.20 ppm, respectively; for the compound **3d** and **3e** there are seven signals corresponding to the eight protons of the norbornadiene; for **3d** all of them are singlets except the C^7H_2, which appear as a multiplet at 0.95 ppm, whereas in the case of the complex **3e** the protons C^7H_2 were exceptionally found as two doublets with the coupling constant $^2J_{H,H} \approx 8$ Hz. The spectroscopic data are in accordance with the reported ones[1]. These observations suggest the absence of an effective symmetry plane in the molecules resulting from the hindered rotation about the carbene – rhodium bond.

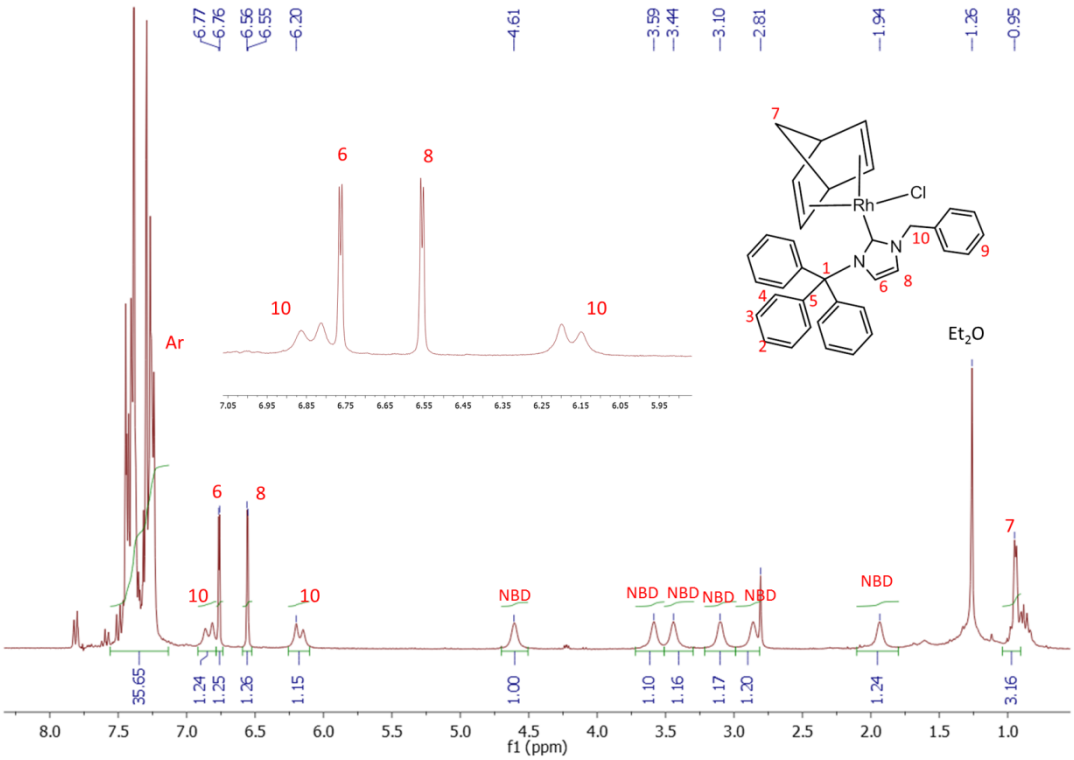

Figure 2.7 ^{1}H NMR spectrum of 3d with the inset showing the decoalesced benzylic and imidazole backbone protons.

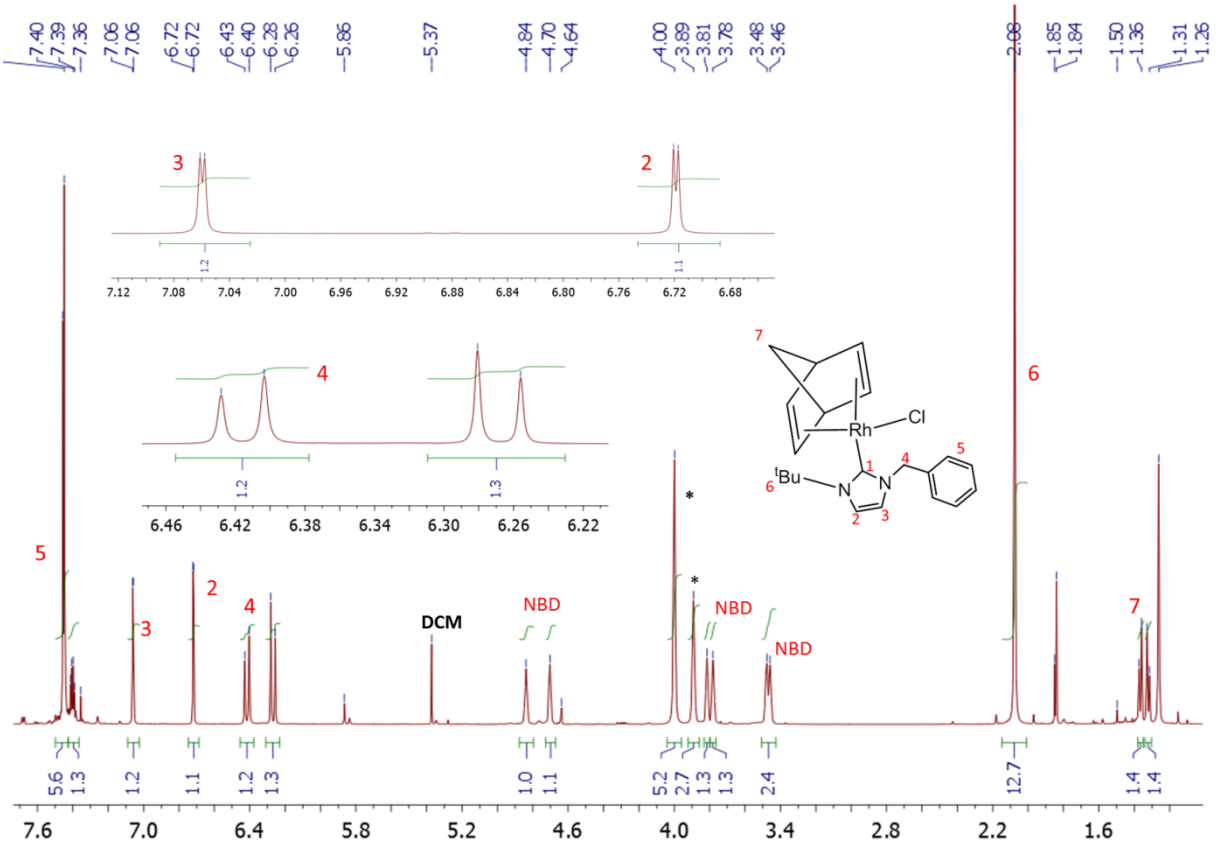

Figure 2.8 ^{1}H NMR spectrum of 3e with the inset showing the decoalesced benzylic and imidazole backbone protons.

All of the complexes **3a-e** show a common feature in the ^{13}C NMR spectra, namely, the appearance of the downfield doublet with the one-bond coupling constants: $^{1}J(^{13}C\text{-}^{103}Rh)$ = 57.8 Hz for **3a**, $^{1}J(^{13}C\text{-}^{103}Rh)$ = 76.8 Hz for **3b**, $^{1}J(^{13}C\text{-}^{103}Rh)$ = 57.8 for **3d** and $^{1}J(^{13}C\text{-}^{103}Rh)$ = 58.5 Hz for **3e** resulting from the coupling of the carbenic carbon nucleus to the rhodium nucleus, occurring naturally as almost entirely one isotope ^{103}Rh with a nuclear spin I = 1/2[52].

The carbon atoms of the norbornadiene ligand appear as four doublets (including the $C^{7}H_2$) in the ^{13}C NMR spectra of **3a** and **3b**, whereas more sophisticated pattern has been found for **3d**: three singlets and three doublets (including the $C^{7}H_2$) and for **3d**, where the resonances appear as doublets and one doublet of doublet (including the $C^{7}H_2$), resulting from the coupling to the metal center, with coupling constants $J(^{13}C\text{-}^{103}Rh)$ ranging from 2.5 to 13 Hz (Figure 2.9). The increasing complexity of the splitting patterns in the ^{13}C NMR spectra going from **3a** to **3e** confirms the influence of the steric encumbrance on the rate of the dynamic processes with respect to the NMR time scale.

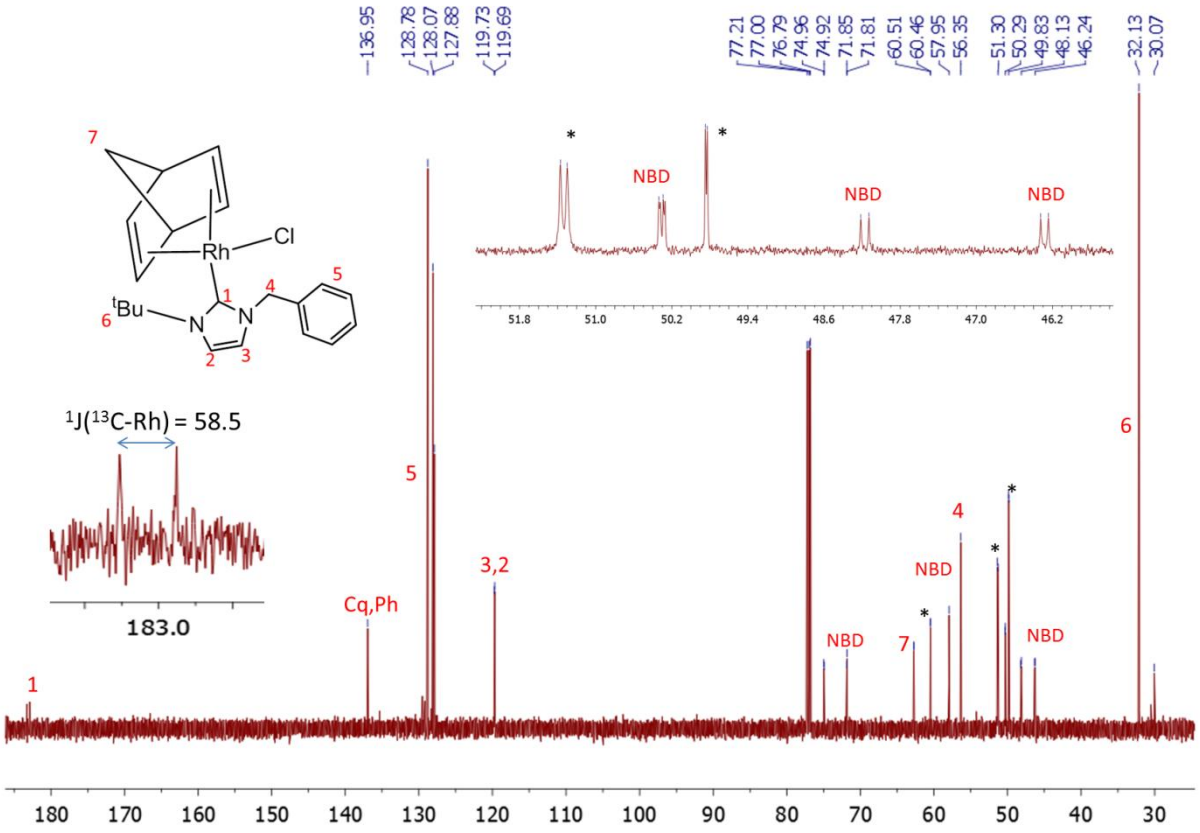

* traces of starting material $[Rh(NBD)Cl]_2$

Figure 2.9 ^{13}C NMR spectrum of 3e.

Table 2.3 Most significant chemical shifts in 13C NMR spectra of the rhodium(I)-NHC complexes 3a-d.

Compounds	NCHN δ (ppm)	CH_{NBD} δ (ppm)	C^7H_2 δ (ppm)
3a	184.8 (d, $J_{C\text{-}Rh}$ = 57.82 Hz)	79.0 (d, $J_{H,H}$ = 6.0 Hz) 51.0 (d, $J_{H,H}$ = 2.5 Hz) 48.3 (d, $J_{H,H}$ = 12.77 Hz)	63.4 (d, $J_{H,H}$ = 5.22 Hz)
3b	185.4 (d, $J_{C\text{-}Rh}$ = 76.80 Hz)	79.1 (d, $J_{H,H}$ = 5.70 Hz) 51.0 (d, $J_{H,H}$ = 5.70 Hz) 48.5 (d, $J_{H,H}$ = 17.00 Hz)	63.3 (d, $J_{H,H}$ = 5.30 Hz)
3d	186.5 (d, $J_{C\text{-}Rh}$ = 55.00 Hz)	73.1 (s) 49.7 (s) 49.0 (s) 45.7 (d, $J_{H,H}$ = 13.00 Hz) 44.7 (d, $J_{H,H}$ = 10.80 Hz)	61.8 (d, $J_{H,H}$ = 5.80 Hz)
3e	183.0 (d, $J_{C\text{-}Rh}$ = 58.5 Hz)	74.9 (d, $J_{H,H}$ = 6.1 Hz) 71.8 (d, $J_{H,H}$ = 6.3 Hz) 57.9 (s) 50.3 (dd, $J_{H,H}$ = 2.5 Hz, $J_{H,H}$ = 7.0 Hz) 48.1 (d, $J_{H,H}$ = 13.0 Hz) 46.2 (d, $J_{H,H}$ = 12.2 Hz)	62.7 (d, $J_{H,H}$ = 5.2 Hz)

2.3.1 Stereodynamics

The stereodynamics and the rotation barriers about the Rh-carbene bond have been determined by means of variable-temperature NMR spectroscopy; the rotation barrier was modulated by increasing the steric hindrance of the N-alkyl substituent (Figure 2.10).

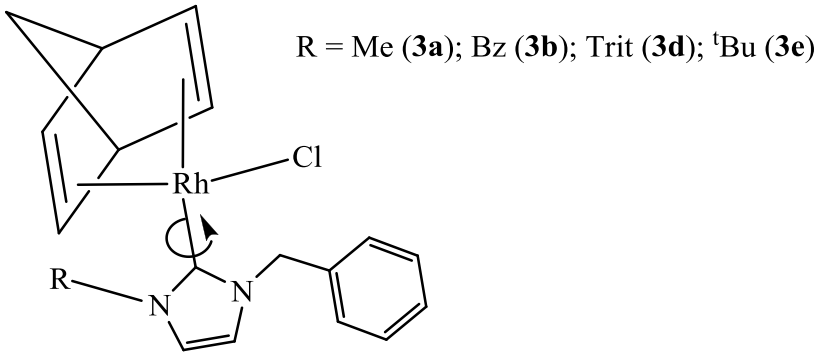

Figure 2.10 The hindered rotation about the Rh-carbene bond.

As it was briefly mentioned before, the direct consequence of the hindered rotation about the Rh – carbene bond is the lack of the effective symmetry plane in these complexes; in fact, the norbornadiene moiety and the chlorine atom are displaced in an out-of-plane disposition with respect to the imidazole ring. If the two side arms are different, the molecule has C_1 symmetry; therefore a pair of conformational enantiomers is generated, as presented in Figure 2.11.

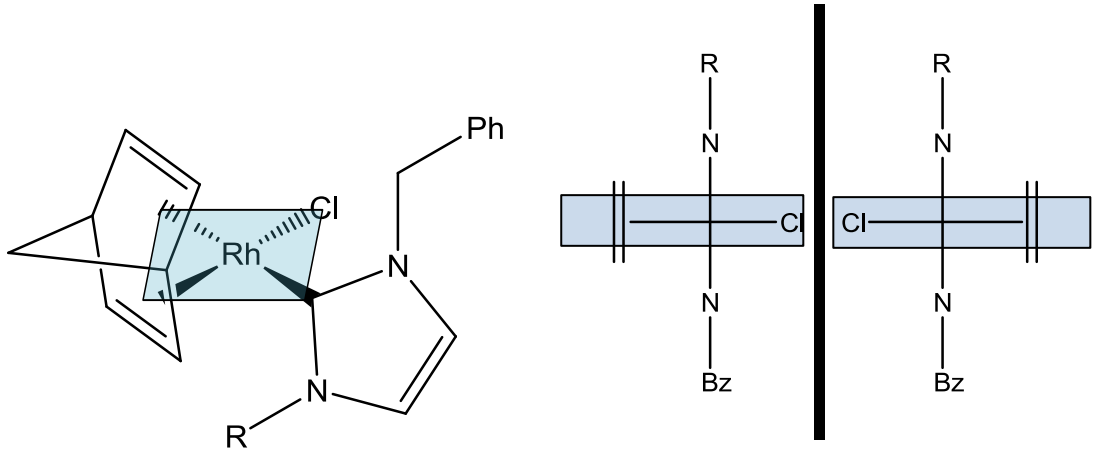

Figure 2.11 Coordination plane of the rhodium(I) in the complexes 3a-e and the two enantiomers generated by the axis of chirality along the Rh-carbene bond.

The ^{1}H NMR spectra of the complex **3a** recorded at a series of temperatures ranging from -30 to 25 °C in 1,1,2,2-tetrachloroethane-d_2 (boiling point 146.5° C) are shown in Figure 2.12. The singlet at 5.73 ppm observed at room temperature, deriving from the benzylic geminal protons broadens on decreasing the temperature and reaches the typical shape of the coalescence at 10 °C. On further lowering the temperature, the resonance decoalesces into AB system, showing first a broad doublet and eventually two doublets which increase in the sharpness and intensity until the minimum -30 °C. A similar behavior is also observed for the signals attributed to the protons of the norbornadiene ligand; the signals broaden on lowering the temperature until coalescence at ~ 10 °C, and then sharpen again in the range of the temperature between 10 and -30 °C.

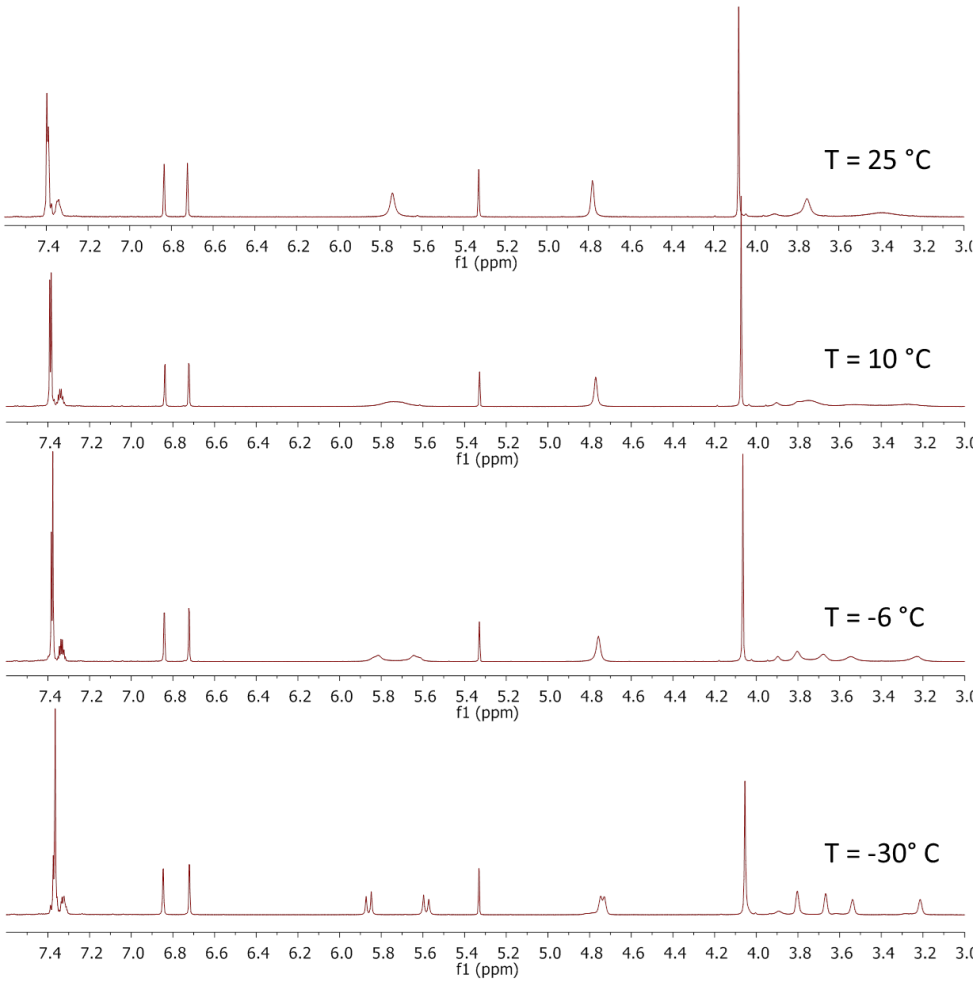

Figure 2.12 ^{1}H NMR spectra of 3a at various temperatures (600 MHz, $C_2D_2Cl_4$).

The VT NMR experiment in case of complex **3b** bearing the two benzyl groups on the N-side arms of the imidazole, which cause a bigger steric hindrance with respect to the previously discussed **3a**, shows that the anisochronous benzylic protons appear as a broad

doublet at room temperature, whereas the coalescence is reached at 32 °C. Subsequently, on further raising the temperature, the resonance sharpens and at 75°C appears as a very sharp, intense singlet. On the other hand, at -10 °C, the splitting pattern characteristic for an AB system has been observed, although the two doublets were not well resolved. In this case, the coalescence of the olefinic norbornadiene protons has not been reached in the range of the temperature investigated (Figure 2.13).

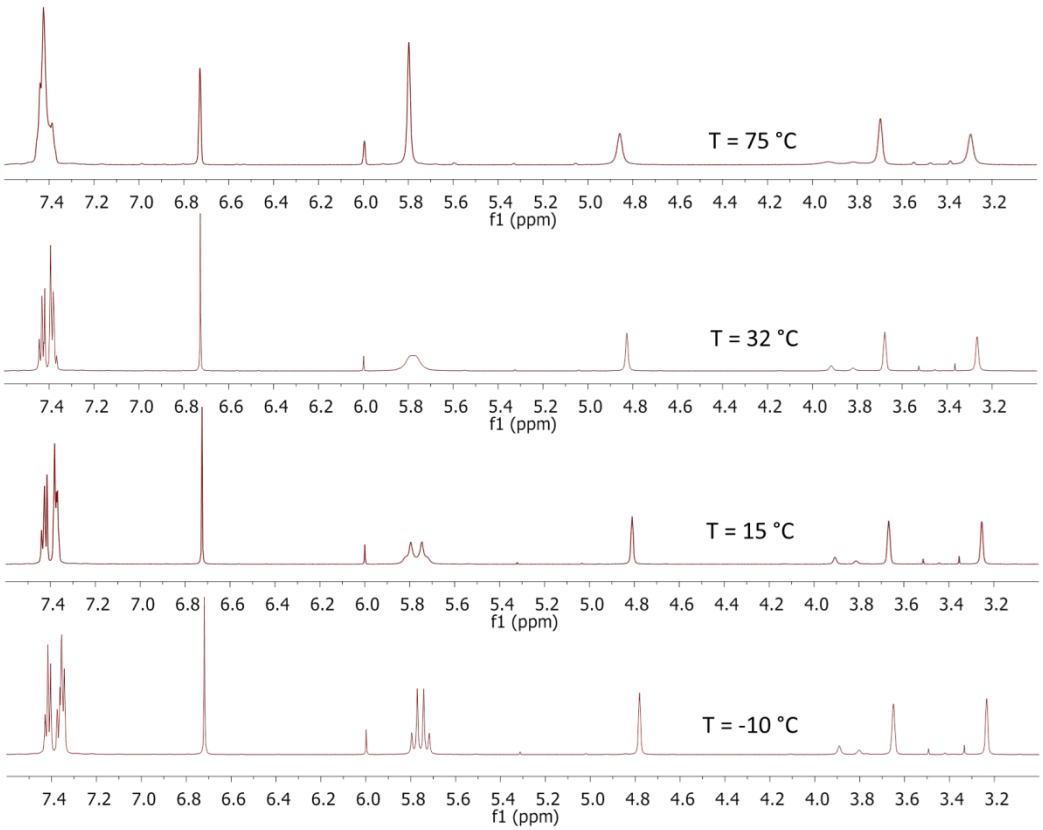

Figure 2.13 ^{1}H NMR spectra of 3a at various temperatures (600 MHz, $C_2D_2Cl_4$).

For the complex **3d**, bearing the trityl group, two VT experiments were performed, in $CDCl_3$ (boiling point 61-62 °C) and in 1,1,2,2-Tetrachloroethane-d_2, respectively. In the first experiment, due to low boiling point of the $CDCl_3$, spectra at temperatures higher than 50 °C could not be acquired and coalescence was not observed. In the second experiment, the obtained spectra indicated some decomposition processes of the investigated complex (See experimental section for more details). A likely explanation of this behavior can be a presence of traces of acid in chlorinated solvents, which, as reported, often lead to the partial regeneration of NHC complexes[53].

The VT NMR analysis was also carried out for the complex **3e** in toluene-d_8 (boiling point 110 °C), but due to the high activation energy of the hindered rotation about the Rh-carbene bond, the coalescence of the benzylic protons was not reached.

Thus, in order to determine the stereodynamics of these two complexes **3d,e** and to calculate the energy barrier, an exchange spectroscopy (EXSY) experiment has been employed. However, the required information was obtained only for the complex **3d;** in case of the **3e**, the means of the dynamic NMR (both VT and EXSY) appeared to be not suitable for the experimental determination of the thermodynamic data, which is in accordance with limitations of this technique reported in the literature[54], namely, that only energy barriers over the range 4.5 – 23 kcal mol^{-1} (18.8 – 96.2 kJ mol^{-1}) can be determined.

2.3.2 Kinetics

The benzylic signals in the spectra of the complexes **3a** and **3b** show coalescence at 10 and 32 °C, respectively. At this temperatures, the kinetic constants for the enantiomerization were accurately determined by calculations from the below equation:

$$\boldsymbol{k = \frac{\pi|\nu_A - \nu_B|}{\sqrt{2}}} \qquad \text{Eq. 2.1}$$

where ν_A and ν_B are the resonant frequencies (expressed in Hz) of nuclei A and B in the absence of the exchange (for the details, see section 1.7.1 of the Introduction chapter). The kinetic constants for the temperatures above and below the coalescence temperature were derived by the means of the lineshape simulation performed over the entire range of temperatures (Figure 2.14).

a)

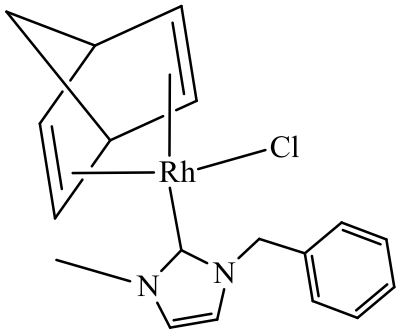

$\Delta G^{\ddagger}$ = 56.5 kJ mol^{-1}

b)

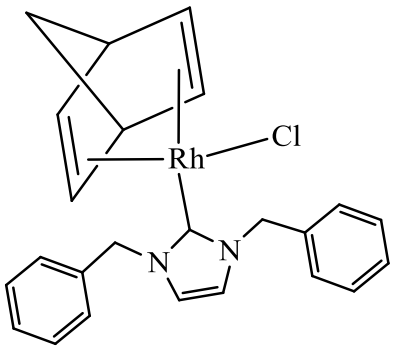

$\Delta G^{\ddagger}$ = 62.7 kJ mol^{-1}

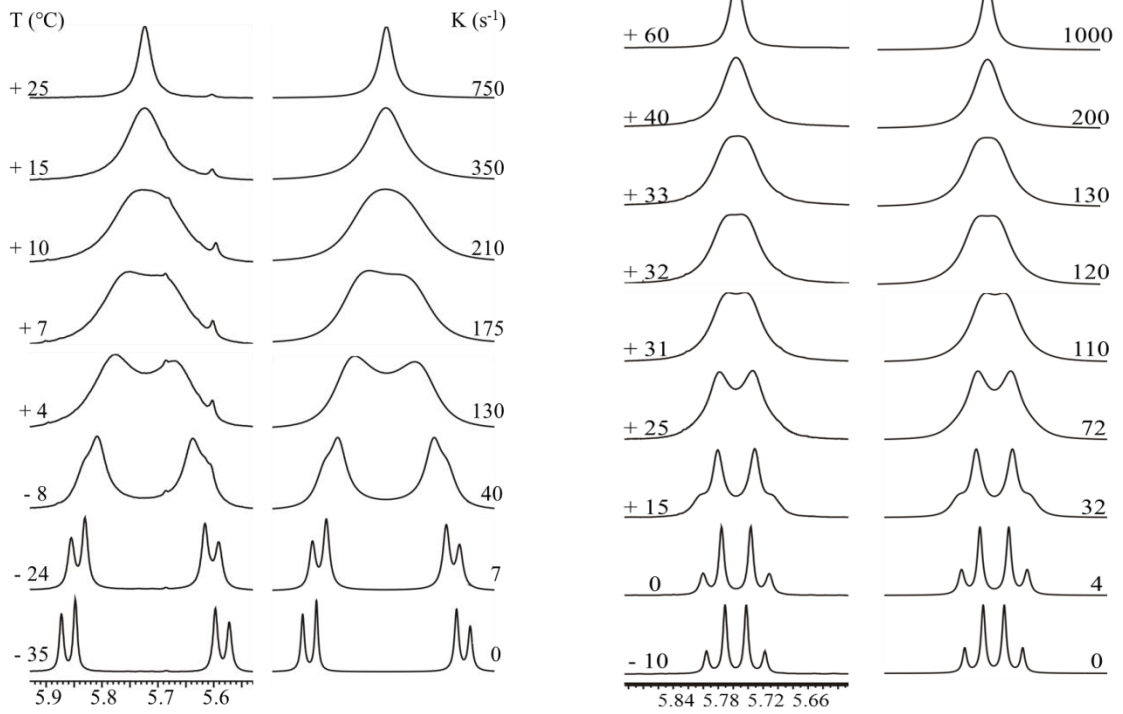

Figure 2.14 Variable-temperature spectra of 3a (a) and 3b (b) showing the evolution of the benzylic CH_2 signals (^{1}H NMR at 600 MHz, $C_2D_2Cl_4$). On the right side of each plot the simulations with the corresponding rate constants are reported.

Subsequently, an activation energies of 56.5 and 62.7 kJ mol^{-1} for **3a** and **3b** respectively, were derived from the Eyring equation. The activation energy was found to be constant with respect to the temperature, indicating a negligible value of the activation entropy. This observation indicates that the observed barrier should be due to steric effects only and it is consistent with the increase of the activation energy between less steric hindered

3a and the more steric hindered **3b** ($\Delta\Delta G^{\ddagger} = 6.2$ kJ mol^{-1}). These data agree very well with those reported by Enders and Gielen[55,56], who proposed a steric origin of the rotational barrier.

The 1D EXSY experiment carried out at four different temperatures: -10, -15, -20 and -25 °C on the complex **3d**, allowed for a determination of kinetic constants for the rotation around the carbon-metal bond (according to a procedure described in the section 1.7.1.2 of the Introduction Chapter). The linear functions of $\ln([A]_{eq} - [A]_t)$ vs. the used array of mixing times: 0.025, 0.05, 0.075 and 0.1 s were ploted for each temperature (Figure 2.15a), affording the kinetic constants, which, as expected, increase with the increment of the temperature. For each temperature, the activation energy was derived by the use of the Eyring equation.

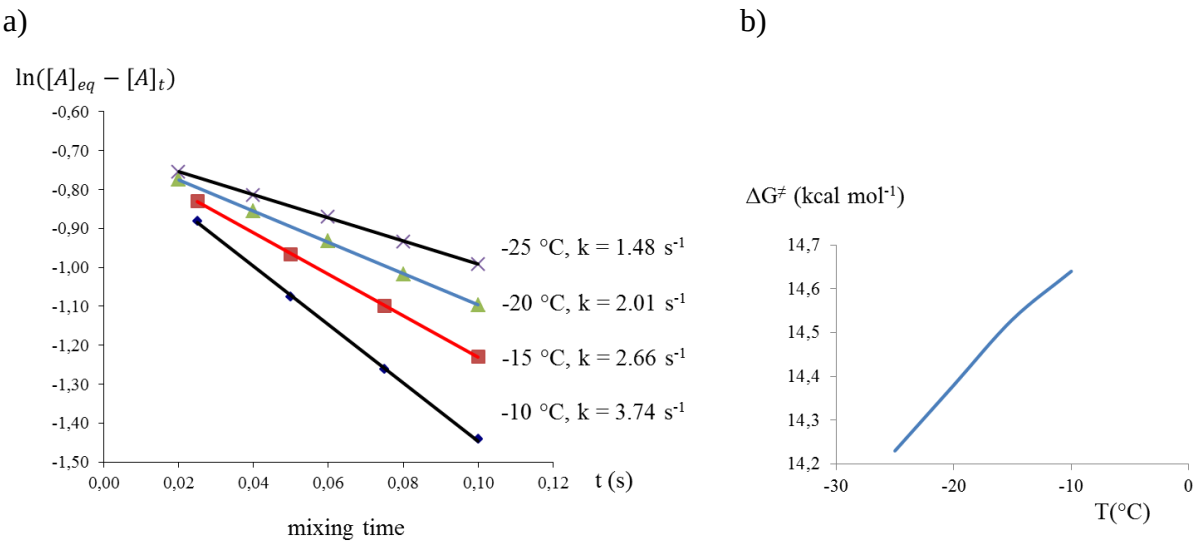

Figure 2.15 The plots of $\ln([A]_{eq} - [A]_t)$ vs. mixing time at different temperatures (a) and the dependence of the activation energy on the temperature (b).

The EXSY experiment showed that the rotational barrier (61.9 kJ mol^{-1}) was identical, within the experimental error, to that obtained in the case of the dibenzyl-substituted compound **3b**; however the plot of the $\Delta G^{\ddagger}$ against the temperature (Figure 2.15b) shows a variation of the former, indicating a negative entropic activation.

As shown in Scheme 2.7, the two enantiomeric ground states GS and GS' can interconvert into each other by two possible transition states due to the rotation around the carbene-rhodium bond.

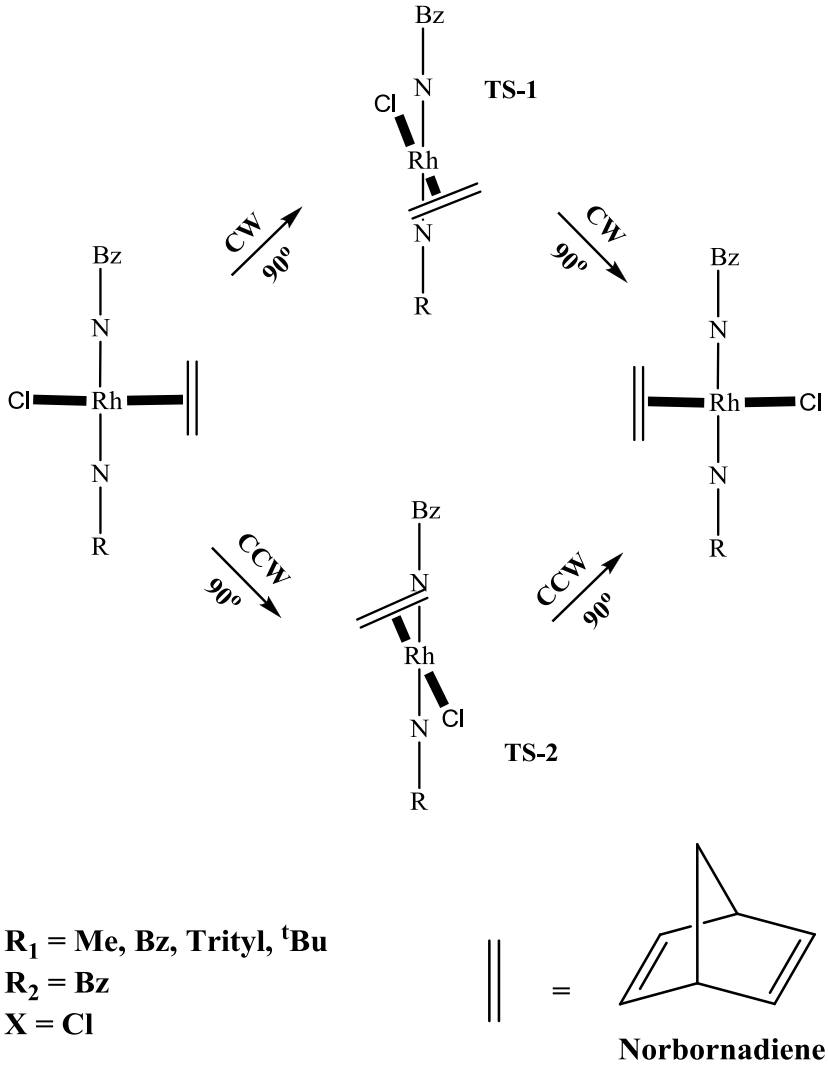

Scheme 2.7 Enantiomerization pathway for compounds 3a-e.

The first one (TS-1) is reached by a 90° clockwise rotation starting from GS and corresponds to the crossing of the chloride atom on the benzylic CH_2 of one of the side arms of the imidazole (denoted as R2), whereas the second transition state (TS-2) takes place when a counterclockwise rotation forces the chloride atom to cross the second alkyl side arm group (R1) on the imidazole. The steric hindrance of the R1 obviously influence the activation energy of the rotational barrier. DFT calculations of the two possible transition states (Table 2.4) suggested that the threshold pathway (i.e., that with the lowest transition-state energy) corresponded in all the cases to the passage of the halogen atom on the benzyl group (TS-1), with the simultaneous crossing of the norbornadiene on the second side arm (R1). The calculations also suggested that the energy barrier is strongly related to the steric hindrance of R1, and for this reason the barrier calculated for compound **3c** is predicted to be very high (100.0 kJ mol^{-1}).

Table 2.4 Calculated and experimental energy barriers for the enantiomerization of 3a-e (energies in kJ mol^{-1}, calculations at the B3LYP/LANL2DZ level).

Compound	TS-1	TS-2	Experimental (kJ mol^{-1})
3a	55.0	58.5	56.5
3b	65.3	78.7	62.7
3c	101.7	115.9	61.9
3d	96.7	119.7	not determined

As can be seen from Table 2.4, the rotation barriers calculated for **3a** and **3b** were consistent with the experimental values, whereas it was not true in the case of **3c**, where the experimental value was equal to that obtained for compound **3b** and much smaller with respect to the calculated one; moreover, as it was already mentioned, the energy barrier derived for **3c** from the data obtained from the EXSY experiment, showed a strong dependence on the temperature, whereas for the two other complexes, the quantity did not vary with the temperature. In particular, the big negative activation entropy derived from simulations (-27 ± 10 eu) indicates that a strongly organized transition state or a different interconversion pathway could take place in the case of compound **3c**. It is very important to highlight that all the discussed here data related to stereodynamics and kinetics of the complexes **3a-e** are in keeping with data reported recently for structurally similar but amide-functionalized rhodium(I)-NHC complexes; this agreement indicates that the influence of the functionalization on the dynamic behavior of the investigated systems is negligible. Hence, as it has been reported in the previous case, the possible explanations for this behavior are: the inversion process may proceed either via a cleavage of the Rh-Cl bond before or during the rotation or by partial dissociation of the trityl group into a contact ionic pair, followed by the rotation of the Rh-Cl moiety and subsequent re-formation of nitrogen-trityl carbon bond; another hypothesis arises from a studies performed by Peris[33] and Nolan[34] and very recently also by Royo[32] on aromatic and aliphatic intramolecular C-H activation in transition metal complexes bearing NHC ligands, mentioned in Section 1.4 of the introduction. As a

consequence of this reactivity, cyclometalated species are formed. In our case, the coordination of one of the carbon atoms of the trityl ligand to the metal center did not occur, which was confirmed by NMR analysis. Nevertheless, it is worth to consider the possible interactions between hydrogen atoms in orto positions of the aromatic rings in trityl ligand with the rhodium center. In order to investigate these interactions, a following reaction should be prepared (which lies in the range of further research in our laboratory), Scheme 2.8;

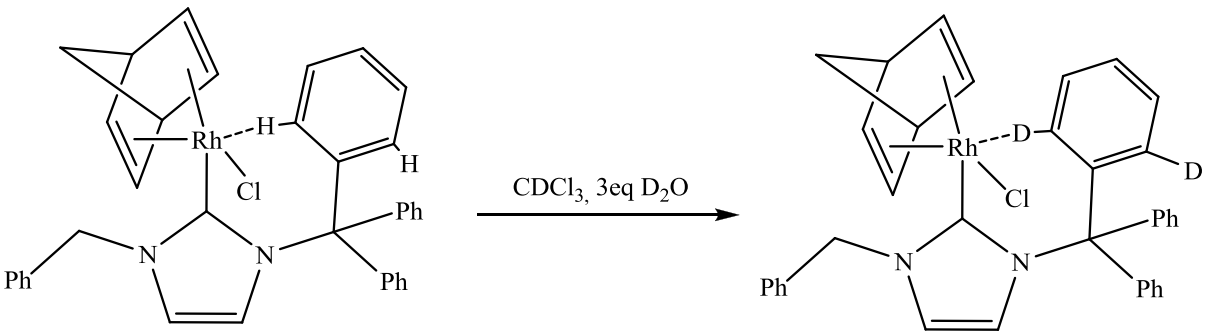

Scheme 2.8 Possible reaction between the rhodium(I)-NHC complex and D_2O.

The hypothesized interactions would weaken the C-H bonds in all the three aromatic rings, enabling the exchange between the proton and deuterium nuclei, which would be observable in NMR spectrum. This concept will be developed beside the framework of this thesis.

Crystal Structure Determination for 3a and 3b. The molecular structures of the rhodium(I) complexes **3a** and **3b** were determined via X-ray diffraction and are reported in Figure 2.16 and Figure 2.17. (Crystal data and experimental details are reported in the experimental part). Crystals of **3a**,**b** suitable for diffraction were grown from a double layer of dichloromethane and petroleum ether (1:4).

The structure of **3a**, which crystallized in a centric space group (P21/c) of the monoclinic crystal system (Z = 4), consists of separated $C_{20}H_{27}ClN_2Rh$ molecules arranged in eclipsed, alternating columns of enantiomers in a 1:1 ratio. The two possible orientations of the benzyl and the CH_3 substituents on the imidazolium ring result from the axial chirality present in the molecule of **3a**. Rhodium shows a classic square-planar coordination and is bonded to the Cl(2) atom, the carbenic C(1) and the bidentate norbornadiene fragment. There is a stronger trans effect observed for the carbene moiety when compared to the chlorine ligand, relying on the difference in bond lengths between the Rh atom and the carbon atoms of the norbornadiene moiety situated in the trans orientation with respect to the chlorine and

the carbene, respectively; the Rh-C(16) and Rh-C(20) contacts trans to the chlorine are 2.083(4) and 2.098(4) Å, respectively, and the Rh-C(14) and Rh-C(15) bond lengths trans to Cl atom are remarkably longer: 2.194(4) and 2.213(4) Å, respectively. It is worth to note that despite the presence of donor chlorides anions, there are not significant intra- or intermolecular hydrogen bonds in the solid state.

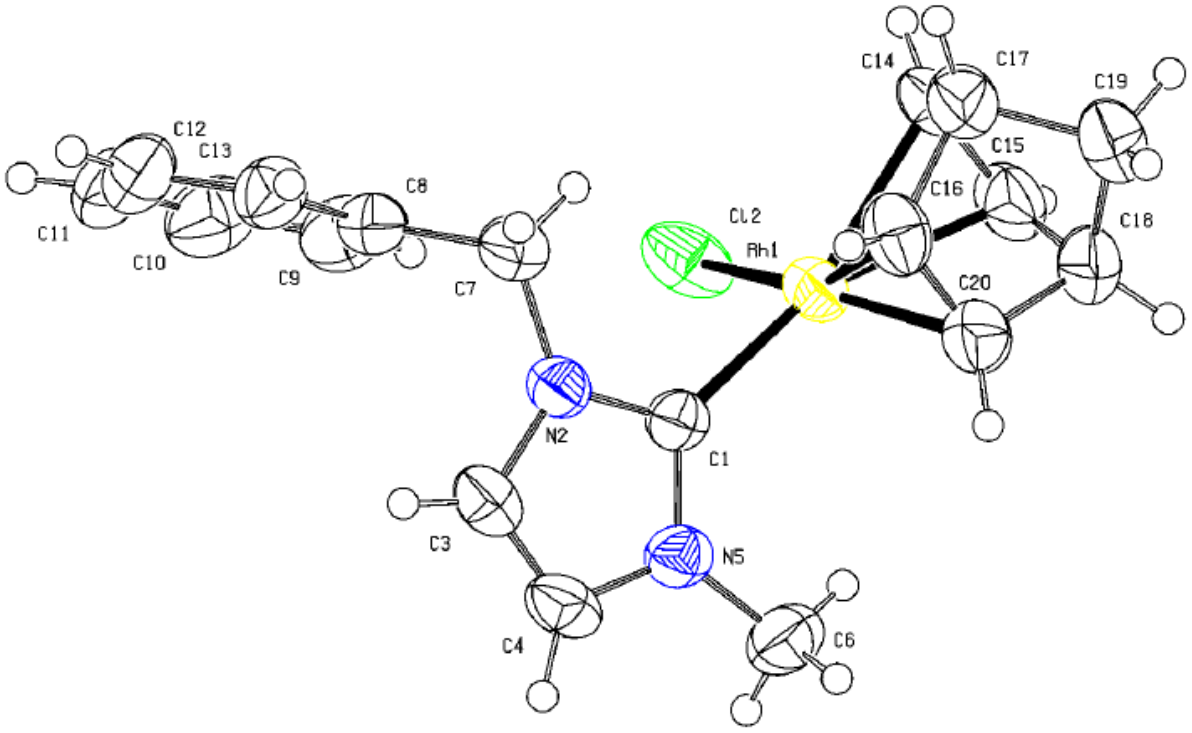

Figure 2.16 ORTEP diagram of 3a depicted with thermal elipsoids at 50% probability. Selected bond distances (Å) and bond angles (deg): Rh(1)-C(1), 2.019(4); Rh(1)-C(16), 2.083(4); Rh(1)-C(20), 2.098(4); Rh(1)-C(14), 2.194(4); Rh(1)-C(15), 2.213(4); C(1)-N(2), 1.353(4); C(1)-N(5), 1.354(4); N(2)-C(1)-N(5), 104.0(3); C(1)-Rh(1)-Cl(2), 90.57(10); C(1)-Rh(1)-C(16), 97.00(15); C(1)-Rh(1)-C(20), 99.27(15); C(1)-Rh(1)-C(14), 156.71(16); C(1)-Rh(1)-C(15), 161.52(16), C(1)-Rh(1)-C(1)-N(2), 101.0(3).

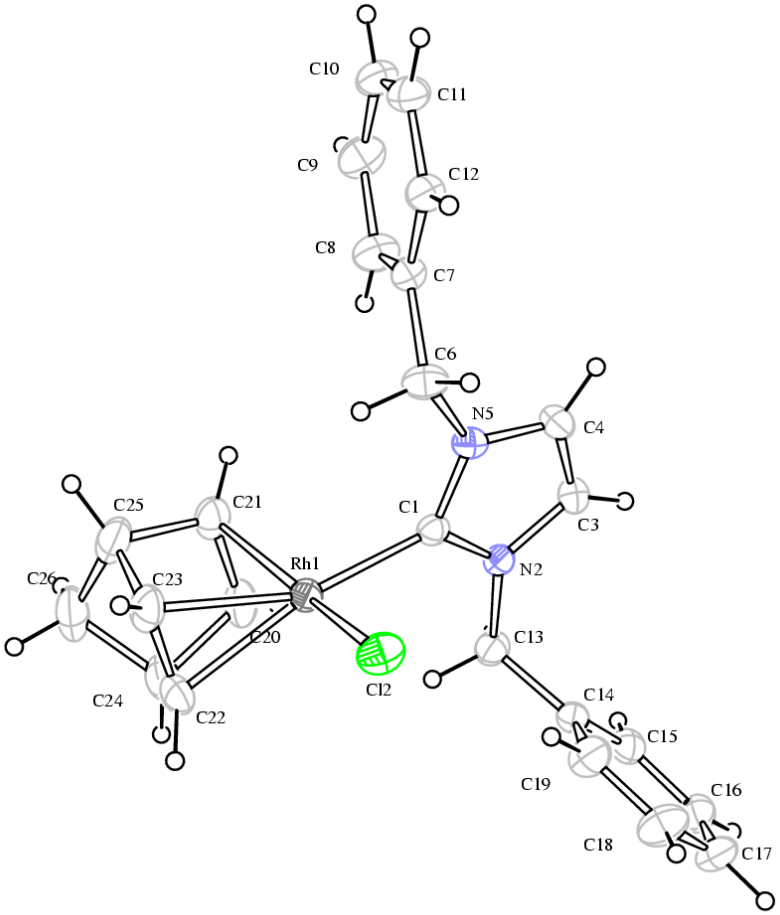

Figure 2.17 ORTEP diagram of 3b depicted with thermal elipsoids at 50% probability. Selected bond distances (Å) and bond angles (deg): Rh(1)-C(1), 2.023(2); Rh(1)-Cl(2), 2.3618(6); Rh(1)-C(20), 2.084(2); Rh(1)-C(21), 2.091(2); Rh(1)-C(22), 2.185(2); Rh(1)-C(23), 2.195(2); C(1)-N(5), 1.353(3); C(1)-N(2), 1.360(3); N(5)-C(1)-N(2), 104.19(17); C(1)-Rh(1)-Cl(2), 90.83(6); C(1)-Rh(1)-C(20), 99.49(9); C(1)-Rh(1)-C(21), 98.63(9); C(1)-Rh(1)-C(22), 161.04(10); C(1)-Rh(1)-C(23), 158.45(9), C(1)-Rh(1)-C(1)-N(2), 102.59(18).

The complex **3b** crystallizes in the centrosymmetric P21/n group of the monoclinic crystal system (Z = 4) and both enantiomers are generated by the center of symmetry, as in the previous case. Similarly, there is also the trans effect observable in the structure of **3b**, with the Rh-$C_{norbornadiene}$ distances shorter when in orientation trans with respect to the carbene moiety than those being trans with respect to the chloride ligand; namely the Rh-C(20) and Rh-C(21) contacts are 2.084(2) and 2.091(2), respectively, whereas Rh-C(22) and Rh-C(23) distances are longer: 2.185(2) and 2.195(2), respectively.

Generally, the crystallographic data are very similar for these two complexes **3a** and **3b** as regards the bond and angle distances and the crystal package. The relevant data are compared in Table 2.5.

Table 2.5 Crystal data for 3a and 3b.

	3a	3b
Rh-C bond length (Å)	2.019(3)	2.023 (2)
Rh-X bond length (Å)	2.3800(11)	2.3618 (6)
C(1)-Rh(1)-C(1)-N(2)	101.0(3)	102.59 (18)

It is worth to mention that both the Rh-$C_{carbene}$ bond distance and the dihedral angle C(1)-Rh(1)-C(1)-N(2) that yields the two enantiomers, whose barrier was observed in solution, are slightly bigger in the case of the more encumbered **3b** complex with comparison to **3a**.

2.4 Synthesis of Iron(II) Complexes

Inspired by the work of Albrecht at al.[27] in which a series of piano-stool iron(II) complexes bearing NHC and CO as ligands were synthesized via a free carbene route relying on a deprotonation of the imidazolium salt with a strong base (KO^tBu) and the subsequent metalation in situ with [FeI(Cp)$(CO)_2$] (Cp = η^5-C_5H_5) as iron(II) precursor, we decided to exploit this synthetic procedure to prepare the iron complexes with our ligands **1a** and **1b**. The conditions specified by Albrecht are reported in Scheme 2.9.

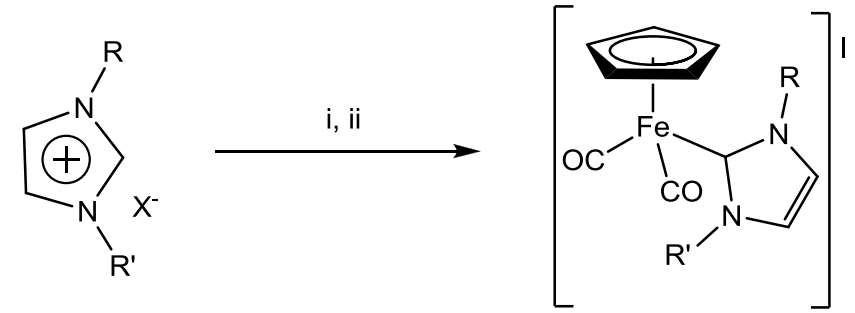

(i) [FeI(Cp)$(CO)_2$], toluene, r.t., 20 h
(ii) KO^tBu, THF, r.t., 1.5 h

Scheme 2.9 Synthetic protocol leading to piano-stool iron(II) complexes.

However, in our hands, despite several attempts under a variety of conditions, we found that this synthetic procedure leads to erratic results. One difficulty consisted in poor solubility of the imidazolium salts in THF, which we tried to overcome making an advantage of ultrasounds emitted by sonicator. Another problematic point of this protocol was the generation of a free carbenes, which requires harsh conditions, such as strong base, and the presence of impurities in the deprotonated Cp-NHC proligand and/or in the iron/carbonyl precursor can seriously compromise this synthesis; this problem has been highlighted recently by Royo[32], who proposed alternative route under mild conditions to iron-NHC complexes, mentioned in section 1.5.1 of the Introduction chapter. Moreover, it was also reported by Youngs at al.[28] and discussed already in section 2.2, that the methylene-linked ligands are particularly sensitive for the side deprotonation of the other acidic protons present in a molecule, leading to the decomposition. Considering these difficulties, we modified the synthetic protocol of Albrecht, and prepared the iron(II)-NHC complexes, by dissolving the imidazolium salt (**1a** or **1b**) with the iron precursor [FeI(Cp)(CO)$_2$] in DMSO, followed by the sonication and the subsequent addition of 1.2 molar equivalent of the base KO^{t}Bu (Scheme 2.10).

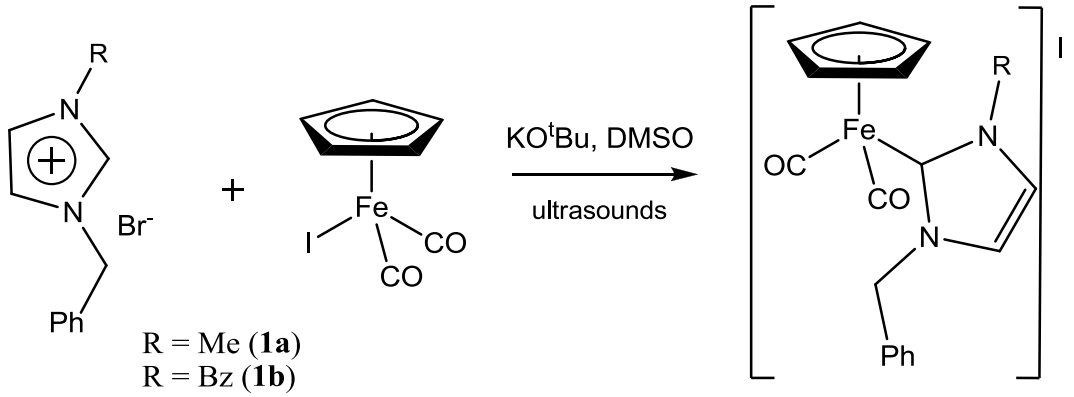

R = Me (**1a**)
R = Bz (**1b**)

Scheme 2.10 Procedure for synthesis of iron(II)-NHC complexes optimized in our laboratory.

The iron complexes in the cationic form have been isolated as brown solids in moderate yields (Y~60%); they are soluble in chlorinated solvents and toluene and completely insoluble in diethyl ether; they are air stable. Formation of the desired complexes was indicated by the presence of the two bands in IR spectrum at ν_s = 2049 and ν_{as} = 2001 cm^{-1}, corresponding to the symmetric and antisymmetric stretchings of the CO molecule. It is noteworthy that the values are not so different from those in the precursor complex [FeI(cp)(CO)$_2$] (2041 and 1997 cm^{-1}), which indicates that the donor strength of the formally neutral carbene ligand to the [Fe(Cp)(CO)$_2$]$^+$ fragment is comparable to that of the anionic iodide[27].

As regards the ^{1}H NMR spectra, their common feature is the expected imidazolium/Cp proton ratio: 2/5. The signal deriving from the Cp ligand appears at chemical shift δ 5.49 ppm which is typical for this group (Figure 2.18).

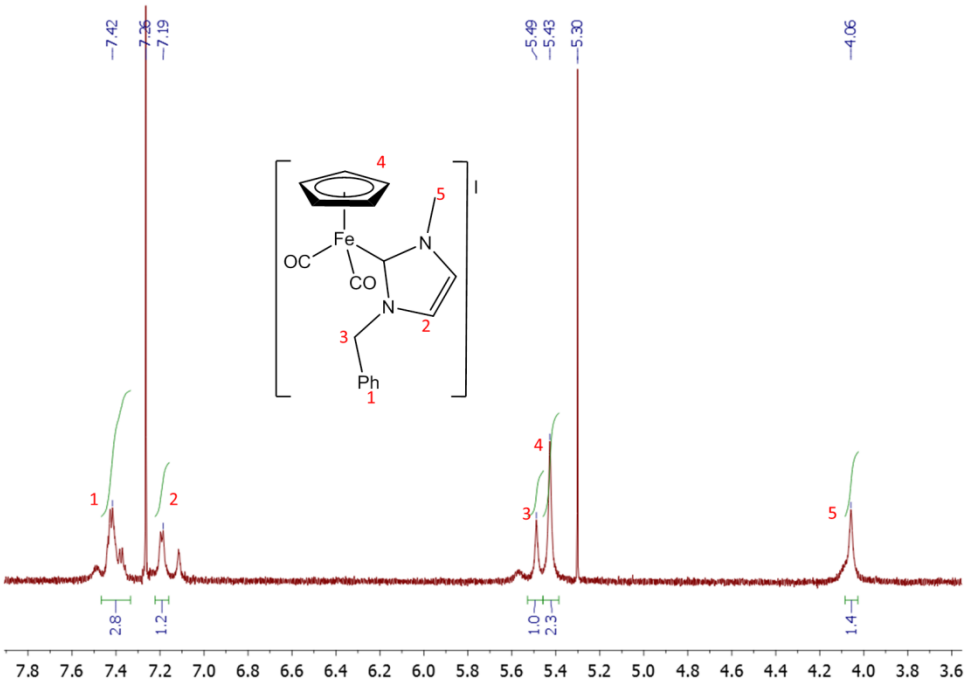

Figure 2.18 ^{1}H NMR spectrum of [FeCp(CO)$_2${1-methyl-3-benzyl-imidazolin-2-ylidene}]I.

In the ^{13}C NMR spectra, the signal attributed to the CO ligands appears in a very low field, at 211.3 ppm, whereas the characteristic signal of carbenic carbon atom bonded to iron is found as a singlet at 164.4 ppm.

The future perspectives of the research in the field of the iron(II)-NHC complexes in our laboratory include a preparation of the corresponding neutral complexes by UV irradiation of the cationic forms, according to equation shown in Scheme 2.11[27]; moreover, different synthetic routes leading to these complexes should be tried and optimized, favorably under mild conditions.

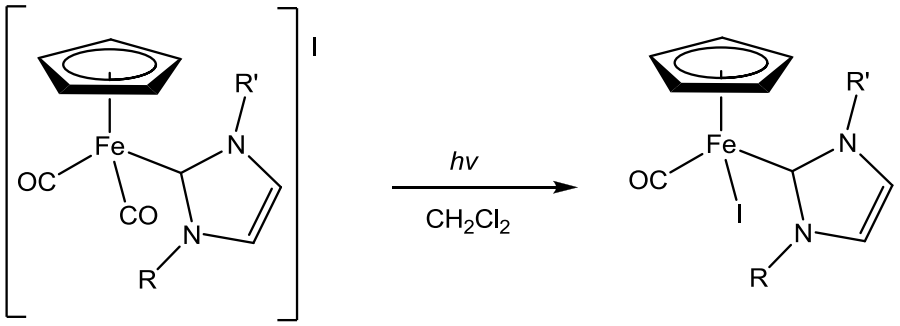

Scheme 2.11 Transformation of the cationic form of a piano-stool iron(II)-NHC complexes to the neutral form induced by *hv* radiation.

A work in this direction has already begun. This procedure consists in a redox reaction of the iron(I) dimer $[Fe_2(Cp)_2(CO)_4]$ with silver triflate in toluene to afford two equivalents of the iron(II) complex possessing one vacancy, since the triflate is a non-coordinating anion (Scheme 2.12).

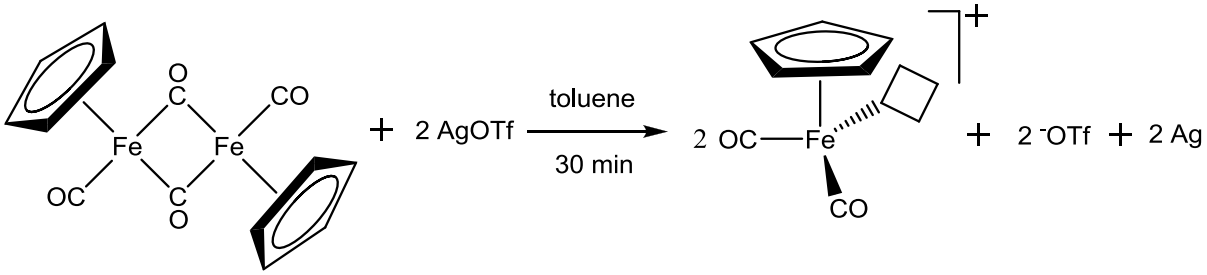

Scheme 2.12 Formation of the iron(II) complex bearing one vacancy in the redox reaction with silver triflate.

A subsequent addition of an imidazolium salt built likewise with a non-coordinating anion should likely lead to the iron(II)-NHC complexes, whereas the same reaction carried out with the imidazolium halides could lead to the side formation of the undesired neutral complex with a halide in the coordination sphere of the iron (Scheme 2.13).

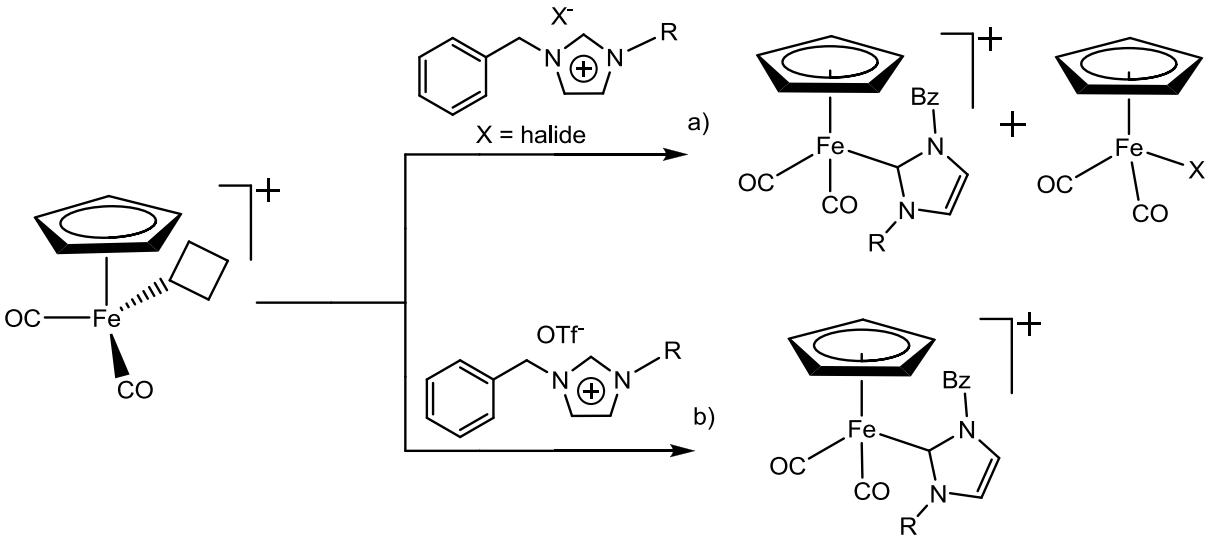

Scheme 2.13 Formation of the piano-stool iron(II)-NHC complexes with halide imidazolium salts (a) and with imidazolium salts built with a non-coordinating anions (b).

With this goal in mind, the ion exchange between bromide and the triflate in the imidazolium salt **1b** has been performed. The 1,3-dibenzyl-imidazolium triflate has been obtained in quantitative yield as a white solid and its formation has been confirmed by ^{1}H, ^{13}C and ^{19}F NMR spectroscopy. The significant high frequency shift of the characteristic signals

deriving from CH_2 and NCHN in the NMR spectra has been observed, when compared to the bromide congener.

The work will be continued beyond the framework of this thesis.

2.5 Catalysis

Hydrosilylation of terminal alkynes with complexes 3a and 3b

The catalytic activity of **3a** and **3b** has been tested in the hydrosilylation of phenylacetylene (PhC≡CH), tolylacetylene (TolC≡CH) and (triethylsilyl)acetylene (Et_3SiC≡CH) with the principal aim to compare their behavior with what was found in the case of amide-functionalized complexes described in the introduction in order to evaluate the influence of the steric hindrance and of the functionalization on the reaction time and selectivity. Moreover, the influence of the catalyst loading (1 mol % or 0.1 mol %) and the temperature at which the reactions were performed, have been also examined.

The catalytic reactions were carried out in three modes characterized by a catalyst loading and a temperature of the reaction: a) catalyst loading: 1 mol % of **3a** at room temperature, b) catalysts loading: 0.1 mol % of **3a** or **3b** at room temperature and c) catalysts loading: 0.1 mol % of **3a** or **3b** at 60 °C; all the reactions were performed in $CDCl_3$ using a slight excess of $HSiMe_2Ph$ and were routinely monitored by ^{1}H NMR spectroscopy.

The hydrosilylation reactions have been proved to be unselective, as previously reported[1,40]; the complexes **3a** and **3b** convert phenylacetylene and tolylacetylene to a mixture of the three possible isomeric vinylsilane derivatives: β-(Z)- or β-(E)-1-silyl-1-alkenes from the anti-Markovnikov addition and α-2-silyl-1-alkene from the Markovnikov addition. Furthermore, the formation of the corresponding alkene has been observed (Scheme 2.14). On the other hand, the hydrosilylation reaction employing the (triethylsilyl)acetylene as a substrate always leads to two products, namely the β-(E)-1-silyl-1-alkene and the α-2-silyl-1-alkene; this behavior is also in line with previous reports[40] (Scheme 2.15).

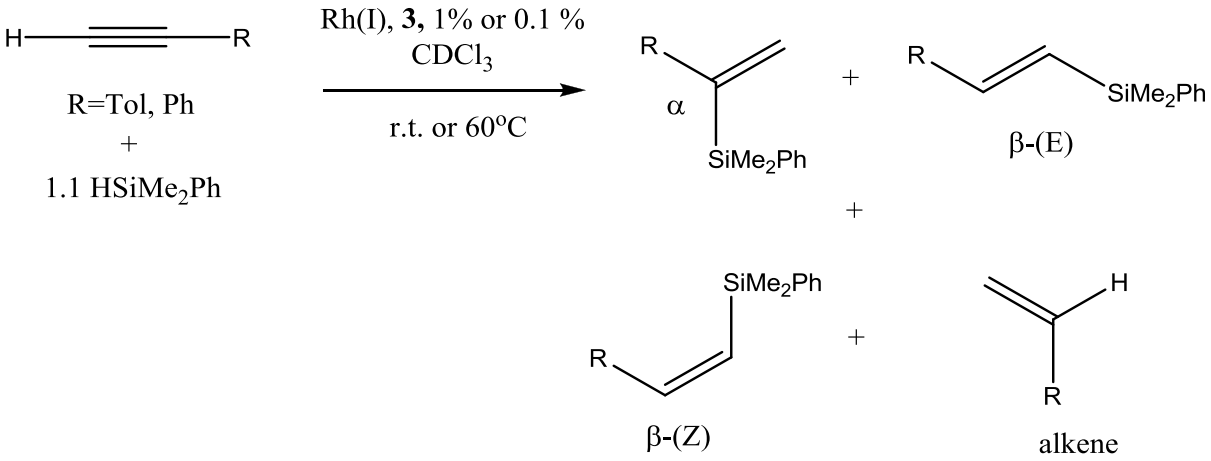

Scheme 2.14 Hydrosilylation of PhC≡CH and TolC≡CH.

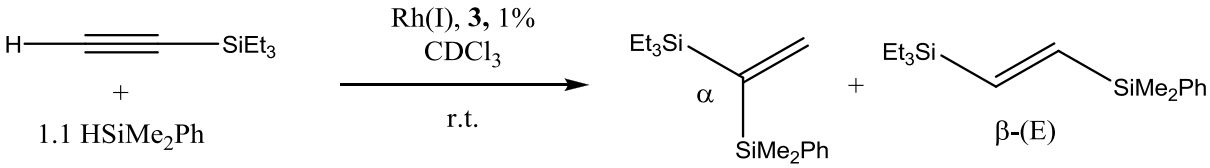

Scheme 2.15 Hydrosilylation of $Et_3SiC{\equiv}CH$.

Catalytic activity of 3a: catalyst loading 1 mol % (T = 25 °C)

The catalyst **3a** in the amount of 1 mol % with respect to the alkynes used, completely converted all the substrates at room temperature (Figure 2.19, Figure 2.20, Figure 2.21); specifically, the most rapid reaction was the one employing (triethylsilyl)acetylene, in which the total conversion was reached after 4h, whereas in cases of phenyl- and tolylacetylene, the reaction was finished after 21 h. As regards the selectivity of the reactions, the β-(Z) vinylsilane was the major product until the substrate completely disappears. However, once a complete conversion is reached, β-(Z) isomerizes to β-(E) vinylsilane, which, at the end of the reaction, is always the major product (Figure 2.19, Figure 2.20). In the case of (triethylsilyl)acetylene, the ratio of the two products: 1-(Dimethylphenylsilyl)-1-(triethylsilyl)ethene and (E)-2-(Dimethylphenylsilyl)-1-(triethylsilyl)ethene is almost constant (50:50), Figure 2.21.

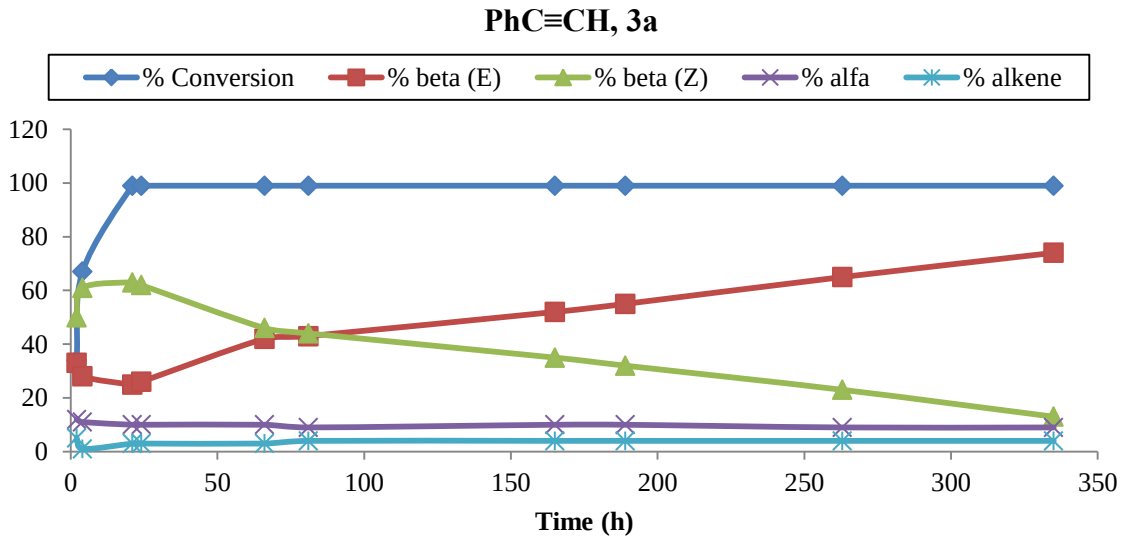

Figure 2.19 Reaction profile of conversion and selectivities vs time for the hydrosilylation of PhC≡CH with 3a.

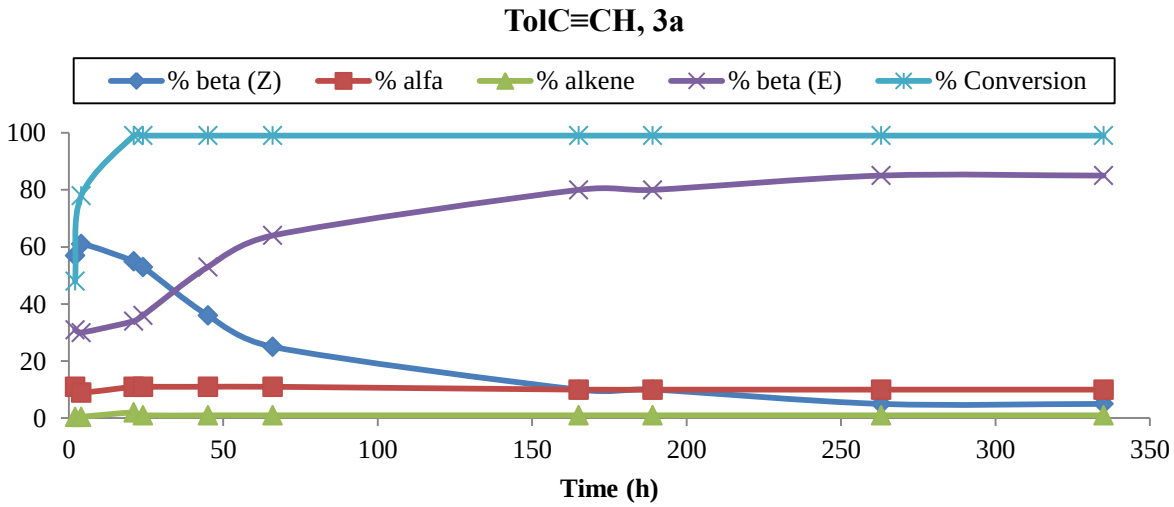

Figure 2.20 Reaction profile of conversion and selectivities vs time for the hydrosilylation of TolC≡CH with 3a.

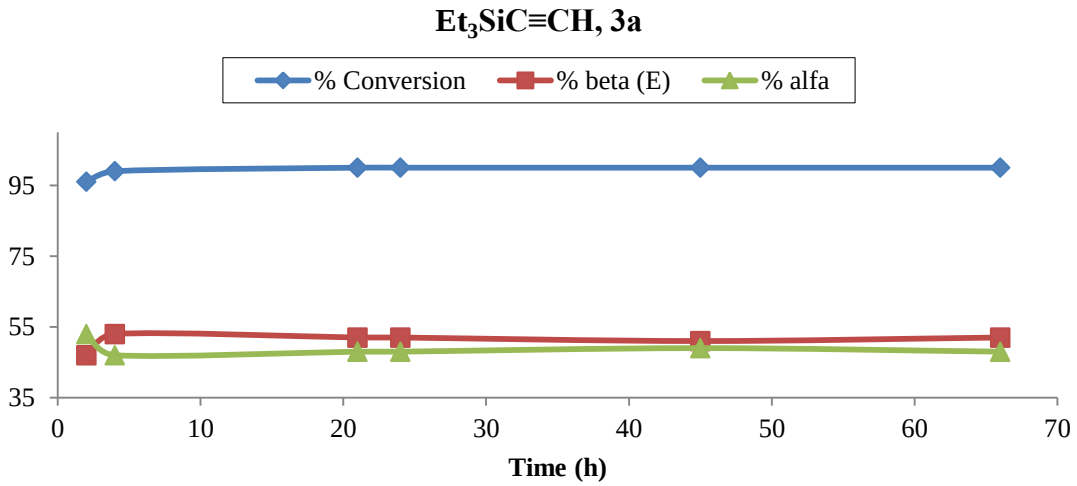

Figure 2.21 Reaction profile of conversion and selectivities vs time for the hydrosilylation of $Et_3SiC{\equiv}CH$ with 3a.

The selectivity in the formation of the products from all the alkynes investigated as a function of time is reported in the bar diagram shown in Figure 2.22. In cases of PhC≡CH and TolC≡CH, as previously discussed, after the complete conversion, the β-(Z) vinylsilane isomerizes to the β-(E) product and the selectivity is slightly better for the latter alkyne, reaching after 263 h the ratio of β-(Z):β-(E) = 5:85, expressed in percent, whereas for the PhC≡CH, after 335 h, the ratio is β-(Z):β-(E) = 13:74. It can also be seen, that the amounts of the two other products of these reactions, the α-2-silyl-1-alkene and the olefin do not vary in the course of the experiment, moreover the latter in the hydrosilylation of the TolC≡CH is formed in such a low quantity as 1%. Regarding the $Et_3C{\equiv}CH$ case, the two resulting products are formed in the percent proportion close to 50:50 and their quantities do not vary with time.

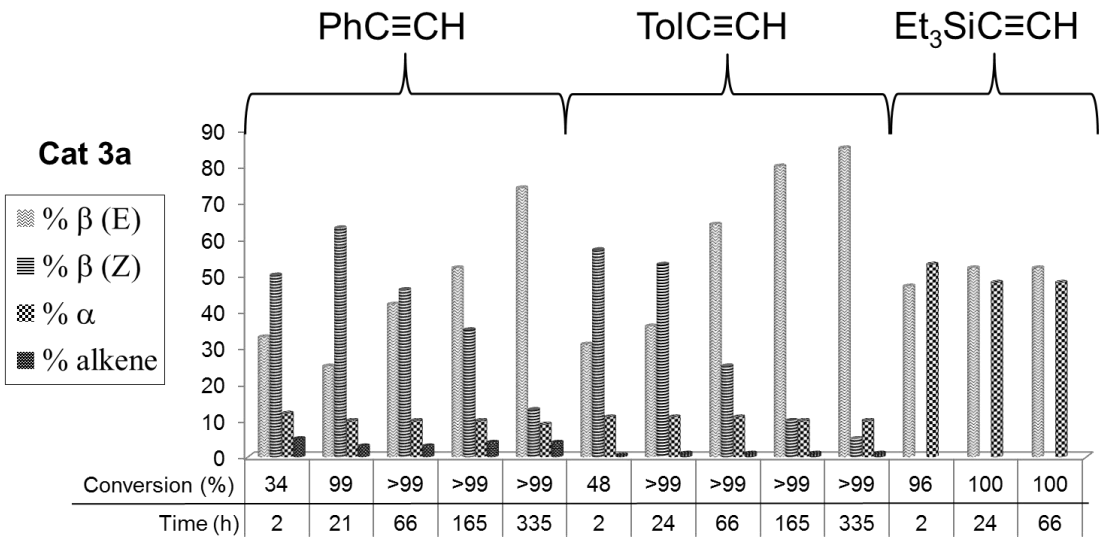

Figure 2.22 Selectivity vs conversion and time for the hydrosilylation of PhC≡CH, TolC≡CH and Et_3SiC≡CH catalyzed by 3a.

Catalytic activity of 3a and 3b: catalysts loading 0.1 mol % (T = 25 °C), PhC≡CH

The reduction of the catalyst loading down to 0.1 mol % in the second experiment significantly affected the catalytic performance. For phenylacetylene, the complete conversion has not been reached within the time put aside the experiment (1080 h) neither in case of **3a** nor **3b** catalyst; after that time, the conversion was 87 and 91% for **3a** and **3b**, respectively; moreover, the reactions required an induction time: 6 h and 8 h for **3a** and **3b**, respectively. In the first stage of the reaction, within the range of 0-121 h, the less encumbered catalyst **3a** showed better reaction rates, however, after that time, the reaction profiles crossed, revealing the higher efficiency of the catalyst **3b** (Figure 2.23). Nevertheless, the reaction employing the **3a** catalyst appeared to be more selective than the other one; for the catalyst **3a**, after 1080 h, the β-(Z) isomer completely (within the experimental error) transformed to the β-(E) vinylsilane: (%)β-(Z):(%)β-(E) = 1:90, while this ratio for the reaction with catalyst **3b** after that time was: (%)β-(Z):(%)β-(E) = 9:76; The graphs in Figure 2.24, Figure 2.25 and Figure 2.26 show that β-(Z) and β-(E) vinylsilane profiles cross much sooner for catalyst **3a** (after 169 h) than for the **3b** (after 504 h) and moreover the isomerization of the β-(Z) into β-(E) began before the complete conversion was reached.

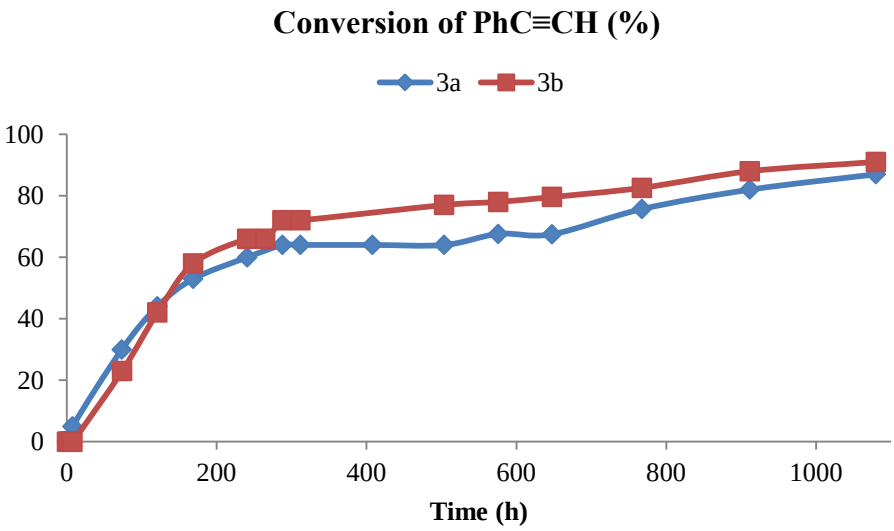

Figure 2.23 Reaction profile of conversion vs time for the hydrosilylation of PhC≡CH with complexes 3a and 3b.

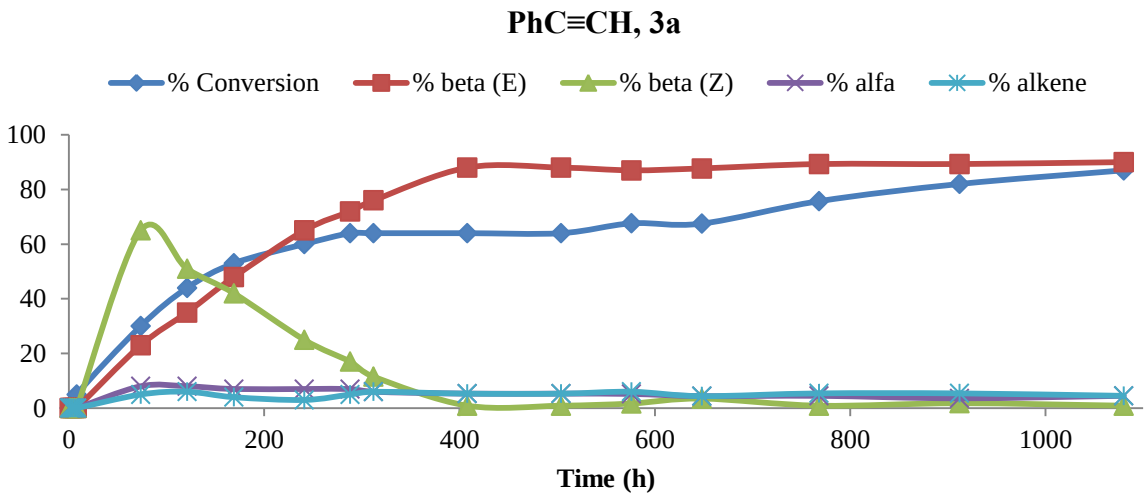

Figure 2.24 Reaction profile of conversion and selectivities vs time for the hydrosilylation of PhC≡CH with 3a.

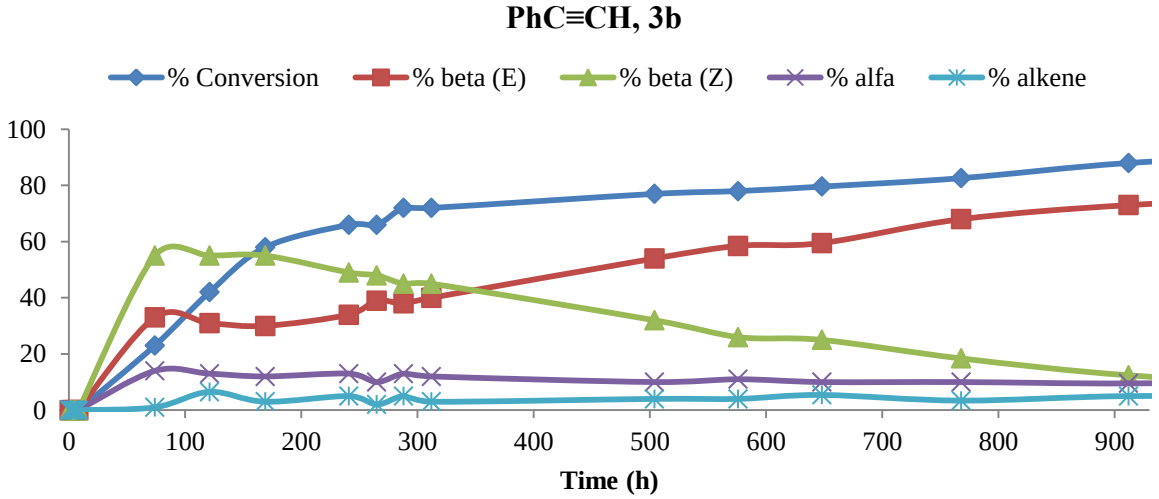

Figure 2.25 Reaction profile of conversion and selectivities vs time for the hydrosilylation of PhC≡CH with 3b.

The influence of the steric hindrance around the metal center of the catalysts on the selectivity of the hydrosilylation reactions can be construed from the bar diagram shown in Figure 2.26. In the case of the reaction catalyzed by **3a**, a steep drop in the amount of the β-(Z) isomer can be observed, whereas a gradual decrease of the amount of this isomer takes place in the reaction with **3b**. For comparison, after 408 h of the reaction with **3a**, the β-(Z) product has been almost completely converted into the β-(E) isomer: β-(Z):β-(E) = 1:88, while after even longer time of 576 h of the reaction with **3b**, the ratio was β-(Z):β-(E) = 26:59. It is important to underline that the lower catalyst loading, even if seriously affected the reaction rate, induced a better selectivity of the obtained products when compared to the 1 mol % catalyst loading, e.g. β-(E) = 74% vs β-(E) = 90% respectively. Additionally, as in the experiment employing 1 mol % of the catalyst, the quantities of alkenes are constant with time.

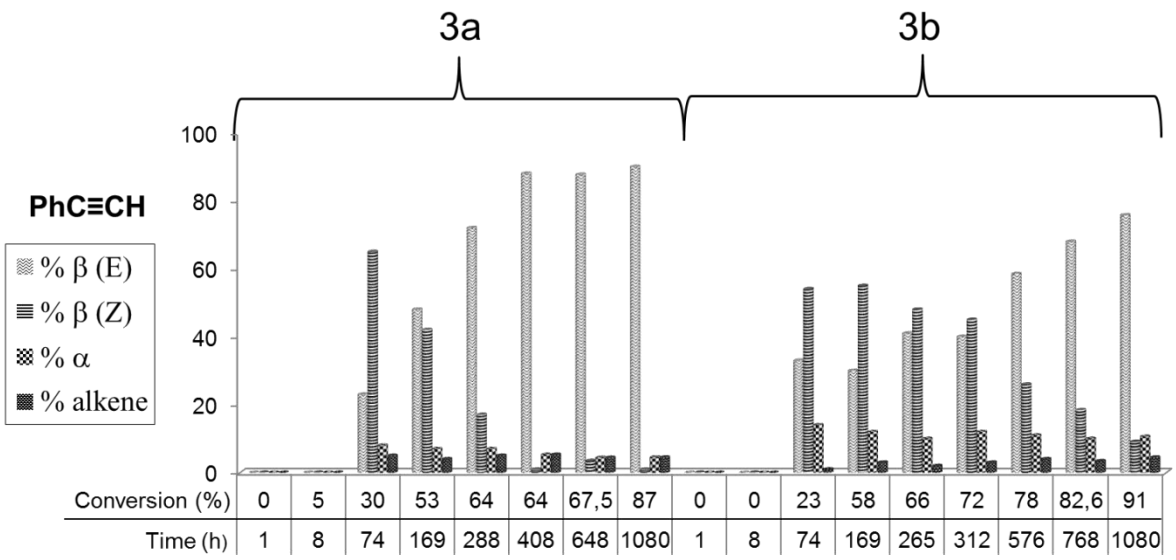

Figure 2.26 Selectivity vs conversion and time for the hydrosilylation of PhC≡CH catalyzed by 3a and 3b.

Catalytic activity of 3a and 3b: catalysts loading 0.1 mol % (T = 25 °C), TolC≡CH

When TolC≡CH was employed as a substrate under the same conditions (catalyst loading and temperature), the reaction rate was slightly faster than for PhC≡CH; The striking observation was, that there was no significant difference between results obtained with **3a** and **3b** catalysts; in both cases the conversion of 99 % has been reached after 648 h and the cross of the profiles of the β-(Z) and β-(E) isomers was observed after 121 h of the reactions (Figure 2.27, Figure 2.28 and Figure 2.30).

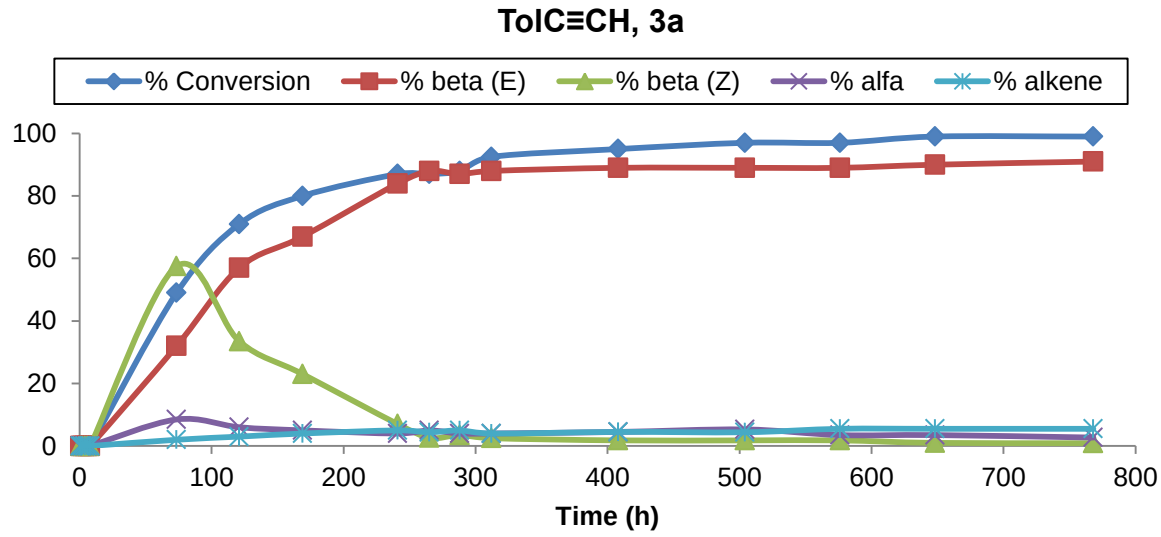

Figure 2.27 Reaction profile of conversion and selectivities vs time for the hydrosilylation of TolC≡CH with 3a.

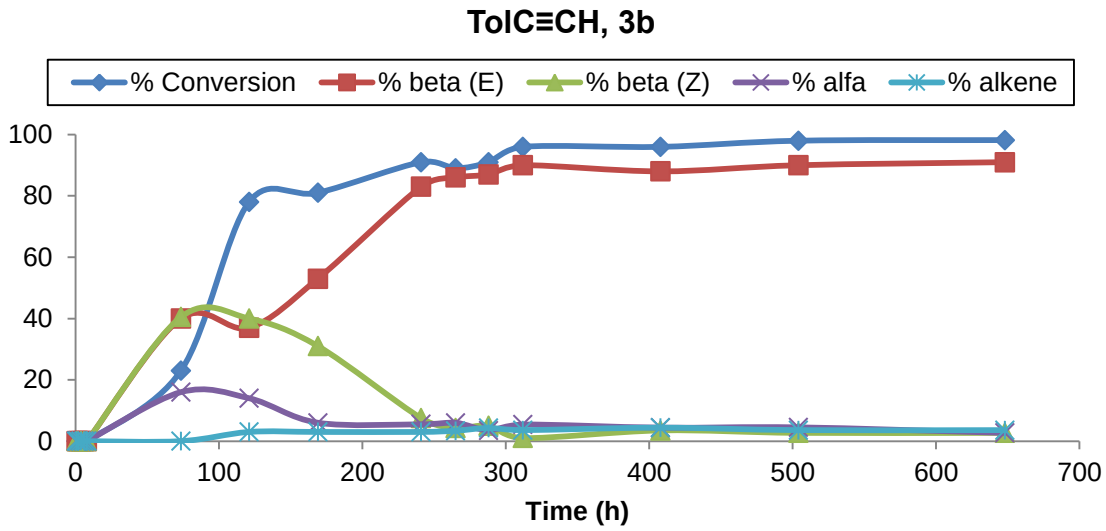

Figure 2.28 Reaction profile of conversion and selectivities vs time for the hydrosilylation of TolC≡CH with 3b.

However, similarly to the hydrosilylation of the phenylacetylene, in the very first stage of the reaction the less encumbered complex **3a** appeared to be more efficient in terms of the rate of the conversion, Figure 2.29.

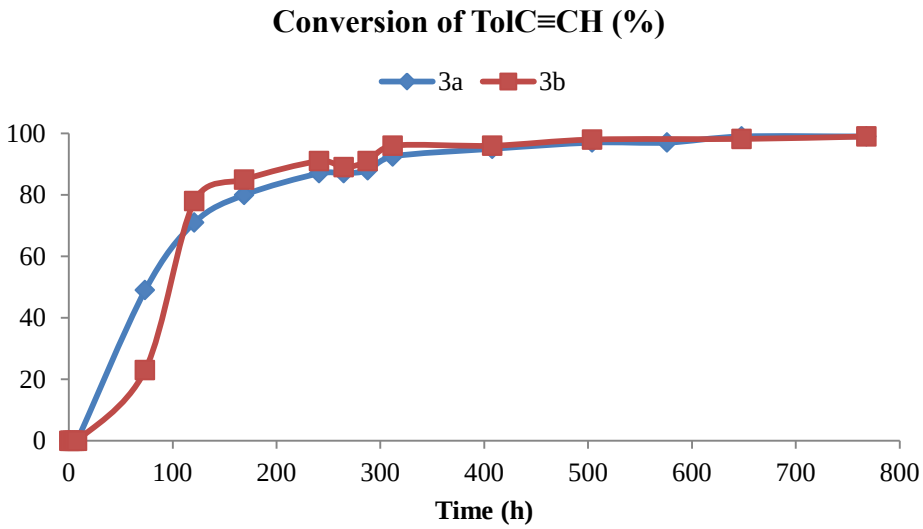

Figure 2.29 Reaction profile of conversion vs time for the hydrosilylation of TolC≡CH with complexes 3a and 3b.

The conversion and selectivity profiles are reported in the bar diagram shown in Figure 2.30. The isomerization of β-(Z) into β-(E) occurs fast with respect to the conversion for both catalysts, which is indicated by relatively big leaps in the profiles of both of the isomers, e.g. difference of 35% in the amount of β-(Z) within 95 h (between 74 and 169 h) with **3a** and 24% within 72 h (between 169 and 241 h) with **3b**. The amount of alkene is constant during

the reactions, whereas the α-2-silyl-1-alkene in the reaction catalyzed by **3b** is formed in the amount of 16%, however, along the reaction, this amount decreases down to 3 %. It is noteworthy that also in this case there is a slight gain in the selectivity with comparison to the reaction carried out with the higher catalyst loading: β-(E) = 85% vs β-(E) = 91%, respectively for 1 mol % of **3a** and 0.1 mol % of **3a**.

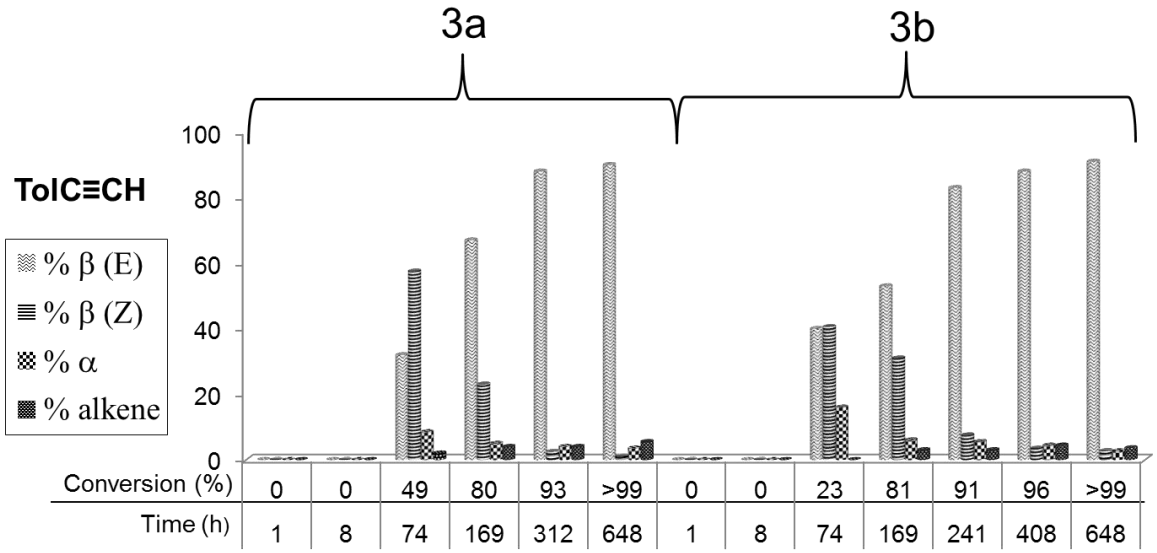

Figure 2.30 Selectivity vs conversion and time for the hydrosilylation of TolC≡CH catalyzed by 3a and 3b.

Catalytic activity of 3a and 3b: catalysts loading 0.1 mol % (T = 60 °C), PhC≡CH

The increase of the temperature from 25 °C to 60 °C, affected significantly the reaction rate and the selectivity. For instance, in the phenylacetylene case, its complete conversion was reached after 80 h with the **3a** as the catalyst, whereas the use of **3b** extended the reaction time until the complete conversion after 149 h (Figure 2.31, Figure 2.32 and Figure 2.33a). The catalytic reactions under these conditions started immediately, the first NMR check after 30 min., showed already 12 and 7.5% of conversion in the presence of **3a** and **3b** catalysts, respectively. Moreover, in the reaction with phenylacetylene, contrary to what was observed in all the previously discussed in this section cases, the cross of the profiles of the β-(Z) and β-(E) isomers did not occur (Figure 2.31). Nevertheless, the initial amounts of these isomers started to change rapidly in opposite directions after first 20 h of the reaction, when there has been already 88% of conversion reached.

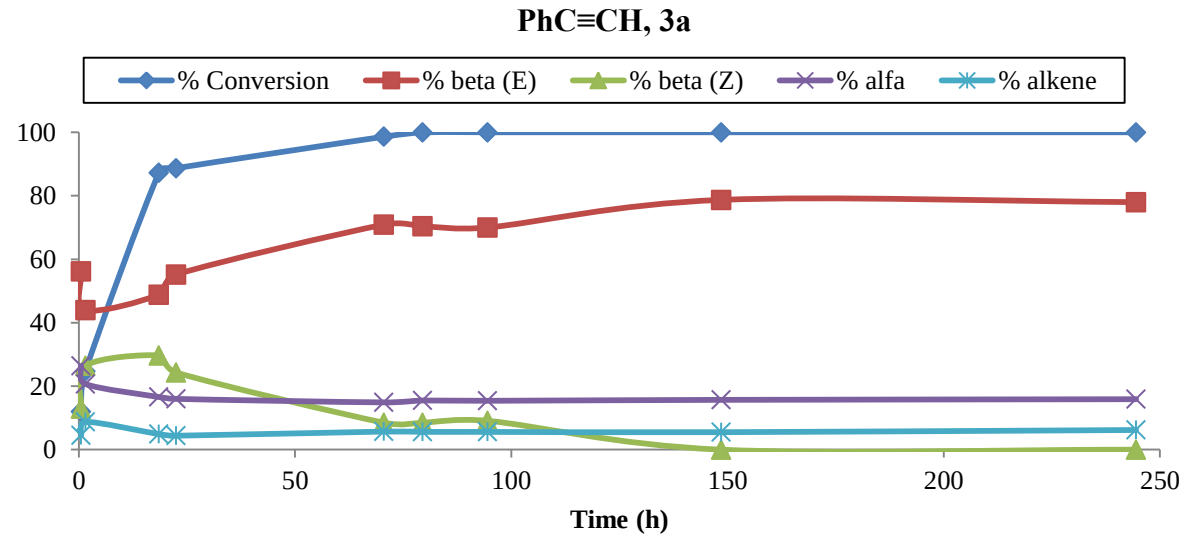

Figure 2.31 Reaction profile of conversion and selectivities vs time for the hydrosilylation of PhC≡CH with 3a, at 60°C.

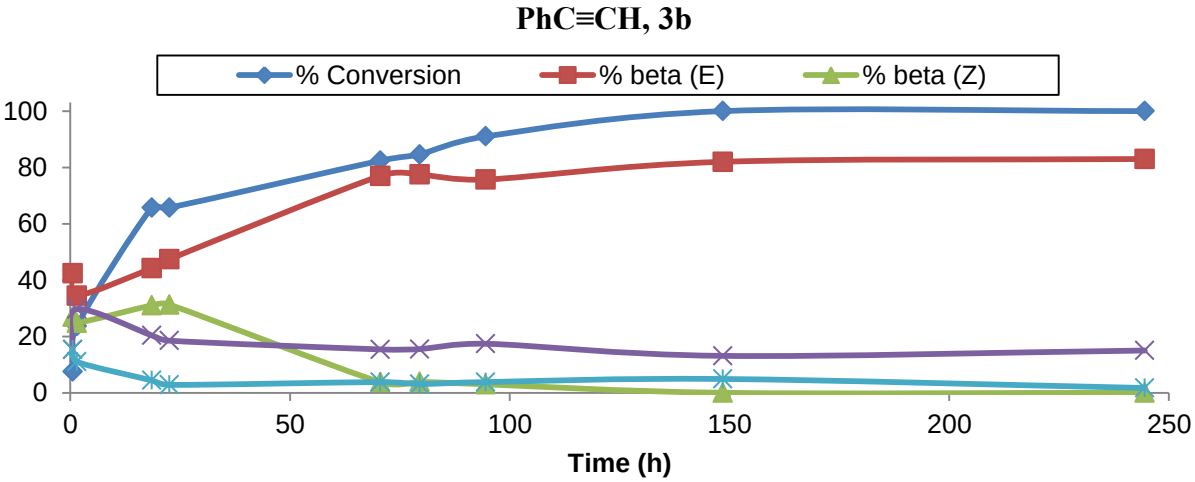

Figure 2.32 Reaction profile of conversion and selectivities vs time for the hydrosilylation of PhC≡CH with 3b, at 60°C.

Catalytic activity of 3a and 3b: catalysts loading 0.1 mol % (T = 60 °C), TolC≡CH

In case of the tolylacetylene, this catalytic reaction is even faster, after first 30 min. there was already 21.4 and 17.6% of conversion reached with **3a** and **3b** catalysts, respectively, whereas the complete conversion was finished after 71 h with both catalysts **3a,b**. Moreover, at this temperature, the **3b** catalyst was found to provide better selectivity of the reactions with comparison to the catalyst **3a**, although, the **3b**, being more encumbered, shows a lower efficiency in terms of the reaction speed (Figure 2.33b).

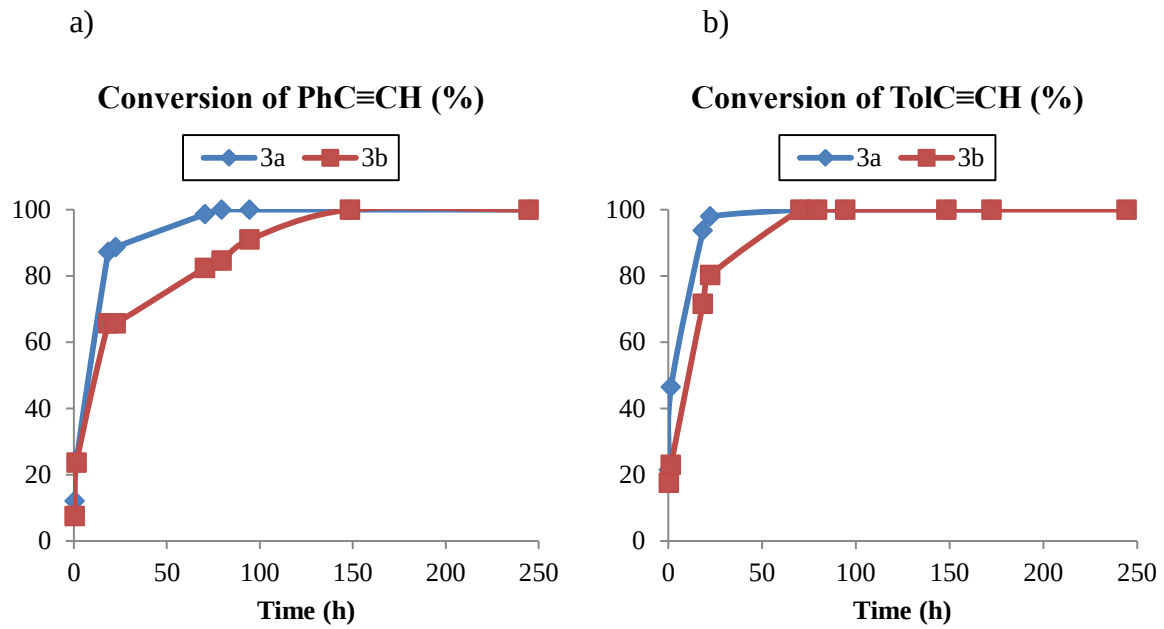

Figure 2.33 Reaction profile of conversion vs time for the hydrosilylation of PhC≡CH (a) and TolC≡CH (b) with complexes 3a and 3b, at 60°C.

The selectivity vs. conversion as a function of time for hydrosilylation of phenylacetylene in the presence of **3a** and **3b** catalysts is summarized in the bar diagram shown in Figure 2.34. From this diagram, the characteristic shape of the β-(E) vinylsilane formation profiles with both **3a** and **3b** catalysts, can be observed; there are minimum points after 19 h (reaction with **3a**) and 2 h (reaction with **3b**), resulting from the slight decrease of the amount of this isomer with respect to its quantity at the beginning, followed by a further gradual increase. At these points, the difference in the amounts of the isomers E and Z is in fact the smallest. However, it is important to highlight that after 149 h of the reactions, the β-(Z) completely disappears, leaving 79% of β-(E) with **3a** and 82% with **3b**. As regards the amount of the α product, there is a noticeable growth under the discussed conditions with respect to the catalytic reactions carried out at room temperature, where the α-2-silyl-1-alkene has been found in most of the cases in the percentage range of 0-6% and in contrast, at 60 °C the amount vary between 26 and 13%.

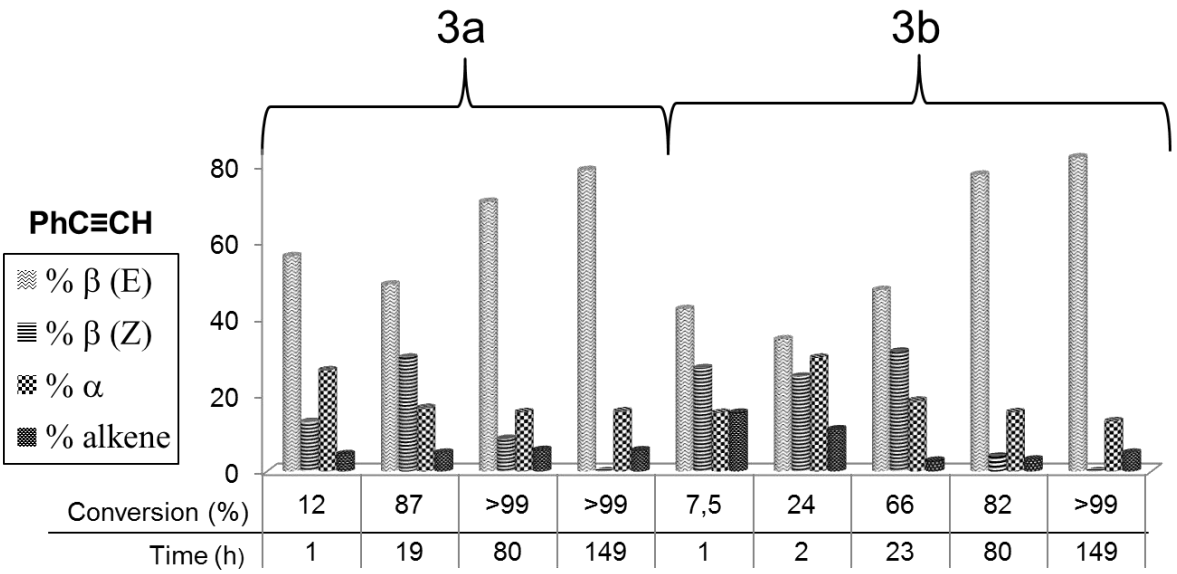

Figure 2.34 Selectivity vs conversion and time for the hydrosilylation of PhC≡CH catalyzed by 3a and 3b, at 60°C.

Regarding the case of TolC≡CH, the bar diagram shown in Figure 2.35 has similar shape to the discussed above for PhC≡CH; however, the difference in speed and selectivity between reactions catalyzed by the two **3a,b** catalysts is significant. Whereas with the former catalyst the hydrosilylation is finished after 149 h with 85% of the β-(E), the reaction catalyzed by the more encumbered **3b** is much faster and more selective, e.g. 93% of the β-(E) after 79 h. Another difference worth to mention is the negligible amount of the alkene formed when compared for the PhC≡CH.

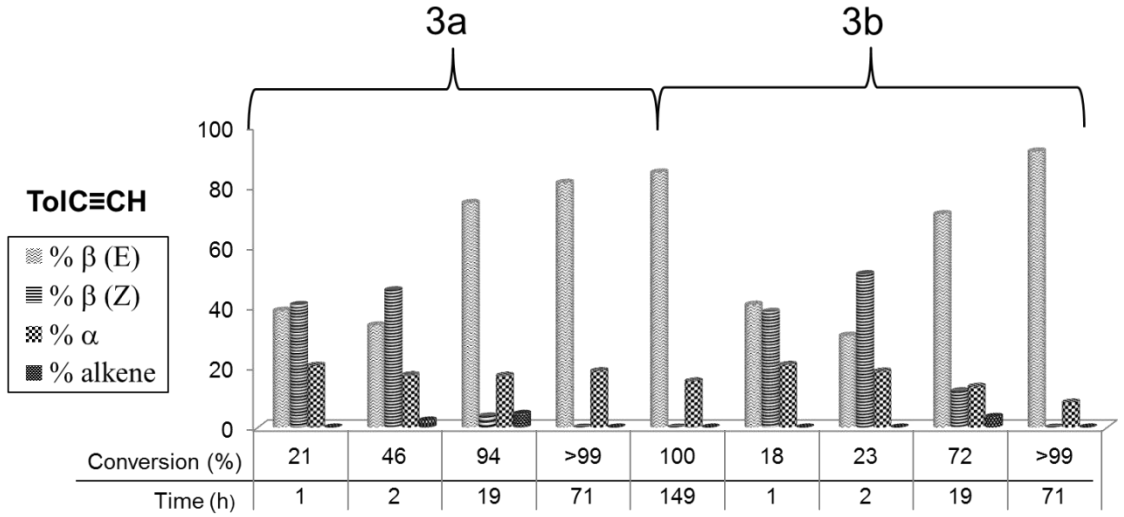

Figure 2.35 Selectivity vs conversion and time for the hydrosilylation of TolC≡CH catalyzed by 3a and 3b, at 60°C.

Summary of catalytic results.

To sum up briefly, the reaction rates were very high, in the range of 4-21 h, when employing 1 mol % of the rhodium(I) catalyst **3a** in the hydrosilylation reactions of phenylacetylene (PhC≡CH), tolylacetylene (TolC≡CH) and (triethylsilyl)acetylene ($Et_3SiC{\equiv}CH$). A tremendous drop of the rates was observed when the amount of the catalyst has been decreased down to 0.1 mol % (768-1080 h, depending on the alkyne used); moderate rates were found for the catalyst loading 0.1 mol % at 60 °C, 71-149 h. As regards the selectivity of these reactions, at room temperature the catalyst **3a** in the amount of 0.1 mol % leads to a slightly better results than the catalyst **3b**, whereas in the same reaction carried out at 60 °C, the **3b** catalyst showed be a little bit more efficient for both the substrates: phenylacetylene and tolylacetylene. Generally, the selectivity is improved when the reaction rate is slown down. (Table 2.6). In the mode (a) of the experiment, the profiles of the two discussed isomers E and Z cross after the complete conversion is reached; in the mode (b) and (c) they cross before the complete conversion is reached, or do not cross at all, as in the case of hydrosilylation of phenylacetylene at 60 °C.

Table 2.6 Comparison of reaction time and selectivity of hydrosilylation reactions of PhC≡CH and TolC≡CH under different conditions and with different catalyst loading.

alkyne	catalyst	Time	Conv (%)	% β-(Z)	% β-(E)
PhC≡CH	**3a** (1%)	335	>99	13	74
PhC≡CH	**3a** (0.1%), r.t.	1080	87	1	90
PhC≡CH	**3b** (0.1%), r.t.	1080	91	9	76
PhC≡CH	**3a** (0.1%), 60 °C	149	>99	0	78
PhC≡CH	**3b** (0.1%), 60 °C	149	>99	0	83
TolC≡CH	**3a** (1%)	263	>99	5	85
TolC≡CH	**3a** (0.1%), r.t.	648	>99	1	90
TolC≡CH	**3b** (0.1%), r.t.	648	>99	3	91
TolC≡CH	**3a** (0.1%), 60 °C	149	>99	0	85
TolC≡CH	**3b** (0.1%), 60 °C	79	>99	0	93

Finally, an interesting behavior has been observed in the course of the analysis of the encumbrance influence of the used catalysts on the reaction rates. The less encumbered catalyst **3a** provides better reaction rates with comparison to the more bulky **3b** for the catalytic reactions carried out at 60 °C; however, when the reactions are performed at room temperature, only in the first stage of the reactions this rule still applies; surprisingly, contrary to intuition and data reported previously[1], the reaction profiles cross, and the **3b** catalyst becomes either more efficient or its efficiency is comparable to **3a** in terms of the rate of the conversions for both phenyl- and tolylacetylene; the graphs proving this behavior for phenylacetylene are presented in Figure 2.36.

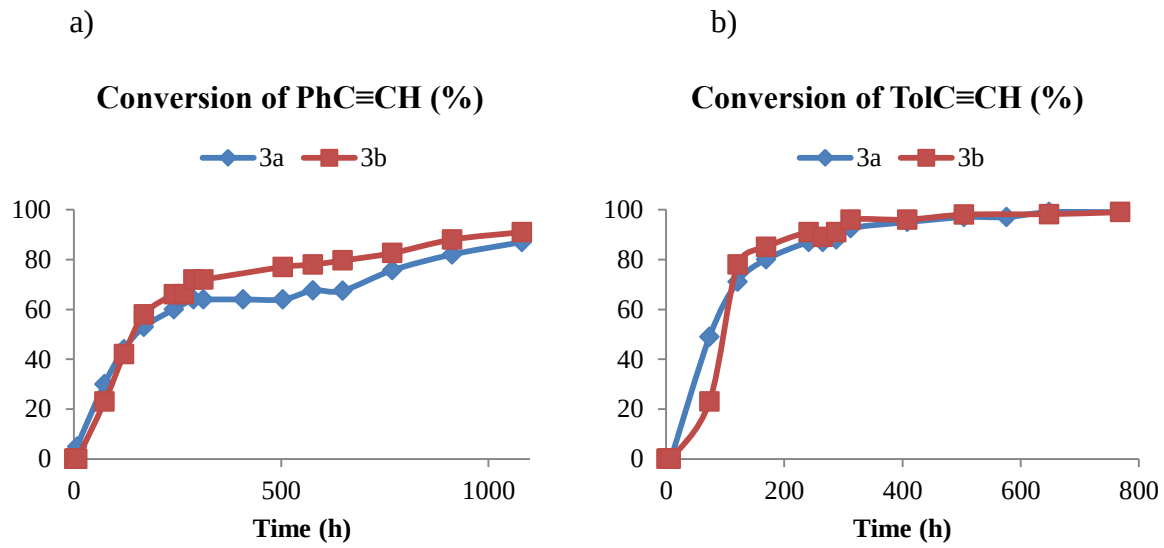

Figure 2.36 Reaction profile of conversion vs time for the hydrosilylation of PhC≡CH (a) and TolC≡CH (b) with complexes 3a and 3b, at room temperature.

Comparison of the catalytic results with those obtained in case of similar, but amide-functionalized complexes, described in the introduction.

Generally, the catalytic reactions employing the amide-functionalized catalyst **3a'** (Figure 2.37) were faster but provided similar selectivity than those catalyzed by **3a**.

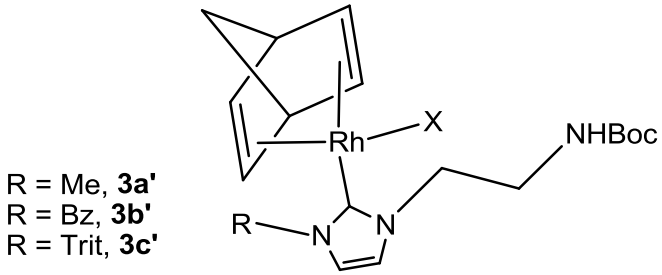

Figure 2.37 Amide-functionalized rhodium complexes 3a', 3b' and 3c'.

The comparison between the time needed to reach the complete conversion and the relative proportions of the isomers β-(E) and β-(Z) are reported in Table 2.7

Table 2.7 Comparison of efficiency of catalysts 3a and 3a'.

alkyne	catalyst	Time needed for conv. >99	Conv (%)	% β-(Z)	% β-(E)
PhC≡CH	3a' (1%), r.t.	6	192	0	75
PhC≡CH	3a (1%), r.t.	21	335	13	74
TolC≡CH	3a' (1%), r.t.	2	6	0	85
TolC≡CH	3a (1%), r.t.	21	263	5	85
$Et_3SiC{\equiv}CH$	3a' (1%), r.t.	2	-	-	-
$Et_3SiC{\equiv}CH$	3a (1%), r.t.	4	-	-	-

As can be seen from the above data, the complete conversion in the reaction employing phenylacetylene as a substrate was reached three times faster in the presence of the catalyst **3a'** when compared to **3a**. Even less time was needed in the hydrosilylation of tolylacetylene with **3a'** (complete conversion after 2 h), whereas no difference has been observed for the two reactions catalyzed by **3a** (21 h). Similarly, the reaction with **3a'** was also faster for $Et_3SiC{\equiv}CH$.

As regards the isomerization of the two β-(Z)- and β-(E)-1-silyl-1-alkenes, for both PhC≡CH and TolC≡CH alkynes, the functionalized catalyst led to the disappearance of the isomer β-(Z), in much shorter time than the **3a** catalyst. Nevertheless, the amount of the formed β-(E) isomer in the end of the reactions with **3a'** and **3a** is the same within the experimental error (β-(E) = 75% and β-(E) = 85% for PhC≡CH and TolC≡CH, respectively).

The examination of the influence of the steric hindrance of the catalysts **3a'-c'** in the amount of 1 mol % on the conversion speed, showed that this dependence is strict, e.g. the more encumbered catalyst slows down the conversion, which was not always the case for the catalysts **3a,b**, as discussed previously.

Figure 2.38 shows the reaction profile obtained in the presence of **3a** catalyst, plotted together with profiles of all the amide-functionalized **3a'-3c'** for direct comparison. The rate provided by **3a** has been found to be smaller than for **3a'**and **3b'** but noticeably higher than for the most encumbered catalyst **3c'**, bearing the trityl group on one of the N-sides of the imidazolium moiety.

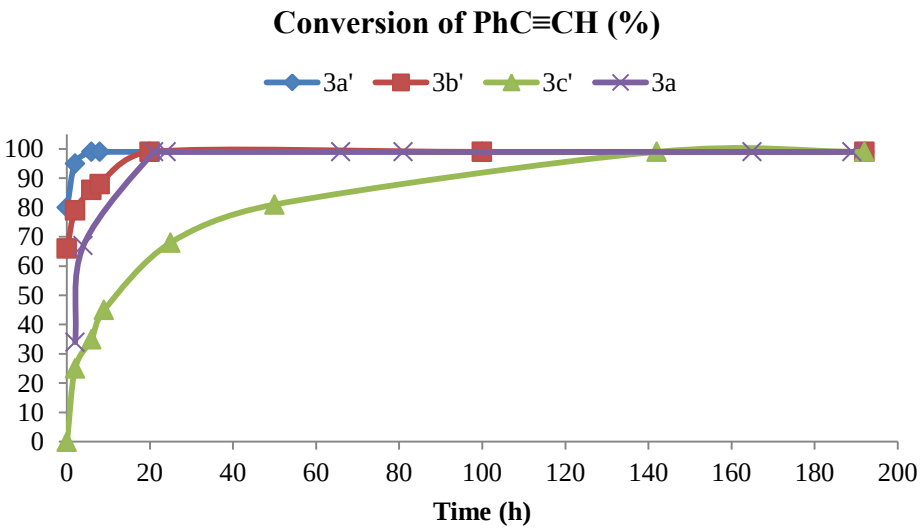

Figure 2.38 Reaction profile of conversion vs time for the hydrosilylation of PhC≡CH with complexes 3a, 3a', 3b' and 3c'.

The quantities of the two other products of the hydrosilylation: α-2-silyl-1-alkene and the corresponding alkene were comparable in these two experiments employing both **3a** and **3a'-c'** catalysts.

All the data discussed above indicate that the functionalization of the N-side arm of the *N*-heterocyclic moiety with a donor group like amide, improves the catalytic activity of the corresponding Rh(I)-complexes. With the same catalyst loading, the functionalized complexes were proved to provide better reaction rates than their alkyl congeners.

3 Conclusions

The research performed in the framework of this Master project included several tasks.

- The **first objective** was the synthesis and full characterization of a series of imidazolium salts [BzImR]X bearing increasingly bulky N-substituents on one side and the benzyl (Bz) group on the other, as a chiral probe.

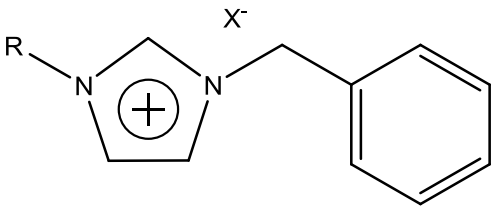

R = Me (**1a**), Bz (**1b**), biphenyl (**1c**), trityl (**1d**), ^{t}Bu (**1e**)

- The **second task** was the use of the imidazolium salts **1** (with the exception of **1c**) for the preparation of a series of silver(I)-NHC complexes $[Ag(NHC)_2][AgX_2]$ (**2**), and their subsequent employment for the synthesis of the corresponding rhodium(I) complexes [Rh(NBD)X(NHC)] (**3**) in high yields (90-75%). All the rhodium complexes display restricted rotation about the metal-carbene bond, which generates a pair of enantiomers.

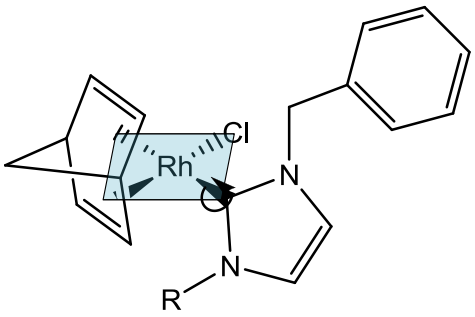

R = Me (**3a**), Bz (**3b**), trityl (**3d**), ^{t}Bu (**3e**)

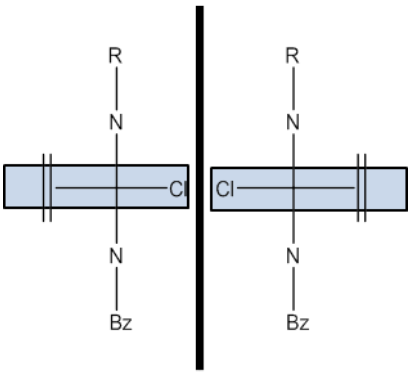

- The **third task** has been the determination of the rotation energy barrier by means of dynamic NMR (VT NMR and 1D EXSY). We found what follows:

i) in the case of the most encumbered complex **3e,** the activation energy exceeds the limit of the experiment, which makes the possibility in the near future to separate the two atropoisomers by the chiral HPLC (High-Performance Liquid Chromatography;

ii) the rotation barriers calculated for the complexes bearing R = Me, Bz (**3a,b**) matched the experimental values (55 and 64 kJ mol^{-1}, respectively);

iii) in the trityl case **3c**, the experimental value (64 kJ mol^{-1}) was equal to that obtained for compound **3b** and much smaller than the calculated one (110 kJ mol^{-1}). In addition, the energy barrier for **3d** showed a strong dependence on the temperature, while the barriers measured for **3a,b** did not show this effect. In particular, the big negative activation entropy derived from simulations (-27 ± 10 eu) indicates that a strongly organized transition state and a different interconversion pathway takes place in the case of the complex **3d**;

iv) these results are in a perfect agreement with those found in the case of the previously investigated rhodium(I)-NHC **3'** complexes bearing amide-functionalized side chain, proving that the influence of the functionalization on the thermodynamics is negligible. Hence, even though no change has been observed in the behavior of these two similar groups of the rhodium complexes, which could have provided a new outlook on the postulated possible interconversion pathways, the just performed research made an important contribution to the further research in this direction.

- The **fourth task** was the investigation of the catalytic activity of the rhodium complexes **3** in the hydrosilylation of terminal alkynes and comparison with the complexes **3'** previously reported within the research group in which this thesis was carried out.

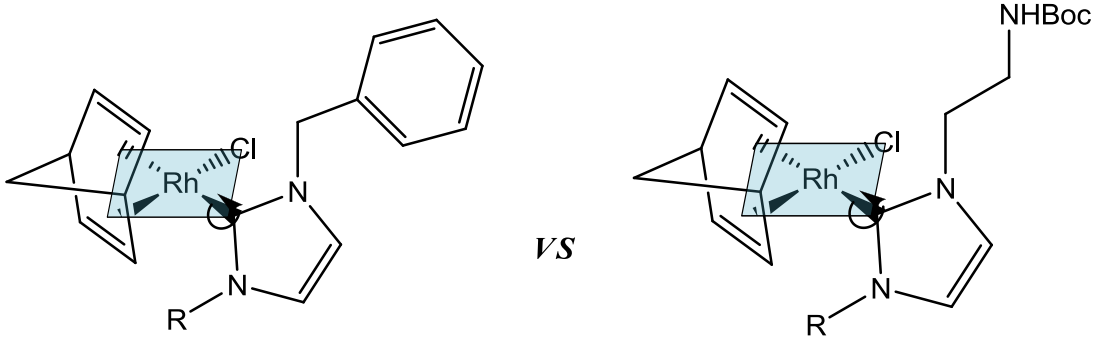

R = Me (**3a**), Bz (**3b**), trityl (**3d**), ^{t}Bu (**3e**)

R = Me (**3a'**), Bz (**3b'**), trityl (**3d'**)

the following observations have been made:

i) the neutral, non-functionalized rhodium(I) complexes are efficient catalysts for the hydrosilylation of terminal alkynes;

ii) the steric hindrance on the N-heterocyclic ligand and on the alkyne substrates affects conversion and selectivity; however, in contrast to the complexes **3'** this influence is not straightforward and vary with the temperature of the experiments;

iii) the functionalization with the amide group improved the rate of the hydrosilylation reactions, however, leading in the end of the reactions to similar selectivity.

- The **last task** was the preparation of novel piano-stool iron (II) complexes, which were synthesized by a literature method optimized in our laboratory.

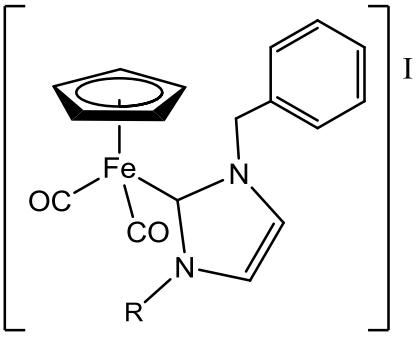

R = Me (**3a**), Bz (**3b**)

3.1 References

(1) Busetto, L.; Cassani, M. C.; Femoni, C.; Mancinelli, M.; Mazzanti, A.; Mazzoni, R.; Solinas, G. *Organometallics* **2011**, *30*, 5258.

(2) Bourissou, D.; Guerret, O.; Gabbaı, P.; Bertrand, G. *Chem. Rev.* **2000**, *100*, 39.

(3) Hoffmann, R. *J. Am. Chem. Soc.* **1968**, *90*, 1475.

(4) Wanzlick, H. W.; Kleiner, H. J. *Angew. Chem.* **1961**, *73*, 493-493.

(5) de Frémont, P.; Marion, N.; Nolan, S. P. *Coord. Chem. Rev.* **2009**, *253*, 862-892.

(6) Dupont, J. *J. Braz. Chem. Soc.* **2004**, *15*, 341-350.

(7) Caló, V.; Del Sole, R.; Nacci, A.; Schingaro, E.; Scordari, F. *Eur. J. Org. Chem. 2010* **2000**, *2000*, 869-871.

(8) Herrmann, W. a. *Angew. Chem., Int. Ed.* **2002**, *41*, 1290-1309.

(9) Scholten, J. D.; Leal, B. C.; Dupont, J. *ACS Catalysis* **2012**, *2*, 184-200.

(10) Ballarin, B.; Busetto, L.; Cristina Cassani, M.; Femoni, C. *Inorg. Chim. Acta* **2010**, *363*, 2055-2064.

(11) http://www.scripps.edu/baran/images/grpmtgpdf/Zografos_Feb_04.pdf.

(12) Gridnev, A. A.; Mihaltseva, I. M. *Synth. Commun.* **1994**, *24*, 1547-1555.

(13) Glorius, F.; Spielkamp, N.; Holle, S.; Goddard, R.; Lehmann, C. W. *Angew. Chem., Int. Ed.* **2004**, *43*, 2850-2852.

(14) Arduengo, A. J. *Acc. Chem. Res.* **1999**, *32*, 913.

(15) http://www.chm.bris.ac.uk/webprojects2002/grant/webcomp/non-crossing.html.

(16) Arduengo, A. J.; Gamper, S. F.; Tamm, M.; Calabrese, J. C.; Davidson, F.; Craig, H. A. *Structure* **1995**, *117*, 572-573.

(17) Wanzlick, H. W.; Schönherr, H. J. *Angew. Chem.* **1968**, *80*, 154-154.

(18) Ofele, K. *Angew. Chem., Int. Ed.* **1968**, *12*, 950.

(19) Arduengo III, A. J.; Dias, H. V. R.; Harlow, R. L.; Kline, M. *J. Am. Chem. Soc.* **1992**, *114*, 5530-5534.

(20) Jean-Baptiste Dit Dominique, F.; Gornitzka, H.; Hemmert, C. *Organometallics* **2010**, *29*, 2868-2873.

(21) Lappert, M. F. *J. Organomet. Chem.* **1988**, *358*, 185-213.

(22) Lin, T.-S.; Luo, M.-Z.; Liu, M.-C. *Tetrahedron* **1995**, *51*, 1055-1068.

(23) Liu, B.; Liu, X.; Chen, C.; Chen, C.; Chen, W. *Organometallics* **2012**, *31*, 282-288.

(24) Lin, I. J. B.; Vasam, C. S. *Coord. Chem. Rev.* **2007**, *251*, 642-670.

(25) Liu, B.; Xia, Q.; Chen, W. *Angew. Chem., Int. Ed.* **2009**, *48*, 5513-6.

(26) Green, J. C.; Scurr, R. G.; Arnold, P. L.; Cloke, G. N. *Chem. Commun.* **1997**, 1963-1964.

(27) Mercs, L.; Labat, G.; Neels, A.; Ehlers, A.; Albrecht, M. *Organometallics* **2006**, *25*, 5648-5656.

(28) Garrison, J. C.; Youngs, W. J. *Chem. Rev.* **2005**, *105*, 3978-4008.

(29) Kandepi, V. V. K. M.; Cardoso, J. M. S.; Peris, E.; Royo, B. *Organometallics* **2010**, *29*, 2777-2782.

(30) Chianese, A. R.; Li, X.; Janzen, M. C.; Faller, J. W.; Crabtree, R. H.; Organomet, W. A. J. *Organometallics* **2003**, *22*, 1663-1667.

(31) Wang, H. M. J.; Lin, I. J. B. *Organometallics* **1998**, *17*, 972-975.

(32) Cardoso, J. M. S.; Royo, B. *Chem. Commun.* **2012**, *48*, 4944-4946.

(33) Corbera, R.; Sanau, M.; Peris, E. *Organometallics* **2006**, *25*, 4002-4008.

(34) Scott, N. M.; Dorta, R.; Stevens, E. D.; Correa, A.; Cavallo, L.; Nolan, S. P. *J. Am. Chem. Soc.* **2005**, *127*, 3516-26.

(35) Bringmann, G.; Price Mortimer, A. J.; Keller, P. A.; Gresser, M. J.; Garner, J.; Breuning, M. *Angew. Chem., Int. Ed.* **2005**, *44*, 5384-5427.

(36) Crabtree, R. *J. Organomet. Chem.* **2005**, *690*, 5451-5457.

(37) Díez-González, S.; Marion, N.; Nolan, S. P. *Chem. Rev.* **2009**, *109*, 3612-76.

(38) Herrmann, W. A.; Öfele, K.; Elison, M.; Kuhn, F. E.; Roesky, P. W. *J. Organomet. Chem. 480*, C7-C9.

(39) Imlinger, N.; Wurst, K.; Buchmeiser, M. R. *J. Organomet. Chem.* **2005**, *690*, 4433-4440.

(40) Jiménez, M. V.; Pérez-Torrente, J. J.; Bartolomé, M. I.; Gierz, V.; Lahoz, F. J.; Oro, L. A. *Organometallics* **2008**, *27*, 224-234.

(41) Patil, S.; Deally, A.; Gleeson, B.; Helge, M.; Paradisi, F.; Tacke, M. *Appl.Organometal.Chem.* **2010**, *24*, 781-793.

(42) Moret, M.-etienne; Chaplin, A. B.; Lawrence, A. K.; Scopelliti, R.; Dyson, P. J. *Organometallics* **2005**, *24*, 4039-4048.

(43) Patil, S.; Claffey, J.; Deally, A.; Hogan, M.; Gleeson, B.; Miguel, L.; Méndez, M.; Müller-bunz, H.; Paradisi, F.; Tacke, M. *Eur. J. Inorg. Chem.* **2010**, 1020-1031.

(44) http://www.personal.psu.edu/the1/sn1ande.htm.

(45) Elango, K.; Srirambalaji, R.; Anantharaman, G. *Tetrahedron Lett.* **2007**, *48*, 9059-9062.

(46) Sauerbrey, S.; Majhi, P. K.; Daniels, J.; Schnakenburg, G.; Brändle, G. M.; Scherer, K.; Streubel, R. *Inorg. Chem.* **2011**, *50*, 793-9.

(47) Fre, P. D.; Scott, N. M.; Stevens, E. D.; Ramnial, T.; Lightbody, O. C.; Macdonald, C. L. B.; Clyburne, J. A. C.; Abernethy, C. D.; Nolan, S. P. *Organometallics* **2005**, *24*, 6301-6309.

(48) Busetto, L.; Cristina Cassani, M.; Femoni, C.; Macchioni, A.; Mazzoni, R.; Zuccaccia, D. *J. Organomet. Chem.* **2008**, *693*, 2579-2591.

(49) Abraham, R. J.; Byrne, J. J.; Griffiths, L.; Perez, M. *Magn. Reson. Chem.* **2006**, *44*, 491-509.

(50) Newman, C. P.; Clarkson, G. J.; Rourke, J. P. *J. Organomet. Chem.* **2007**, *692*, 4962-4968.

(51) Kline, M.; Harlow, R. L. *J. Am. Chem. Soc.* **1991**, *113*, 363-365.

(52) Kuhn, H.; Woodgate, G. K. *Nature* **1950**, *166*, 906.

(53) Gaillard, S.; Slawin, A. M. Z.; Nolan, S. P. *Chem. Commun.* **2010**, *46*, 2742-2744.

(54) Casarini, D.; Lunazzi, L.; Mazzanti, A. *Eur. J. Org. Chem.* **2010**, *2010*, 2035-2056.

(55) Enders, D.; Gielen, H.; Runsink, J.; Breuer, K.; Brode, S.; Boehn, K. *Eur. J. Inorg. Chem.* **1998**, 913-919.

(56) Enders, D.; Gielen, H. *J. Organomet. Chem.* **2001**, *618*, 70-80.

(57) Sabbah, M.; Soulère, L.; Reverchon, S.; Queneau, Y.; Doutheau, A. *Bioorg. Med. Chem.* **2011**, *19*, 4868-75.

(58) Hirtenlehner, C.; Krims, C.; Hölbling, J.; List, M.; Zabel, M.; Fleck, M.; Berger, R. J. F.; Schoefberger, W.; Monkowius, U. *Dalton Trans.* **2011**, *40*, 9899-9910.

(59) Sheldrick, G. M. *SADABS Program for Absorption Correction Using Area Detector Data* **1996**.

4 EXPERIMENTAL SECTION

Materials and Procedures. All reactions were carried out under argon using standard Schlenk techniques. Solvents were dried and distilled under nitrogen prior to use; the deuterated solvents, used after being appropriately dried and degassed, were stored in ampules under argon on 4Å molecular sieves. The prepared derivatives were characterized by elemental analysis and spectroscopic methods. The IR spectra were recorded with a FT-IR Perkin-Elmer Spectrum 2000 spectrometer. The NMR spectra were recorded using Varian Inova 300 (^{1}H, 300.1; ^{13}C, 75.5 MHz), Varian MercuryPlus VX 400 (^{1}H, 399.9; ^{13}C, 100.6 MHz), Varian Inova 600 (^{1}H, 599.7; ^{13}C, 150.8 MHz) instruments. The spectra were referenced internally to residual solvent resonances, and unless otherwise stated, they were recorded at 298 K for characterization purposes; full ^{1}H and ^{13}C NMR assignments were done, when necessary, by gCOSY, gHSQC, gHMBC, NOESY and DEPT-135 NMR experiments using standard Varian pulse sequences; J.Young valve NMR tubes (Wilmad) were used to carry out NMR experiments under inert conditions. The abbreviation SDBS refers to Spectral Database for Organic Compounds. ESI-MS analyses were performed by direct injection of methanol solutions of the metal complexes using a Waters ZQ 4000 mass spectrometer. Elemental analyses were performed on a Thermo-Quest Flash 1112 Series EA instrument. The chemicals 1-methylimidazole, 1-benzylimidazole, benzyl bromide, *tert*-butyl bromide and Ag_2O were used as purchased from Aldrich; $[Rh(NBD)Cl]_2$ and $FeI(CO)_2Cp$ was purchased from Strem and used as received; the chemicals glyoxal and formaldehyde were used as purchased from Farmitalia Carlo Erba; *tert*-butylamine was purchased from Merck. The starting building blocks 1-*tert*-butylimidazole[46], trityl chloride[1], 1-benzyl-3-methyl-imidazolium bromide (**1a**)[41,42], 1,3-dibenzyl-imidazolium bromide (**1b**)[43], were prepared according to literature procedures or modified literature methods. Phenylacetylene, 1-hexyne, 4-ethynyltoluene, triethylsililacetylene were used as purchased from Sigma Aldrich. Petroleum ether (Etp) refers to a fraction of bp 60-80 °C. The reactions were monitored by thin-layer chromatography (TLC) on highly purified silica gel on polyester (w/UV indicator) and visualized using UV light (254 nm). Column chromatography was carried out under argon on silica gel previously heated at about 200 °C while a slow stream of a dry nitrogen was passed through it; Celite was dried in an oven at 150 °C. Melting points were taken with a Stuart Scientific SMP3 melting point apparatus and were uncorrected. Sonication was

performed on Elma S10H device with ultrasound frequency: 37 kHz and effective power (30W).

4.1 Synthesis of 1-benzyl-3-methyl-imidazolium bromide (1a)

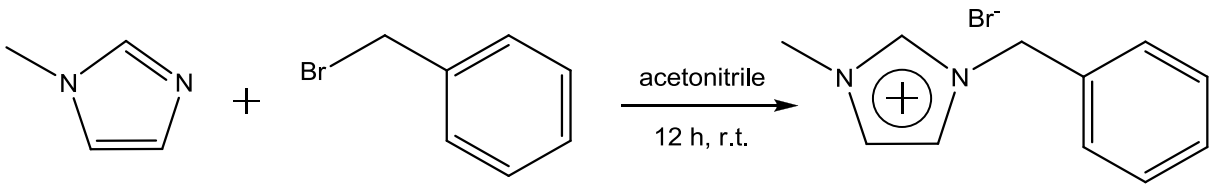

1a

This product was synthesized using a literature method[41,42]. In a 100 mL round-bottom flask to a solution of 1-methylimidazole (0.24 mL, 3.0 mmol) in acetonitrile (15 mL), an equivalent molar amount of benzyl bromide (0.36 mL, 3.0 mmol) was added. After stirring for 12 h at room temperature, the solvent was removed under vacuum, and the resulting pale yellow, viscous oil was thoroughly washed with diethyl ether (3 x 10 mL), Etp and hexane. After separation from the washings the oil was kept under vacuum at 40 °C for several hours to yield 0.720 g (Y = 94%) of **1a**.

Anal. Calcd for $C_{11}H_{13}BrN_2$: C, 52.19; H, 5.18; Br, 31.57; N, 11.07. Found: C, 52.01; H, 5.30; Br, 31.52; N, 11.01.

ESI-MS (MeOH, m/z): 173 (100) $[C_{11}H_{13}N_2]^+$; 79 (100), 81 (97) $[Br]^-$.

a)

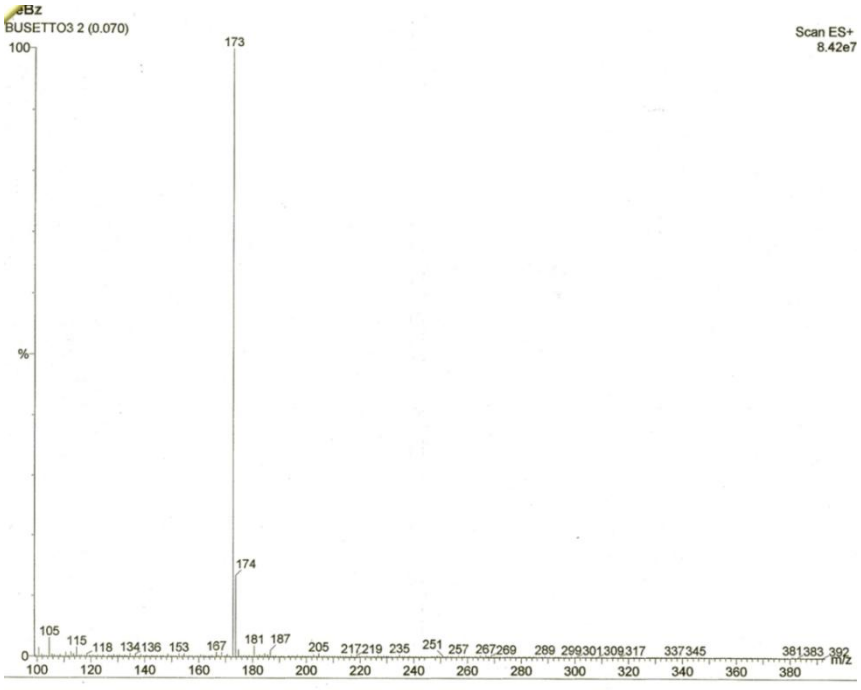

b)

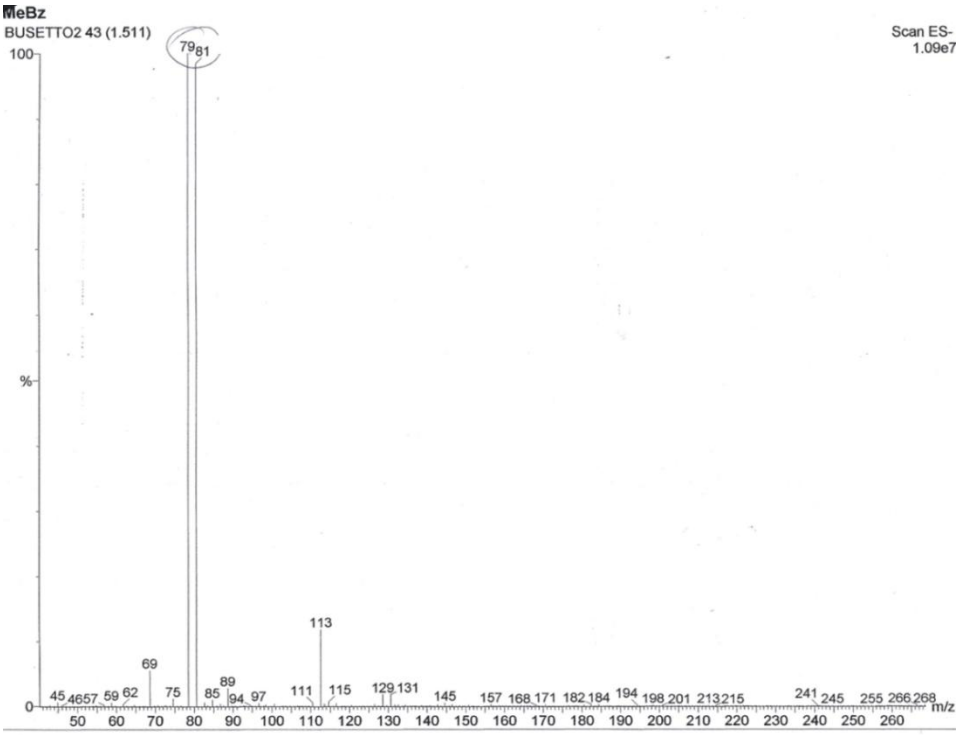

Figure 4.1 ESI-MS spectra of 1a, cation spectrum (a), anion spectrum (b).

^{1}H NMR (400 MHz, $CDCl_3$): δ 10.58 (s, 1H, NCHN), 7.48 (s, 1H, CH_{im}), 7.47-7.46 (m, 1H, Ph), 7.41-7.39 (m, 3H, CH_{im} + Ph), 7.30 (s, 1H, Ph), 7.23 (s, 1H, Ph), 5.57 (s, 2H, CH_2Ph), 4.08 (s, 3H, CH_3).

a)

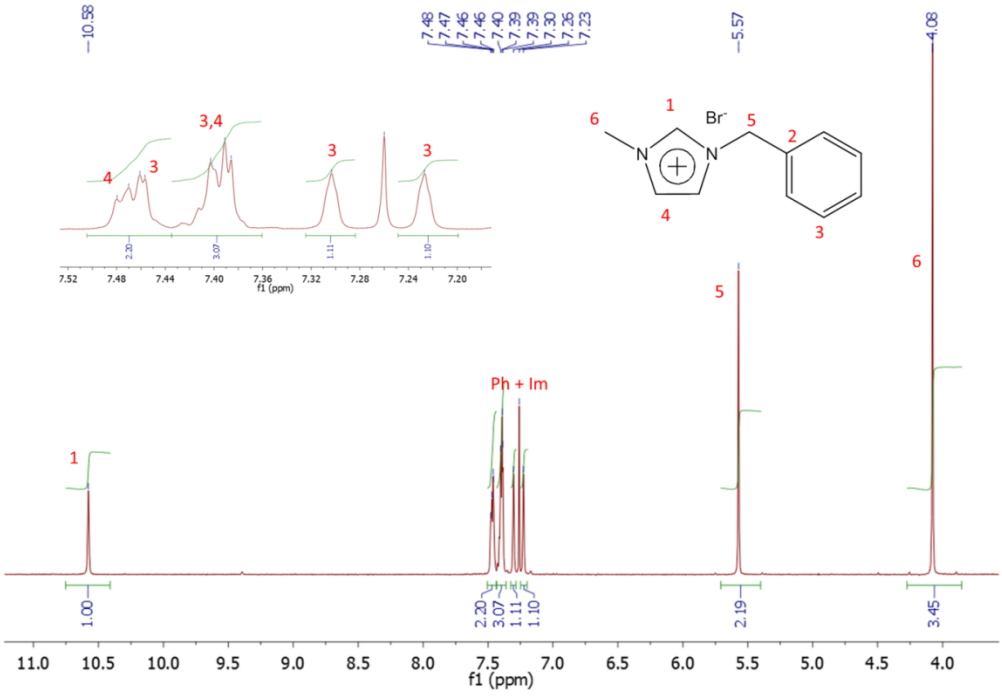

Figure 4.2 ^{1}H NMR spectrum of 1a with the inset showing zoomed aromatic region of the spectrum.

^{13}C NMR (100 MHz, $CDCl_3$): δ 137.93 (NCHN), 132.68 (Cq, Ph), 129.62 (Ph), 129.51 (Ph), 129.02 (Ph), 123.22 (CH_{im}), 121.63 (CH_{im}), 53.57 (CH_2Ph), 36.86 (CH_3).

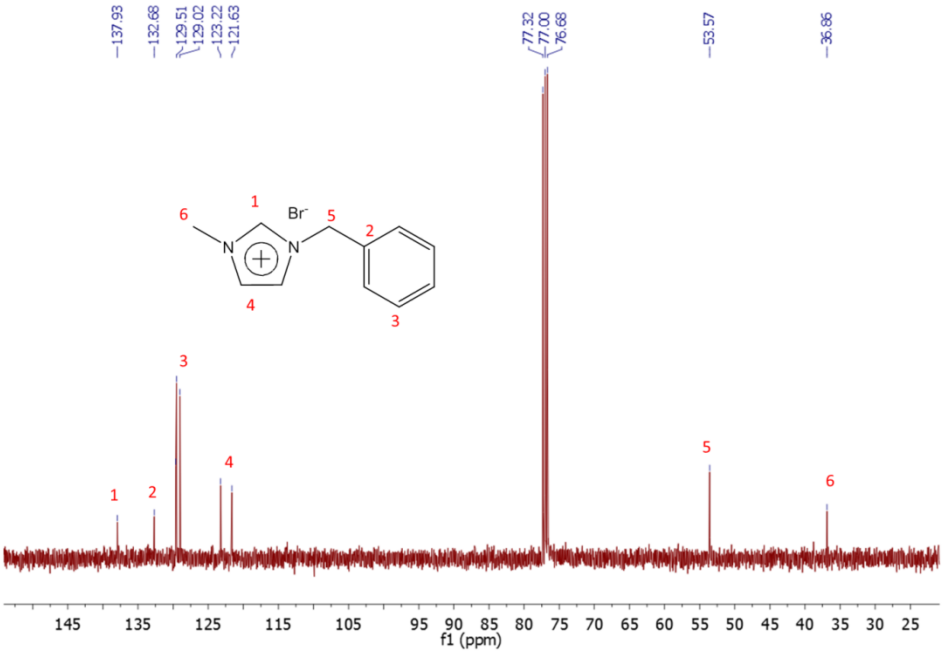

Figure 4.3 ^{13}C NMR spectrum of 1a.

Supplementary spectra related to the synthesis:
1-methylimidazole

^{1}H NMR (400 MHz, $CDCl_3$): δ 7.47 (s, 1H, NCHN), 7.03 (s, 1H, CH_{im}), 6.86 (s, 1H, CH_{im}), 3.67 (s, 3H, CH_3). SDBS: **^{1}H NMR (400 MHz, $CDCl_3$):** δ 7.385 (s, 1H, NCHN), 7.011 (s, 1H, CH_{im}), 6.863 (s, 1H, CH_{im}), 3.641 (s, 3H, CH_3).

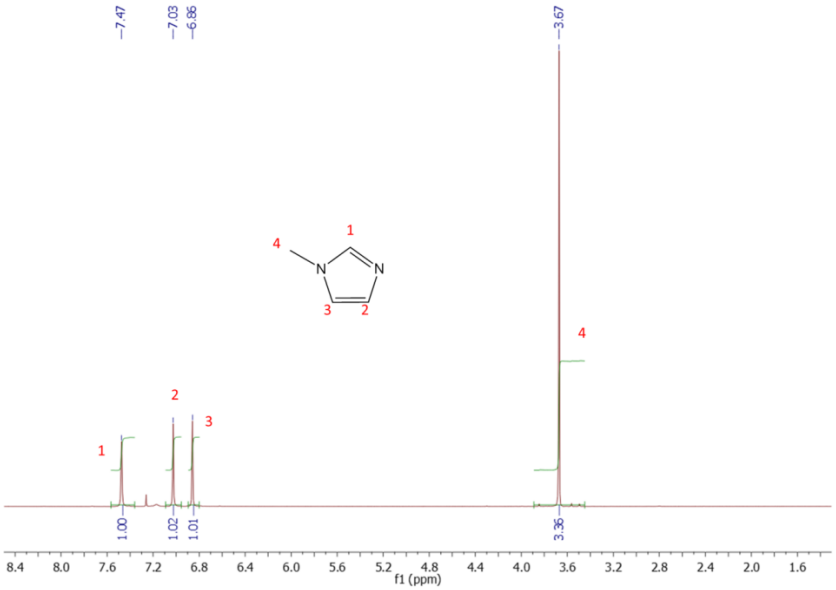

Figure 4.4 ^{1}H NMR spectrum of 1-methylimidazole.

^{13}C NMR (100 MHz, $CDCl_3$): δ 137.68 (NCHN), 129.10 (CH_{im}), 120.01 (CH_{im}), 33.27 (CH_3). SDBS: **^{13}C NMR (25 MHz, $CDCl_3$)**: δ 137.79 (NCHN), 129.17 (CH_{im}), 120.20 (CH_{im}), 33.14 (CH_3).

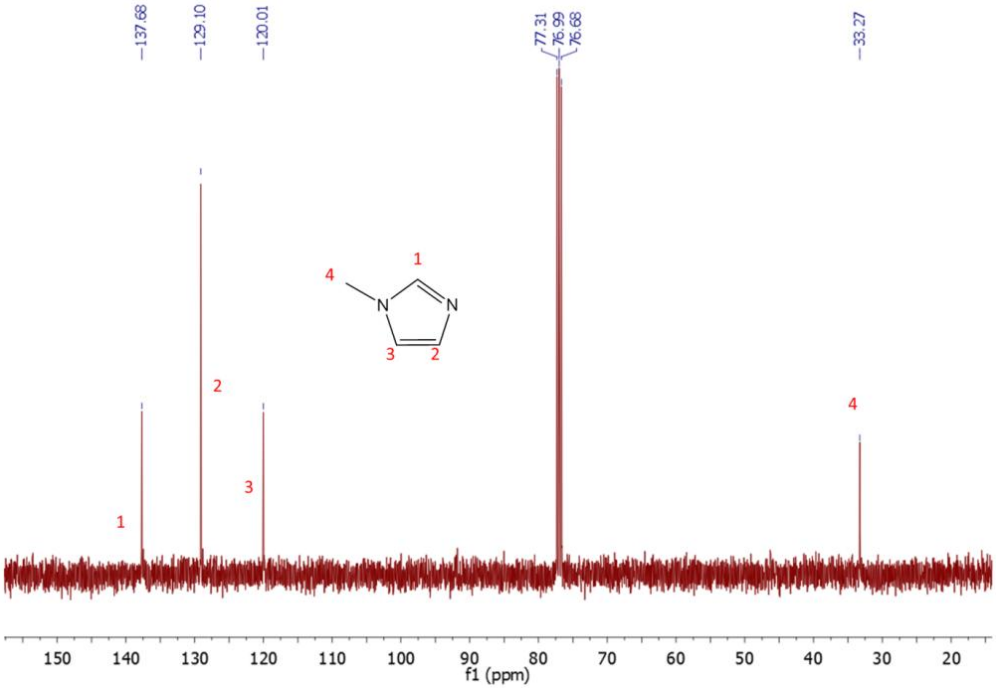

Figure 4.5 ^{13}C NMR spectrum of 1-methylimidazole.

4.2 Synthesis of 1,3-dibenzyl-imidazolium bromide (1b)

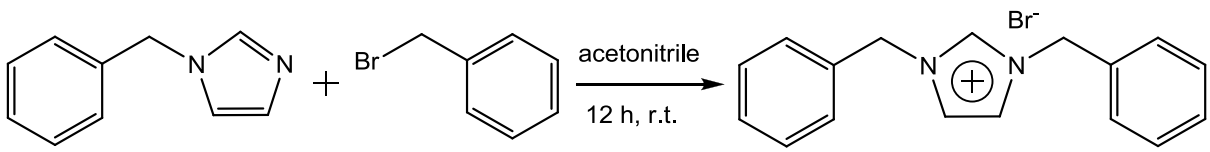

1b

This product was synthesized using a literature method[43]. In a 100 mL round-bottom flask to a solution of 1-benzylimidazole (0.48 g, 3.0 mmol) in acetonitrile (15 mL), an equivalent molar amount of benzyl bromide (0.36 mL, 3.0 mmol) was added. After stirring for 12 h at room temperature, the solvent was removed under vacuum, and the resulting pale yellow, viscous oil was thoroughly washed with diethyl ether (10 mL) and Etp (10 mL). After separation from the washings the oil was kept under vacuum at 40 °C for several hours to yield 0.98 g (Y = 99%) of **1b**.

Anal. Calc.d for $C_{17}H_{17}BrN_2$: C, 62.02; H, 5.20; Br, 24.27; N, 8.51. Found: C, 61.79; H, 5.03; Br, 24.39; N, 8.28.

ESI-MS (MeOH, m/z): 249 (100) $[C_{17}H_{17}N_2]^+$; 79 (97), 81 (100) $[Br]^-$.

a)

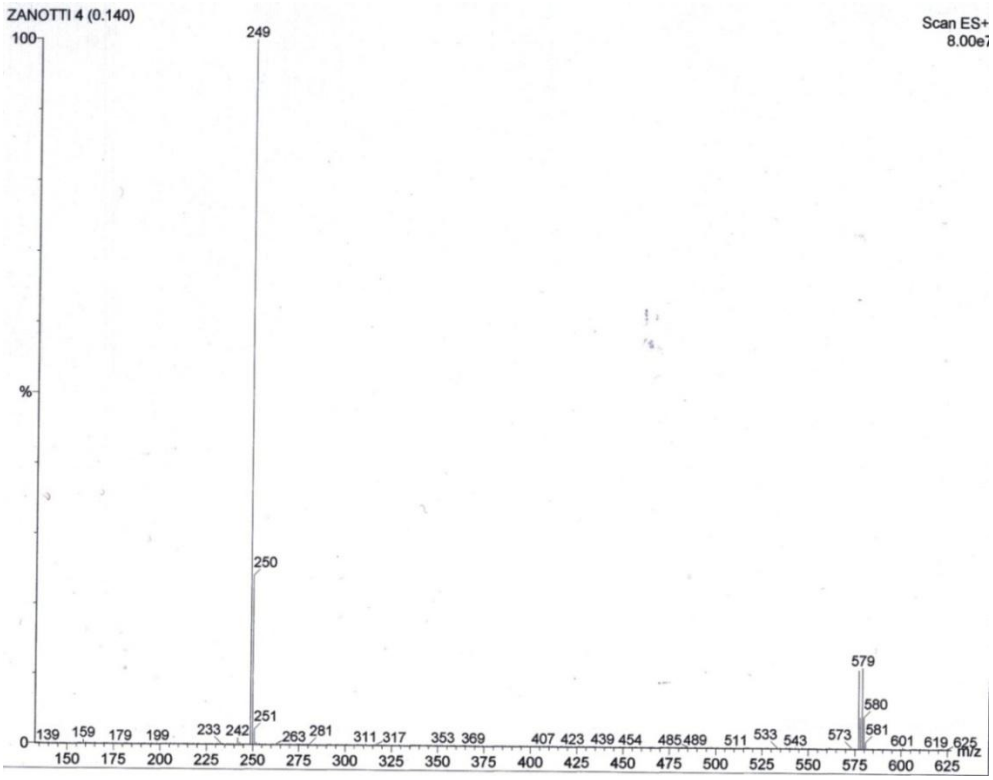

b)

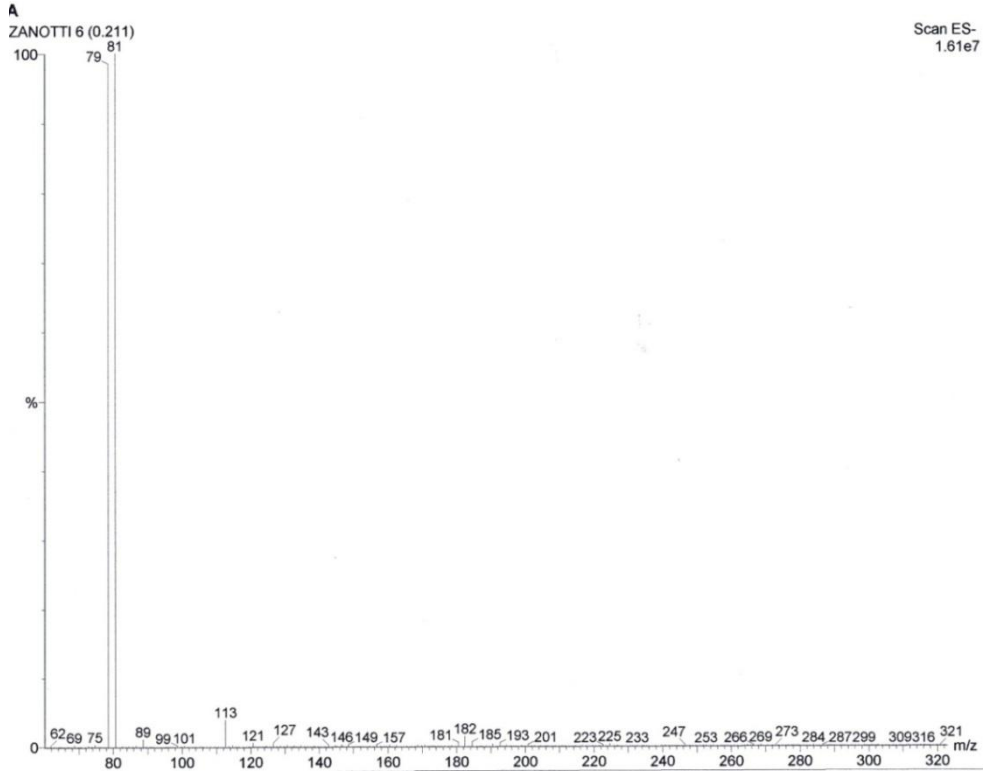

Figure 4.6 ESI-MS spectra of 1b, cation spectrum (a), anion spectrum (b).

^{1}H NMR (400 MHz, $CDCl_3$): δ 10.59 (s, 1H, NCHN), 7.43 (m, 4H, Ph), 7.41 (d, 2H, $J_{H,H}$ = 1.5 Hz, CH_{im}), 7.28 (m, 6H, Ph), 5.50 (s, 4H, CH_2Ph).

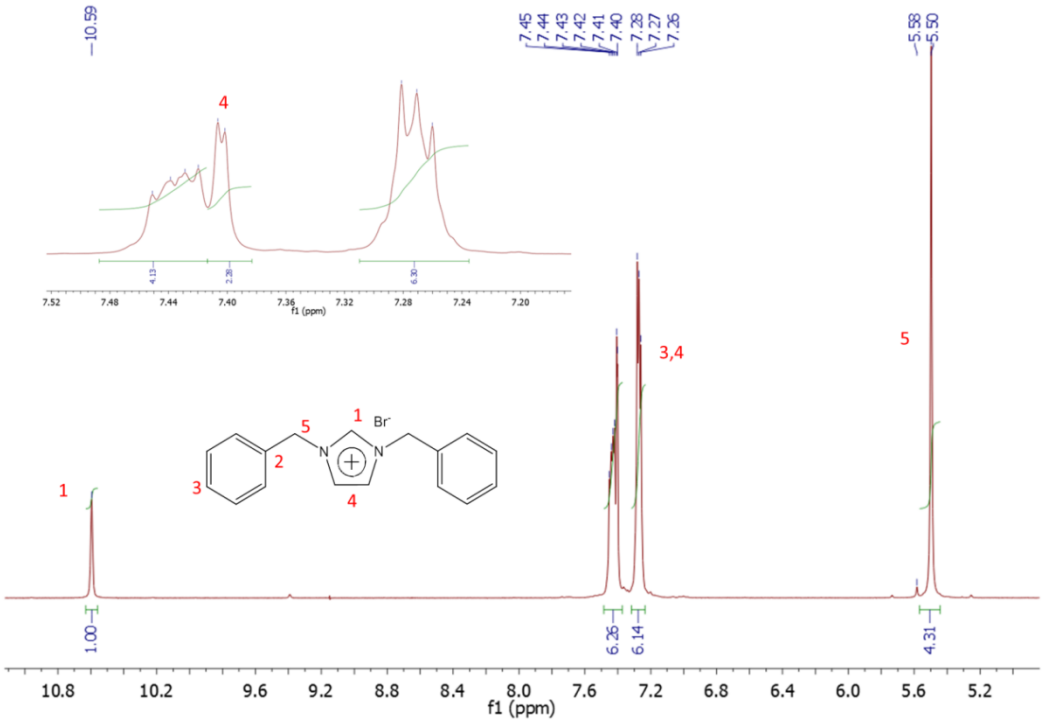

Figure 4.7 ^{1}H NMR spectrum of 1b with the inset showing signals deriving from imidazole backbone protons.

^{13}C NMR (100 MHz, $CDCl_3$): δ 136.34 (NCHN), 132.76 (Cq, Ph), 129.21 (Ph), 129.15 (Ph), 128.78 (Ph), 122.01 (CH_{im}), 53.01 (CH_2Ph).

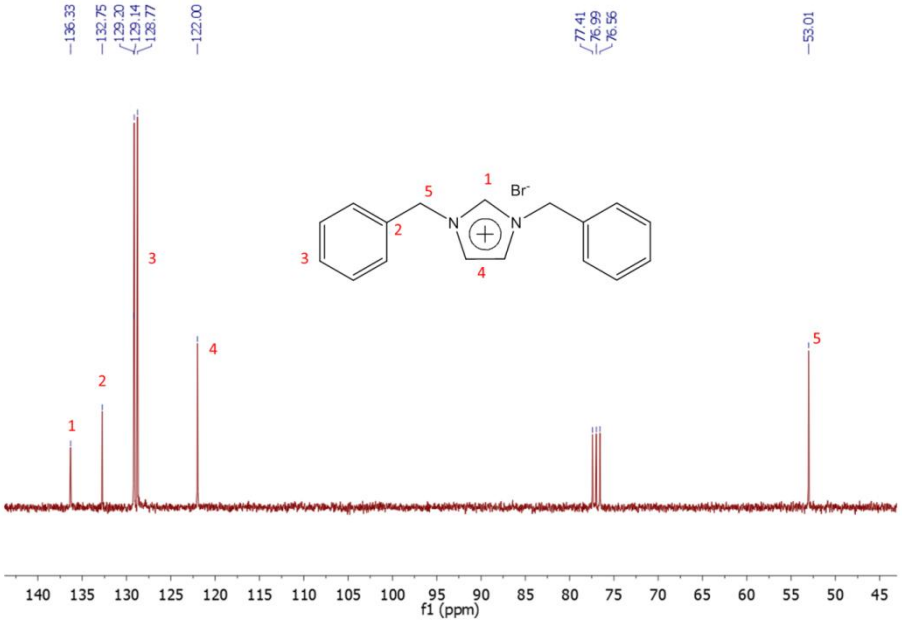

Figure 4.8 ^{13}C NMR spectrum of 1b.

Supplementary spectra related to the synthesis:

1-benzylimidazole

^{1}H NMR (400 MHz, $CDCl_3$): δ 7.66 (s, 1H, NCHN), 7.35 (m, 3H, Ph), 7.15 (d, 2H, $J_{H,H}$ = 6 Hz, Ph), 7.09 (s, 1H, CH_{im}), 6.90 (s, 1H, CH_{im}), 5.13 (s, 2H, CH_2Ph). SDBS: **^{1}H NMR (400 MHz, $CDCl_3$):** δ 7.530 (s, 1H, NCHN), 7.33 (m, 3H, Ph), 7.141 (m, 2H, Ph), 7.082 (s, 1H, CH_{im}), 6.891 (s, 1H, CH_{im}), 5.095 (s, 2H, CH_2Ph).

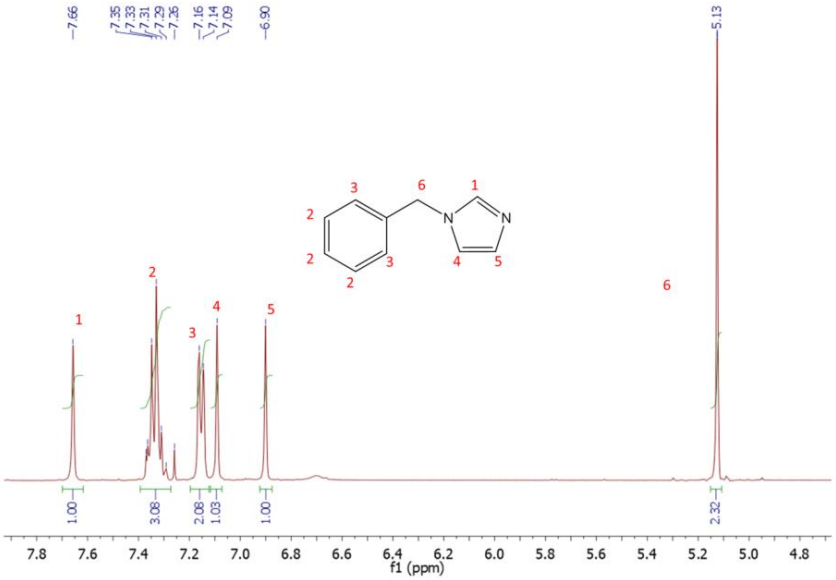

Figure 4.9 ^{1}H NMR spectrum of 1-benzylimidazole.

^{13}C NMR (100 MHz, $CDCl_3$): δ 137.32 (NCHN), 136.06 (Cq, Ph), 129.57 (CH_{im}), 128.91 (Ph), 128.20 (Ph), 127.22 (Ph), 119.23 (CH_{im}), 50.75 (CH_2Ph). SDBS: **^{13}C NMR (25 MHz, $CDCl_3$)**: δ 137.43 (NCHN), 136.24 (Cq, Ph), 129.80 (CH_{im}), 128.95 (Ph), 128.21 (Ph), 127.26 (Ph), 119.26 (CH_{im}), 50.72 (CH_2Ph).

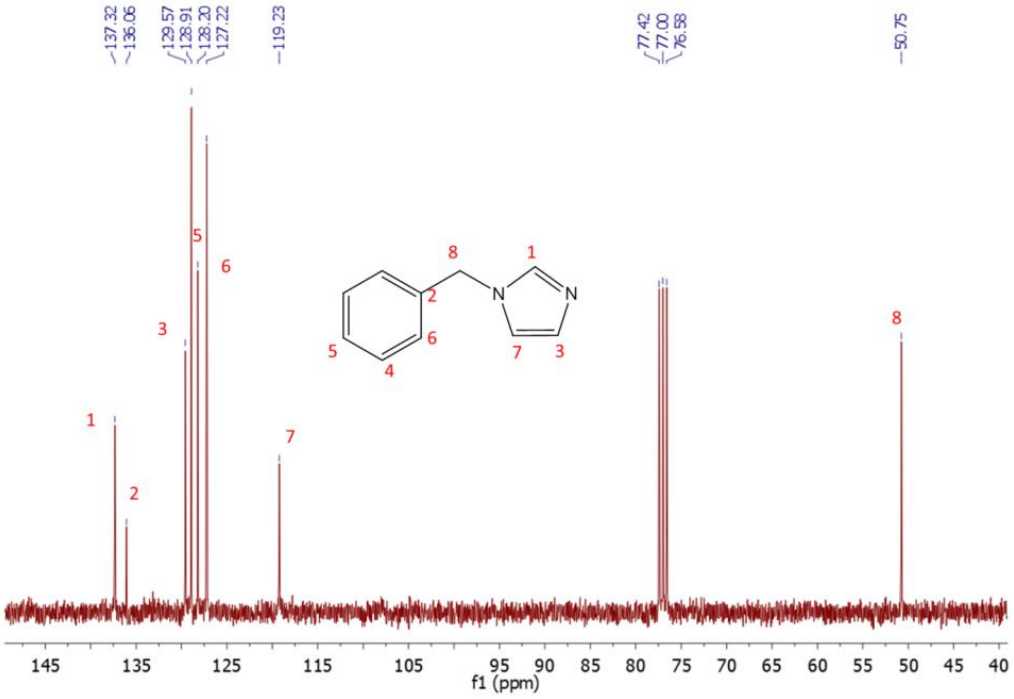

Figure 4.10 ^{13}C NMR spectrum of 1-benzylimidazole.

4.3 Synthesis of 1-benzyl-3-diphenylmethylimidazolium chloride (1c)

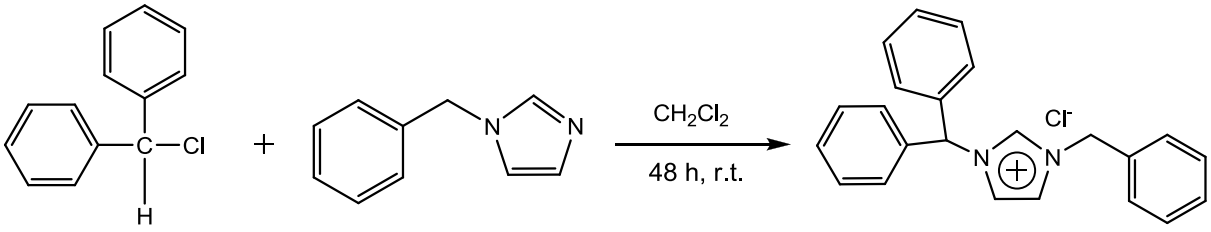

1c

This product was synthesized using a modified literature method[57]. In a Schlenk to a solution of 1-benzylimidazole (0.25 g, 1.58 mmol) in CH_2Cl_2 (10 mL), diphenylmethyl chloride (0.28 mL, 4.74 mmol) was added. After stirring for 48 h at room temperature, the solvent was removed under vacuum, and the resulting pale yellow viscous oil was thoroughly washed with diethyl ether (3 x 10 mL). After separation from the washings the oil was kept under vacuum for several hours to yield **1c**.

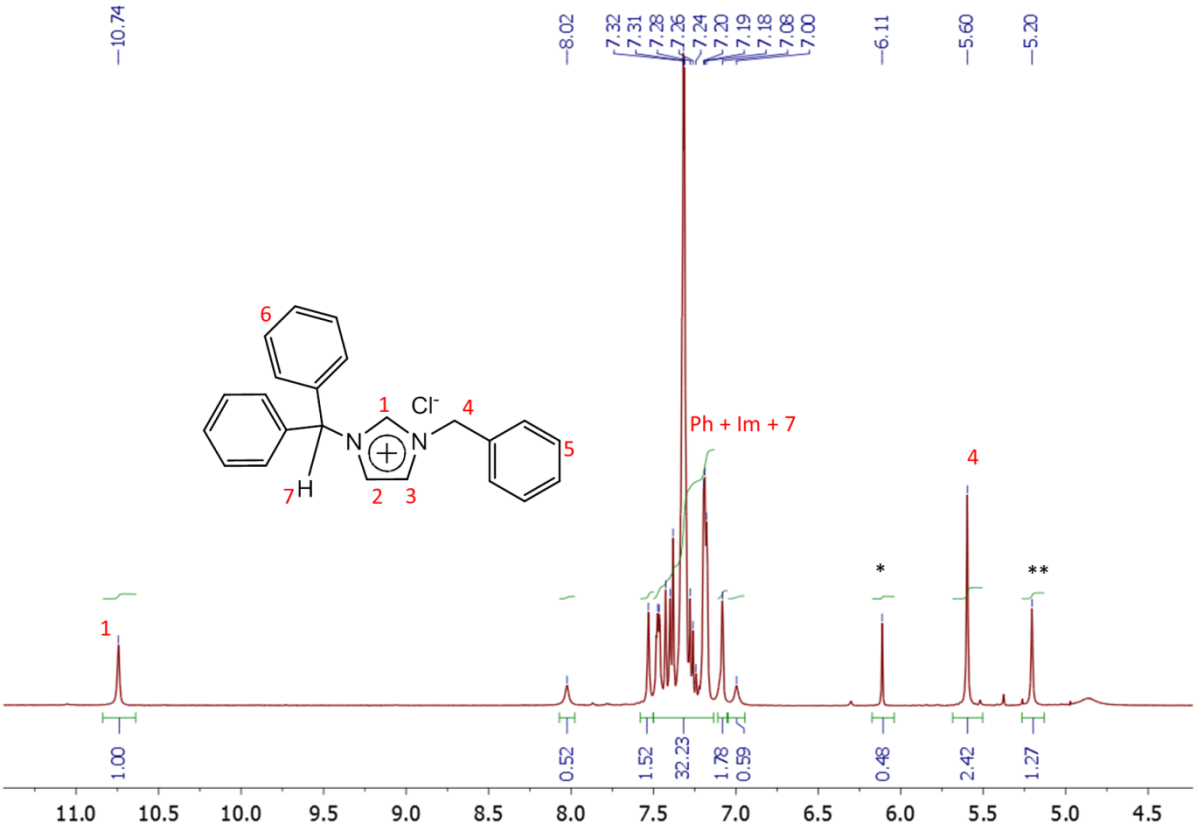

***** Traces of starting material: diphenylmethyl chloride.

** Impurity

Figure 4.11 ^{1}H NMR spectrum of 1c.

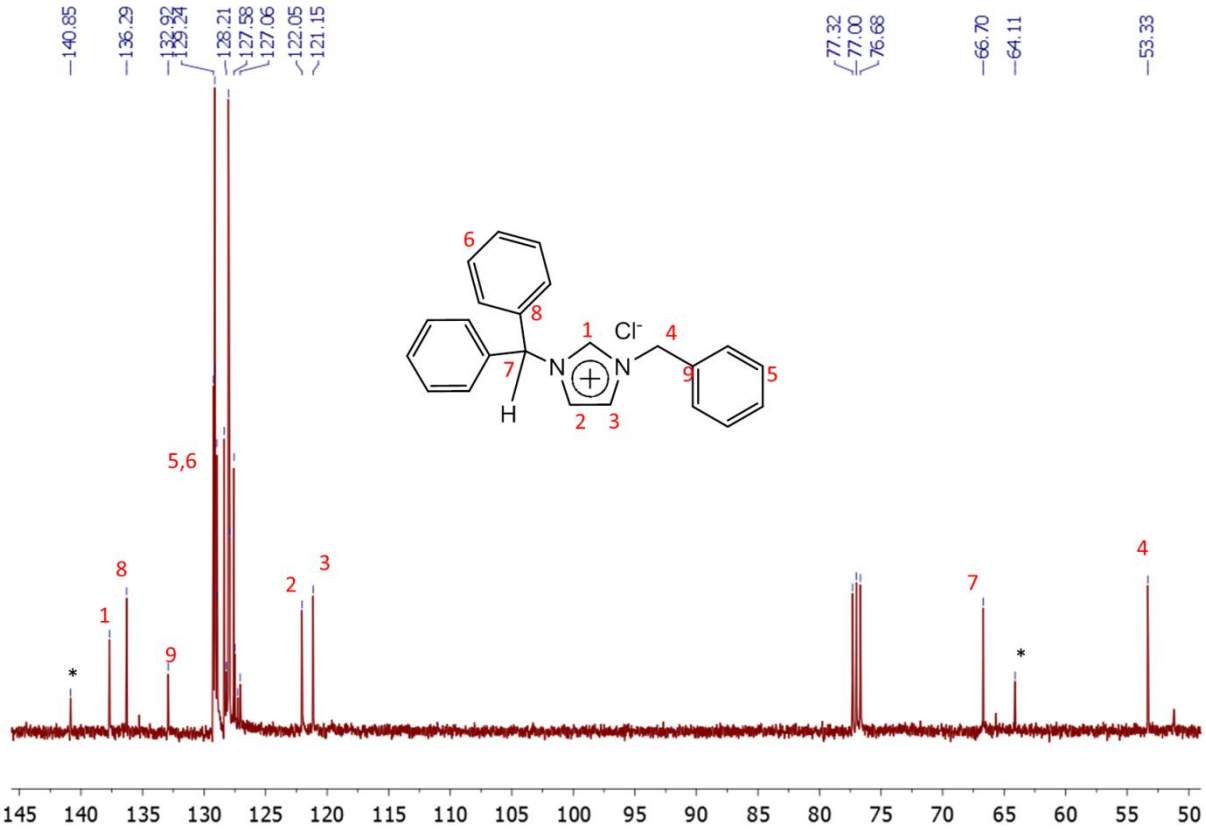

***** Traces of starting material: diphenylmethyl chloride.

Figure 4.12 ^{13}C NMR spectrum of 1c.

Supplementary spectra related to the synthesis:

<u>Diphenylmethyl chloride</u>

SDBS: **^{1}H NMR (90 MHz, $CDCl_3$):** δ 7.57-7.08 (m, 10H, Ph), 6.11 (s, 1H, CH)
SDBS: **^{13}C NMR (90 MHz, $CDCl_3$):** δ 141.0 (Cq, Ph), 128.4 (Ph), 127.9 (Ph), 127.7 (Ph), 64.2 (CH)

4.4 Synthesis of 1-benzyl-3-trityl-imidazolium chloride (1d)

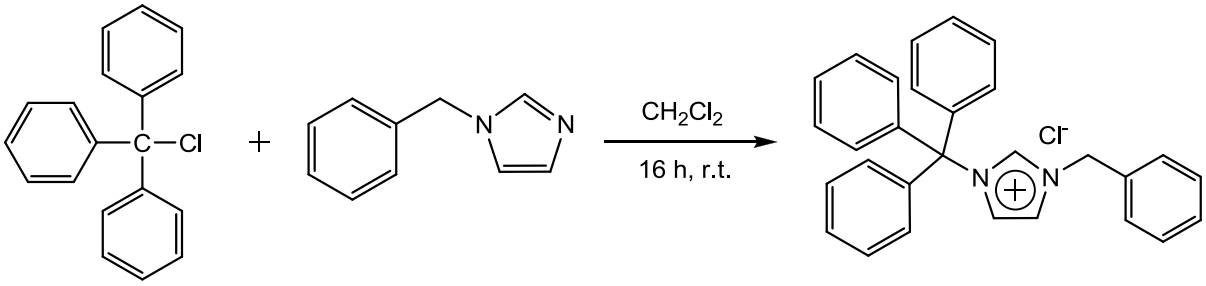

1d

In a Schlenk tube to a solution of trityl chloride (0.18 g, 0.64 mmol) dissolved in CH_2Cl_2 (10 mL), 1-benzylimidazole (0.10 g, 0.65 mmol) was added. After stirring for 16 h at room temperature, the solvent was removed under vacuum and the resulting solid was thoroughly washed with diethyl ether (3 x 10 mL) to yield 0.25 g (89%) of a white solid identified as **1d**.

Anal. Calc.d for $C_{29}H_{25}ClN_2$: C, 79.71; H, 5.77; Cl, 8.11; N, 6.41. Found: C, 79.52; H, 5.43; Cl, 8.32; N, 6.05.

ESI-MS (MeOH, m/z): 401 (100) $[C_{29}H_{25}N_2]^+$; In the ESI-MS(-) spectrum, no peaks were observed.

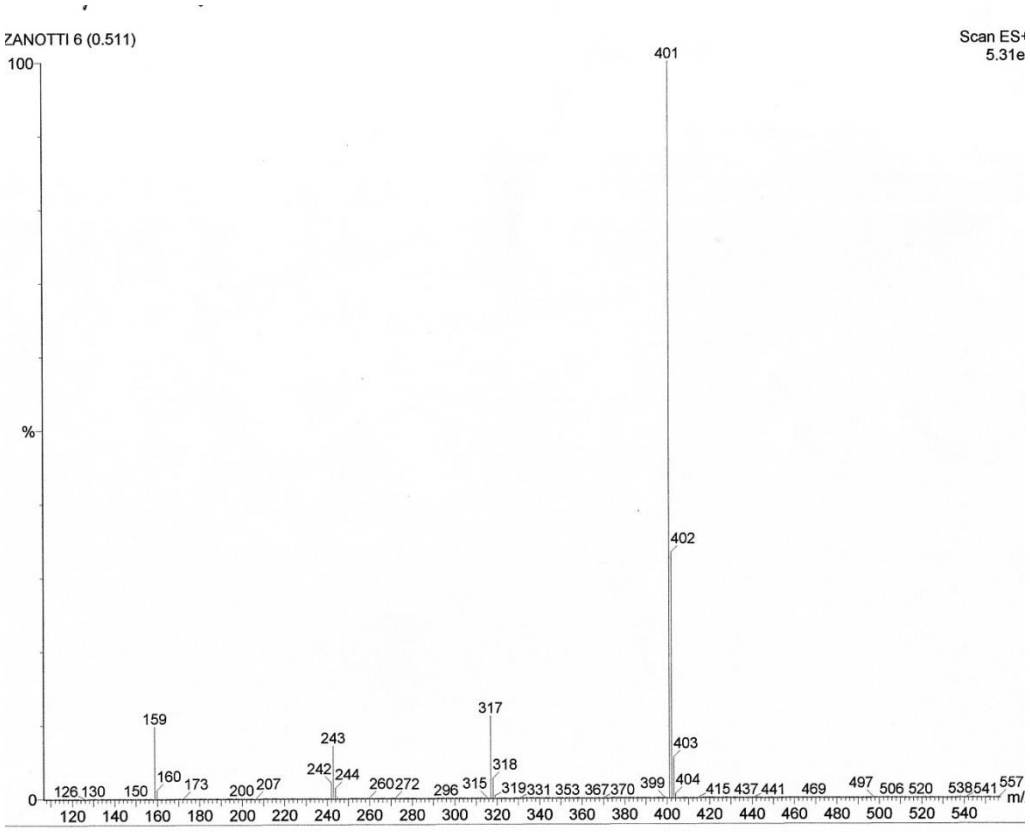

Figure 4.13 ESI-MS(+) spectrum of 1d.

^{1}H NMR (300 MHz, $CDCl_3$): δ 9.92 (s, 1H, NCHN), 7.65 (s, 1H, CH_{Im}), 7.49-7.11 (m, 20H, Ph), 6.93 (s, 1H, CH_{Im}), 5.97 (s, 2H, CH_2Ph).

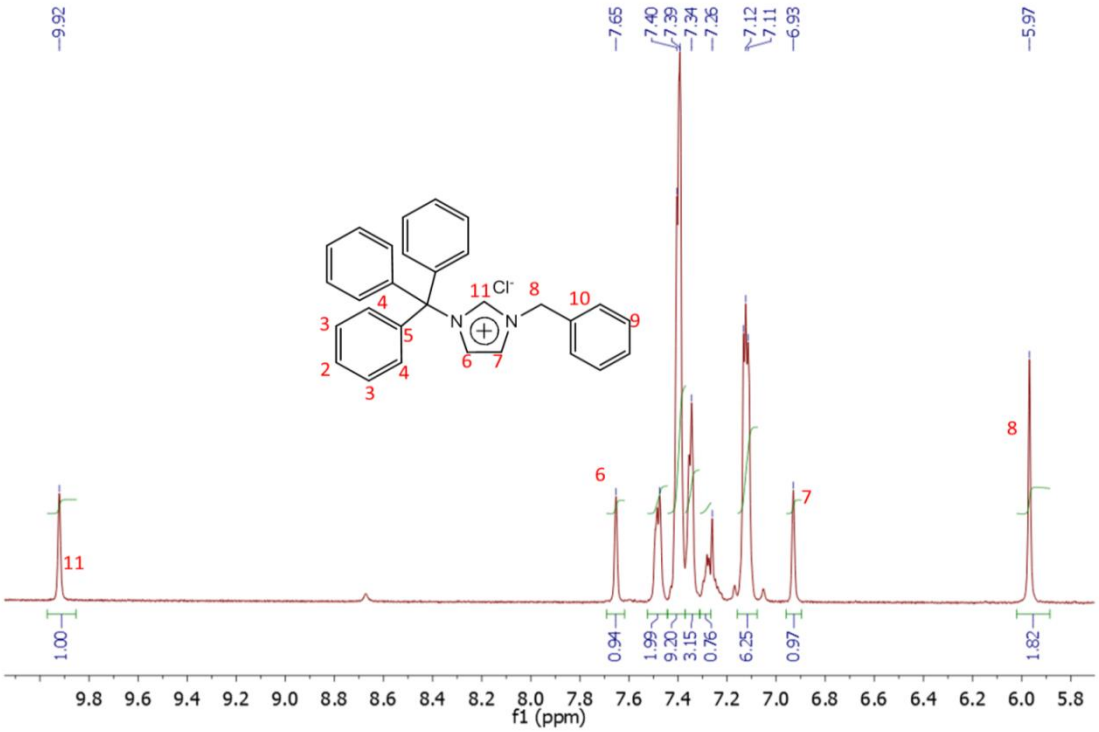

Figure 4.14 ^{1}H NMR spectrum of 1d.

^{13}C NMR (100 MHz, $CDCl_3$): δ 139.56 (C_5), 138.28 (NCHN), 133.54 (C_{10}), 129.63-127.66 (Ph), 123.69 (CH_{im}), 121.84 (CH_{im}), 79.77 (C_1), 53.92 (CH_2Ph).

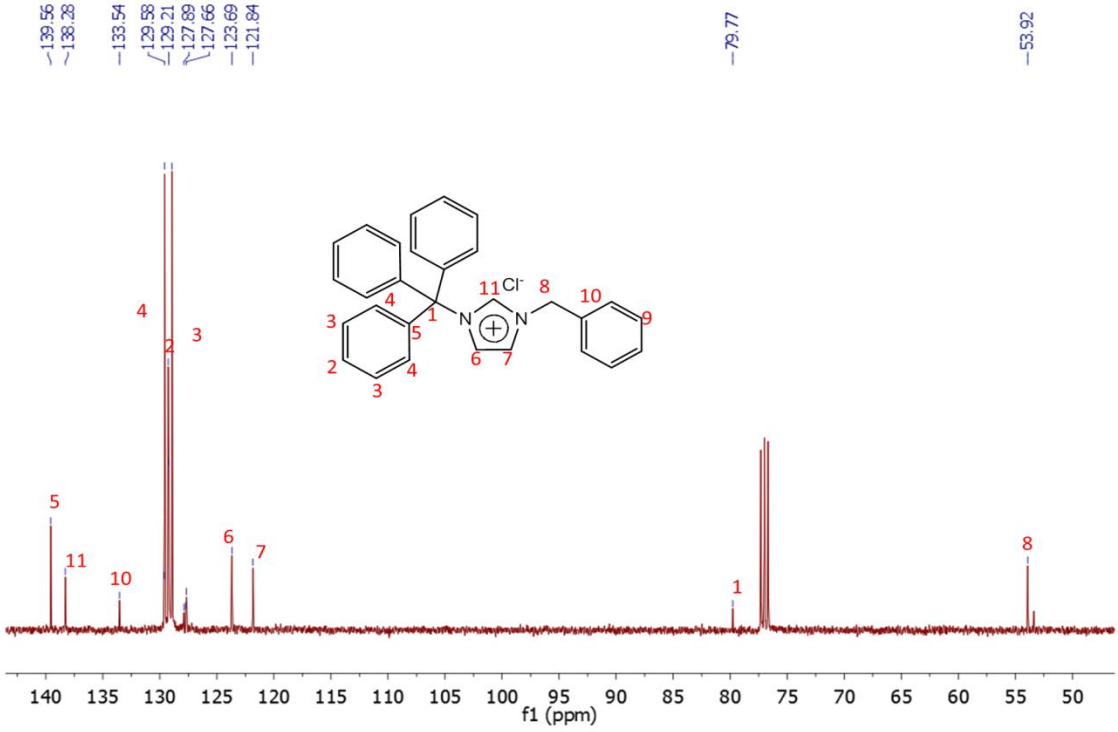

Figure 4.15 ^{13}C NMR spectrum of 1d.

Supplementary spectra related to the synthesis:

Trityl chloride
SDBS: **^{1}H NMR (90 MHz, $CDCl_3$):** δ 7.37 – 7.16 (m, 15H, Ph)
SDBS: **^{13}C NMR (90 MHz, $CDCl_3$):** δ 145.2 (Cq, Ph), 129.6 (Ph), 127.8 (Ph), 127.6 (Ph), 81.3 (Cq)

Supplementary spectra of a product of hydrolysis of **1d**.

Trityl hydroxide

^{1}H NMR (300 MHz, $CDCl_3$): δ 7.36 – 7.27 (m, 15H, Ph). SDBS: no data
^{13}C NMR (100 MHz, $CDCl_3$): δ 146.82 (Cq), 127.91 (Ph), 127.24 (Ph), 82.00 (C_{OH}). SDBS:
^{13}C NMR (100 MHz, $CDCl_3$): δ 146.88 (Cq), 127.93 (Ph), 127.22 (Ph), 82.02 (C_{OH}).

4.5 Synthesis of 1-benzyl-3-tertbutylimidazolium bromide (1e)

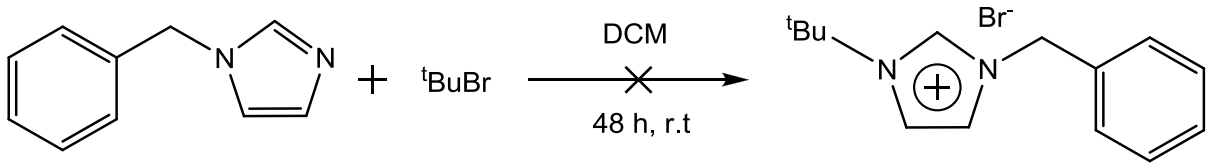

1e

In a Schlenk to a solution of 1-benzylimidazole (0.25 g, 1.58 mmol) in CH_2Cl_2 (5 mL), *tert*-butyl bromide (0.53 ml, 4.74 mmol) was added. After stirring for 48 h at room temperature, the solvent was removed under vacuum, and the resulting pale yellow viscous oil was thoroughly washed with diethyl ether (3 x 10 mL). After separation from the washings the oil was kept under vacuum for several hours to yield crude product.

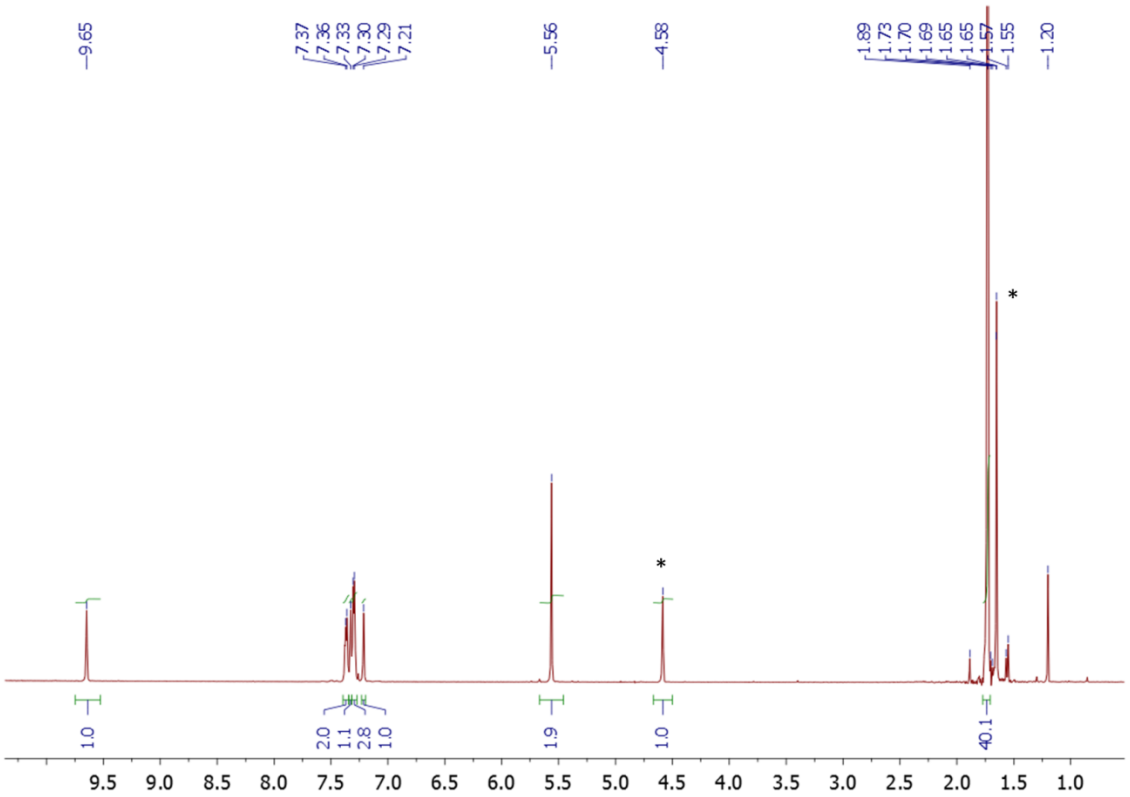

* Product of E1 elimination: 2-methylpropene

Figure 4.16 ^{1}H NMR spectrum of the crude product.

4.6 Synthesis of 1-tert-butylimidazole (Debus-Radziszewski reaction)

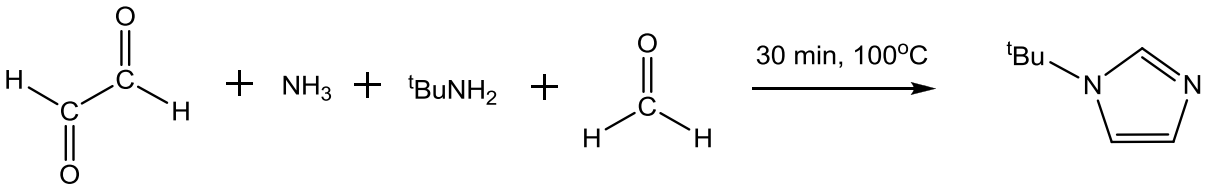

This product was synthesized using a literature method[46]. In a 100 mL three-necked flask connected to two dropping funnels and a condenser, was placed 50 mL of distilled water. One dropping funnel contained a mixture of 40% aqueous glyoxal (11.5 mL, 0.10 mol) and 40% aqueous formaldehyde (8.1 mL, 0.10 mol), the other *tert*-butylamine (10.6 mL, 0.10 mol) and 25% aqueous ammonia (6.8 mL, 0.10 mol). The water was heated until boiling, and then both solutions were added simultaneously. The reaction mixture turned brown and was stirred for 30 min at 100°C after complete addition and then cooled to room temperature. After removal of the water by rotatory evaporator, the crude product was purified via vacuum distillation (bp. 53°C/0.9mbar) and **1-*tert*-butylimidazole** was obtained as a very pale yellow liquid (1.49 g, 12%).

^{1}H NMR (400 MHz, $CDCl_3$): δ 7.60 (s, 1H, NCHN), 7.05 (s, 1H, CH_{im}), 7.03 (s, 1H, CH_{im}), 1.57 (s, 9H, CH_3, ^{t}Bu).

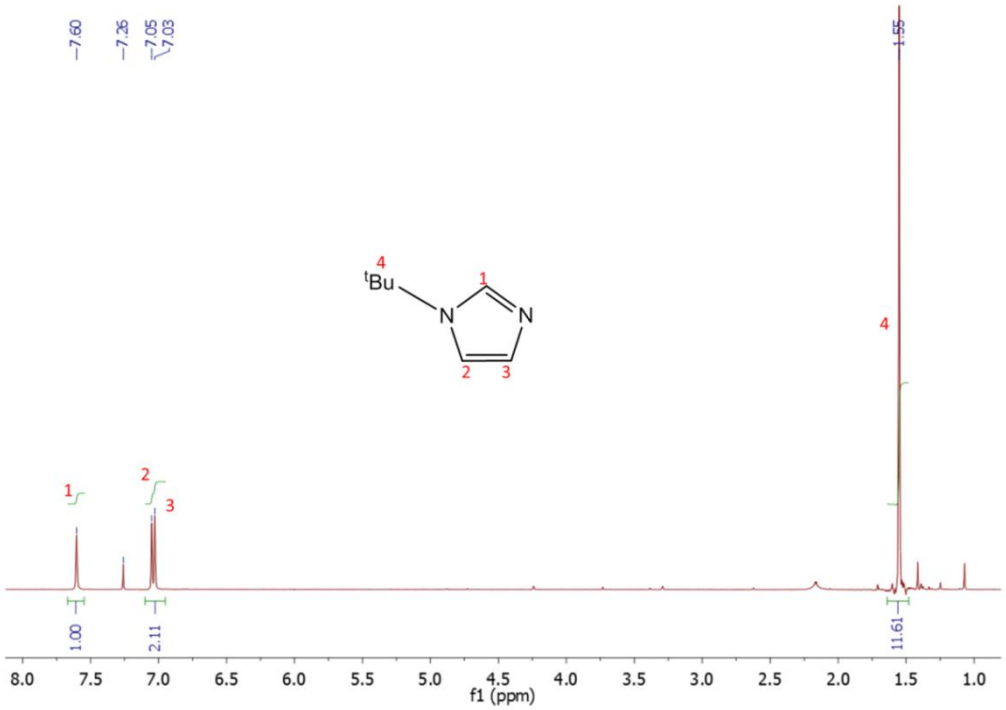

Figure 4.17 ^{1}H NMR spectrum of 1-*tert*-butylimidazole.

^{13}C NMR (100 MHz, $CDCl_3$): δ 134.33 (NCHN), 129.06 (C_{im}), 116.27 (Cq^{t}Bu), 30.62 (CH_3, ^{t}Bu).

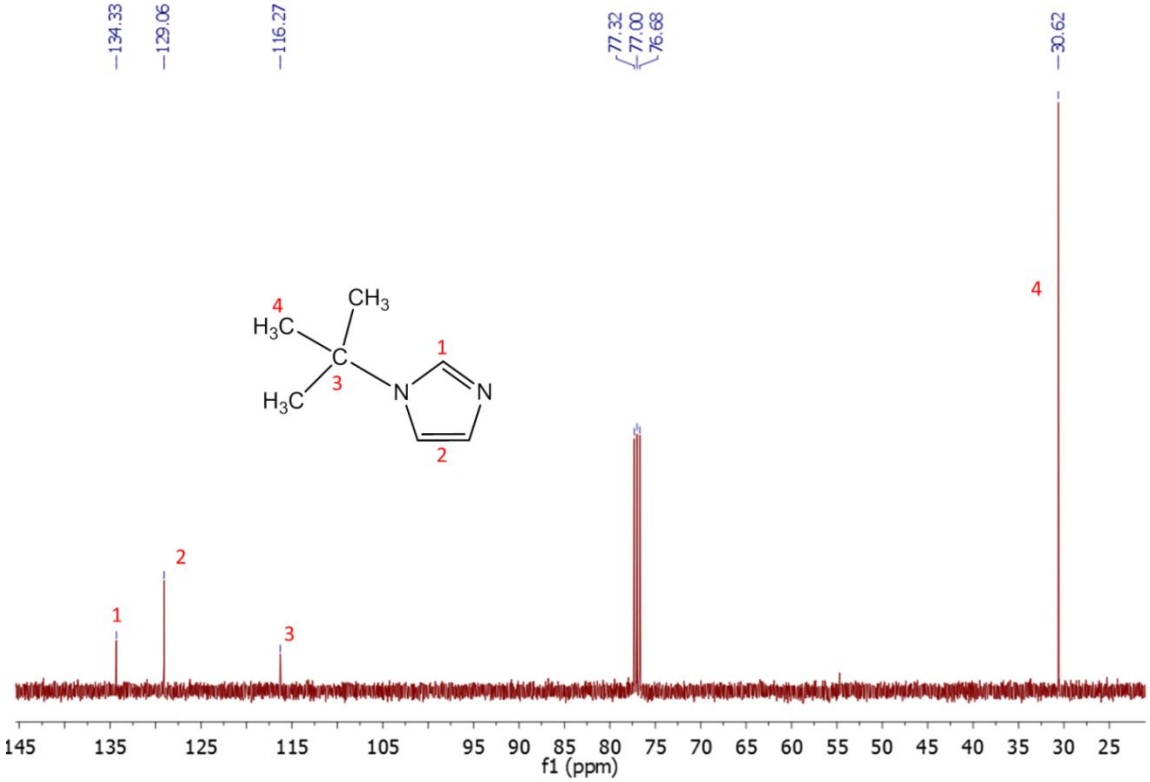

Figure 4.18 ^{13}C NMR spectrum of 1-*tert*-butylimidazole.

4.7 Synthesis of 1-benzyl-3-tert-butylimidazolium bromide (1e)

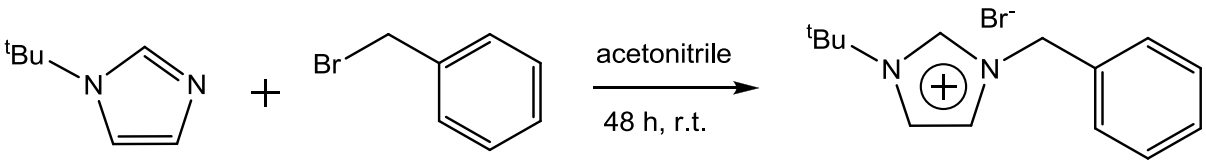

1e

This product was synthesized using a modified literature method[33]. In a Schlenk to a solution of 1-*tert*-butylimidazole (0.17 g, 1.40 mmol) in acetonitrile (5 mL), an equivalent molar amount of benzyl bromide (0.15 mL, 1.40 mmol) was added. After stirring for 48 h at room temperature, the solvent was removed under vacuum, and the resulting white solid was thoroughly washed with diethyl ether (2 x 4 mL). After separation from the washings the solid was kept under vacuum for 1 hour to yield 0.33 g (83%) of **1e**.

Anal. Calcd (%) for $C_{14}H_{19}BrN_2$: C, 56.96; H, 6.49; Br, 27.07; N, 9.49. Found: C, 56.68; H, 6.26; Br, 26.86; N, 9.20.

ESI-MS (MeOH, m/z): 215 (100) $[C_{14}H_{19}N_2]^+$; 79 (100), 81 (97) $[Br]^-$.

a)

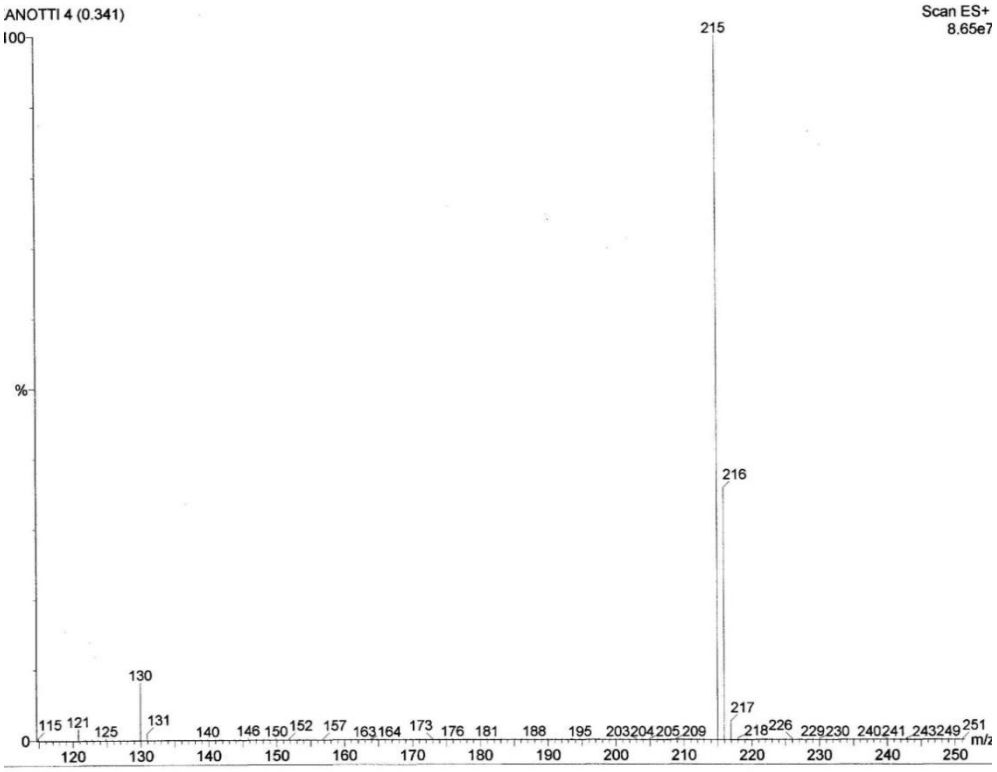

b)

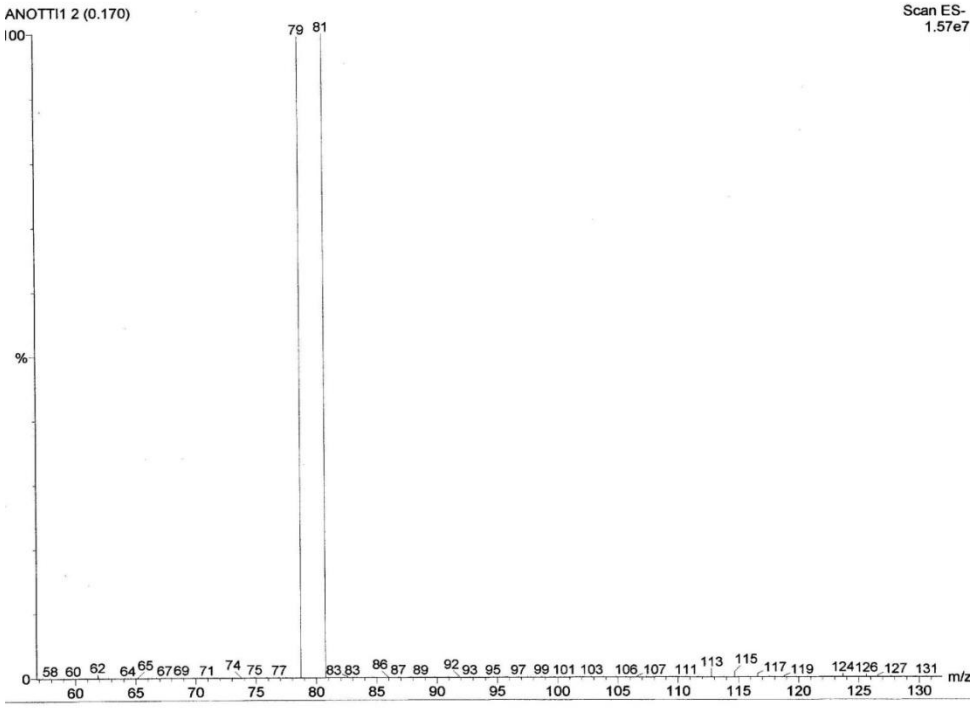

Figure 4.19 ESI-MS spectra of 1a, cation spectrum (a), anion spectrum (b).

^{1}H NMR (400 MHz, $CDCl_3$): δ 10.66 (s, 1H, NCHN), 7.55 (dd, 1H, $^3J_{H,H} \approx {}^4J_{H,H}$ = 1.82 Hz, CH_{im}), 7.51 (m, 2H, Ph), 7.45 (dd, 1H, $^3J_{H,H} \approx {}^4J_{H,H}$ = 1.80 Hz, CH_{im}), 5.62 (s, 2H, CH_2Ph), (s, 9H, CH_3, tBu).

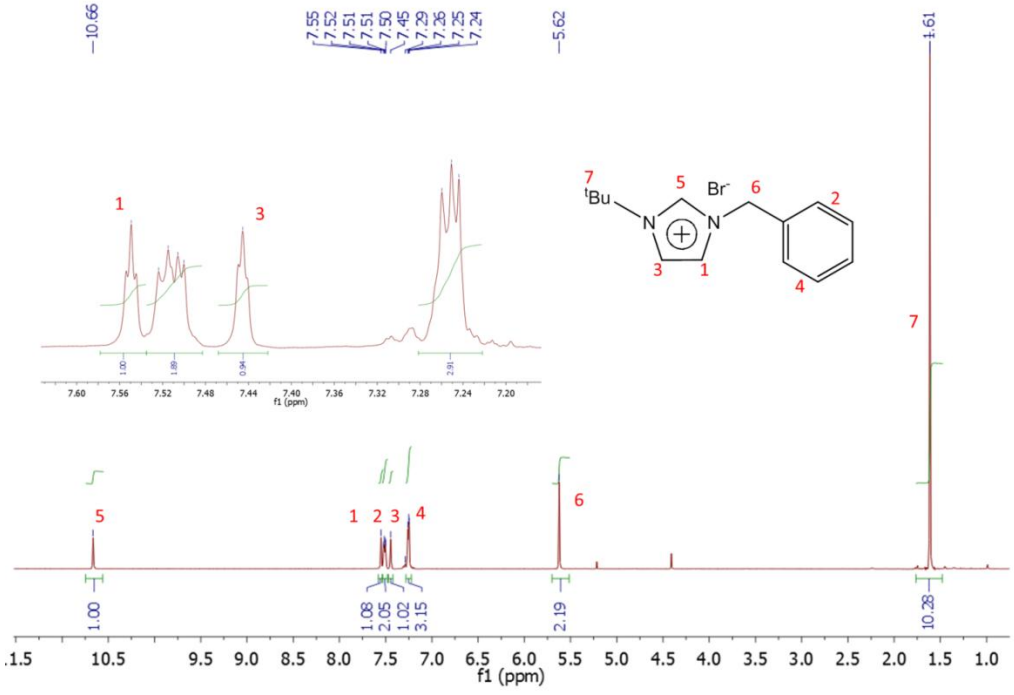

Figure 4.20 ^{1}H NMR spectrum of 1e with the inset showing signals deriving from imidazole backbone protons.

^{13}C NMR (100 MHz, $CDCl_3$): δ 137.47 (NCHN), 133.28 (Cq, Ph), 129.00 (Ph), 128.14 (Ph), 121.96 (CH_{im}), 119.75 (CH_{im}), 60.21 (Cq, ^{t}Bu), 52.66 (CH_2Ph), 29.91 (CH_3, ^{t}Bu).

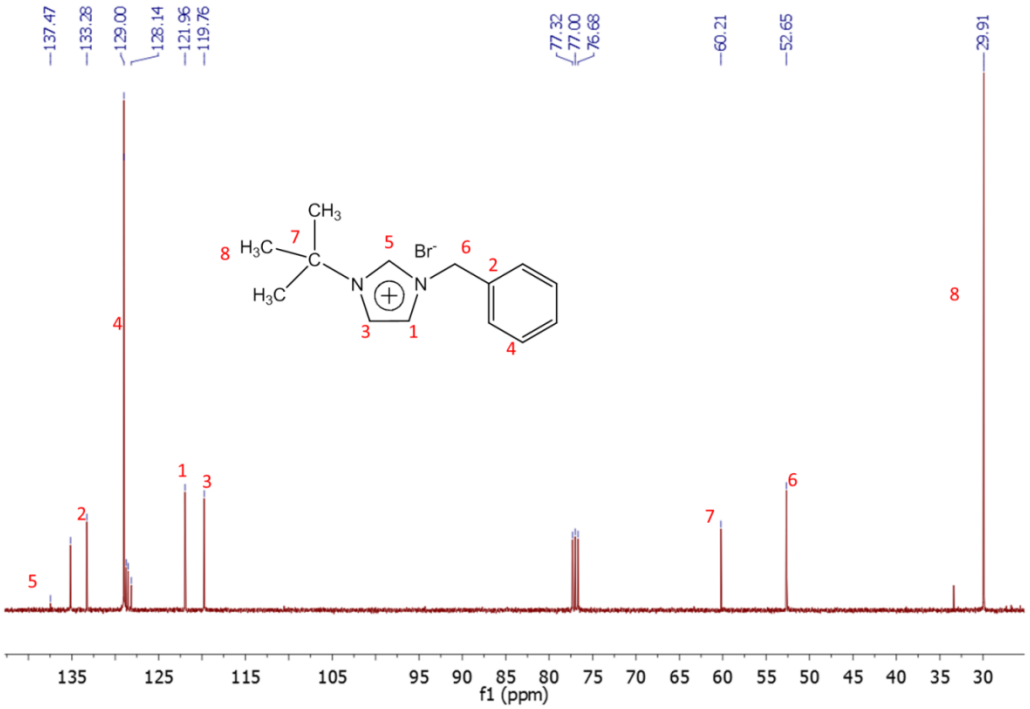

Figure 4.21 ^{13}C NMR spectrum of 1e.

4.8 Synthesis of 1,3-dibenzyl-imidazolium triflate

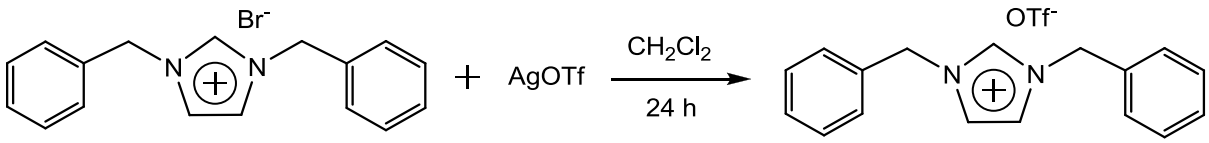

In a Schlenk to a solution of 1,3-dibenzyl-imidazolium bromide (0.440 g, 1.34 mmol) in dichloromethane (3 mL) stirred for 5 min, silver triflate (0.346 g, 1.34 mmol) was added. After stirring for 24 h at room temperature, the solvent was removed under vacuum, and the resulting white solid was thoroughly washed with diethyl ether (3 x 10 mL). After separation from the washings the solid was kept under vacuum at 40 °C for several hours to yield 0.720 g (Y = 99%) of **1,3-dibenzyl-imidazolium triflate.**

^{1}H NMR (400 MHz, $CDCl_3$): δ 9.52 (s, 1H, NCHN), 7.39-7.31 (m, 10H, Ph), 7.22 (d, 2H, $J_{H,H}$ = 1.47 Hz, CH_{im}), 5.33 (s, 4H, CH_2Ph).

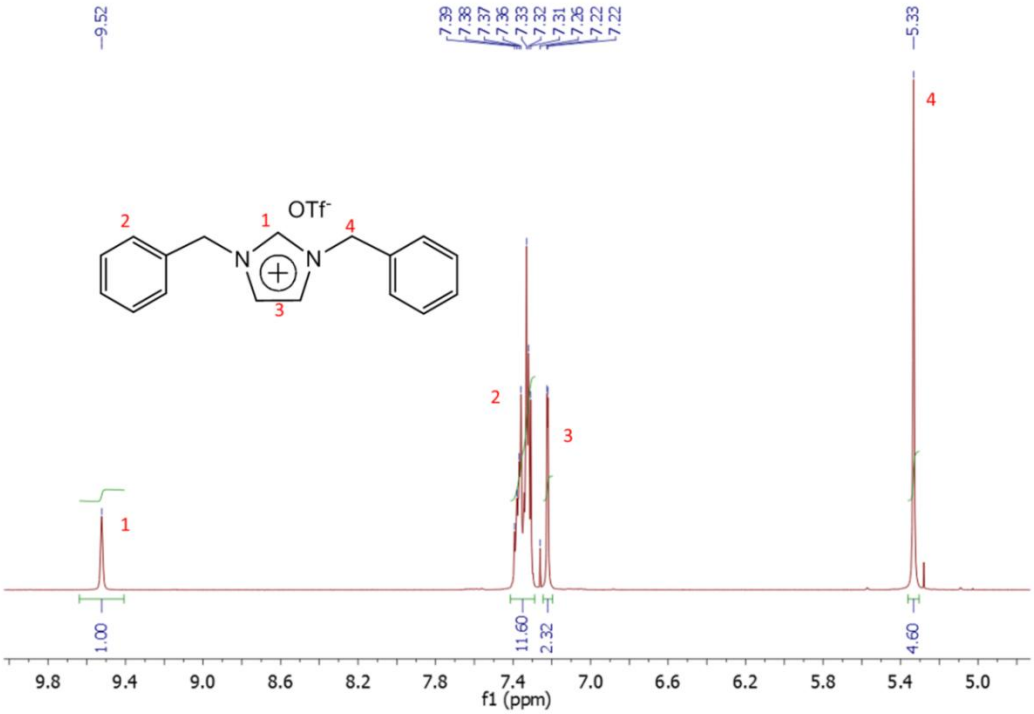

Figure 4.22 ^{1}H NMR spectrum of 1,3-dibenzyl-imidazolium triflate.

^{13}C NMR (100 MHz, $CDCl_3$): δ 136.1 (NCHN), 132.6 (Cq, Ph), 129.4 (Ph), 129.3 (Ph), 128.8 (Ph), 122.1 (CH_{im}), 53.4 (CH_2Ph).

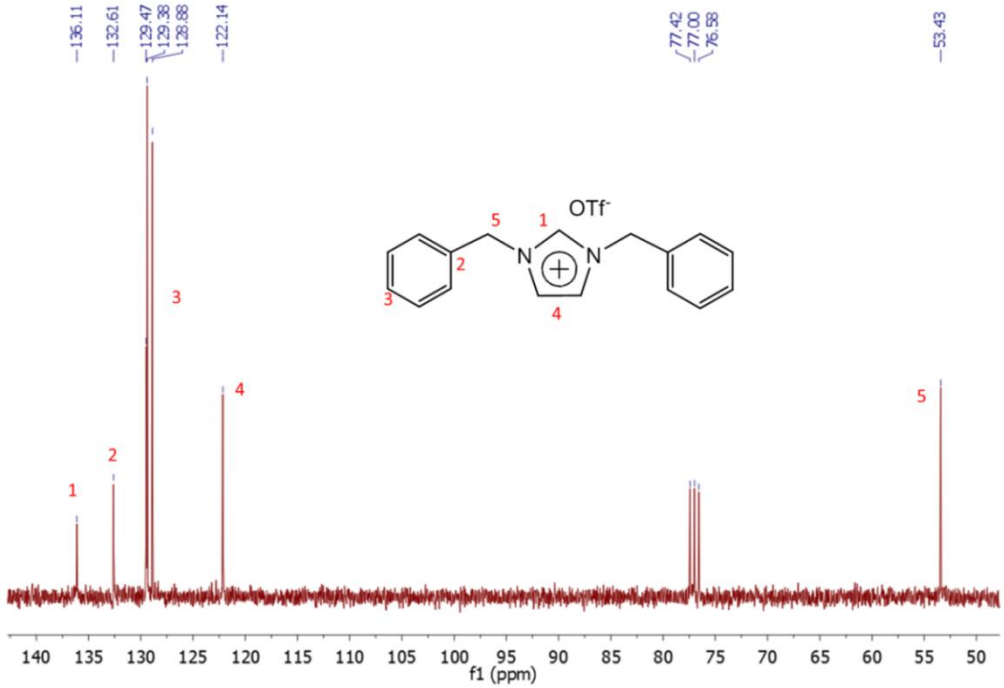

Figure 4.23 ^{13}C NMR spectrum of 1,3-dibenzyl-imidazolium triflate.

4.9 Reaction of 1a with KO^{t}Bu

Removal of the acidic proton with a strong base (0.9 equivalents).

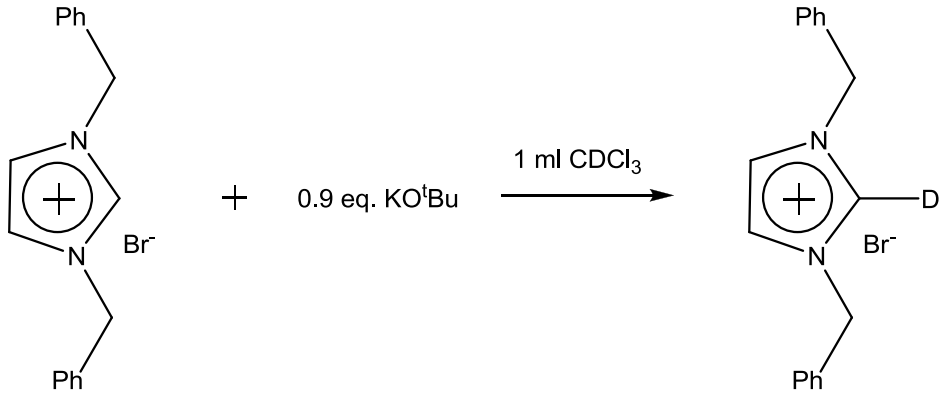

The salt **2b** was dissolved in deuterated $CDCl_3$, then the KO^{t}Bu base was added to the reaction mixture and stirred for 5 min. After this time, the above reaction was checked by NMR.

^{1}H NMR (600 MHz, $CDCl_3$): δ 7.38 (m, 6H, Ph + CH_{im}), 7.20 (m, 6H, Ph + CH_{im}), 5.43 (s, 4H, CH_2Ph).

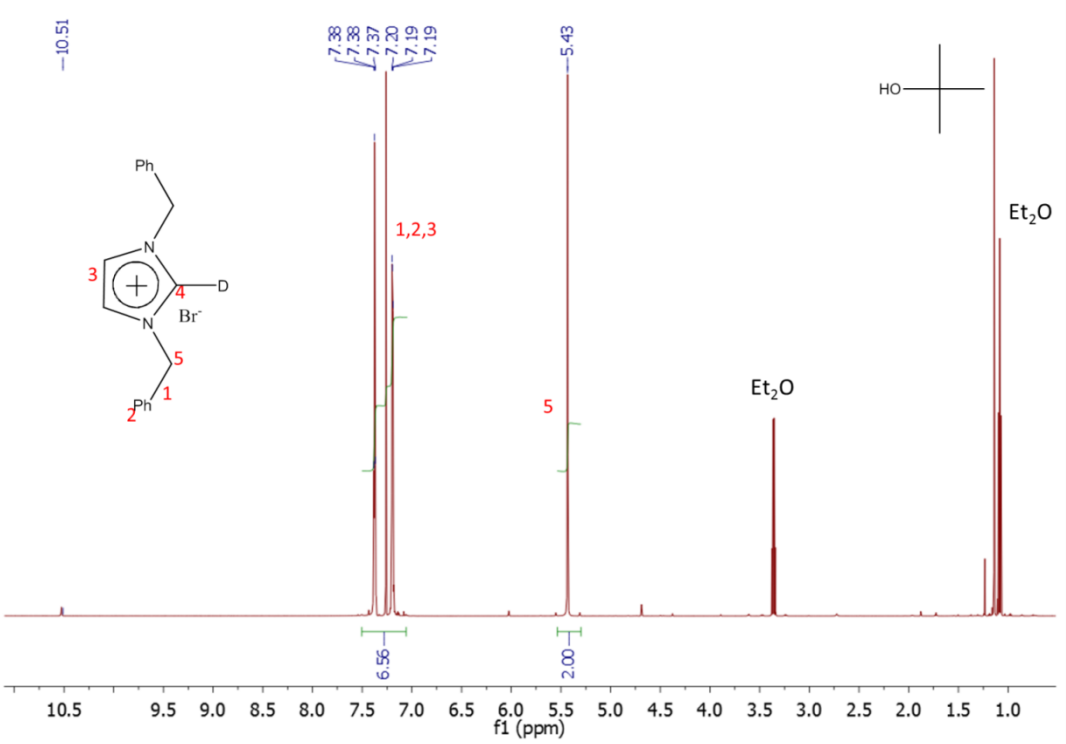

Figure 4.24 ^{1}H NMR spectrum of deuterated 1,3-dibenzyl-imidazolin-2-ylidene.

^{13}C NMR (150 MHz, $CDCl_3$): δ 132.80 (Cq, Ph), 129.01 (Ph), 128.79 (Ph), 128.42 (Ph), 121.94 (CH_{im}), 52.84 (CH_2Ph).

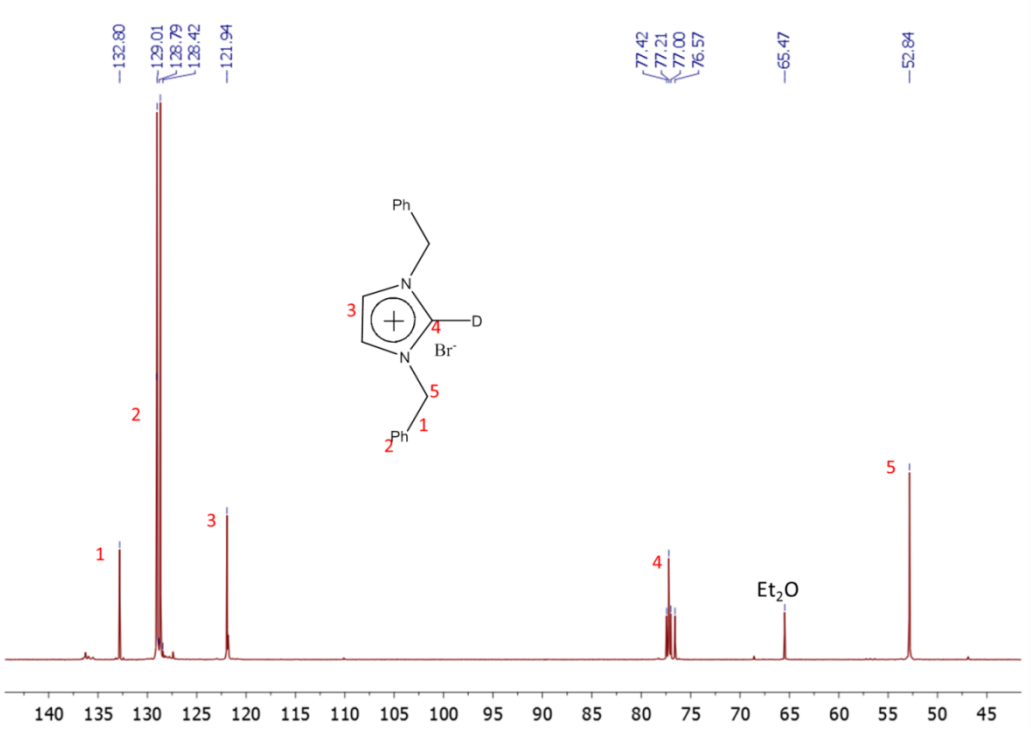

Figure 4.25 ^{13} C NMR spectrum of deuterated 1,3-dibenzyl-imidazolin-2-ylidene.

4.10 Synthesis of 1-benzyl-3-methyl-imidazolin-2-ylidene silver bromide (2a)

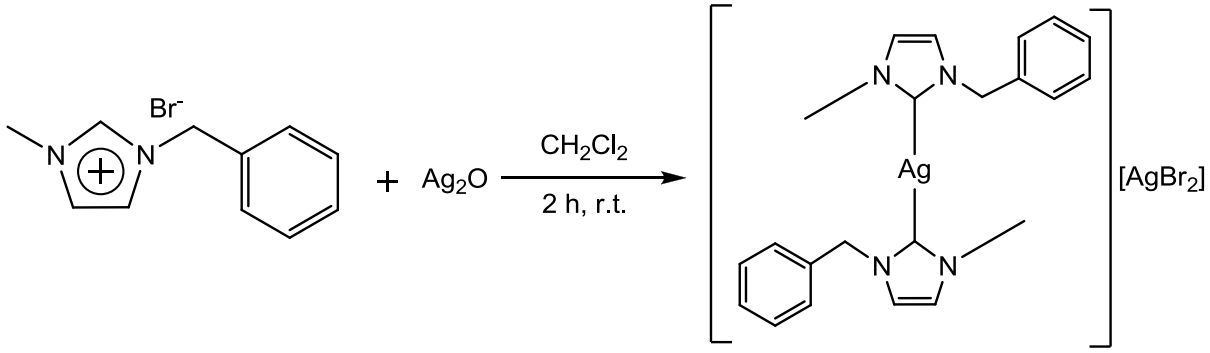

1a **2a**

This product was synthesized using a literature method[58]. To a solution of **1a** (0.25 g, 0.97 mmol) in CH_2Cl_2 (10 mL) stirred in a Schlenk, Ag_2O (0.15 g, 0.63 mmol) was added. The reaction mixture was stirred for 2 h at room temperature; in the end of the reaction a colorless solution and a small amount of the black solid of Ag_2O was found in the Schlenk, which was subsequently filtered on Celite and the solvent was removed under vacuum to afford 0.32 g (82%) of a white solid identified as **2a**.

ESI-MS (MeOH, m/z): 173 (100) $[C_{11}H_{13}N_2]^+$; 451 (45) $[C_{22}H_{24}N_4Ag]^+$. In the ESI-MS(-) spectrum, no peaks were observed.

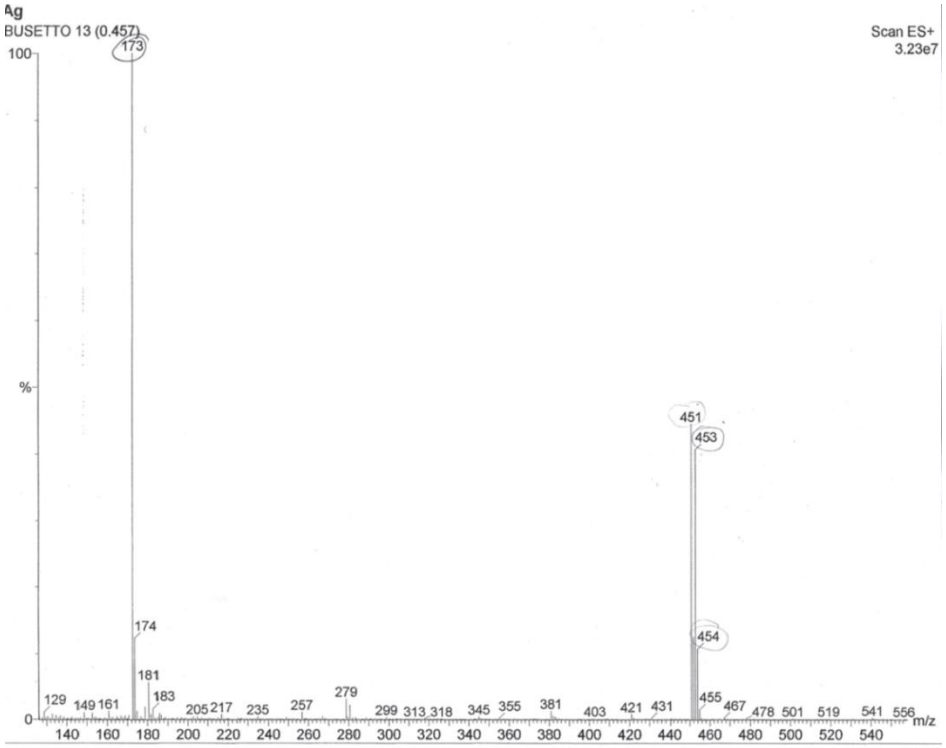

Figure 4.26 ESI-MS(+) spectrum of 2a.

^{1}H NMR (400 MHz, $CDCl_3$): δ 7.34 (m, 3H, Ph), 6.98 (d, 1H, $J_{H,H}$ = 1.79 Hz, CH_{im}), 6.93 (d, 1H, $J_{H,H}$ = 1.80 Hz, CH_{im}), 5.28 (s, 2H, CH_2Ph), 3.84 (s, 3H, CH_3).

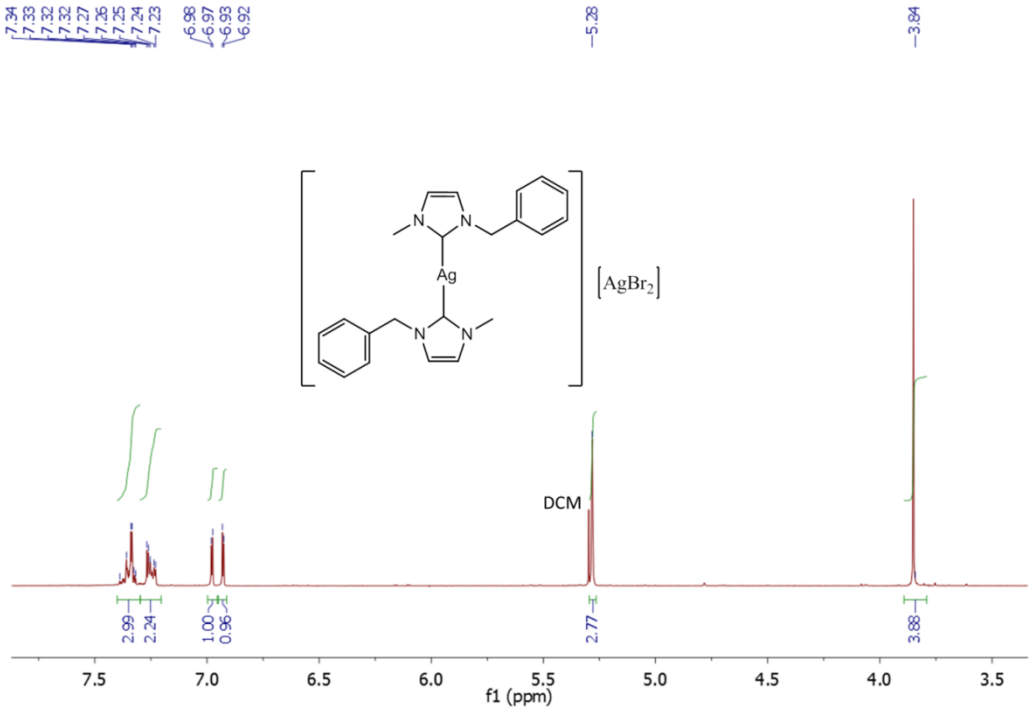

Figure 4.27 ^{1}H NMR spectrum of 2a.

^{13}C NMR (100 MHz, $CDCl_3$): δ 181.87 (s, C-Ag), 135.45 (Cq, Ph), 129.11 (Ph), 128.65 (Ph), 127.81 (Ph), 122.53 (CH_{im}), 121.08 (CH_{im}), 55.87 (CH_2Ph), 38.73 (CH_3).

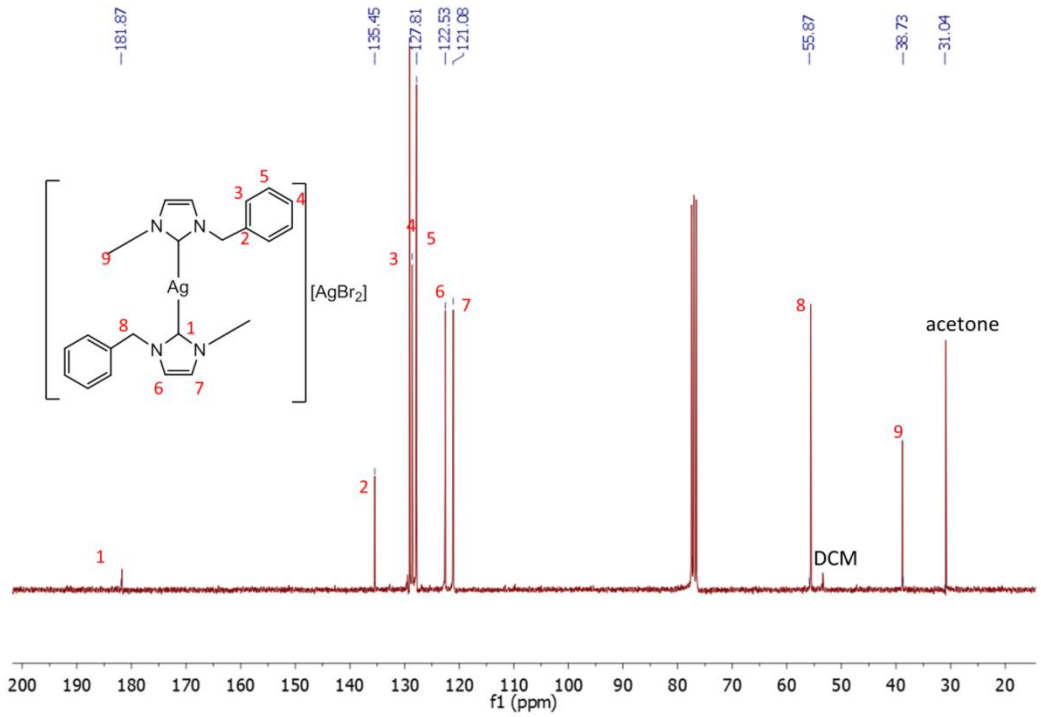

Figure 4.28 ^{13}C NMR spectrum of 2a.

4.11 Synthesis of 1,3-dibenzyl-imidazolin-2-ylidene silver bromide (2b)

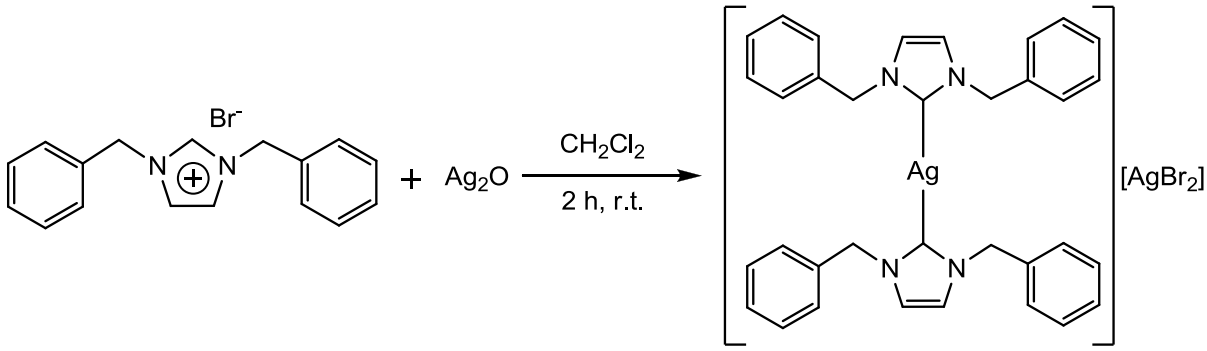

1b **2b**

This product was synthesized using a literature method[43]. To a solution of **1b**, (0.20 g, 0.61 mmol) in DCM (ca. 10 mL) stirred in a Schlenk, Ag_2O (0.09 g, 0.39 mmol) was added. The reaction mixture was stirred for 2 h at room temperature; in the end of the reaction a colorless solution and a small amount of the black solid of Ag_2O was found in the Schlenk, which was subsequently filtered on Celite and the solvent was removed under vacuum to afford 0.28 g (95%) of a white solid identified as **2b**.

The characterization of **2b** by ESI-MS is in progress.

^{1}H NMR (400 MHz, $CDCl_3$): δ 7.29 – 7.18 (m, 10H, Ph), 6.99 (s, 2H, CH_{im}), 5.21 (s, 4H, CH_2Ph).

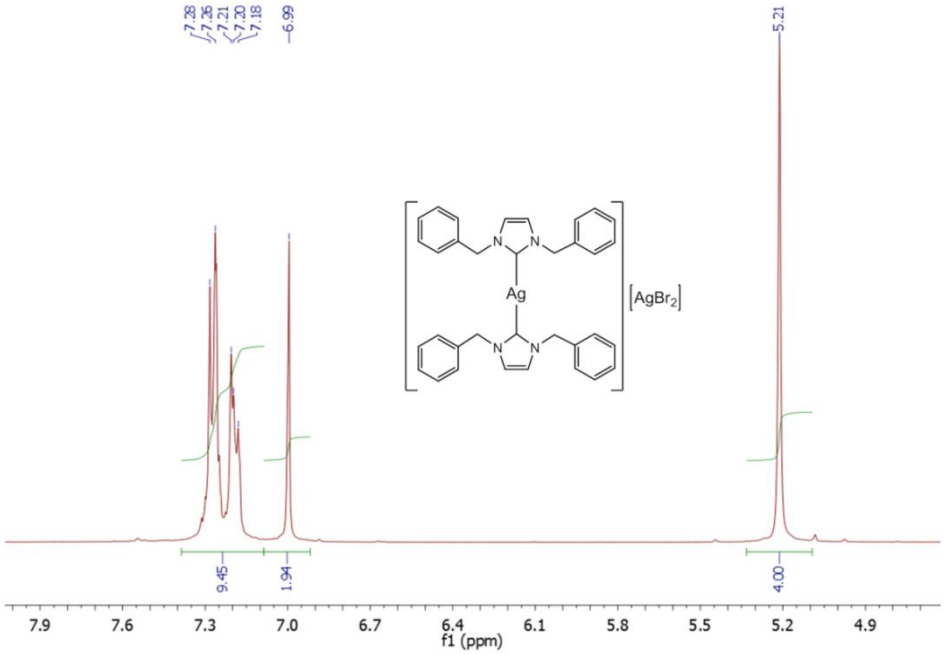

Figure 4.29 ^{1}H NMR spectrum of 2b.

^{13}C NMR (100 MHz, $CDCl_3$): δ 180.60 (s, C-Ag), 135.50 (Cq, Ph), 128.80 (Ph), 128.25 (Ph), 127.55 (Ph), 121.62 (C_{im}), 55.33 (CH_2Ph).

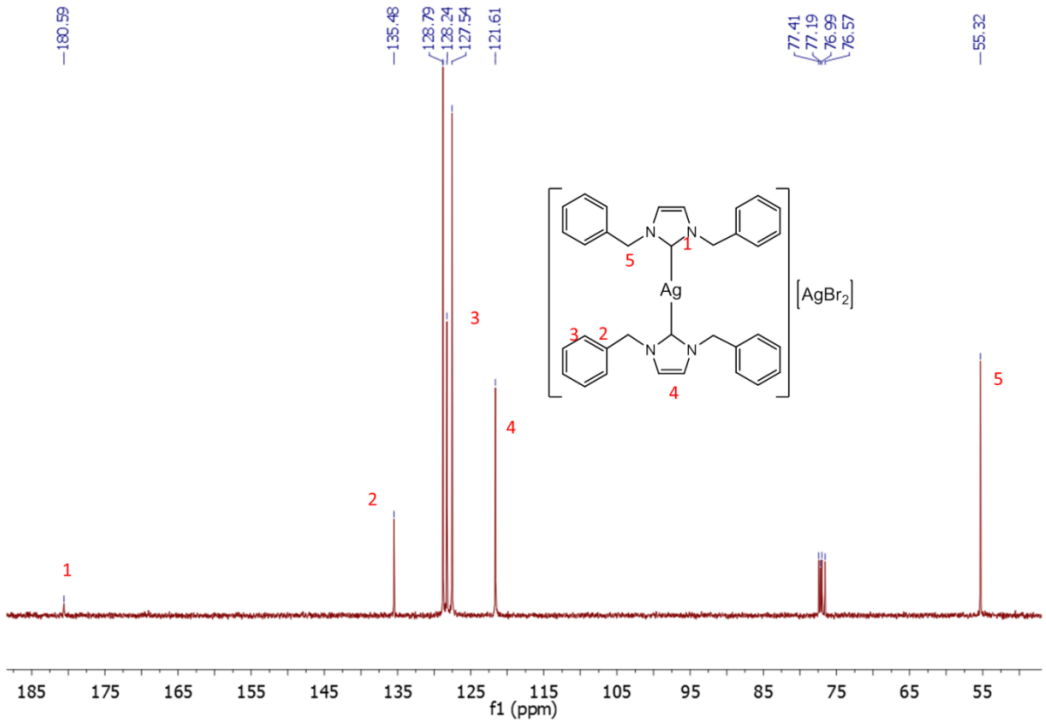

Figure 4.30 ^{13}C NMR spectrum of 2b.

4.12 Synthesis of 1-benzyl-3-trityl-imidazolin-2-ylidene silver bromide (2d).

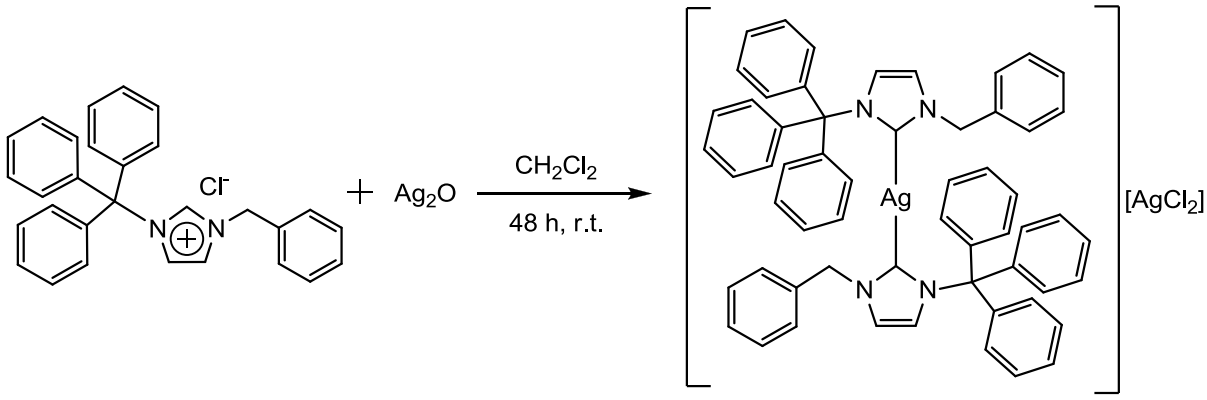

1d **2d**

To a solution of **1d**, (0.05 g, 0.17 mmol) in CH_2Cl_2 (ca. 10 mL) stirred in a Schlenk, Ag_2O (0.03 g, 0.11 mmol) was added. The reaction mixture was stirred for 48 h at room temperature; in the end of the reaction a colorless solution and a small amount of the black solid of Ag_2O was found in the Schlenk, which was subsequently filtered on Celite and after characterizing the crude material by NMR, it was instantaneously used for the preparation of the corresponding rhodium complex **3d**.

^{1}H NMR (300 MHz, $CDCl_3$): δ 7.34-7.21 (m, 20H, Ph), 7.03 (d, 1H, $J_{H,H}$ = 1.90 Hz, CH_{Im}), 6.91 (d, 1H, $J_{H,H}$ = 1.90 Hz, CH_{Im}), 5.25 (s, 2H, CH_2Ph).

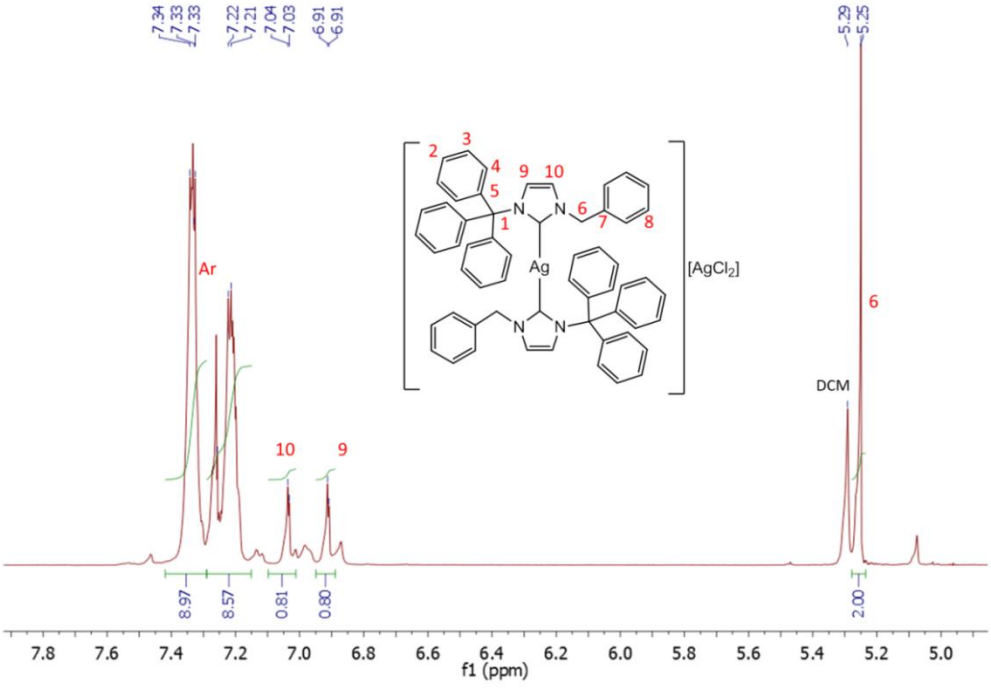

Figure 4.31 ^{1}H NMR spectrum of 2d.

^{13}C NMR (100 MHz, $CDCl_3$): δ 185 (d, J_{Ag-C} = 236 Hz, C-Ag), 141.91 (C_5), 135.36 (C_7), 129.84 (Ph), 128.90 (Ph), 128.42 (Ph), 128.18 (Ph), 127.76 (Ph), 127.68 (Ph), 127.55 (Ph), 126.99 (Ph), 123.82 (CH_{im}), 118.86 (CH_{im}), 77.75 (Cq_{Trit}), 56.81 (CH_2Ph).

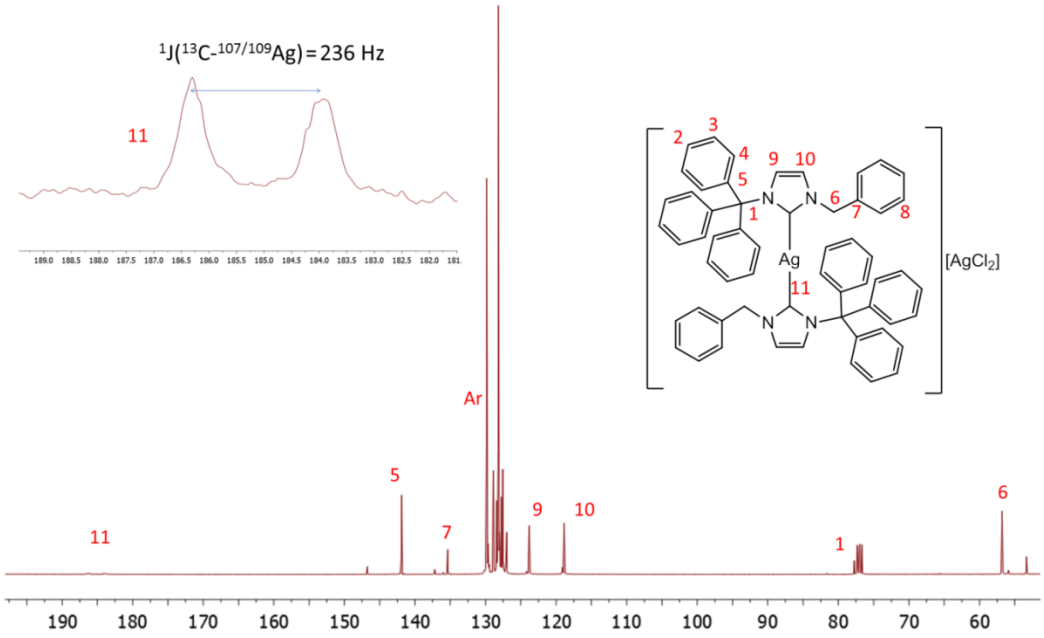

Figure 4.32 ^{13}C NMR spectrum of 2d with the inset showing the downfield doublet with the $^{1}J(^{13}C-^{107/109}Ag)$ = 236 Hz.

4.13 Synthesis of 1-benzyl-3-tert-butyl-imidazolin-2-ylidene silver bromide (2e)

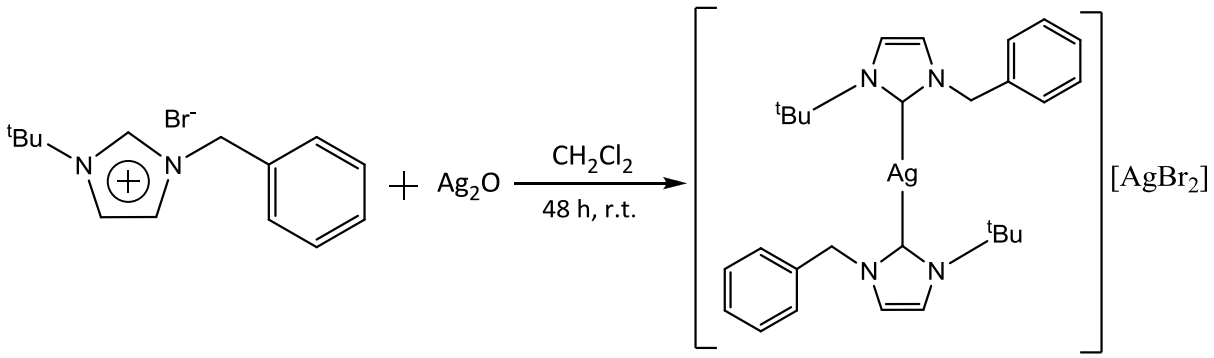

1e **2e**

To a solution of **1e**, (0.066 g, 0.22 mmol) in CH_2Cl_2 (5 mL) stirred in a Schlenk, (0.026 g, 0.11 mmol) of Ag_2O was added. The suspension was stirred for 48 h. In the end of the reaction, a colorless solution and a small amount of the black solid of Ag_2O was found in the Schlenk and a silver mirror on its walls. The solvent was removed under vacuum and deuterated chloroform was added for NMR analysis.

ESI-MS (MeOH, m/z): 537 (30) $[C_{28}H_{38}AgN_4]^+$; 321 (18) $[C_{14}H_{18}AgN_2]^+$. In the ESI-MS(-) spectrum, no peaks were observed.

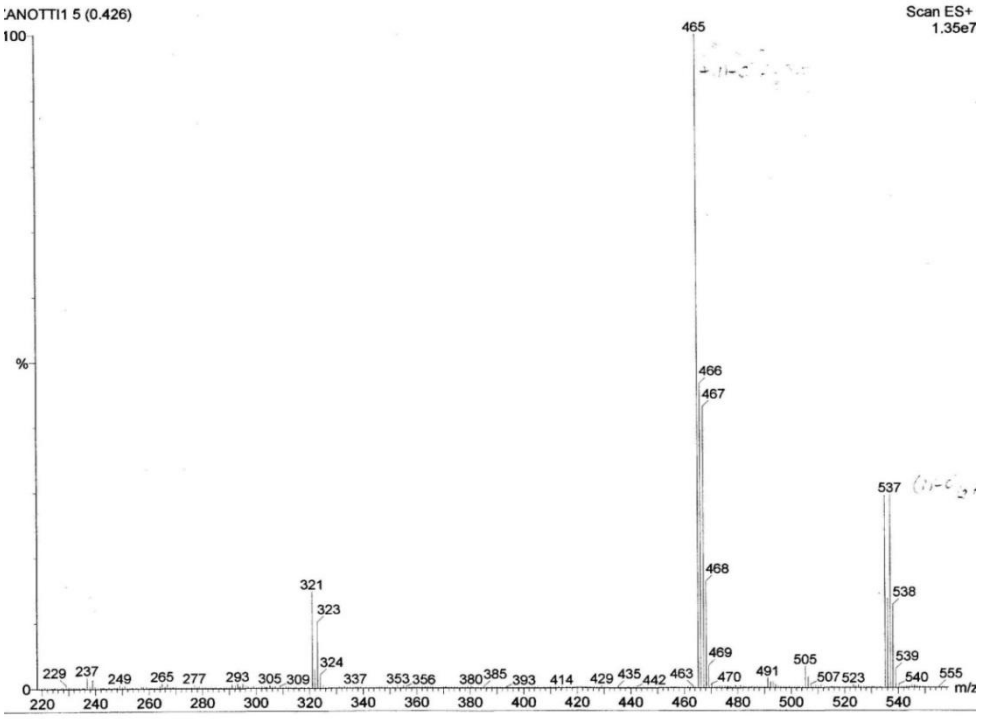

Figure 4.33 ESI-MS(+) spectrum of 2e.

^{1}H NMR (300 MHz, $CDCl_3$): δ 7.32 (m, 3H, Ph), 7.21 (m, 2H, Ph), 7.16 (d, 1H, $J_{H,H}$ = 1.88 Hz, CH_{im}), 6.90 (d, 1H, $J_{H,H}$ = 1.88 Hz, CH_{im}), 5.32 (s, 2H, CH_2Ph), 1.72 (s, 9H, ^{t}Bu).

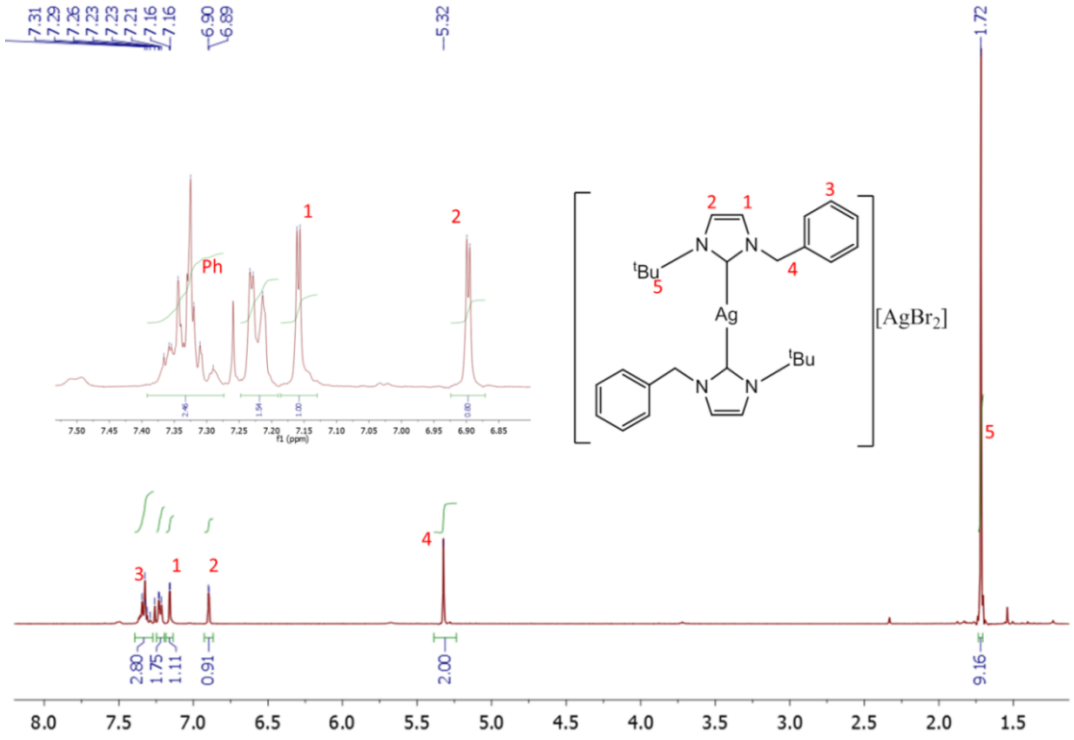

Figure 4.34 ^{1}H NMR spectrum of 2e with the inset showing the downfield doublet with the $^1J(^{13}C\text{-}^{107/109}Ag)$ = 236 Hz.

^{1}H NMR (400 MHz, DMSO-d_6): δ 7.62 (s, 1H, CH_{im}) 7.53 (s, 1H, CH_{im}), 7.42-7.30 (m, 5H, Ph), 5.35 (s, 2H, CH_2Ph), 1.64 (s, 9H, ^{t}Bu).

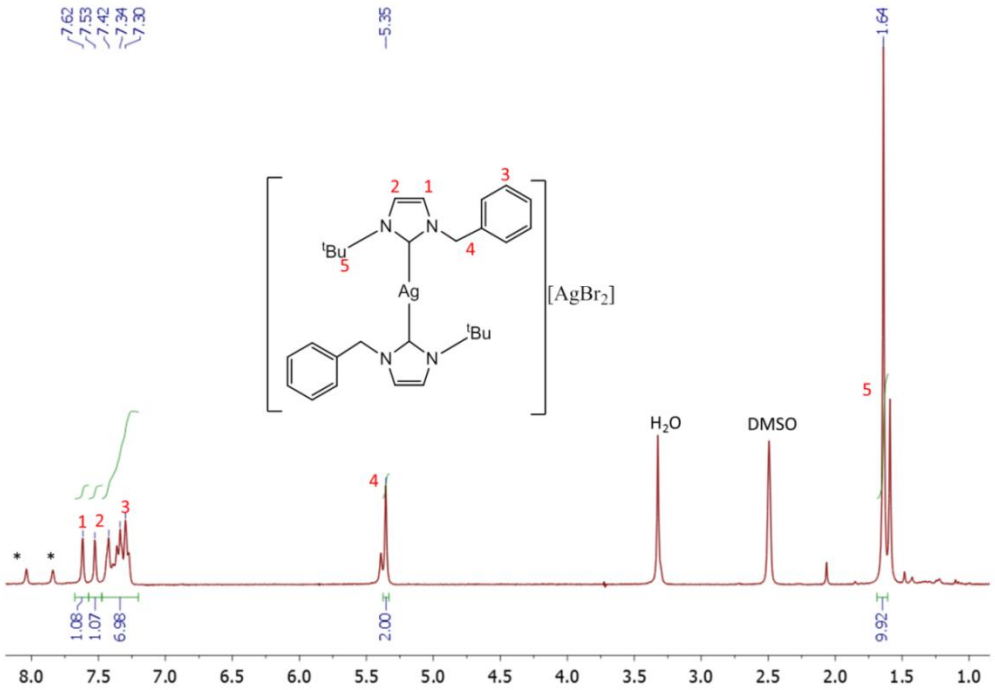

Figure 4.35 ^{1}H NMR spectrum of 2e (*impurities).

^{13}C NMR (100 MHz, CDCL$_3$): δ 178.24 (s, C-Ag), 135.41 (Cq, Ph), 129.04 (Ph), 128.58 (Ph), 127.76 (Ph), 119.35 (CH_{im}), 57.90 (Cq ^{t}Bu), 56.92 (CH_2Ph), 31.78 (^{t}Bu).

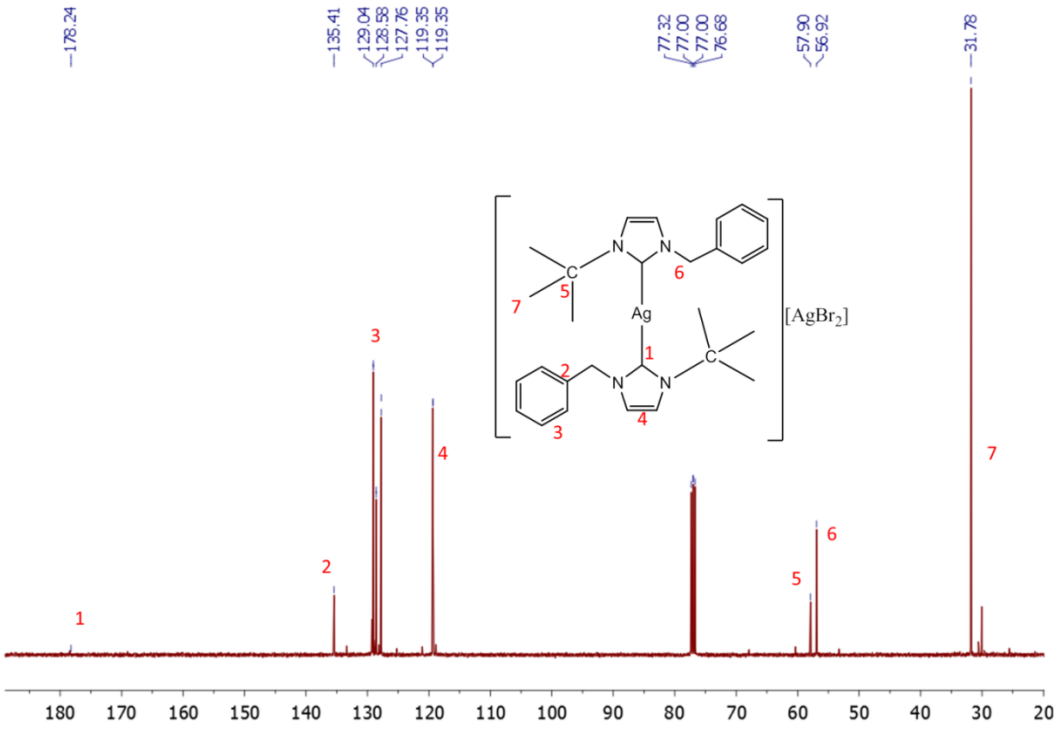

Figure 4.36 ^{13}C NMR spectrum of 2e.

4.14 Synthesis of [Rh(NBD)Cl{1-benzyl-3-methyl-imidazolin-2- ylidene}] (3a).

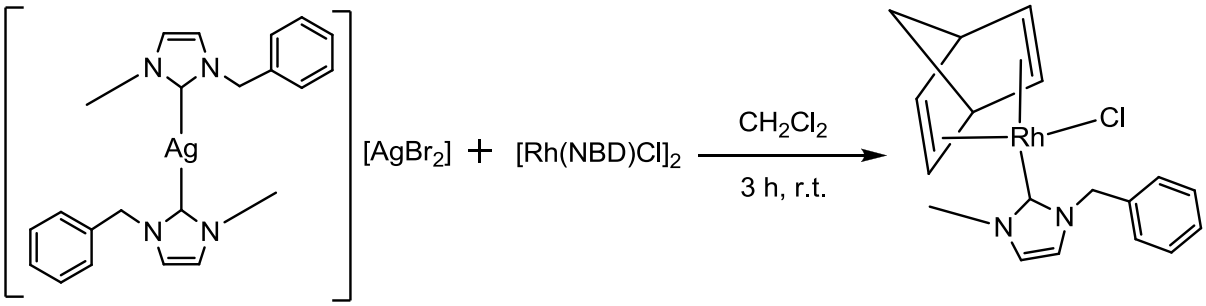

2a **3a**

The silver complex **2a** was prepared according to the procedure described in section: *Synthesis of 1-methyl-3-benzyl-imidazolin-2-ylidene silver bromide* and instantaneously used for a preparation of the rhodium(I) complex. The suspension of **2a** was filtered on Celite, and the filtrate was added to a solution of $[Rh(NBD)Cl]_2$ (0.12 g, 0.53 mmol) in CH_2Cl_2. After stirring for 3 h at room temperature, the pale yellow solid of AgBr was filtered off, and the solvent was removed under vacuum. The crude material was purified by column chromatography on silica gel using first CH_2Cl_2 and then CH_2Cl_2/MeOH [100:3 (v/v)] as eluent to afford 0.281 g (72 %) of **3a** as a yellow solid. Rf: 0.33 (CH_2Cl_2/MeOH, 100:3).

Anal. Calc.d for $C_{18}H_{20}ClN_2Rh$: C, 53.68; H, 5.01; Cl, 8.80; N, 6.96; Rh, 25.55. Found: C, 53.25; H, 5.30; Cl, 8.62; N,6.73; Rh, 25.38.

ESI-MS (MeOH, m/z): 367 (28) $[C_{18}H_{20}N_2Rh]^+$; 539 (100) $[C_{29}H_{32}N_4Rh]^+$;
In the ESI-MS(-) spectrum, no peaks were observed.

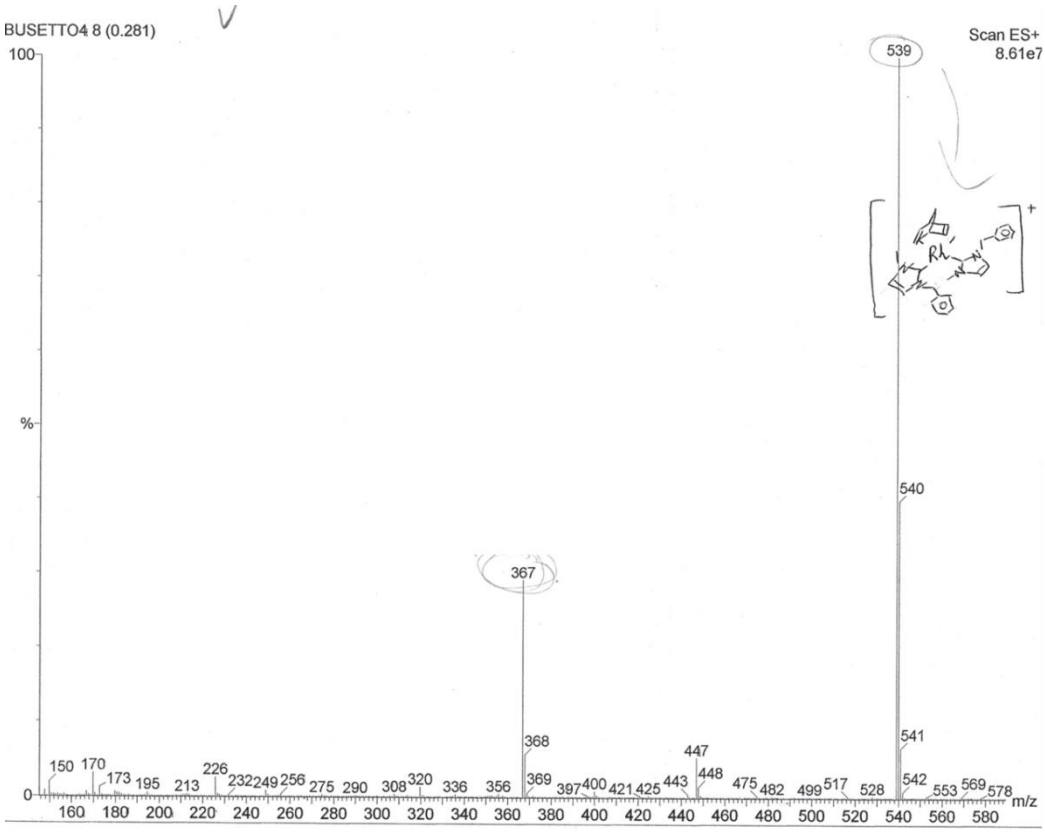

Figure 4.37 ESI-MS(+) spectrum of 3a.

^{1}H NMR (300 MHz, $CDCl_3$): δ 7.35 (m, 5H, Ph), 6.76 (s, 1H, CH_{im}), 6.65 (s, 1H, CH_{im}), 5.72 (s, 2H, CH_2Ph), 4.84 (s, 2H, CH_{NBD}), 4.08 (s, 3H, CH_3), 3.72 (s, 2H, CH_{NBD}), 3.36 (br s, 2H, CH_{NBD}), 1.30 (m, 2H, C^7H_2).

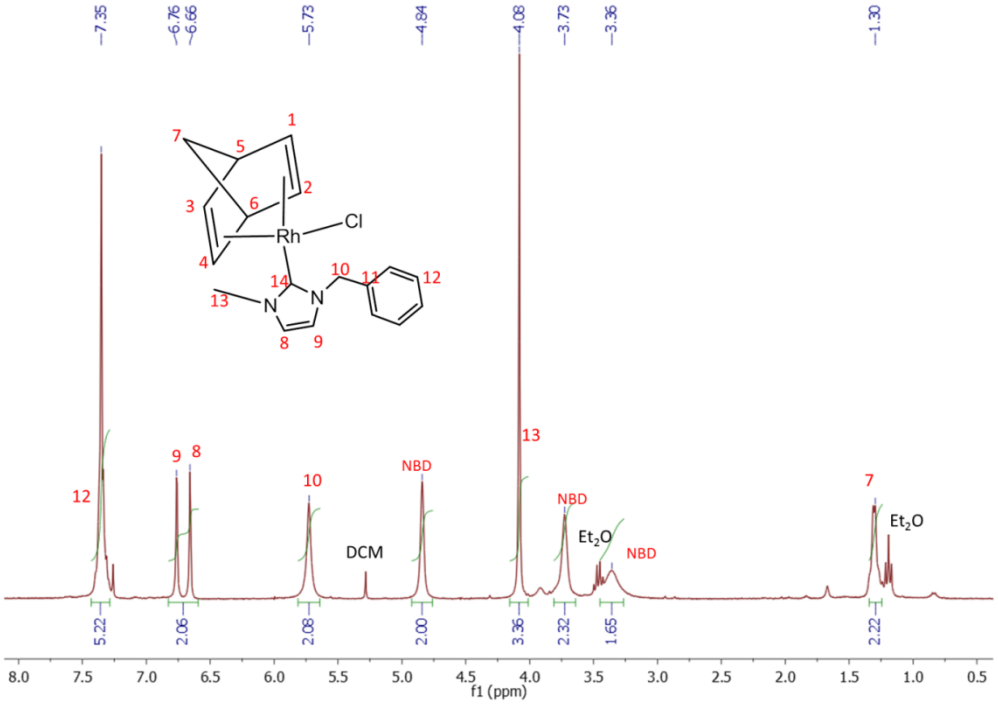

Figure 4.38 ^{1}H NMR spectrum of 3a.

^{13}C NMR (100 MHz, CDCL$_3$): δ 184.8 (d, $J_{C\text{-}Rh}$ = 57.82 Hz), 136.92 (Cq, Ph), 128.80 (Ph), 128.27 (Ph), 128.09 (Ph), 122.24 (CH_{im}), 120.72 (CH_{im}), 79.00 (d, J = 6,04 Hz, CH_{NBD}), 63.4 (d, J = 5.22 Hz, CH_{NBD}), 54.33 (CH_2Ph), 51.02 (d, J = 2.49 Hz, CH_{NBD}), 48.3 (d, J = 12.77 Hz, CH_{NBD}), 37.77 (CH_3).

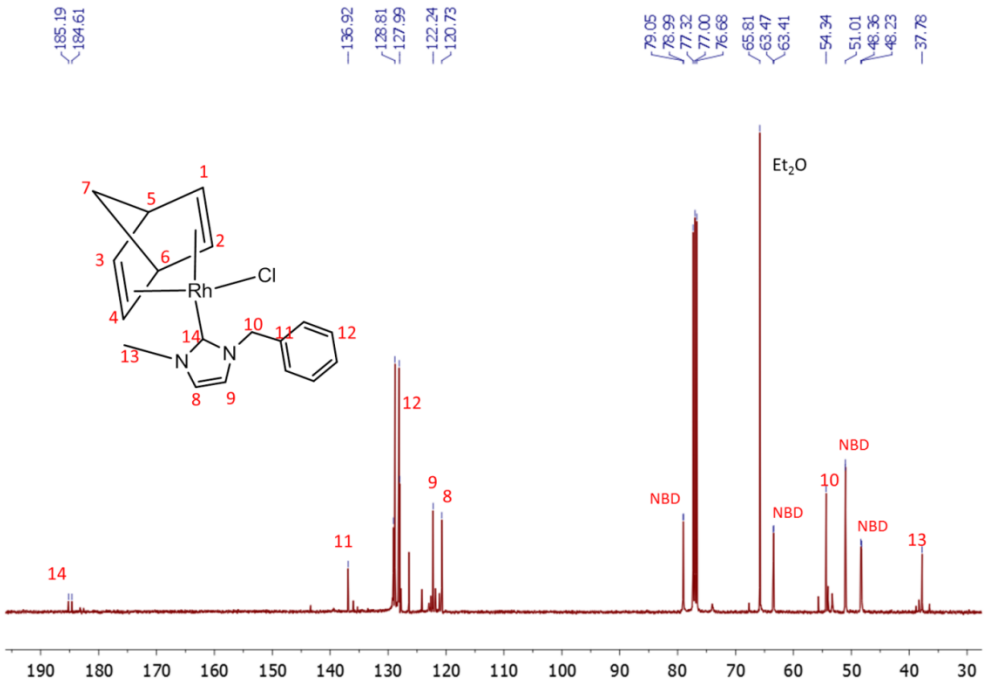

Figure 4.39 ^{13}C NMR spectrum of 3a.

4.15 Synthesis of [Rh(NBD)Cl{1,3-dibenzyl-imidazolin-2- ylidene}] (3b)

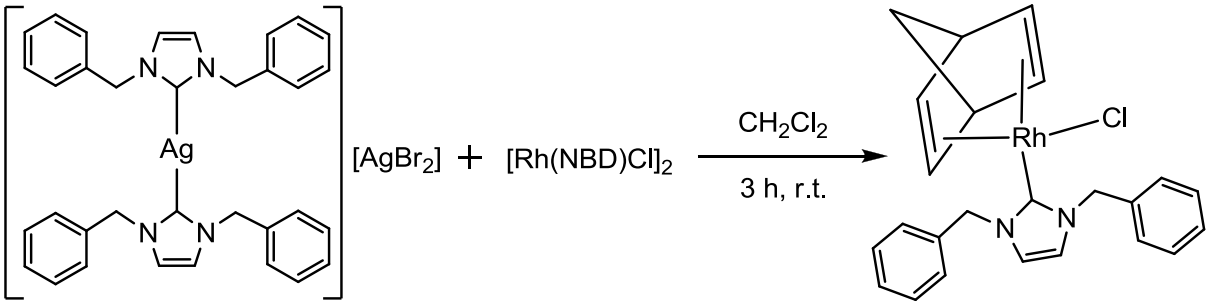

2b **3b**

Silver complex **2b** was prepared according to the procedure described in section: *Synthesis of 1,3-dibenzyl-imidazolin-2-ylidene silver bromide* and instantaneously used for a preparation of the rhodium(I) complex. The suspension of **2b** was filtered on Celite, and the filtrate was added to a solution of $[Rh(NBD)Cl]_2$ (0.14 g, 0.30 mmol) in CH_2Cl_2. After stirring for 3 h the pale yellow precipitate of AgBr was filtered off, and the solvent was removed under vacuum. The crude material was purified by column chromatography on silica gel using first CH_2Cl_2 and then CH_2Cl_2/MeOH [100:3 (v/v)] as eluent to afford 0.25 g (86%) of **3b** as a yellow solid. Rf: 0.45 (CH_2Cl_2/MeOH, 100:3).

Anal. Calc.d for $C_{24}H_{24}ClN_2Rh$: C, 60.20; H, 5.05; Cl, 7.40; N, 5.85; Rh, 21.49. Found: C, 59.75; H, 5.32; Cl, 8.62; N,6.73, Rh, 21.26.

ESI-MS (MeOH, m/z): 443 (100) $[C_{24}H_{24}N_2Rh]^+$.
In the ESI-MS(-) spectrum, no peaks were observed.

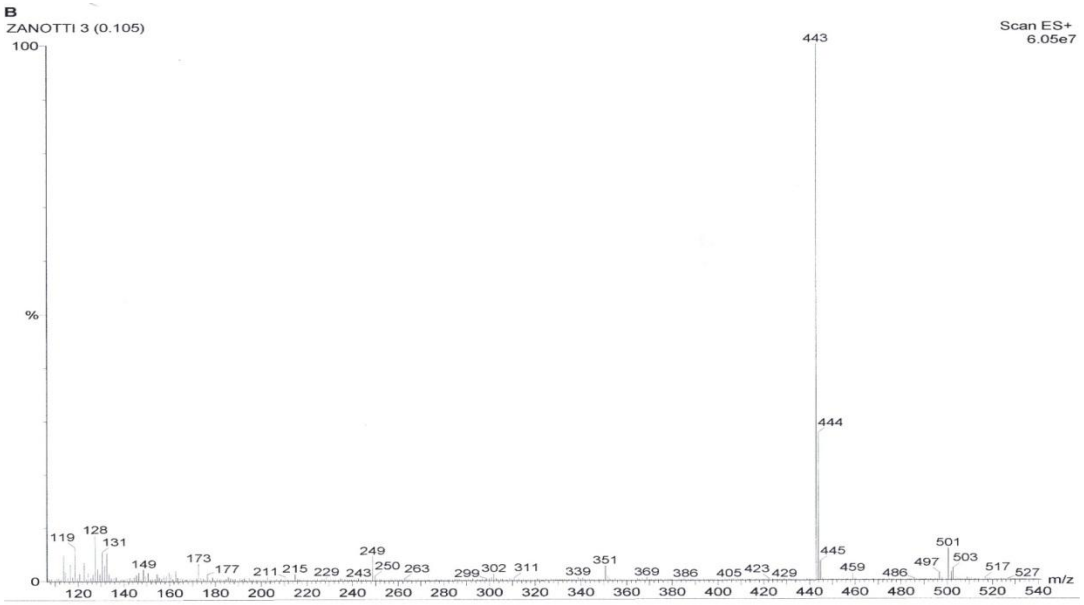

Figure 4.40 ESI-MS(+) spectrum of 3b.

^{1}H NMR (300 MHz, $CDCl_3$): δ 7.31 (m, 10H, Ph), 6.61 (s, 2H, CH_{im}), 5.73 (br s, 4H, CH_2Ph), 4.78 (s, 2H, CH_{NBD}), 3.60 (s, 2H, CH_{NBD}), 3.20 (d, 2H, $J_{H,H}$ = 1.9 Hz, CH_{NBD}), 1.20 (br d, 2H, $J_{H,H}$ = 1.4 Hz, C^7H_2).

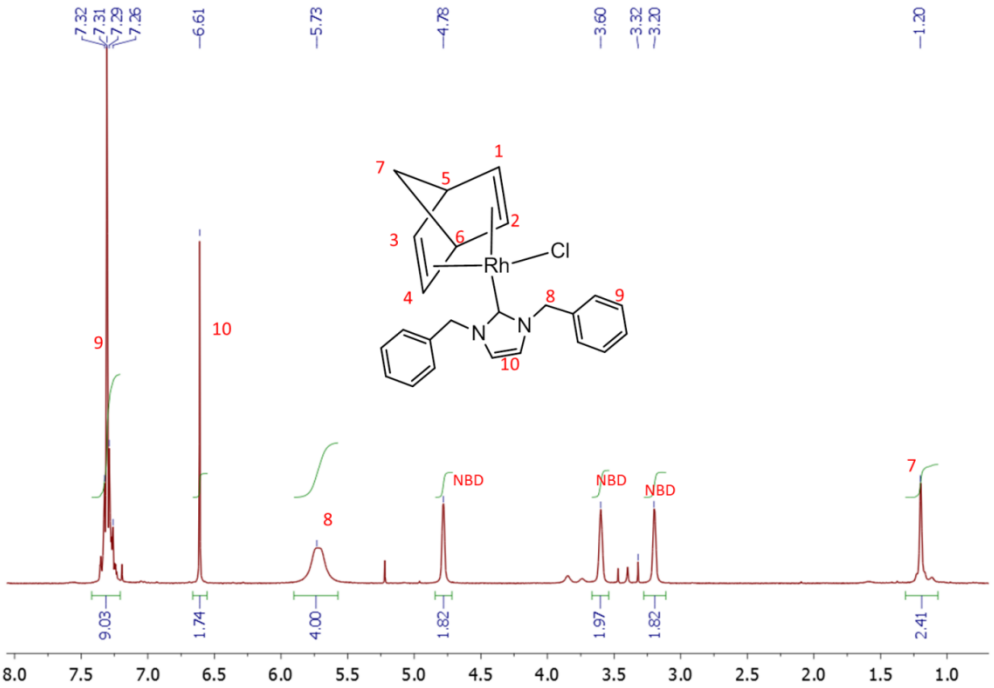

Figure 4.41 ^{1}H NMR spectrum of 3b.

^{13}C NMR (100 MHz, $CDCl_3$): δ 185.45 (d, $J_{C\text{-}Rh}$ = 76.8 Hz), 136.87 (Cq, Ph), 128.86 (Ph), 128.61 (Ph), 128.03 (Ph), 121.08 (CH_{im}), 120.72 (CH_{im}), 79.11 (d, J = 5.7 Hz, CH_{NBD}), 63.30 (d, J = 5.3 Hz, C^7H_2), 54.55 (CH_2Ph), 51.01 (d, J = 2.0 Hz, CH_{NBD}), 48.5 (d, J = 17 Hz, CH_{NBD}). (overnight)

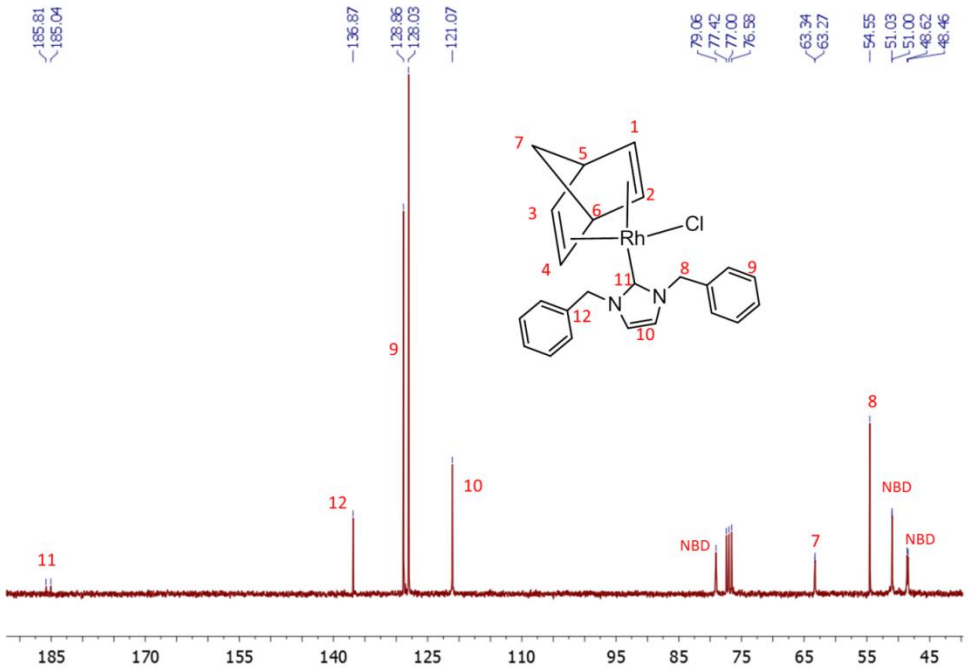

Figure 4.42 ^{13}C NMR spectrum of 3b.

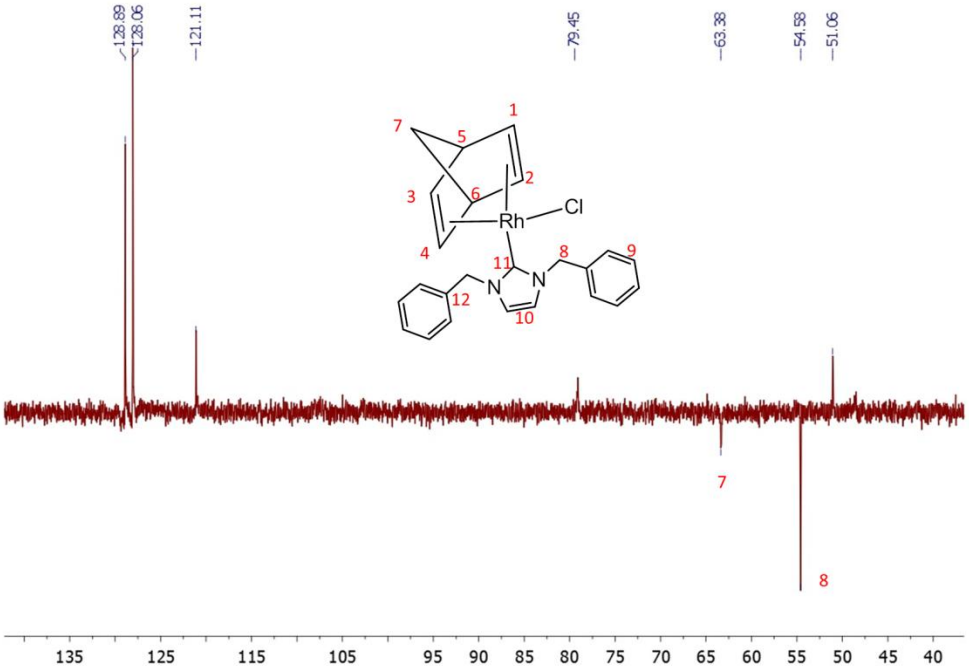

Figure 4.43 DEPT-135 spectrum of 3b.

4.16 Synthesis of [Rh(NBD)Cl{1-benzyl-3-trityl-imidazolin-2-ylidene}] (3d)

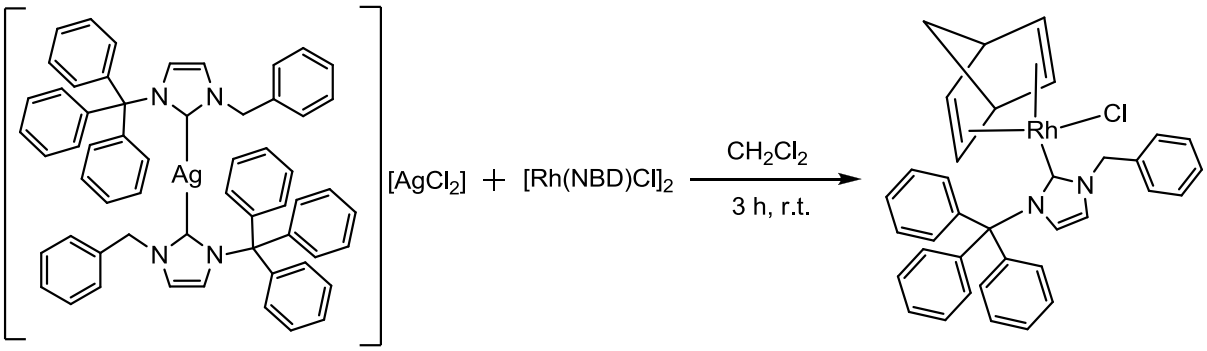

2d **3d**

Silver complex **2c** was prepared according to the procedure described in section: *Synthesis of 1-benzyl-3-trityl-imidazolin-2-ylidene silver bromide* and instantaneously used for a preparation of the rhodium(I) complex. The suspension of **2c** was filtered on Celite, and the filtrate was added to a solution of $[Rh(NBD)Cl]_2$ (0.04 g, 0.17 mmol) in CH_2Cl_2. After stirring for 3 h the white AgCl was filtered off, and the solvent was removed under vacuum. The crude material was purified by column chromatography on silica gel treated with 5% v/v triethylamine in diethyl ether, using diethyl ether/CH_2Cl_2, 1:1 v/v, to afford 0.07 g (66 %) of **3d** as a yellow solid. Rf: 0.55 (Et_2O/CH_2Cl_2, 50:50)

ESI-MS (MeOH, m/z): 595 (100) $[C_{36}H_{32}N_2Rh]^+$.

In the ESI-MS(-) spectrum, no peaks were observed.

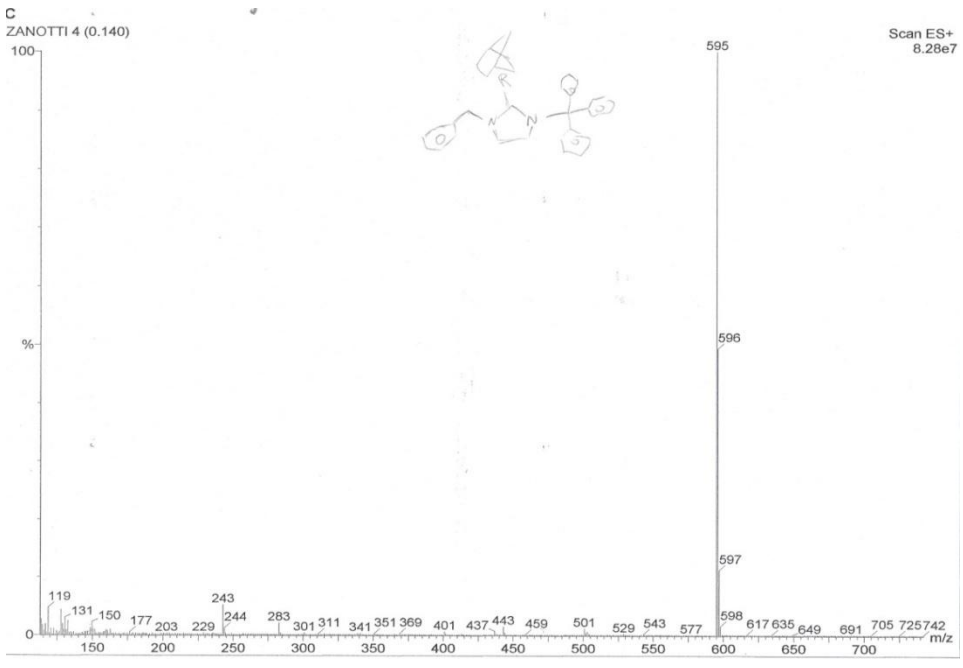

Figure 4.44 ESI-MS(+) spectrum of 3d.

Anal. Calc.d for $C_{36}H_{32}ClN_2Rh$: C, 68.52; H, 5.11; Cl, 5.62; N, 4.44; Rh, 16.31. Found: C, 68.39; H, 4.94; Cl, 5.36; N, 4.22; Rh, 16.25.

^{1}H NMR (300 MHz, $CDCl_3$): δ 7.45 – 7.24 (m, 20H, Ph), 6.84 (d, 1H, $J_{H,H}$ = 15.06 Hz, CH_2Ph), 6.76 (d, 1H, $J_{H,H}$ = 2.06 Hz, CH_{Im}), 6.56 (d, 1H, $J_{H,H}$ = 1.97 Hz, CH_{Im}), 6.17 (d, 1H, $J_{H,H}$ = 14.79 Hz, CH_2Ph), 4.61 (br s, 1H, CH_{NBD}), 3.59 (br s, 1H, CH_{NBD}), 3.44 (br s, 1H, CH_{NBD}), 3.10 (br s, 1H, CH_{NBD}), 2.87 (br s, 1H, CH_{NBD}), 1.94 (br s, 1H, CH_{NBD}), 0.87 (m, 2H, C^7H_2).

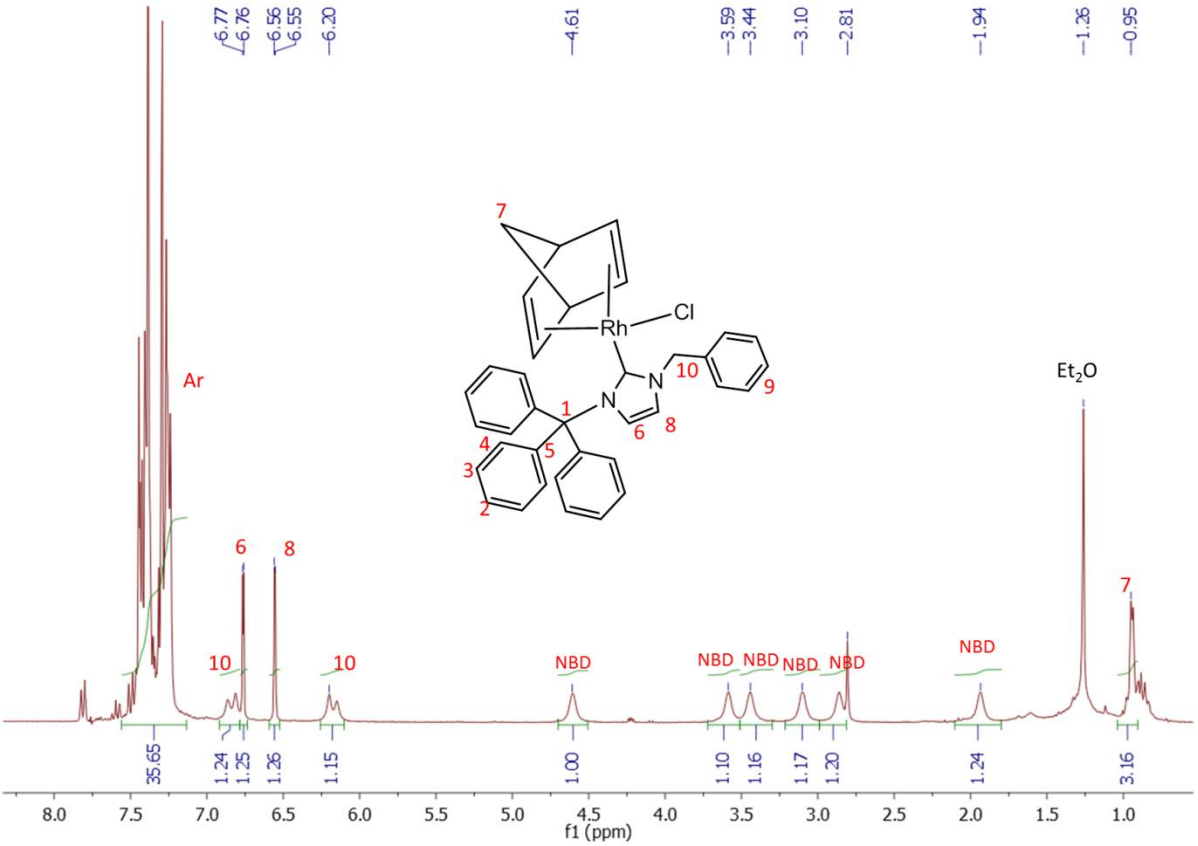

Figure 4.45 ^{1}H NMR spectrum of 3d.

^{13}C NMR (100 MHz, $CDCl_3$): δ 186.57 (d, $J_{C\text{-}Rh}$= 55 Hz), 142.39 (C_5), 137.51 (C_{12}), 129.07 (Ph), 128.86 (Ph), 128.26 (Ph), 128.09 (Ph), 127.91 (Ph), 127.53 (Ph), 127.24 (Ph), 124.29 (CH_{im}), 120.70 (CH_{im}), 82.01 ($Cq_{trityl\ hydroxide}$), 76.58 (Cq_{Trit}), 73.13 (s, CH_{NBD}), 61.82 (d, C^7H_2, $J_{H,H}$ = 5.8 Hz), 57.23 (CH_2Ph), 49.72 (CH_{NBD}), 49.01 (CH_{NBD}), 45.72 (d, C_{NBD}, $J_{H,H}$ = 13 Hz), 44.74 (d, CH_{NBD}, $J_{H,H}$ = 10.8 Hz), (overnight).

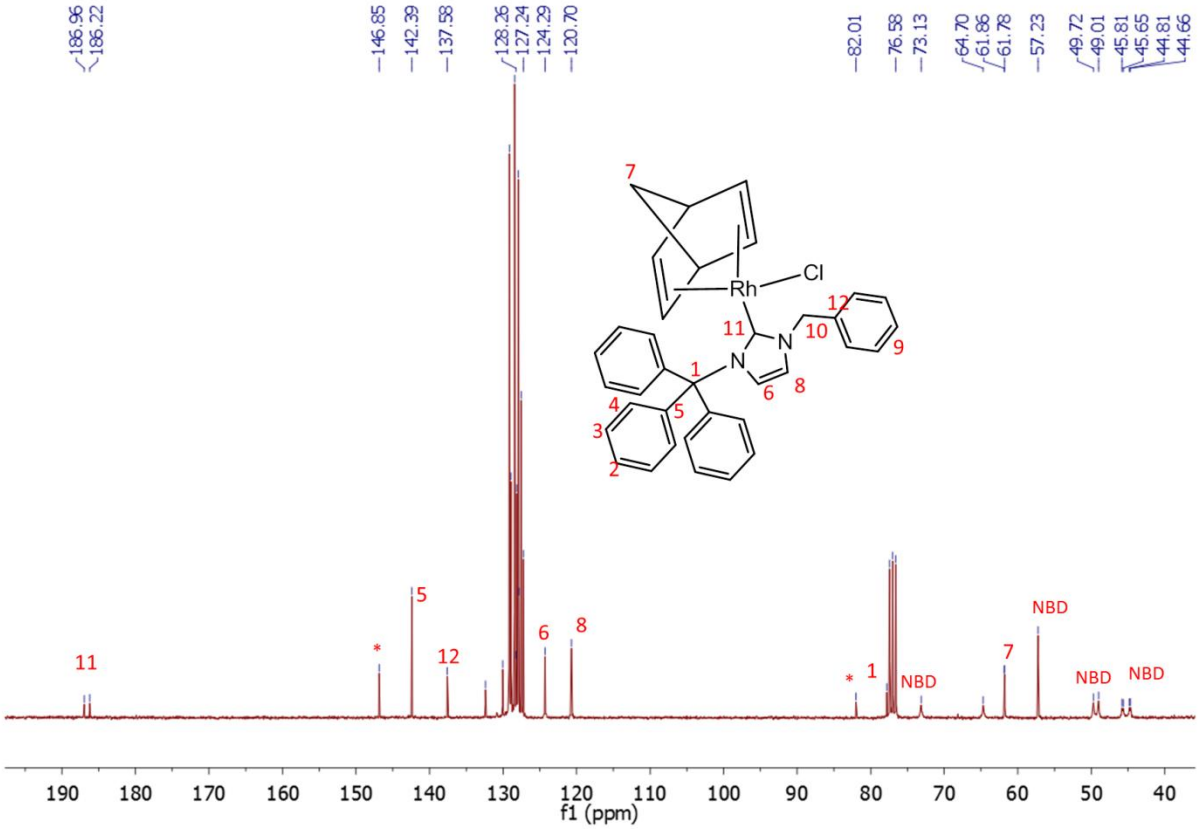

*trityl hydroxide

Figure 4.46 ^{13}C NMR spectrum of 3d.

4.17 Synthesis of [Rh(NBD)Cl{1-benzyl-3-tert-butyl-imidazolin-2- ylidene}] (3e)

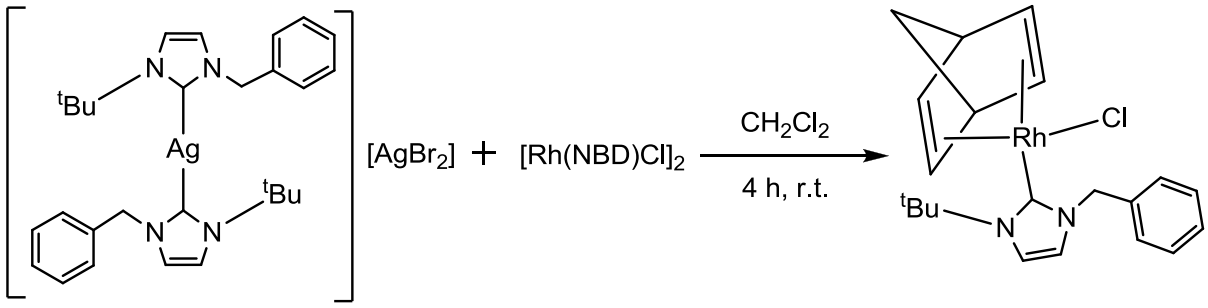

2e **3e**

Silver complex **2e** was prepared according to the procedure described in section: *Synthesis of 1-benzyl-3-tert-butyl-imidazolin-2-ylidene silver bromide* and instantaneously used for a preparation of the rhodium (I) complex. The suspension of **2e** was filtered in Pasteur plug (cotton + celite), and the filtrate was added to a solution of $[Rh(NBD)Cl]_2$ (0.025 g, 0.05 mmol) in CH_2Cl_2. After stirring for 4 h the white AgBr was filtered off, and the solvent was

removed under vacuum. The resulting yellow solid of **3e** was dissolved in deuterated dimethyl sulfoxide with a few drops of deuterated chloroform and analysed by NMR.

Anal. Calc.d for $C_{21}H_{26}ClN_2Rh$: C, 56.70; H, 5.89; Cl, 7.97; N, 6.30; Rh, 23.14. Found: C, 56.51; H, 5.57; Cl, 8.12; N, 6.03, Rh, 22.92.

^{1}H NMR (600 MHz, $CDCl_3$): δ 7.46 – 7.45 (m, 4H, Ph), 7.41 – 7.39 (m, 1H, Ph), 7.06 (d, 1H, $J_{H,H}$ = 1.97 Hz, CH_{im}), 6.72 (d, 1H, $J_{H,H}$ = 2.03 Hz, CH_{Im}), 6.41 (d, 1H, $J_{H,H}$ = 15.09 Hz, CH_2Ph), 6.27 (d, 1H, $J_{H,H}$ = 15.09 Hz, CH_2Ph), 4.84 (m, 1H, CH_{NBD}), 4.70 (m, 1H, CH_{NBD}), 3.81 (br s, 1H, CH_{NBD}), 3.78 (br s, 1H, CH_{NBD}), 3.47 (m, 2H, CH_{NBD}), 2.08 (s, 9H, ^{t}Bu), 1.36 (d, 1H, C^7H_2, $J_{H,H}$ = 8.00 Hz), 1.31 (d, 1H, C^7H_2, $J_{H,H}$ = 7.99 Hz).

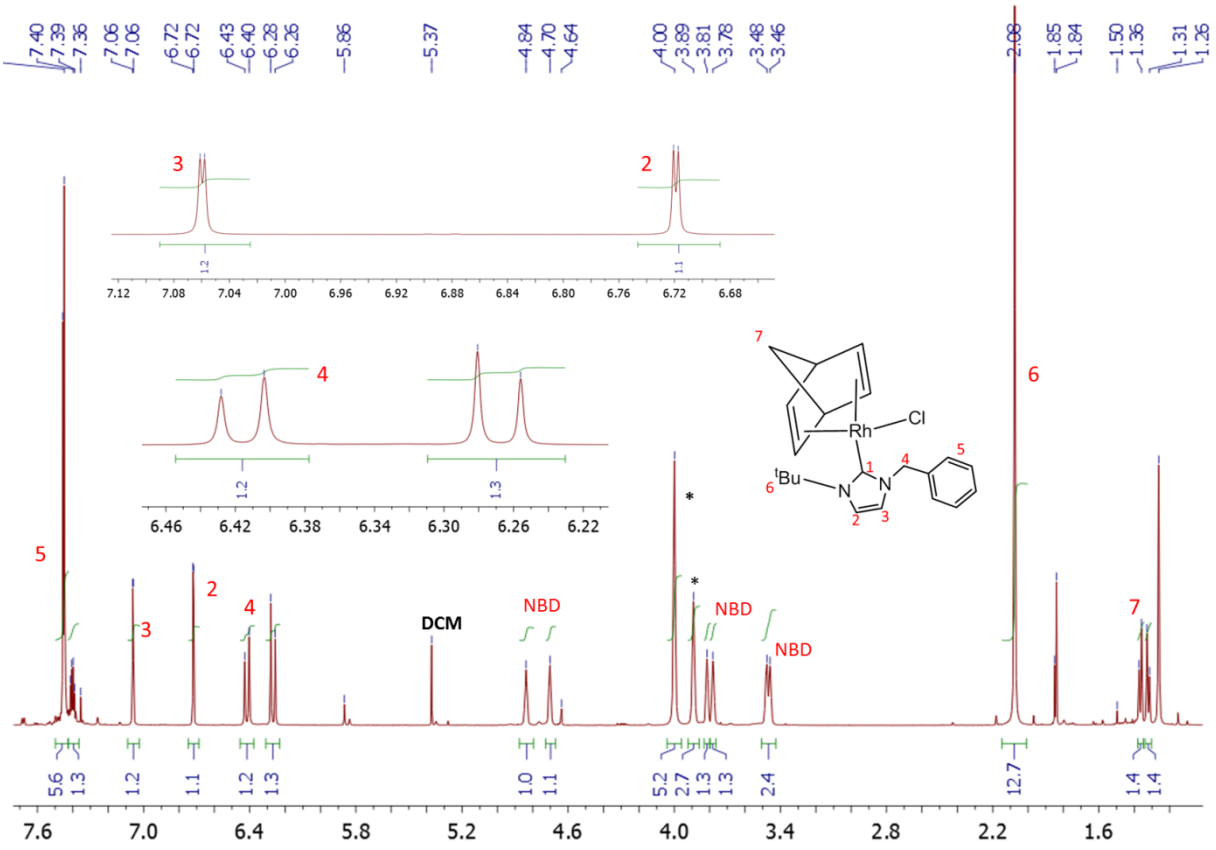

Figure 4.47 ^{1}H NMR spectrum of 3e.

^{13}C NMR (600 MHz, $CDCl_3$): δ 183.0 (d, $J_{C\text{-}Rh}$= 58.5 Hz), 136.9 (Cq,Ph), 128.7 (Ph), 128.0 (Ph), 127.8 (Ph), 119.7 (CH_{im}), 119.6 (CH_{im}), 74.9 (d, C_{NBD}, $J_{H,H}$ = 6.1 Hz), 71.8 (d, C_{NBD}, $J_{H,H}$ = 6.3 Hz), 62.7 (d, C^7H_2, $J_{H,H}$ = 5.2 Hz), 57.9 (s, C_{NBD}), 56.3 (CH_2Ph), 50.3 (dd, C_{NBD}, $J_{H,H}$ = 2.5 Hz, $J_{H,H}$ = 7.0 Hz), 48.1 (d, C_{NBD}, $J_{H,H}$ = 13.0 Hz), 46.2 (d, CH_{NBD}, $J_{H,H}$ = 12.2 Hz), 32.1 (^{t}Bu).

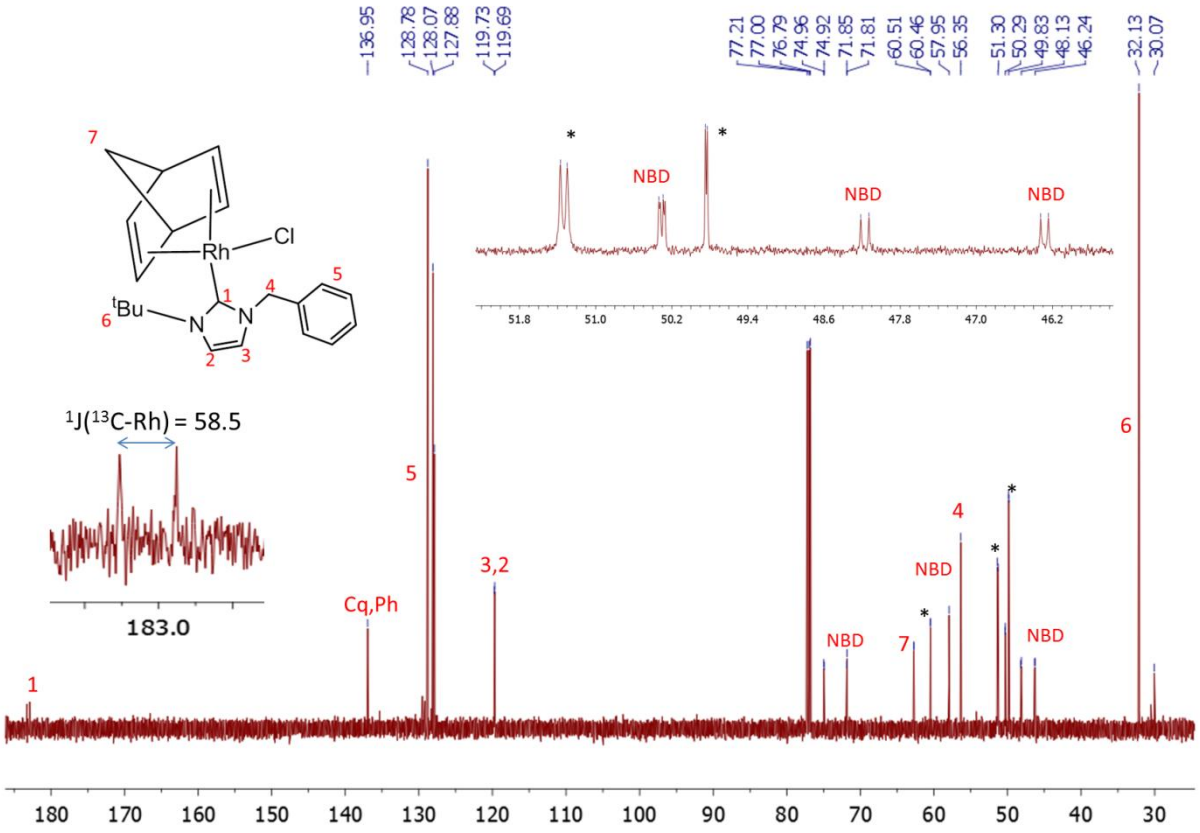

Figure 4.48 ^{13}C NMR spectrum of 3d.

4.18 Synthesis of [FeCp(CO)2{1-benzyl-3-methyl-imidazolin-2-ylidene}]I

The iron complexes were synthesized using a literature method[27].

a) To a suspension of imidazolium salt **1a** (0.107 g, 4.20 mmol) in dry THF (0.5 mL), KO^{t}Bu (1.2 eq, 0.057 g, 5.08 mmol) was added and the mixture was sonicated at 35°C for 15 min; Then the solution was poured to a solution of [FeI(Cp)(CO)$_2$] (0.9 eq., 0.115 g, 3.78 mmol) in 1.3 mL of dry toluene. After 3h the formed precipitate was separated from the solvent by a filtration, washed once with dry toluene (1mL), and then extracted with dry DCM (2 x 2 mL). The solvent was evaporated in vacuum affording the crude product: [FeCp(CO)$_2${1-methyl-3-benzyl-imidazolin-2-ylidene}]I.

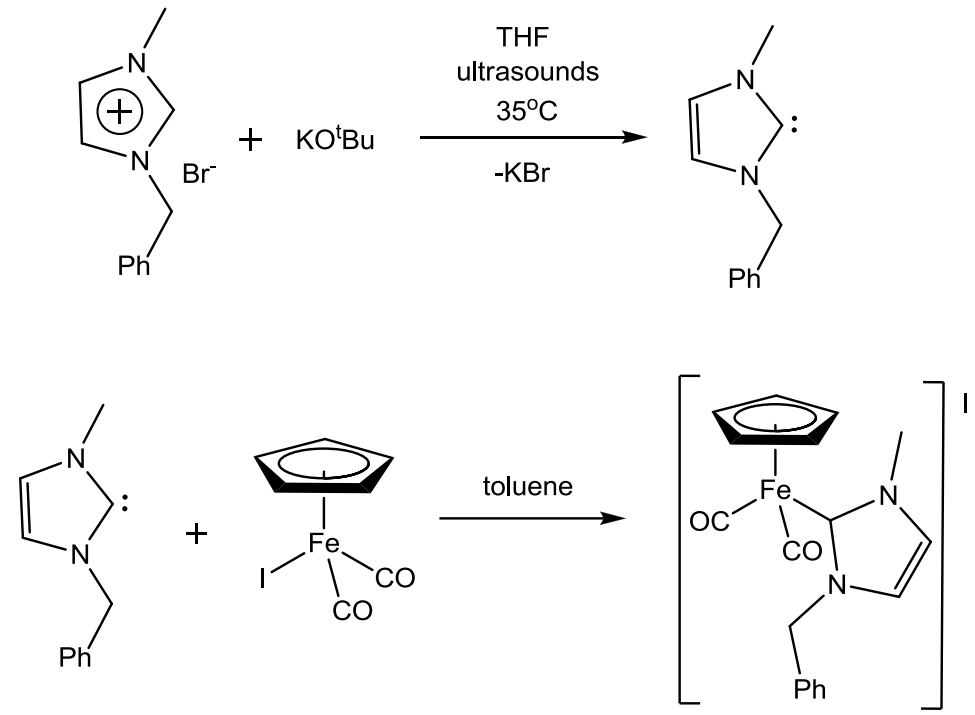

IR (CH_2Cl_2 cm^{-1}): 2047 (νCO), 2000 (νCO).

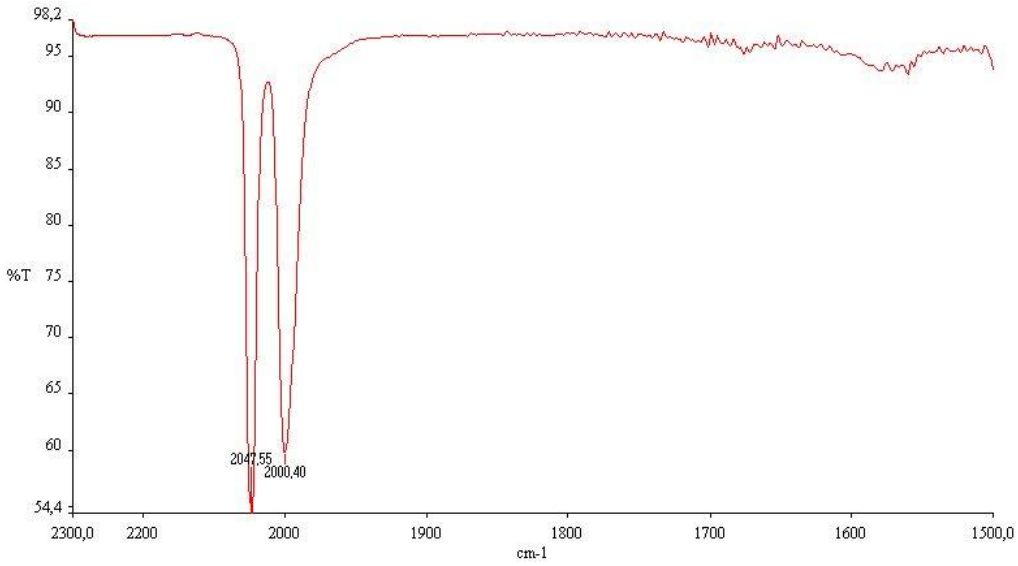

Figure 4.49 IR spectrum of [$FeCp(CO)_2${1-methyl-3-benzyl-imidazolin-2-ylidene}]I.

^{1}H NMR (300 MHz, $CDCl_3$): δ 7.43-7.19 (5H, Ph), 7.12 (2H, CH_{im}), 5.48 (2H, CH_2Ph), 5.39 (5H, Cp), 4.03 (3H, CH_3).

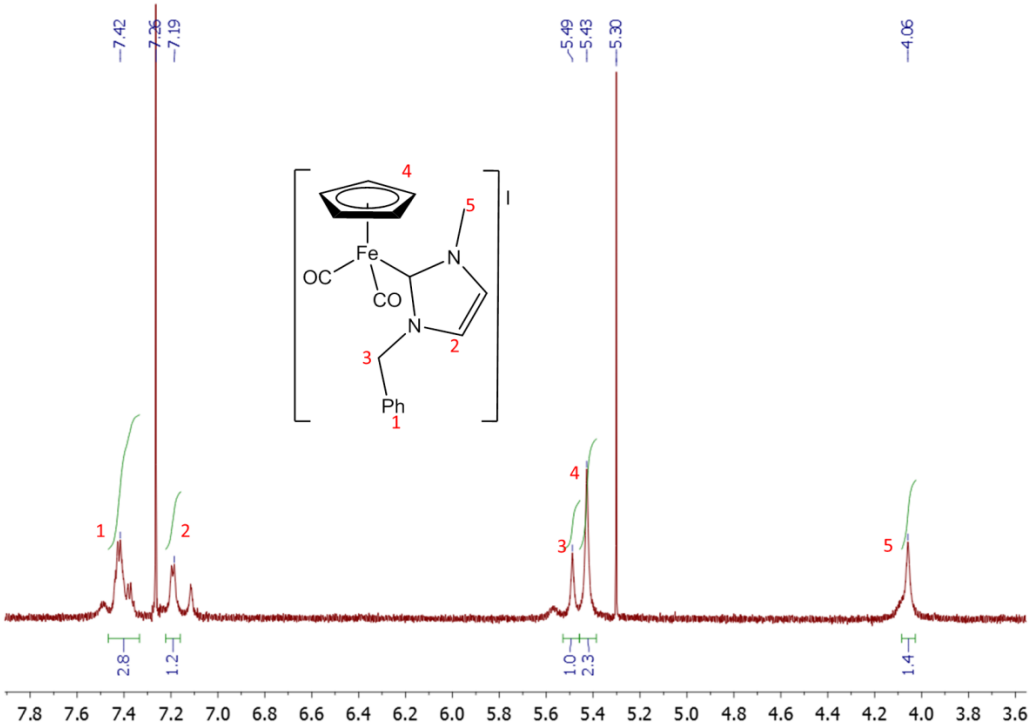

Figure 4.50 ^{1}H NMR spectrum of [$FeCp(CO)_2${1-methyl-3-benzyl-imidazolin-2-ylidene}]I.

^{13}C NMR (75 MHz, $CDCl_3$): δ 211.3 (2xCO), 164.4 (C-Fe), 134.6 (Cq), 129.6 (Ph), 129.4 (Ph), 128.8 (Ph), 127.9 (CH_{im})127.3 (CH_{im}), 87.6 (Cp), 55.8 (CH_2Ph), 41.3 (CH_3).

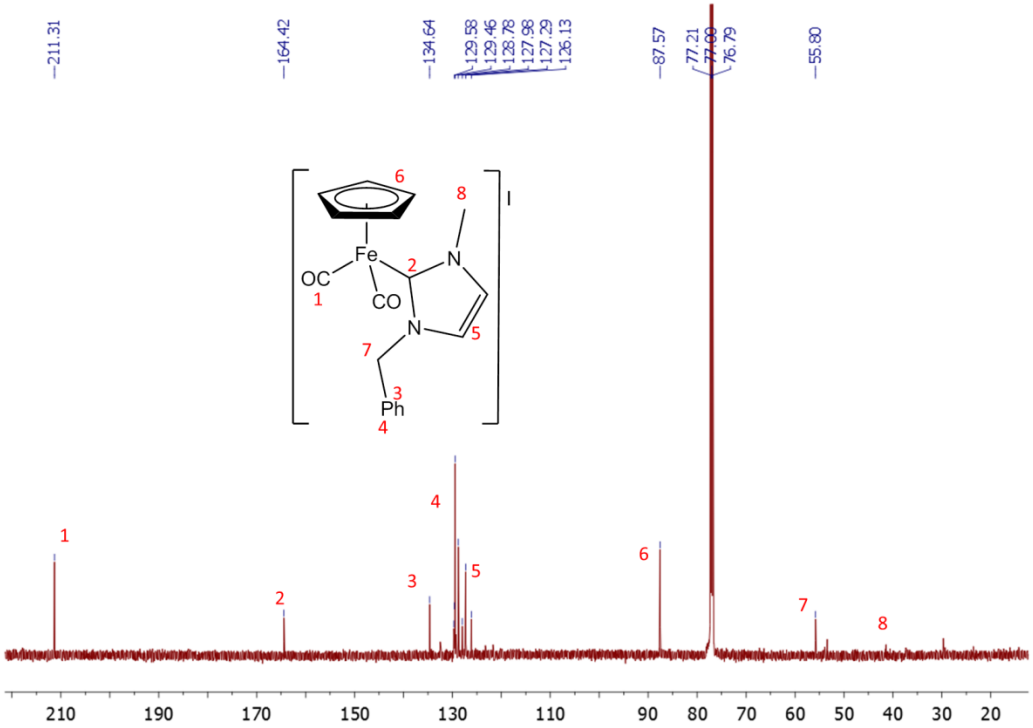

Figure 4.51 ^{13}C NMR spectrum of [$FeCp(CO)_2${1-methyl-3-benzyl-imidazolin-2-ylidene}]I.

b) The imidazolium salt **1a** (0.100 g, 0.39 mmol) and the iron precursor $FeI(CO)_2Cp$ (0.120 g, 0.39 mmol) were placed in a Schlenk and dissolved in DMSO-d_6 with the aid of ultrasounds. The complete dissolution of the two solid compounds was reached after 10 min and subsequently a small excess (1.1 eq., 0.048 g, 0.43 mmol) of a base KO^tBu was added. After the addition, ultrasounds were applied for next 10 min to afford brown oil in a bottom of the Schlenk identified by IR as the desired product [$Fe(CO)_2Cp${1-methyl-3-benzyl-imidazolin-2-ylidene}]I. The solvent above the oil was decanted and 10 ml of diethyl ether was added. After one week the solvent was removed in vacuum and the resulting solid was dissolved in deuterated chloroform for NMR analysis.

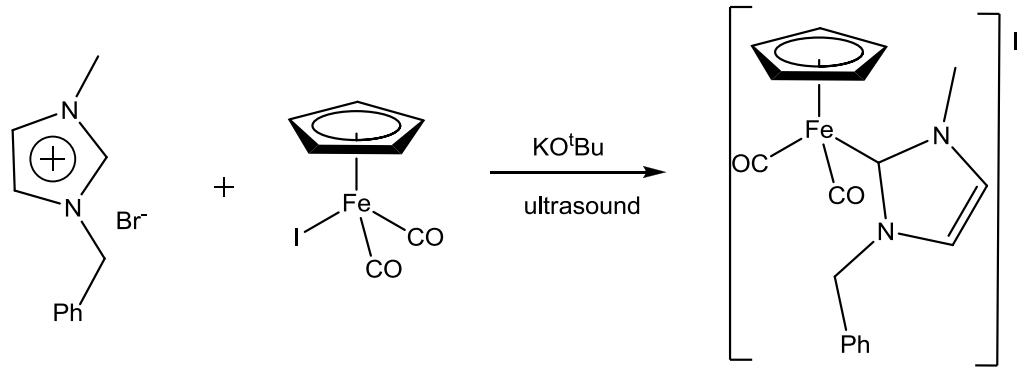

^{1}H NMR (300 MHz, $CDCl_3$): δ 7.53 (3H, Ph), 7.33-7.30 (2H, Ph), 7.09-7.08 (2H, CH_{im}), 5.44 (2H, CH_2Ph), 5.31 (5H, Cp), 3.95 (3H, CH_3).

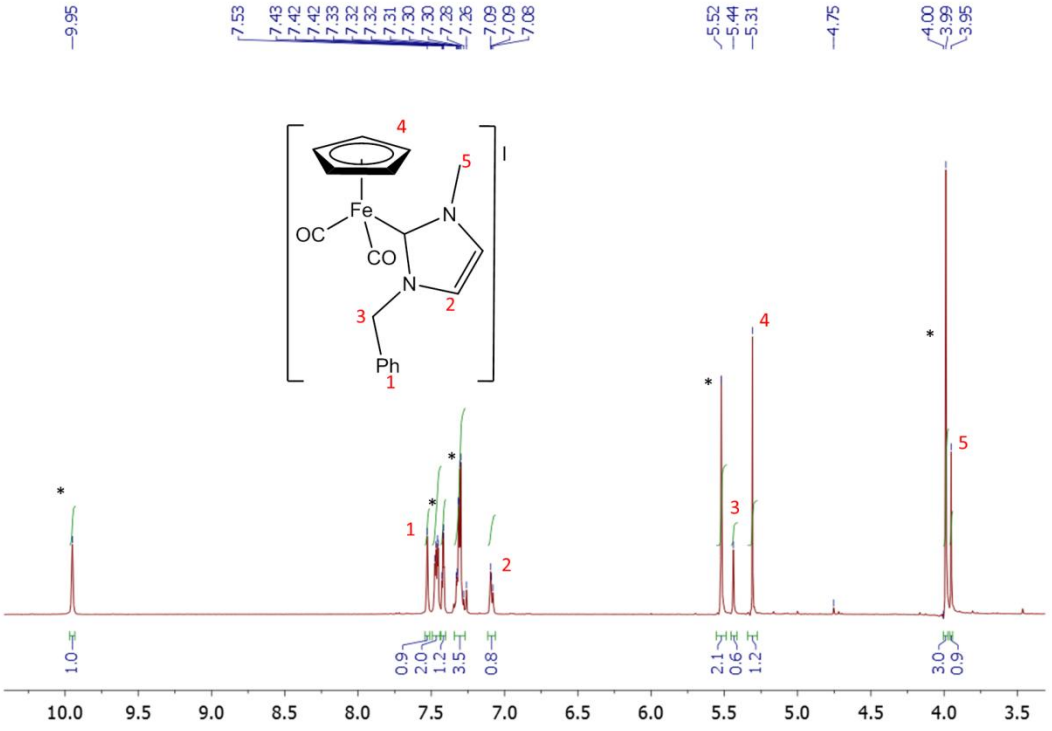

* Traces of **1a**.

Figure 4.52 ^{1}H NMR spectrum of [FeCp(CO)2{1-methyl-3-benzyl-imidazolin-2-ylidene}]I.

^{13}C NMR (75 MHz, $CDCl_3$): δ 210.9 (2xCO), 164.9 (C-Fe), 134.6 (Cq), 129.3-126.9 (Ph) 127.4 (CH_{im}), 125.8 (CH_{im}), 87.0 (Cp), 55.4 (CH_2Ph), 40.8 (CH_3).

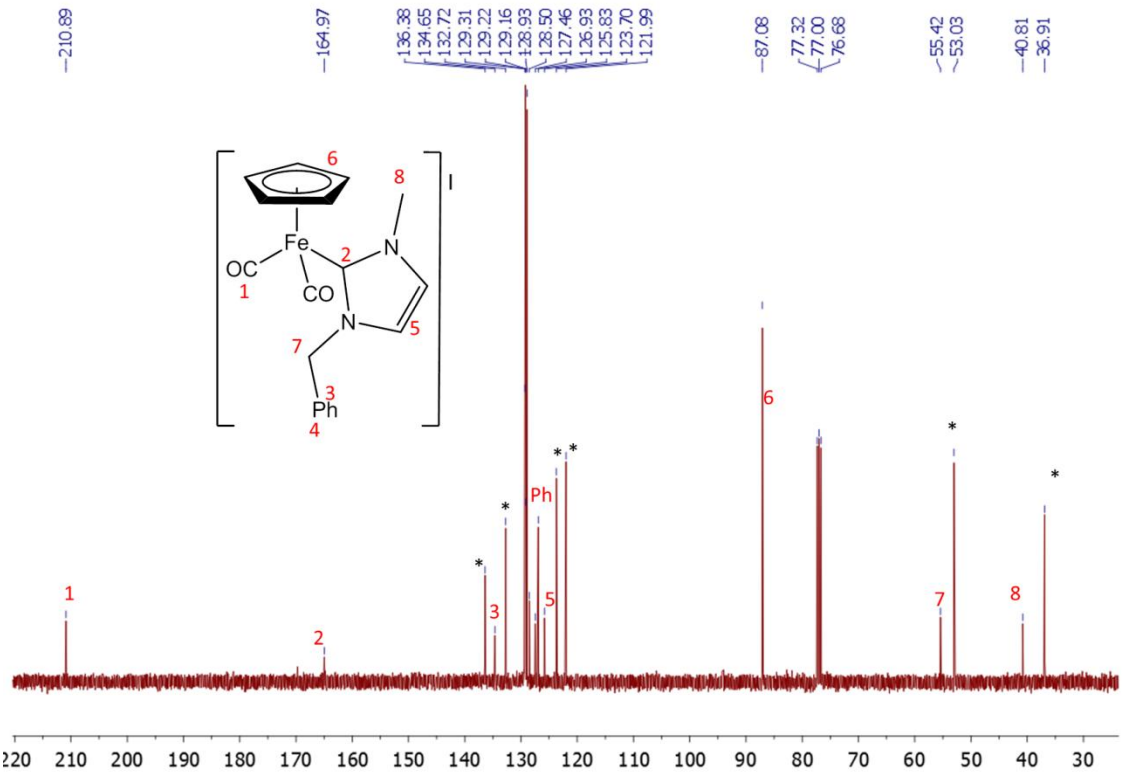

* Traces of **1a**.

Figure 4.53 ^{13}C NMR spectrum of [FeCp(CO)$_2${1-methyl-3-benzyl-imidazolin-2-ylidene}]I.

4.19 Synthesis of $[Fe(CO)_2Cp]^+$ (Fp^+)

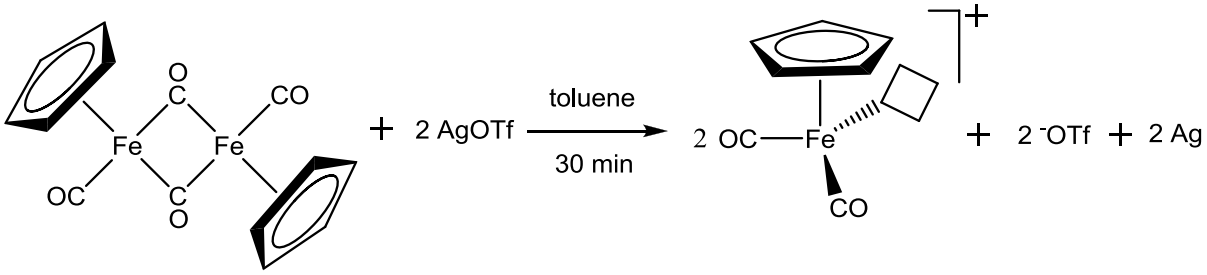

In a Schlenk to a solution the iron precursor $FeI(CO)_2Cp$ (0.20 g, 0.57 mmol) in toluene (10 mL) stirred for 5 min, silver triflate (0.288 g, 1.12 mmol) was added. The Schlenk was protected against a sunlight with aluminium foil. Instantaneously after the addition of the silver triflate, a silver mirror was observed on the walls of the Schlenk. After stirring for 30 min at room temperature, the reaction mixture turns to a red color, indicating the presence of Fp^+.

4.20 VT NMR

NMR spectra were recorded using spectrometers operating at fields of 9.6 and 14.4 T (400 and 600 MHz for 1H). The NMR tubes containing the compounds were prepared under an argon atmosphere using a vacuum line. Low-temperature ^{1}H spectra were acquired without spinning using a 5 mm dual direct probe with a 6000 Hz (at 400 MHz) or 9000 Hz (at 600 MHz) sweep width, 40° tip angle pulse width, 3 s acquisition time, and 1 s delay time. A shifted sine bell weighting function equal to the acquisition time (i.e., 3 s) was applied before the Fourier transformation. Usually 32 to 64 scans were collected. When operating the NMR apparatus at low temperature, a flow of dry nitrogen was first passed through a precooling unit adjusted to -50°C. Then the gas entered into an inox steel heat-exchanger immersed in liquid nitrogen and connected to the NMR probe head by a vacuum-insulated transfer line. Gas flows of 10 to 20 L min^{-1} were required to descend to the desired temperature. Temperature calibrations were performed before the experiments, using a digital thermometer and a Cu/Ni thermocouple placed in an NMR tube filled with isopentane for the low-temperature range and with tetrachloroethane for the high-temperature range. The conditions were kept as identical as possible with all subsequent work. In particular, the sample was not spun and the gas flow was the same as that used during the acquisition of the spectra. The uncertainty in temperature measurements can be estimated from the calibration curve as ±2 °C. Line shape simulations were performed using a PC version of the QCPE DNMR6program. Electronic superimposition of the original spectrum and of the simulated one enabled the determination of the most reliable rate constant. The rate constants, thus obtained at various temperatures, afforded the free energy of activation $\Delta G^{\ddagger}$ by applying the Eyring equation. $\Delta H^{\ddagger}$ and $\Delta S^{\ddagger}$ were evaluated by linear regression of the $\Delta G^{\ddagger}$ value vs the temperature. Except for **3c**, in all cases investigated, the activation energy $\Delta G^{\ddagger}$ was found to be virtually invariant in the given temperature range, thus implying a very small or negligible activation entropy $\Delta S^{\ddagger}$.

4.20.1 [Rh(NBD)Cl{1-methyl-3-benzyl-imidazolin-2- ylidene}] 3a

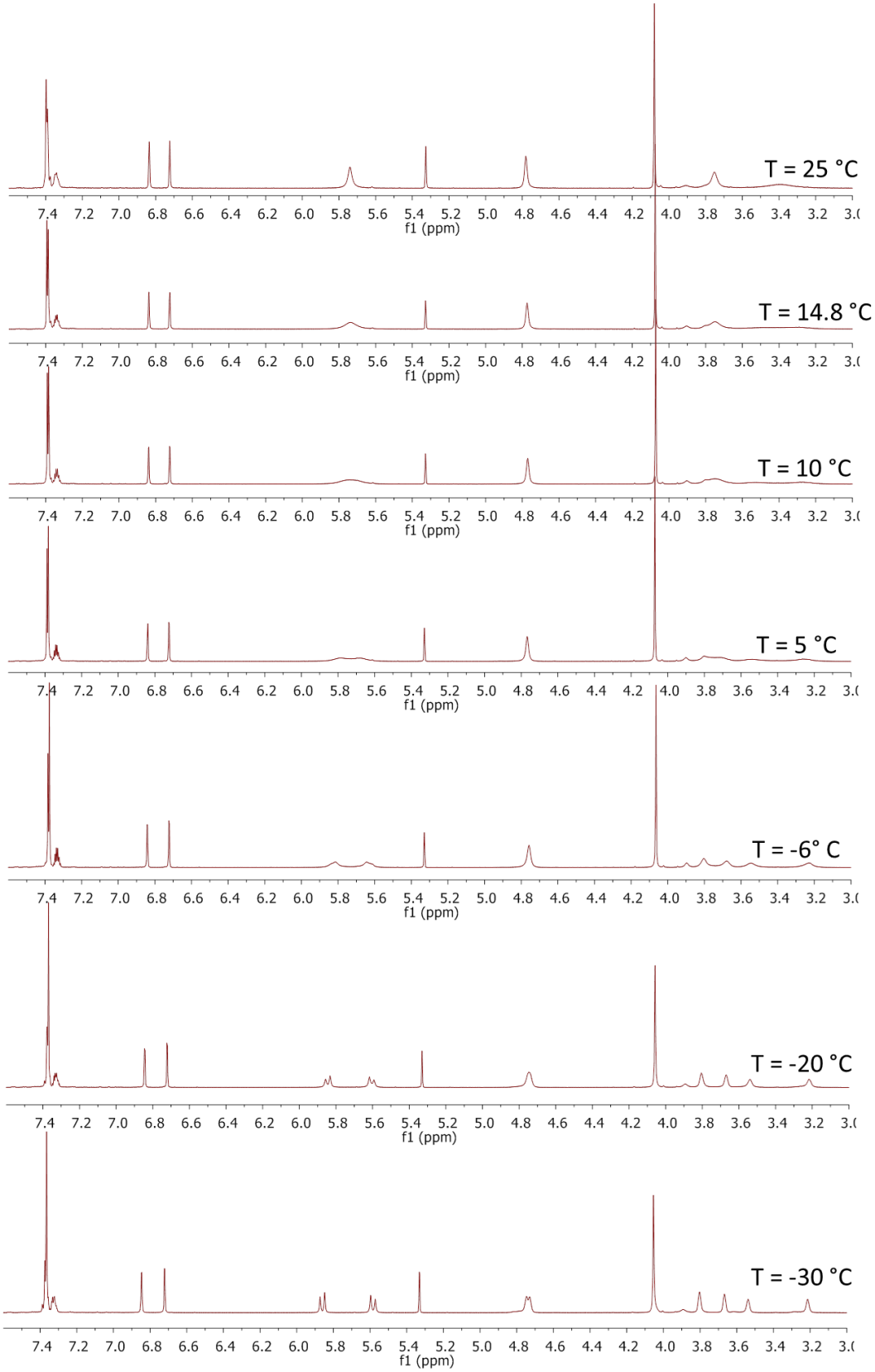

Figure 4.54 ^{1}H NMR spectra of 3a at various temperatures (600 MHz, $C_2D_2Cl_4$).

4.20.2 [Rh(NBD)Cl{1-benzyl-3-benzyl-imidazolin-2- ylidene}], 3b

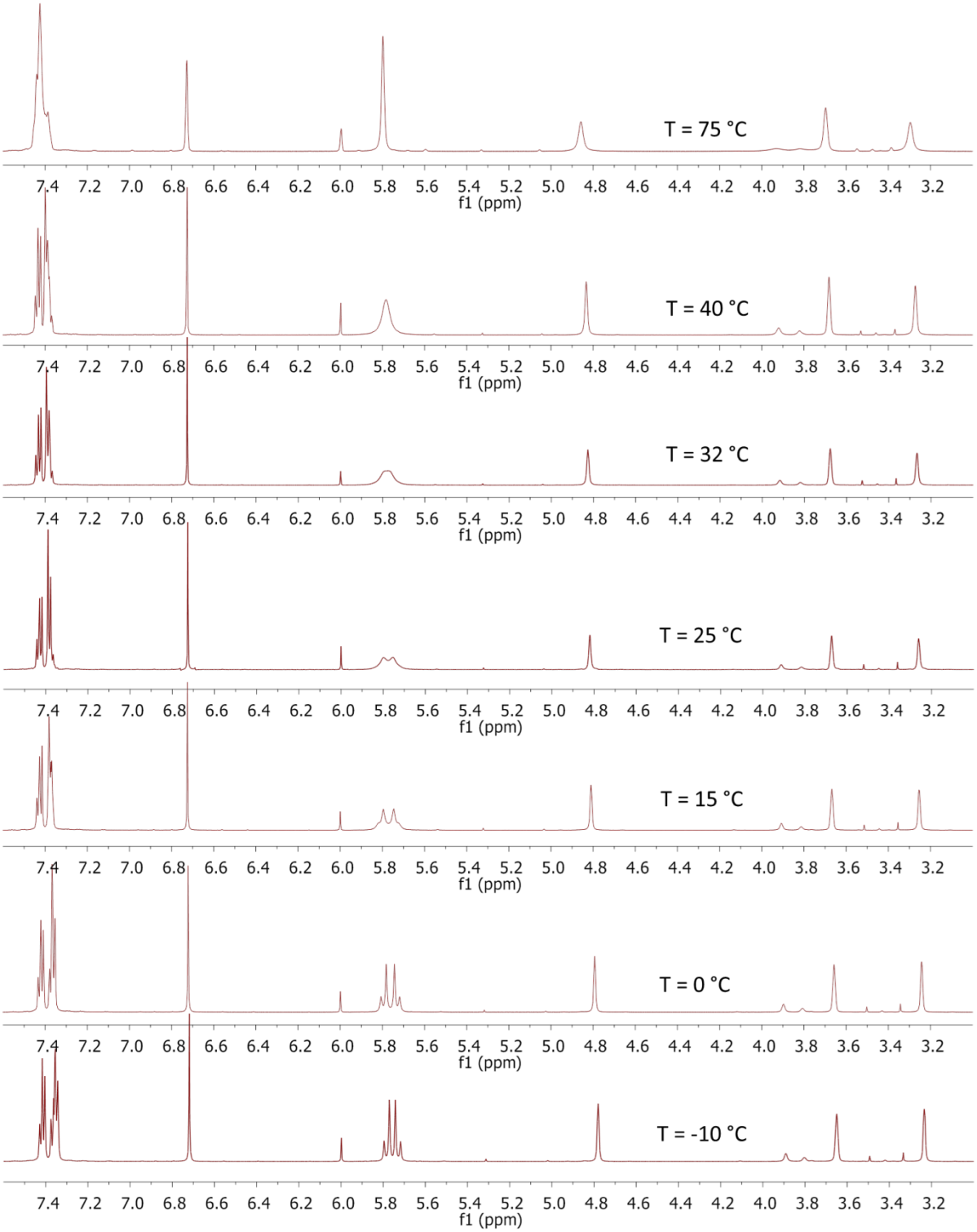

Figure 4.55 ^{1}H NMR spectra of 3b at various temperatures (600 MHz, $C_2D_2Cl_4$).

4.20.3 [Rh(NBD)Cl{1-benzyl-3-trityl-imidazolin-2- ylidene}], 3d

a) $CDCl_3$

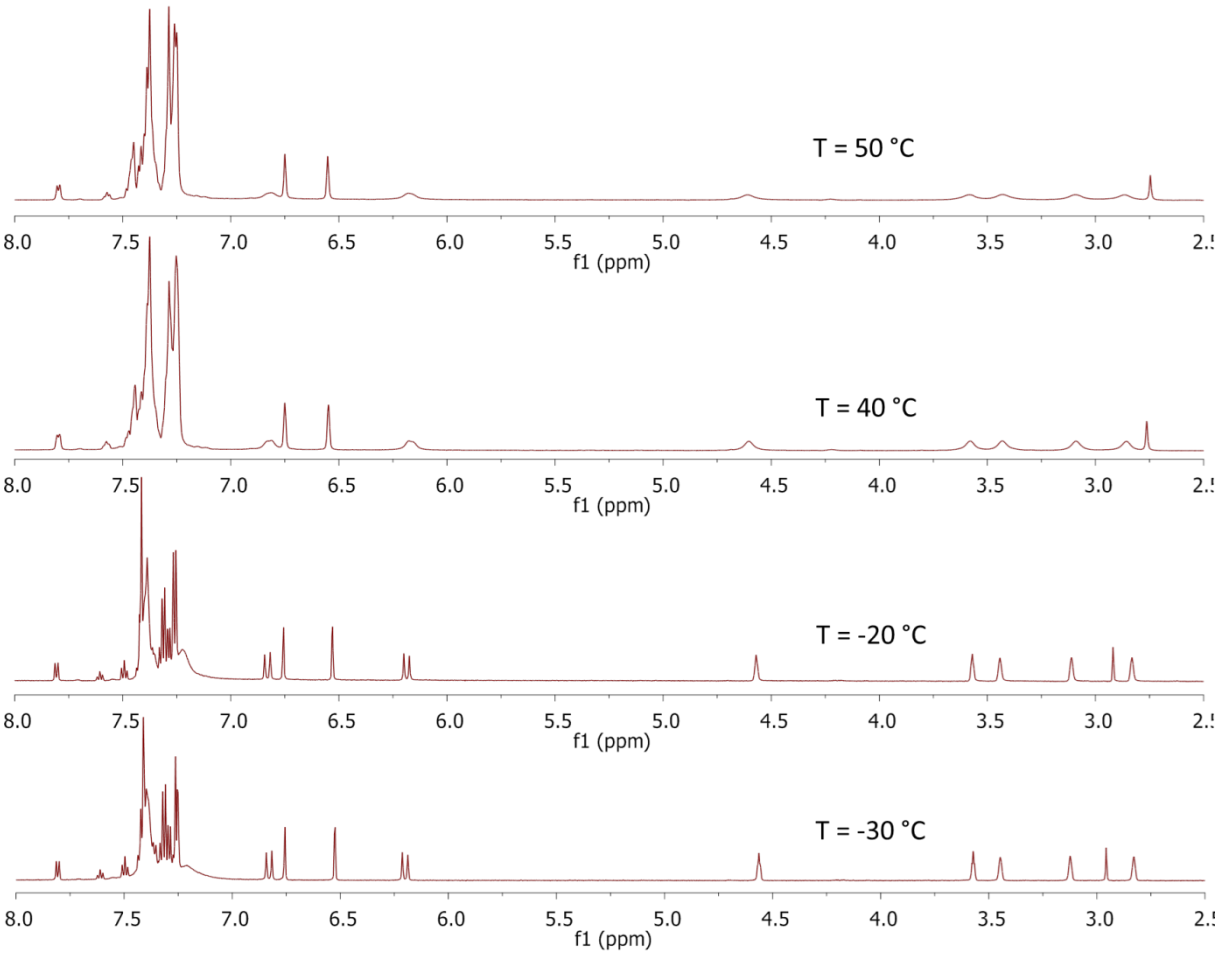

Figure 4.56 ^{1}H NMR spectra of 3d at various temperatures (600 MHz, $CDCl_3$).

b) $C_2D_2Cl_4$

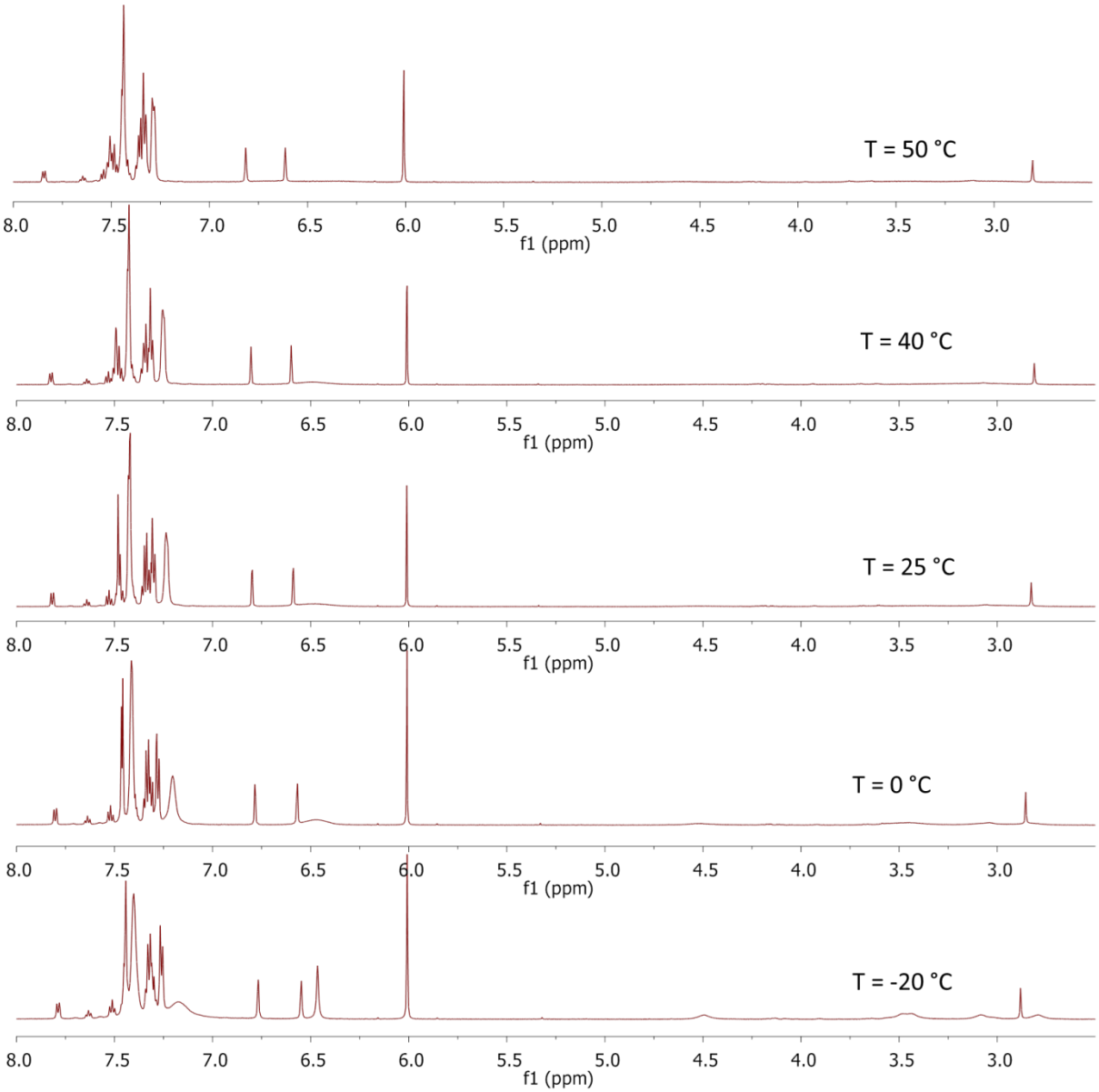

Figure 4.57 ^{1}H NMR spectra of 3d at various temperatures (600 MHz, $C_2D_2Cl_4$).

4.21 X-ray structure determination for 2b, 3a and 3b.

Crystal data were collected at room temperature on a Bruker APEX II diffractometer equipped with a CCD detector operating at 50 kV and 30 mA, using graphite-monochromated Mo Kα radiation (λ = 0.71073 Å). An empirical absorption correction was applied on both structures by using SADABS[59]. They were solved by direct methods and refined by full-matrix least-squares based on all data using F^2 with SHELXL97. All non-hydrogen atoms were refined anisotropically, with the exception of the hydrogen atoms, which were set

geometrically and given fixed isotropic thermal parameters. Crystal data are collected in Table 4.1.

Table 4.1 Crystal data and data collection and refinement parameters for 2b, 3a and 3b.

	2b	**3a**	**3b**
formula	$C_{34}H_{32}AgBrN_4$	$C_{18}H_{20}ClN_2Rh$	$C_{24}H_{24}ClN_2Rh$
fw	684.42	402.72	478.81
T, K	296(2)	296(2)	296(2)
λ, Å	0.71073	0.71073	0.71073
cryst syst	monoclinic	monoclinic	monoclinic
space group	P2(1)/*n*	P2(1)/*c*	P2(1)/*n*
a, Å	13.3816(14)	10.5190 (6)	11.3295(6)
b, Å	9.8169(11)	10.7555(6)	10.5864(6)
c, Å	23.974(3)	14.8470(9)	18.0379(9)
α, deg	90	90	90
β, deg	104.4500(10)	90.5320(10)	106.8260(10)
γ, deg	90	90	90
cell volume, $Å^3$	3049.8(6)	1679.67(17)	2070.82(19)
Z	4	4	4
D_c, g cm^{-3}	1.491	1.593	0.965
μ, mm^{-1}	2.000	1.173	0.965
F(000)	1384	816	1.536
cryst size, mm	0.20 x 0.15 x 0.12	0.20 x 0.15 x 0.10	0.25 x 0.25 x 0.
θ limits, deg	1.60 to 24.99	1.94 to 24.99	1.91 to 25.00
index ranges	$-15 \le h \le 15$, $-11 \le k \le 11$, $28 \le l \le 28$	$-12 \le h \le 12$, $-12 \le k \le 12$, $-17 \le l \le 17$	$-13 \le h \le 13$, $-12 \le k \le 12$, $-21 \le l \le 21$
reflns collected indep	28358	15678	19412
indep reflns	5368 [R(int) = 0.0301]	2959 [R(int) = 0.0362]	3655 [R(int) = 0.0234]
completeness to θ = 25.00°	100.0%	100.0%	100.0%
data/restraints/params	5368 / 0 / 361	2959 / 0 / 200	3655 / 0 / 253

goodness on fit on F^2	1.051	1.051	1.044
R_1 ($I > 2\sigma(I)$)	0.0756	0.0319	0.0218
wR_2 (all data)	0.2494	0.0445	0.0261
largest diff peak and hole, e Å^{-3}	2.881 and -2.671	0.800 and -0.313	0.331 and -0.285
Rh-C bond length (Å)		2.019(3)	2.023 (2)
Rh-X bond length (Å)		2.3800(11)	2.3618 (6)

4.22 Catalysis.

General Procedure for the Hydrosilylation of 1-Alkynes with $HSiMe_2Ph$.

A) Catalyst: 3a, 1 mol %, room temperature

A J. Young valve NMR tube was charged under argon with the catalyst precursor **3a** (7.7 x 10^{-4} mmol), $CDCl_3$ (0.6 mL), the corresponding alkyne (Ph≡CH, TolC≡CH, ^{n}BuC≡CH, Et_3Si≡CH (0.077 mmol), and a slight excess of $HSiMe_2Ph$ (0.085 mmol). The solution was kept at T = 25°C and monitored by ^{1}H NMR spectroscopy. The resulting products were characterized by ^{1}HNMR and by comparison with similar compounds reported in the literature[1].

B) Catalysts: 3a and 3b; 0,1 mol %, room temperature

J. Young valve NMR tubes were charged under argon with the catalyst precursors **3a** and **3b** (7.7 x 10^{-5} mmol), $CDCl_3$ (0.6 mL) and for each catalysts the corresponding alkynes (Ph≡CH, TolC≡CH, and ^{n}BuC≡CH (0.077 mmol), and a slight excess of $HSiMe_2Ph$ (0.085 mmol). The solution was kept at T = 25°C and monitored by ^{1}H NMR spectroscopy. The products were characterized by ^{1}HNMR.

C) Catalysts: 3a and 3b; 0,1 mol %, T=60°C

J. Young valve NMR tubes were charged under argon with the catalyst precursors **3a** and **3b** (7.7 x 10^{-5} mmol), $CDCl_3$ (0.6 mL) and for each catalysts the corresponding alkynes

(Ph≡CH, TolC≡CH, and ^{n}BuC≡CH (0.077 mmol), and a slight excess of $HSiMe_2Ph$ (0.085 mmol). The solution was kept at T = 60°C in an oil bath and monitored by ^{1}H NMR spectroscopy. The products were characterized by ^{1}HNMR.

Conversions and selectivities for the studied hydrosilylation reactions have been calculated from integration of peaks in ^{1}H-NMR spectra, assigned to isomeric products presented in Schemes 1, 2 and 3[1].

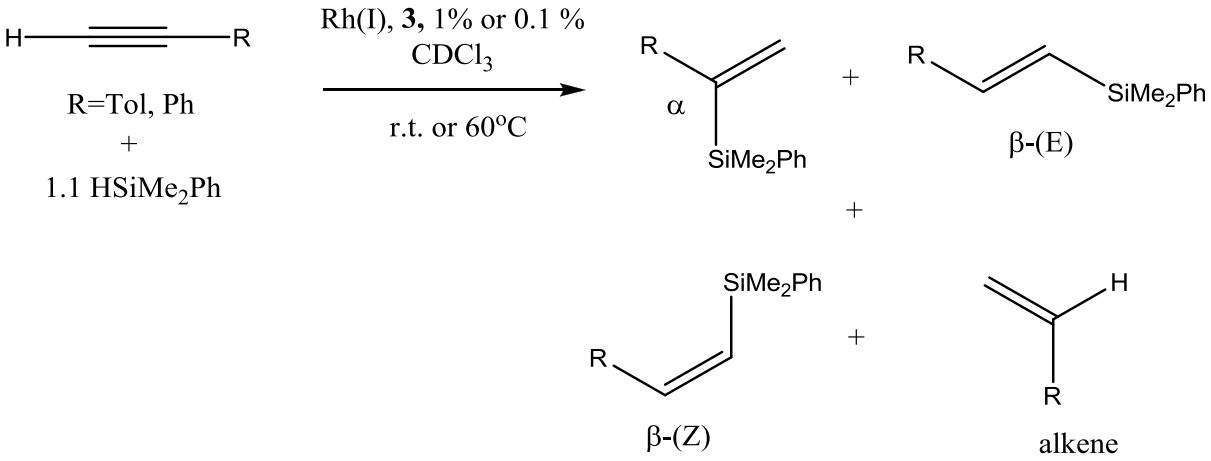

Scheme 4.1 Hydrosilylation of PhC≡CH and TolC≡CH.

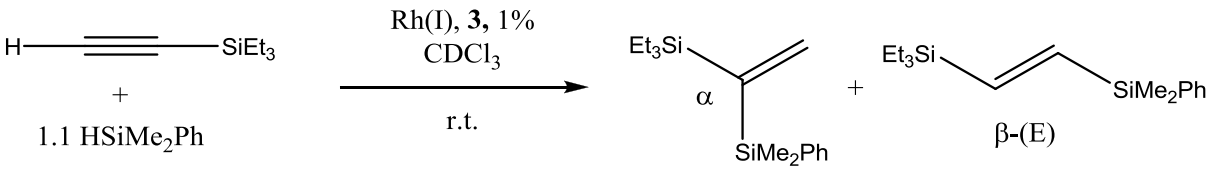

Scheme 4.2 Hydrosilylation of Et_3SiC≡CH.

Hydrosilylation products: ^{1}H-NMR characterizations.

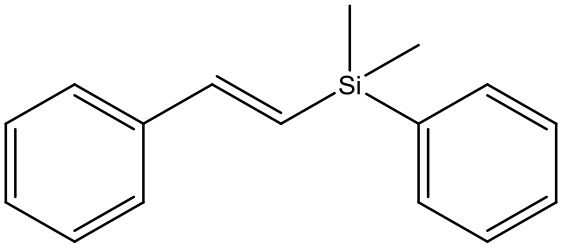

(E)-2- (dimethyl(phenyl)silyl)-1-phenyl-ethene

^{1}H NMR ($CDCl_3$, 300 MHz): δ 7.6-7.2 (m, 5H), 7.0 (d, $J_{H,H}$ = 19 Hz, 1H), 6.6 (d, $J_{H,H}$ = 19 Hz, 1H), 0.36 (s, 6H) ppm.

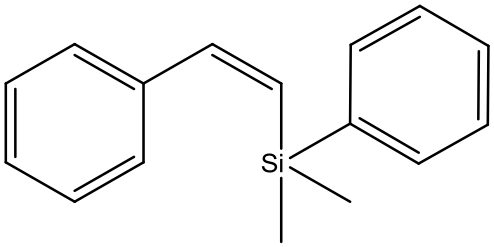

(Z)-2- (dimethyl(phenyl)silyl)-1-phenyl-ethene

^{1}H NMR ($CDCl_3$, 300 MHz): δ 7.6-7.2 (m, 5H), 7.5 (d, $J_{H,H}$ = 15 Hz, 1H), 6.0 (d, $J_{H,H}$ = 15 Hz, 1H), 0.36 (s, 6H) ppm.

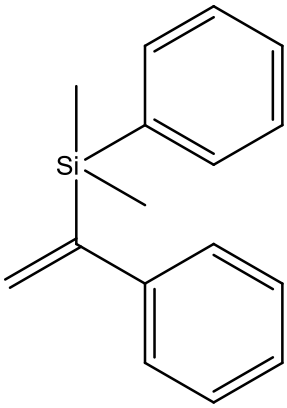

1-(dimethyl(phenyl)silyl)-1-phenyl-ethene

^{1}H NMR ($CDCl_3$, 300 MHz): δ 7.6-7.3 (m, 5H), 5.98 (d, $J_{H,H}$ = 2.9 Hz, 1H,), 5.66 (d, $J_{H,H}$ = 2.9 Hz, 1H), 0.41 (s, 6H) ppm.

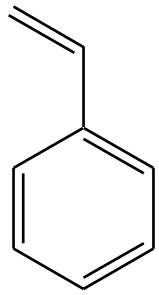

Styrene

^{1}H NMR ($CDCl_3$, 300 MHz): δ 7.50-7.10 (m, 5H), 6.69 (dd, $J_{H,H}$ = 18.0, 11.0 Hz, 1H), 5.74 (d, $J_{H,H}$ = 18.0, 1H), 5.22 (d, $J_{H,H}$ = 11.0 Hz, 1H).

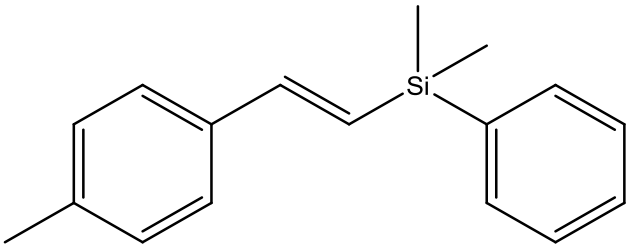

(E)-2- (dimethyl(phenyl)silyl)-1-tolyl-ethene

^{1}H-NMR ($CDCl_3$): δ 7.60-7.16 (m, 9H), 6.96 (d, $J_{H,H}$ = 19.2 Hz, 1H), 6.45 (d, $J_{H,H}$ = 19.2 Hz, 1H), 2.36 (s, 3H), 0.49 (s, 6H) ppm.

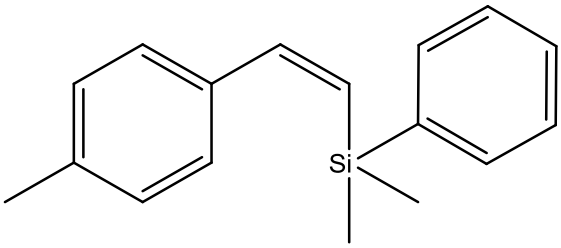

(Z)-2- (dimethyl(phenyl)silyl)-1-tolyl-ethene

^{1}H-NMR ($CDCl_3$): δ 7.60–7.52 (m, 2H), 7.43 (d, $J_{H,H}$ = 15.3 Hz, 1H), 7.38–7.32 (m, 3H), 7.13 (d, $J_{H,H}$ = 8.1 Hz, 2H), 7.06 (d, $J_{H,H}$ = 8.1 Hz, 2H), 5.96 (d, $J_{H,H}$ = 15.0 Hz, 1H), 2.30 (s, 3H), 0.28 (s, 6H) ppm.

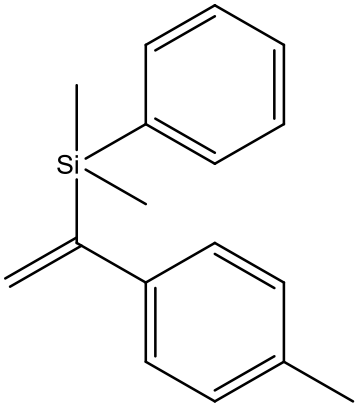

1-(dimethyl(phenyl)silyl)-1-tolyl-ethene

^{1}H NMR ($CDCl_3$, 300 MHz): δ 7.6-7.3 (m, 4H), 5.93 (d, 1H, $J_{H,H}$ = 2.9 Hz), 5.66 (d, 1H, $J_{H,H}$ = 2.9 Hz), 2.35 (s, 3H), 0.30 (s, 6H) ppm.

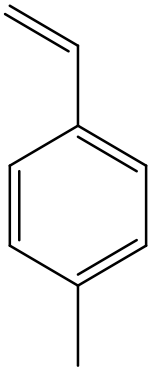

4-Methylstyrene

^{1}H NMR ($CDCl_3$, 300 MHz): δ 7.39 (d, $J_{H,H}$ = 8.0 Hz, 2H), 7.20 (d, $J_{H,H}$ = 8.0 Hz, 2H), 6.77 (dd, $J_{H,H}$ = 18.0, 11.0 Hz, 1H), 5.78 (d, $J_{H,H}$ = 18.0, 1H), 5.26 (d, $J_{H,H}$ = 11.0 Hz, 1H), 2.41 (s, 3H).

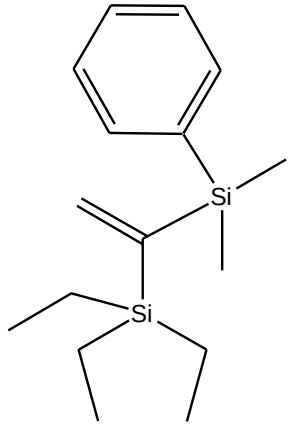

1-(Dimethylphenylsilyl)-1-(triethylsilyl)ethene

^{1}H NMR ($CDCl_3$, 300 MHz): δ 7.35-7.19 (m, 5H,Ph), AB system (δ_A = 6.40, δ_B = 6.42, $J_{A,B}$ = 5.2, 2H, CH), 0.64 (t, $J_{H,H}$ = 7.8 Hz, 6H, CH_2), 0.32 (q, $J_{H,H}$ = 7.8 Hz, 9H, CH_3), 0.19 (s, 6H, CH_3).

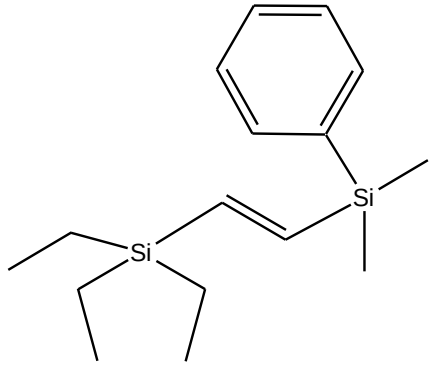

(E)-2-(Dimethylphenylsilyl)-1-(triethylsilyl)ethene

^{1}H NMR ($CDCl_3$, 300 MHz): δ 7.32-7.15 (m, 5H,Ph), AB system (δ_A = 6.76, δ_B = 6.65, $J_{A,B}$ = 22.8, 2H, CH), 0.76 (t, $J_{H,H}$ = 8.0 Hz, 6H, CH_2), 0.41 (q, $J_{H,H}$ = 8.0 Hz, 9H, CH_3), 0.15 (s, 6H, CH_3).

Selected examples of conversions and selectivities calculations from ^{1}H-NMR.

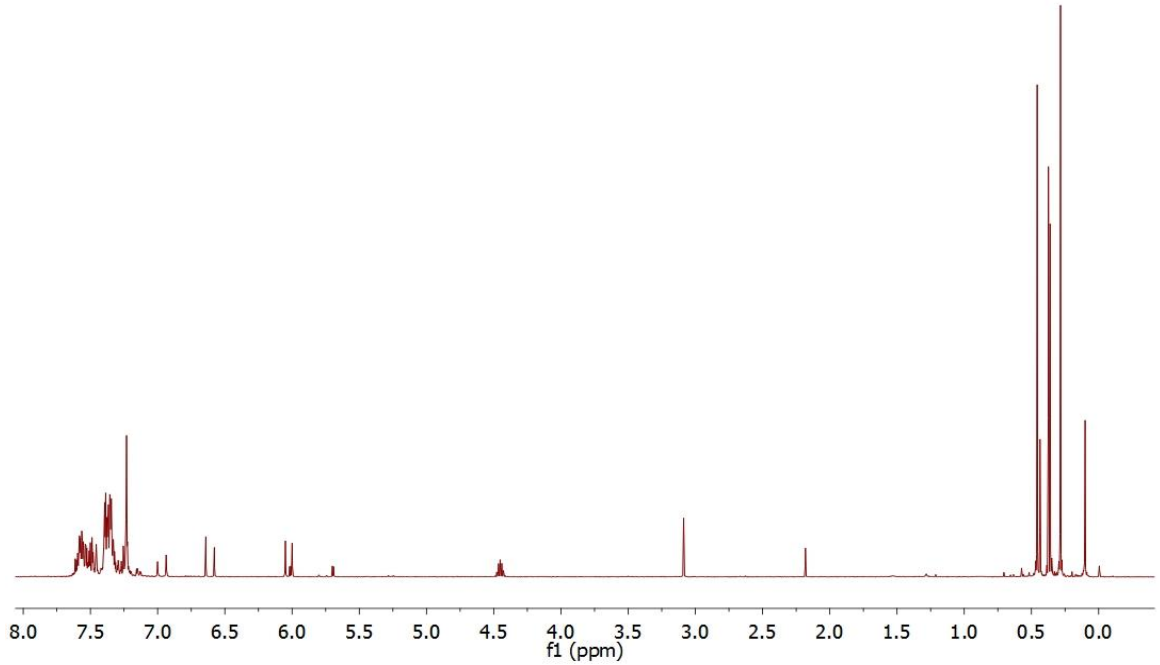

Figure 4.58 Hydrosilylation of PhC≡CH with 0.1% 3b; t = 312 h, conversion = 72%, selectivities: β(E) = 40%; β(Z) = 45%; α = 12%; alkene = 3%.

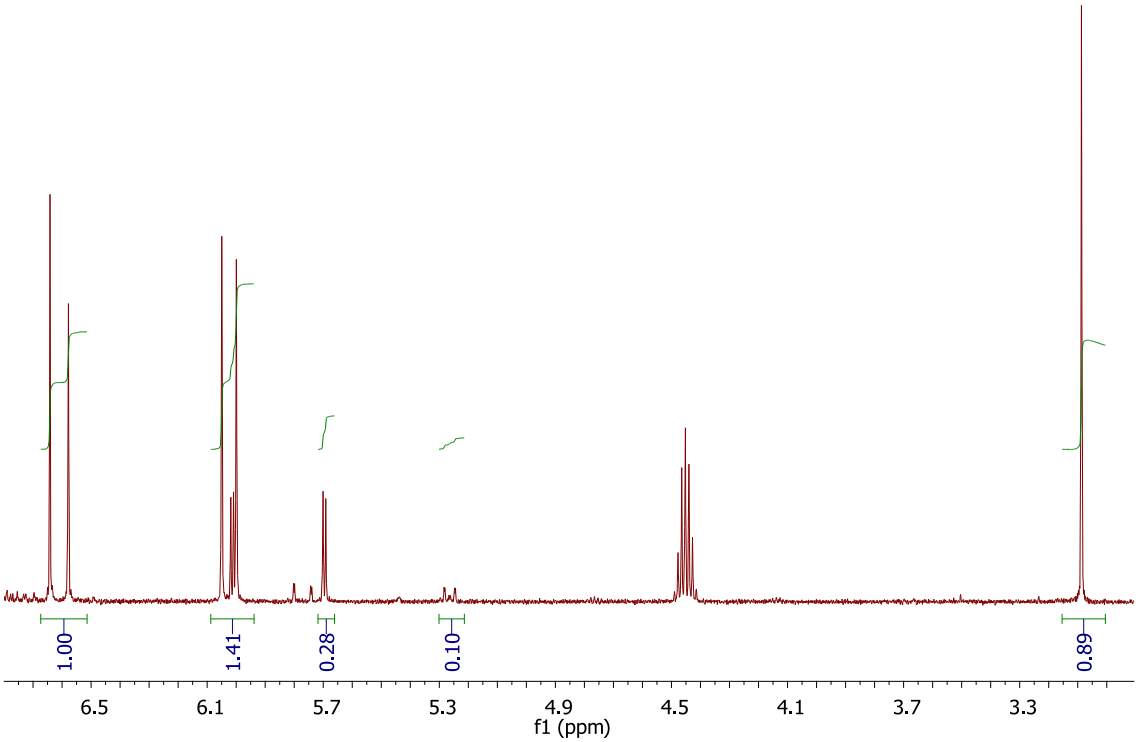

Figure 4.59 Hydrosilylation of PhC≡CH with 0.1% 3b; *t* = 312 h, conversion = 72%, selectivities: β(E) = 40%; β(Z) = 45%; α = 12%; alkene = 3%, enlargement of the spectrum and integration.

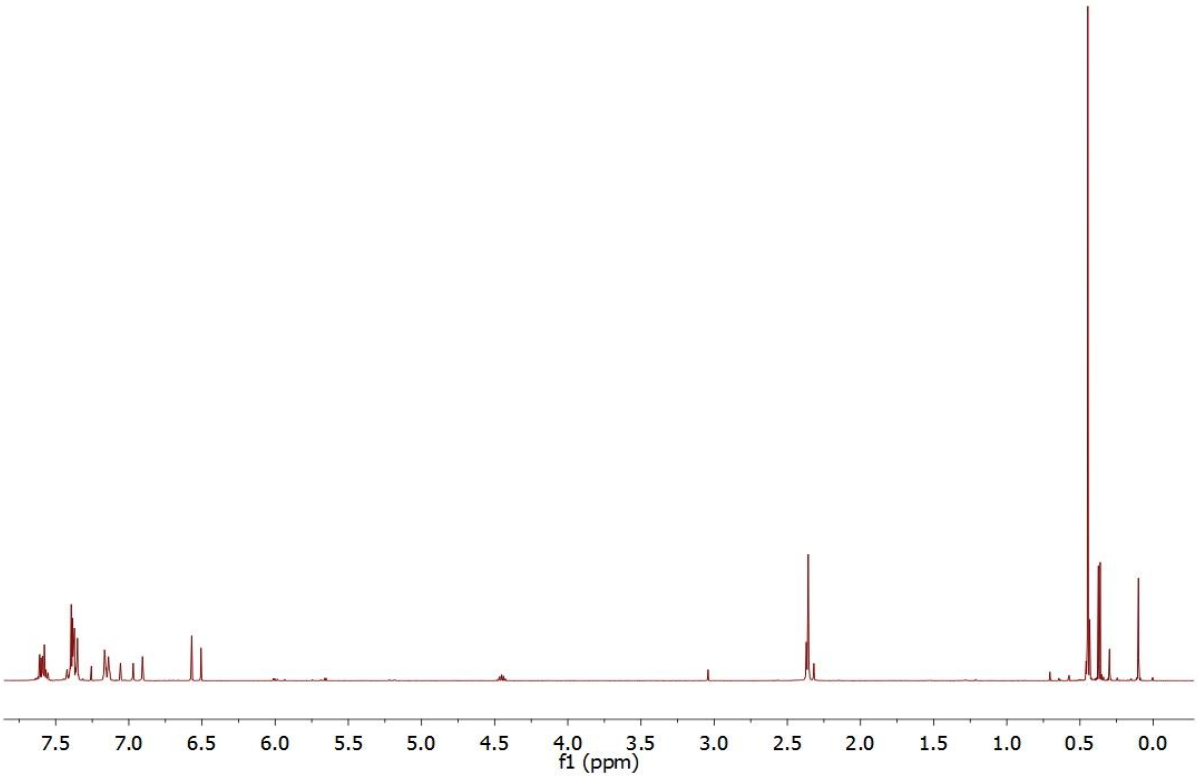

Figure 4.60 Hydrosilylation of TolC≡CH with 0.1% 3b; t = 288 h, conversion = 88%, selectivities: β(E) = 87%; β(Z) = 3.5%; α = 4%; alkene = 5%.

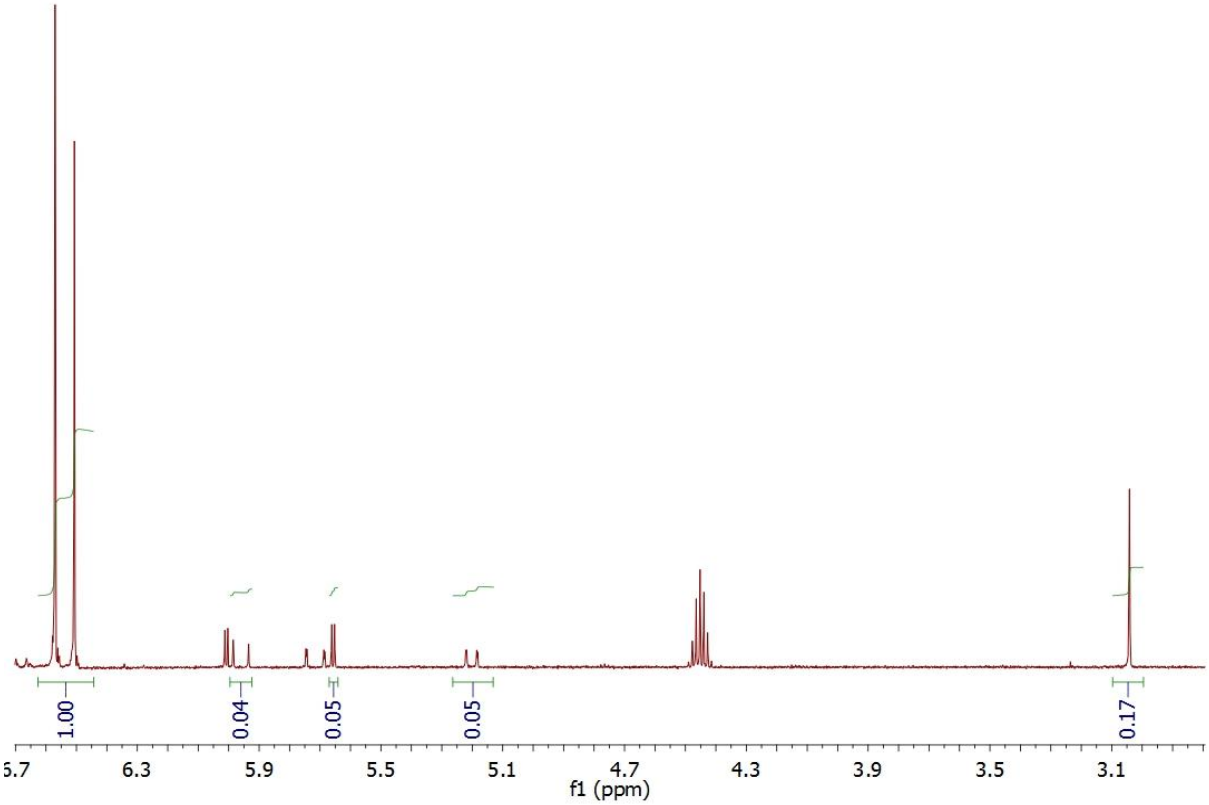

Figure 4.61 Hydrosilylation of TolC≡CH with 0.1% 3b; t = 288 h, conversion = 88%, selectivities: β(E) = 87%; β(Z) = 3.5%; α = 4%; alkene = 5%, enlargement of the spectrum and integration.

A) Catalyst: 3a, 1 mol %, room temperature

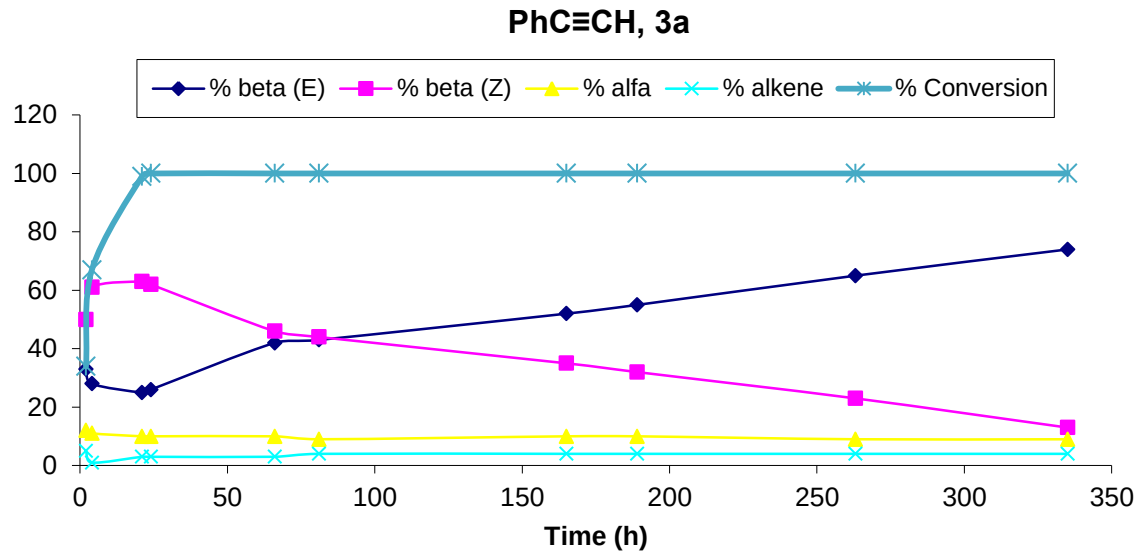

Figure 4.62 Reaction profile of conversion and selectivities vs time for the hydrosilylation of PhC≡CH with 3a.

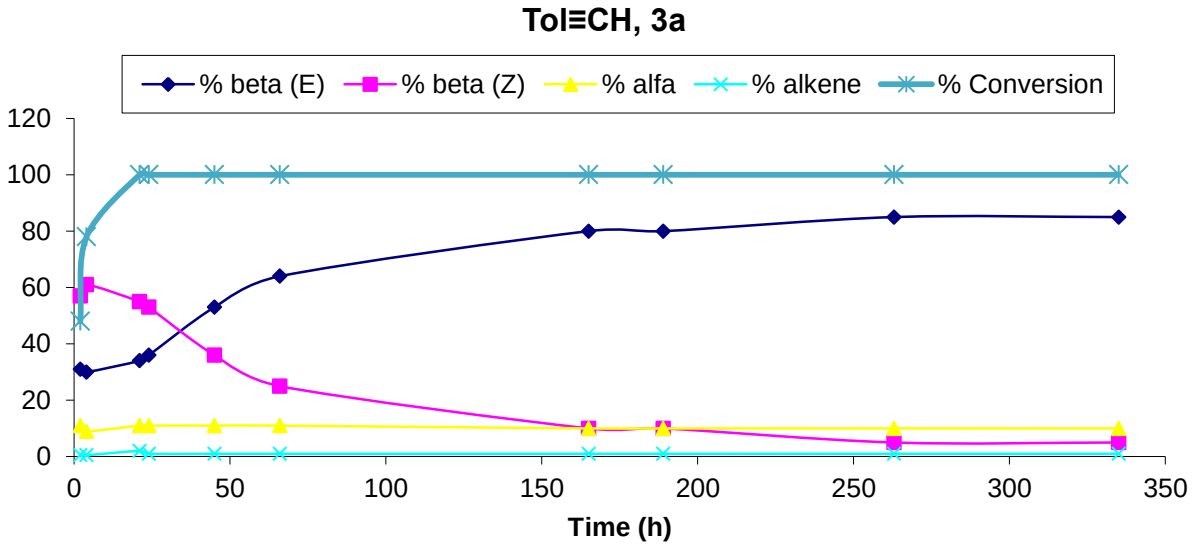

Figure 4.63 Reaction profile of conversion and selectivities vs time for the hydrosilylation of TolC≡CH with 3a.

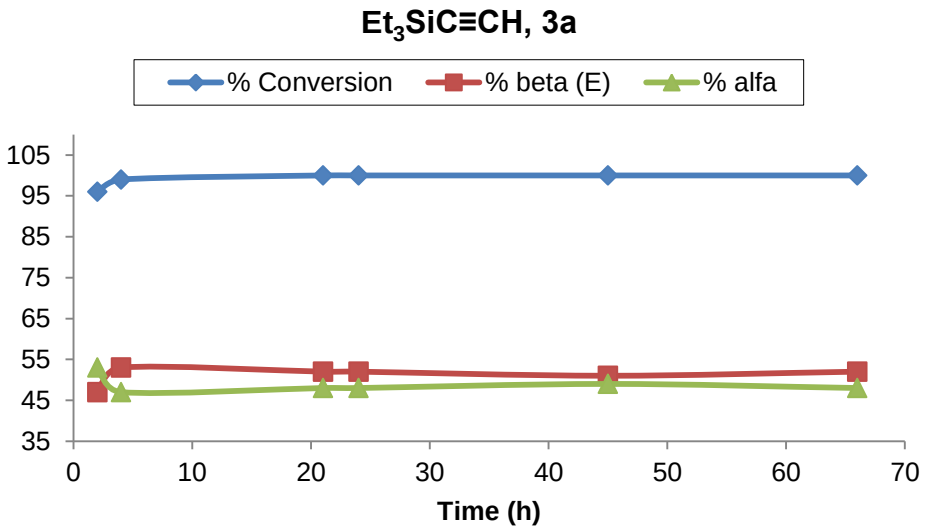

Figure 4.64 Reaction profile of conversion and selectivities vs time for the hydrosilylation of $Et_3SiC{\equiv}CH$ with 3a.

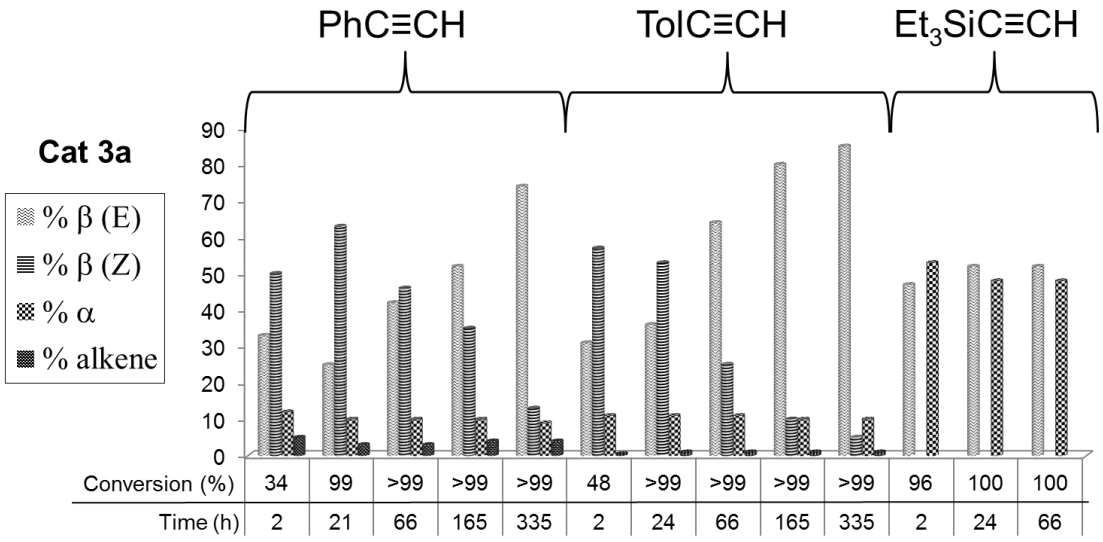

Figure 4.65 Selectivity vs conversion and time for the hydrosilylation of PhC≡CH, TolC≡CH and $Et_3SiC{\equiv}CH$ catalysed by 3a.

B) Catalysts: 3a and 3b; 0,1 mol %, room temperature

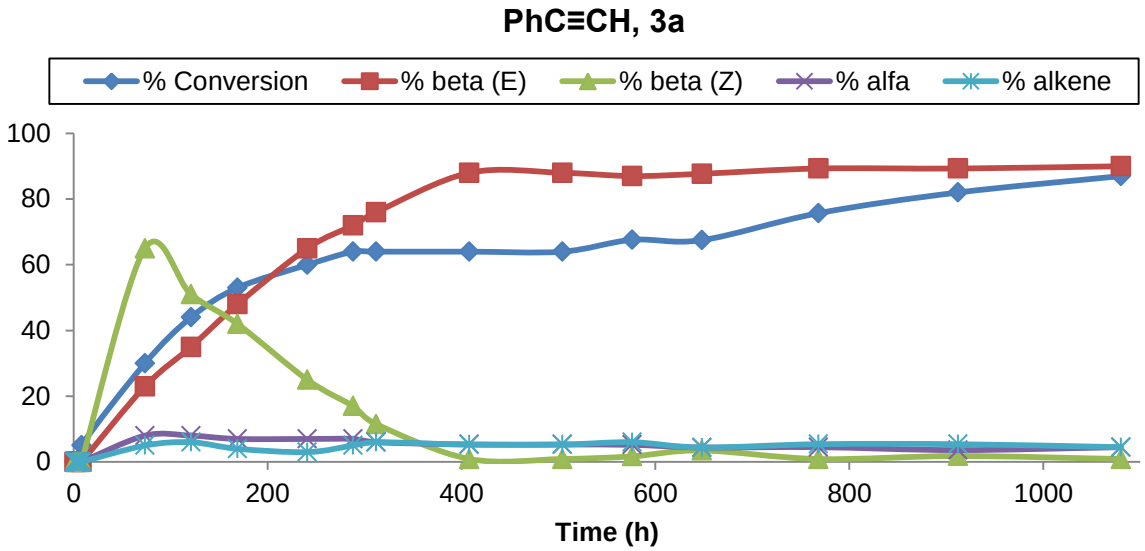

Figure 4.66 Reaction profile of conversion and selectivities vs time for the hydrosilylation of PhC≡CH with 3a.

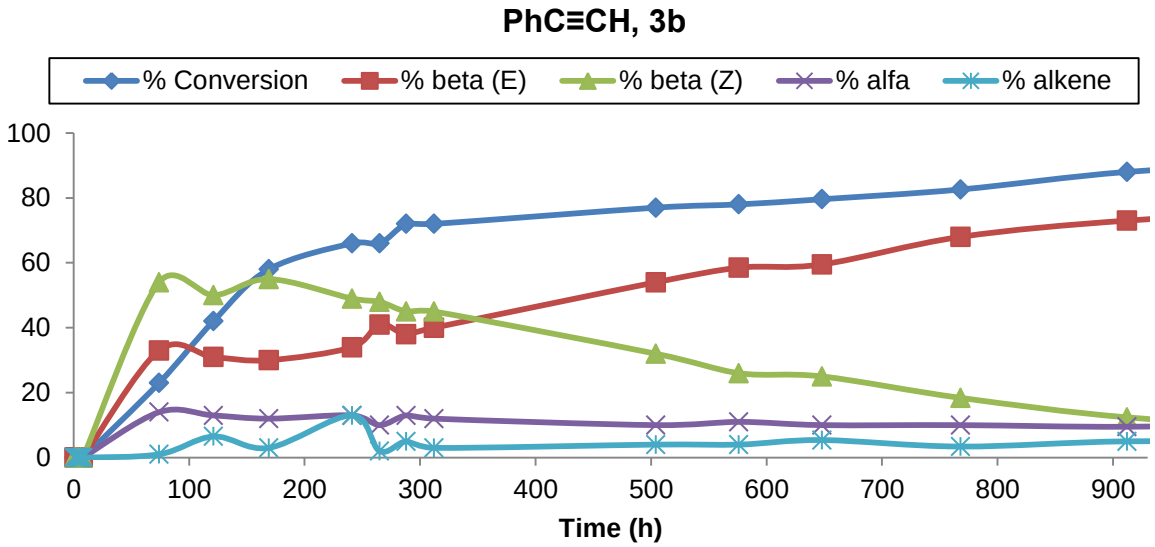

Figure 4.67 Reaction profile of conversion and selectivities vs time for the hydrosilylation of PhC≡CH with 3b.

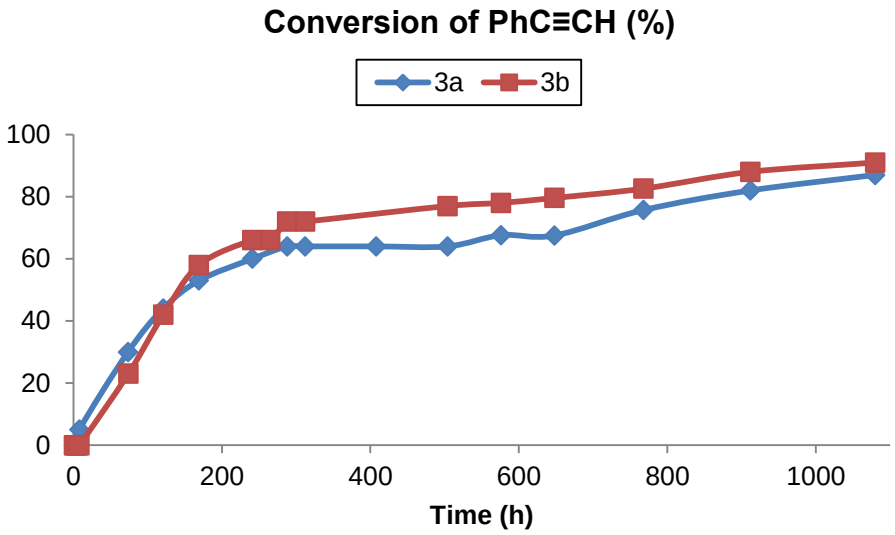

Figure 4.68 Reaction profile of conversion vs time for the hydrosilylation of PhC≡CH with complexes 3a and 3b.

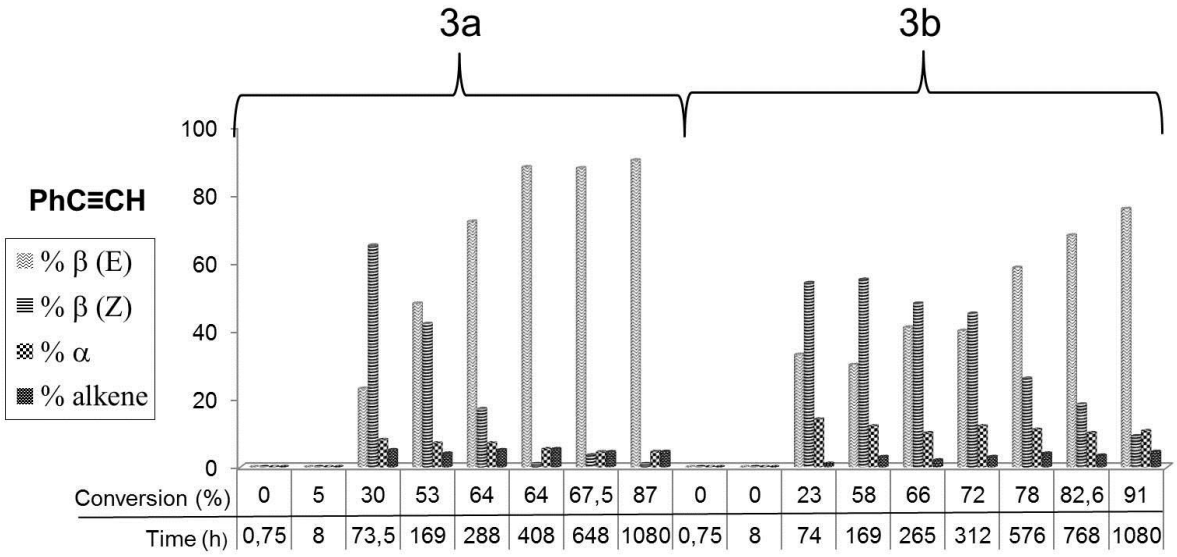

Figure 4.69 Selectivity vs conversion and time for the hydrosilylation of PhC≡CH catalyzed by 3a and 3b.

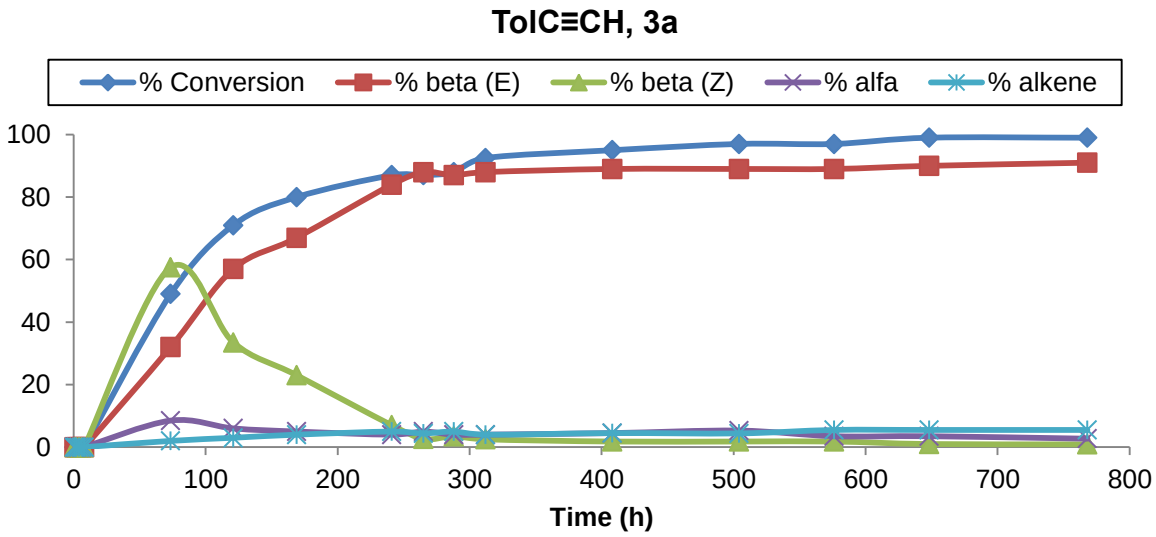

Figure 4.70 Reaction profile of conversion and selectivities vs time for the hydrosilylation of TolC≡CH with 3a.

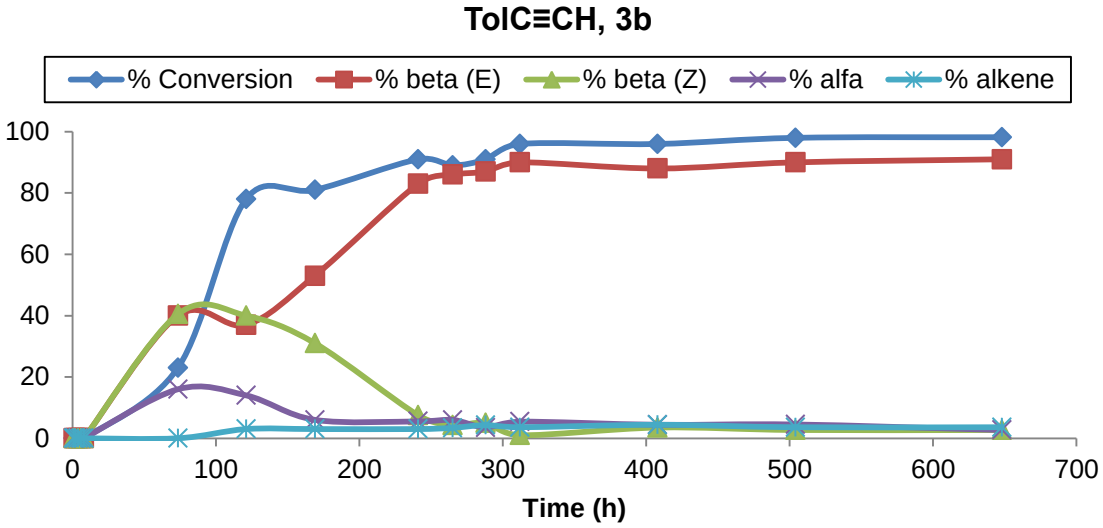

Figure 4.71 Reaction profile of conversion and selectivities vs time for the hydrosilylation of TolC≡CH with 3b.

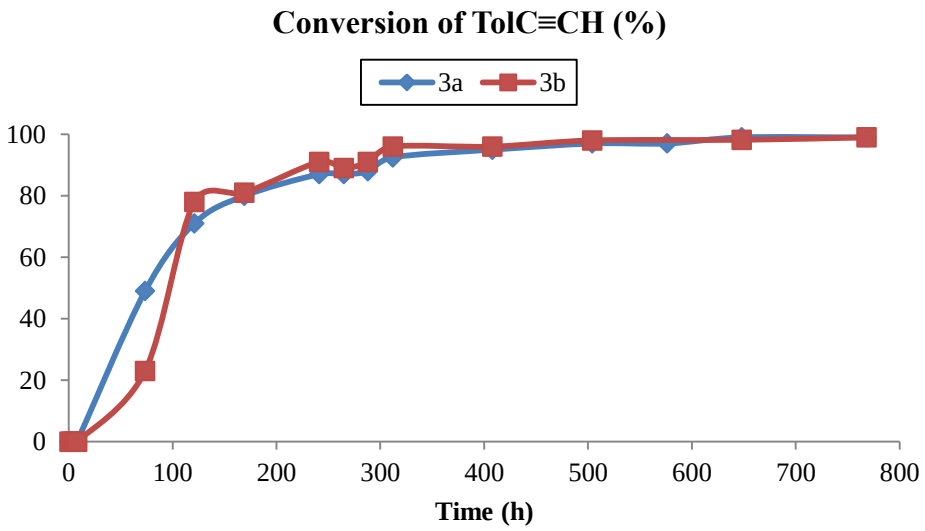

Figure 4.72 Reaction profile of conversion vs time for the hydrosilylation of TolC≡CH with complexes 3a and 3b.

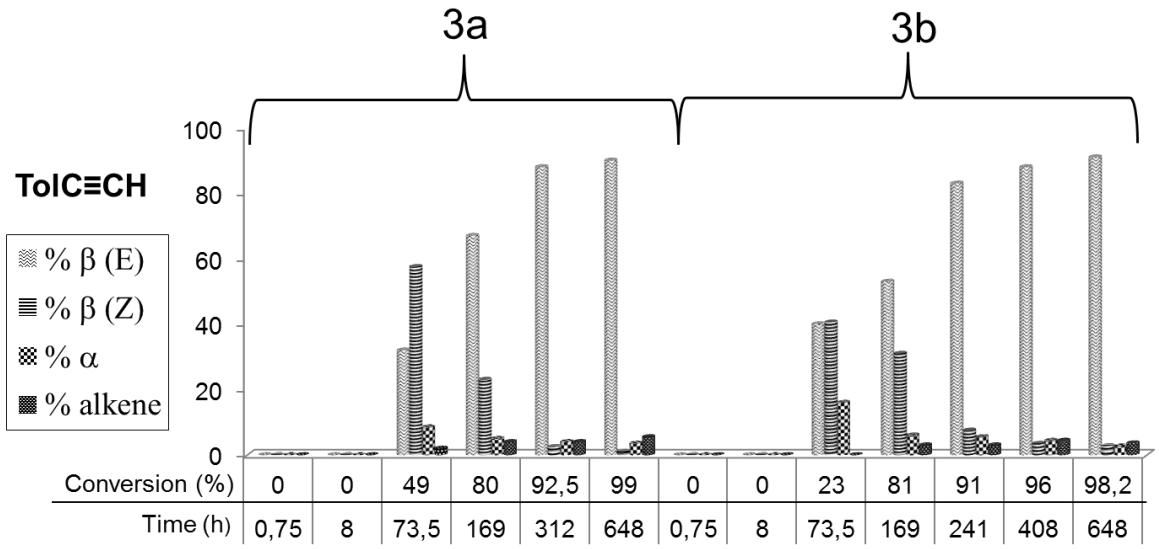

Figure 4.73 Selectivity vs conversion and time for the hydrosilylation of TolC≡CH catalyzed by 3a and 3b.

C) Catalysts: 3a and 3b; 0,1 mol %, T=60°

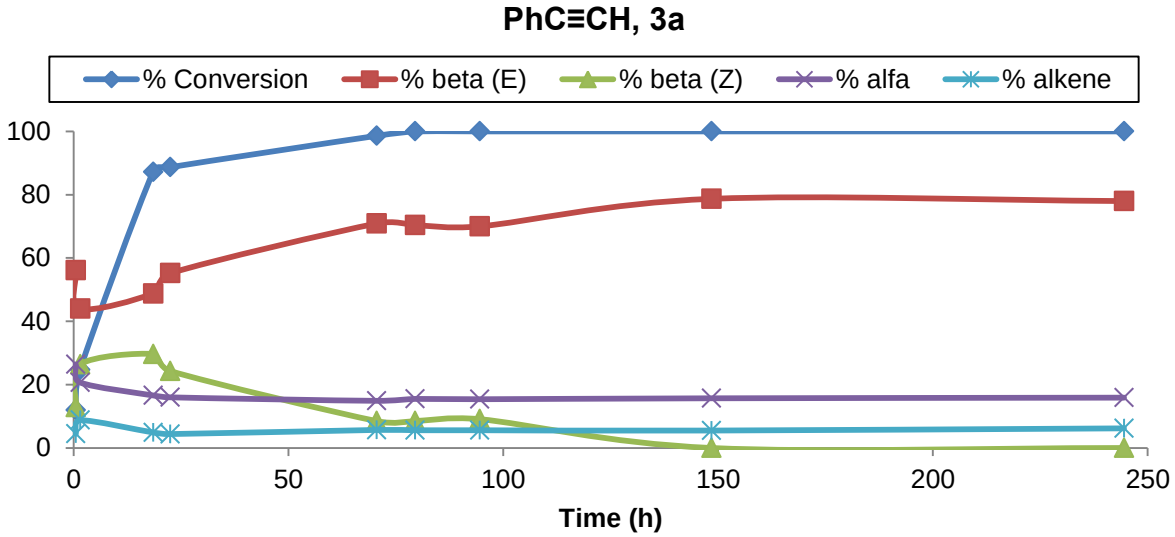

Figure 4.74 Reaction profile of conversion and selectivities vs time for the hydrosilylation of PhC≡CH with 3a, at 60°C.

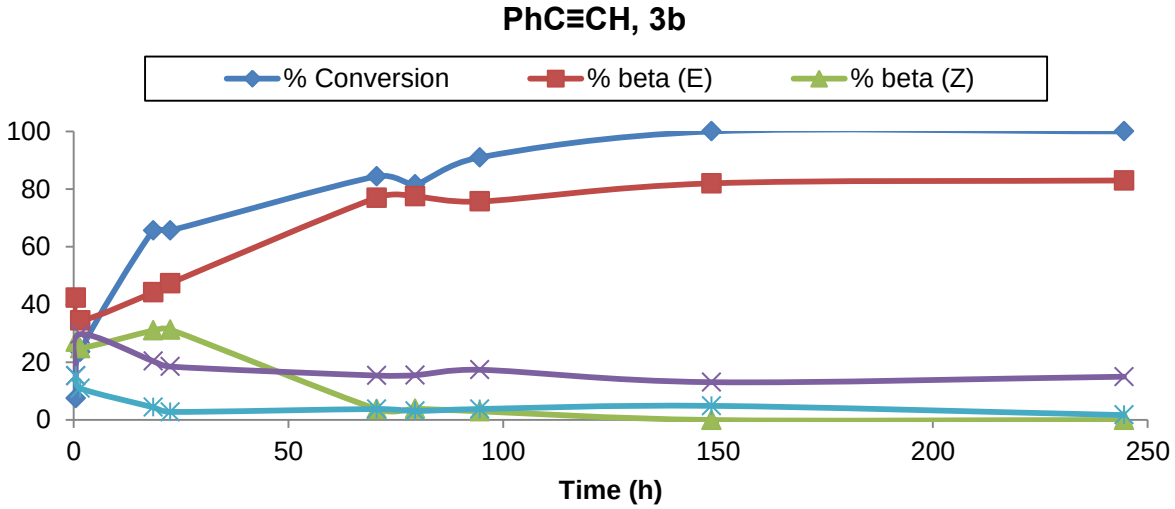

Figure 4.75 Reaction profile of conversion and selectivities vs time for the hydrosilylation of PhC≡CH with 3b, at 60°C.

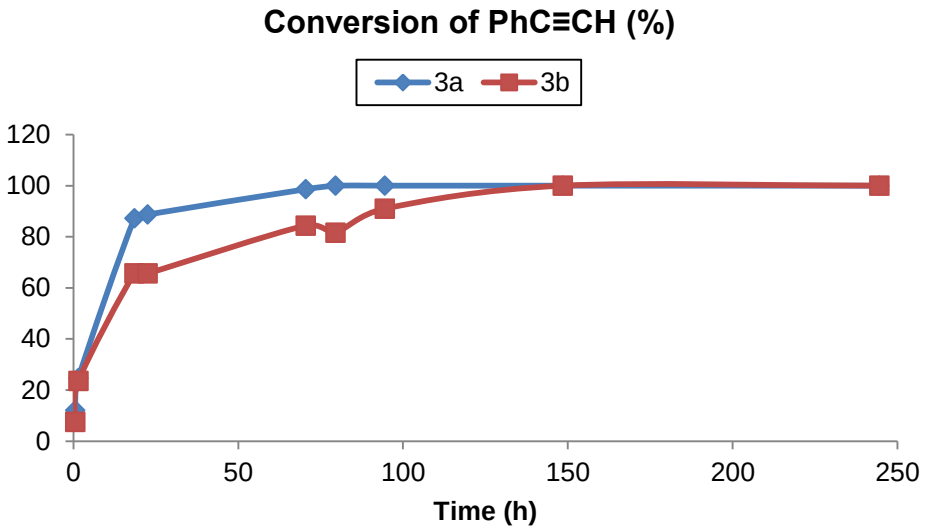

Figure 4.76 Reaction profile of conversion vs time for the hydrosilylation of PhC≡CH with complexes 3a and 3b, at 60°C.

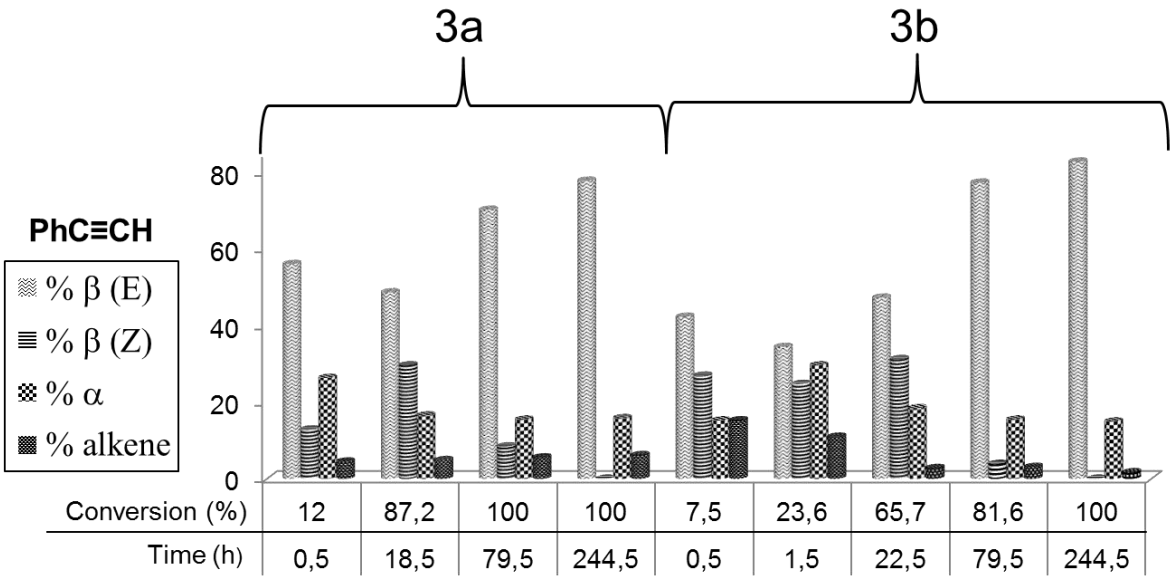

Figure 4.77 Selectivity vs conversion and time for the hydrosilylation of PhC≡CH catalyzed by 3a and 3b, at 60°C.

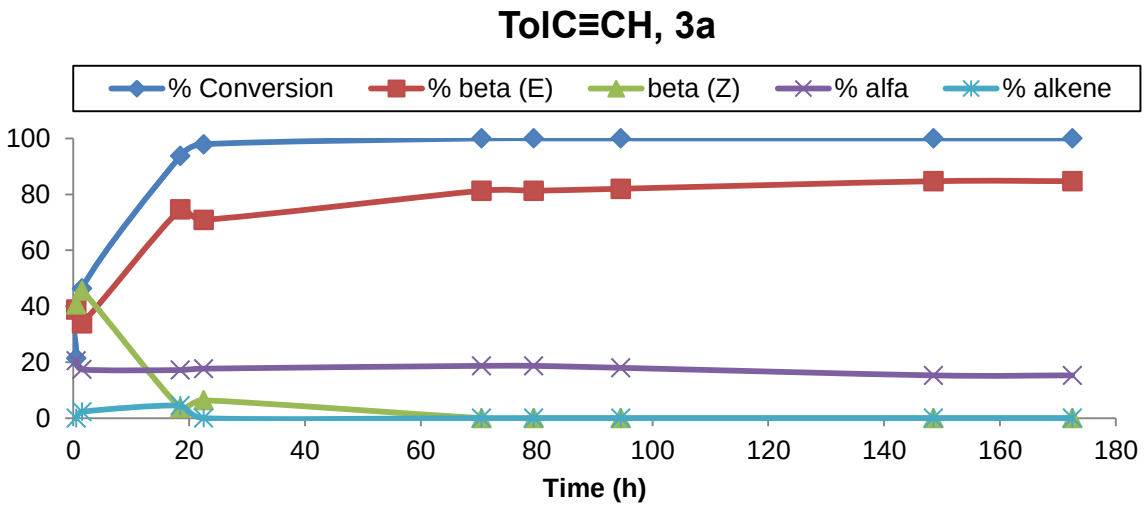

Figure 4.78 Reaction profile of conversion and selectivities vs time for the hydrosilylation of TolC≡CH with 3a, at 60°C.

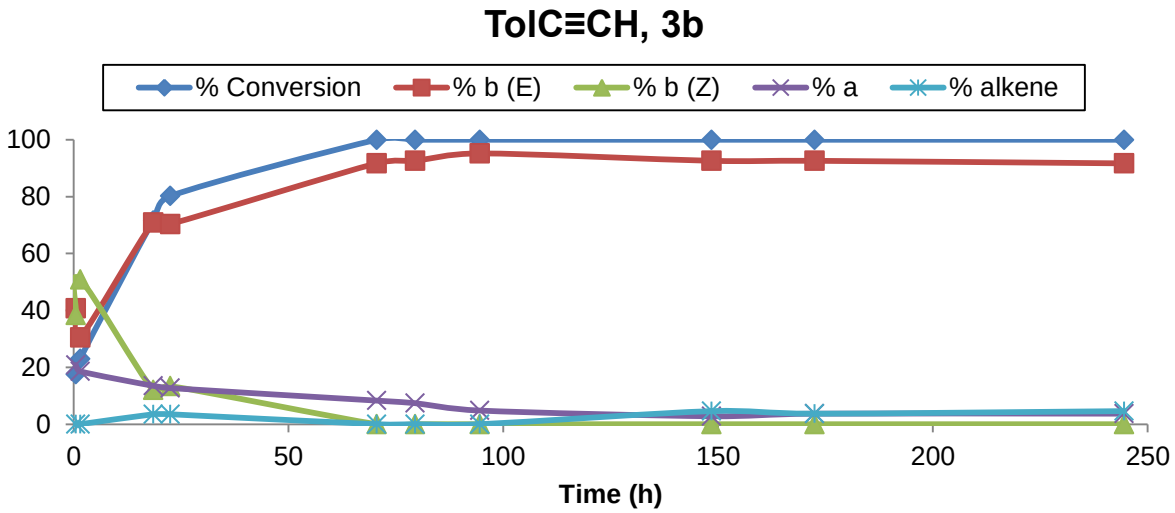

Figure 4.79 Reaction profile of conversion and selectivities vs time for the hydrosilylation of TolC≡CH with 3b, at 60°C.

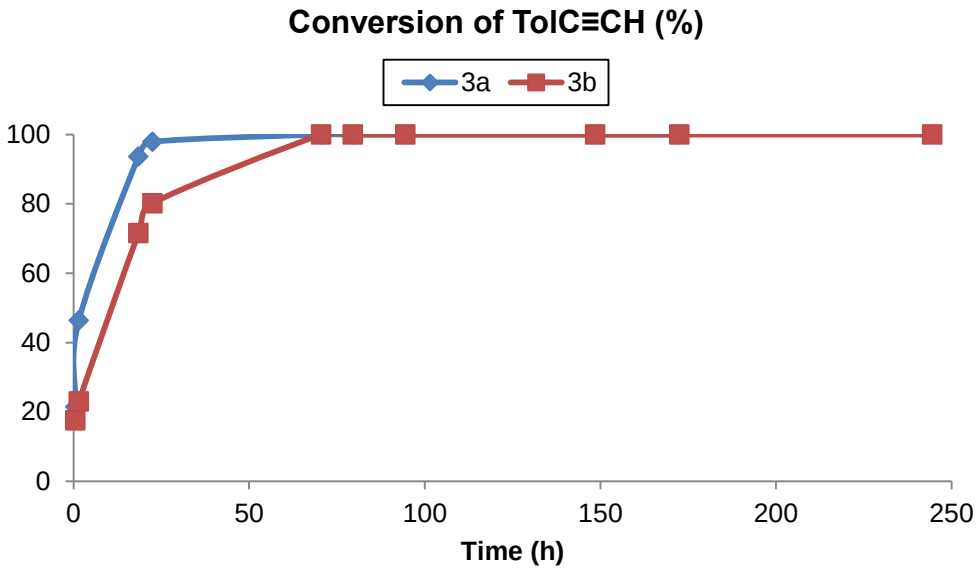

Figure 4.80 Reaction profile of conversion vs time for the hydrosilylation of TolC≡CH with complexes 3a and 3b, at 60°C.

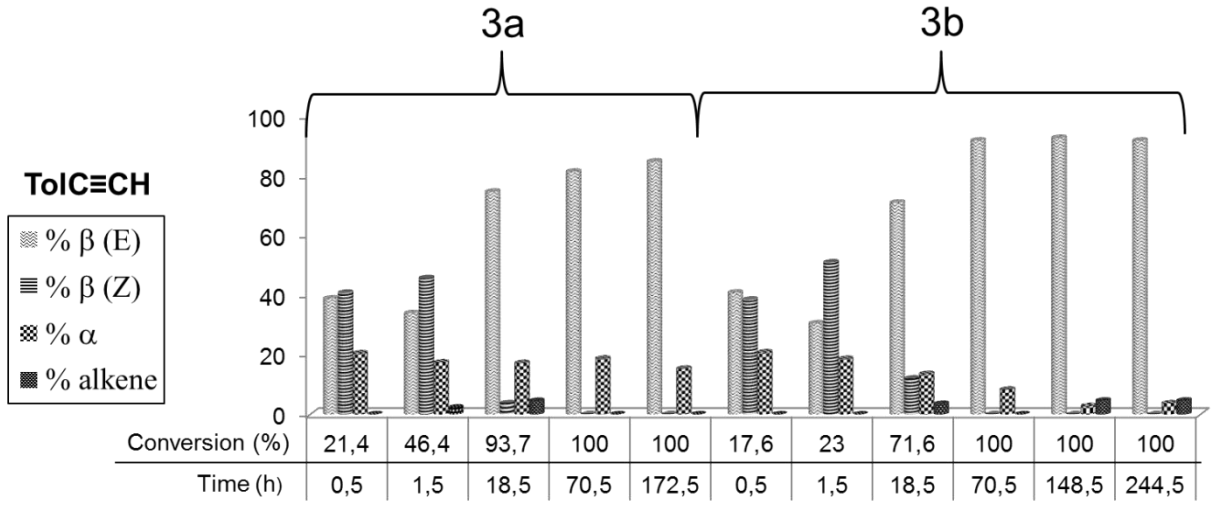

Conversion (%)	21,4	46,4	93,7	100	100	17,6	23	71,6	100	100	100
Time (h)	0,5	1,5	18,5	70,5	172,5	0,5	1,5	18,5	70,5	148,5	244,5

Figure 4.81 Selectivity vs conversion and time for the hydrosilylation of TolC≡CH catalyzed by 3a and 3b, at 60°C.

4.23 References

(1) Busetto, L.; Cassani, M. C.; Femoni, C.; Mancinelli, M.; Mazzanti, A.; Mazzoni, R.; Solinas, G. *Organometallics* **2011**, *30*, 5258.

(2) Bourissou, D.; Guerret, O.; Gabbaı, P.; Bertrand, G. *Chem. Rev.* **2000**, *100*, 39.

(3) Hoffmann, R. *J. Am. Chem. Soc.* **1968**, *90*, 1475.

(4) Wanzlick, H. W.; Kleiner, H. J. *Angew. Chem.* **1961**, *73*, 493-493.

(5) de Frémont, P.; Marion, N.; Nolan, S. P. *Coord. Chem. Rev.* **2009**, *253*, 862-892.

(6) Dupont, J. *J. Braz. Chem. Soc.* **2004**, *15*, 341-350.

(7) Caló, V.; Del Sole, R.; Nacci, A.; Schingaro, E.; Scordari, F. *Eur. J. Org. Chem. 2010* **2000**, *2000*, 869-871.

(8) Herrmann, W. a. *Angew. Chem., Int. Ed.* **2002**, *41*, 1290-1309.

(9) Scholten, J. D.; Leal, B. C.; Dupont, J. *ACS Catalysis* **2012**, *2*, 184-200.

(10) Ballarin, B.; Busetto, L.; Cristina Cassani, M.; Femoni, C. *Inorg. Chim. Acta* **2010**, *363*, 2055-2064.

(11) http://www.scripps.edu/baran/images/grpmtgpdf/Zografos_Feb_04.pdf.

(12) Gridnev, A. A.; Mihaltseva, I. M. *Synth. Commun.* **1994**, *24*, 1547-1555.

(13) Glorius, F.; Spielkamp, N.; Holle, S.; Goddard, R.; Lehmann, C. W. *Angew. Chem., Int. Ed.* **2004**, *43*, 2850-2852.

(14) Arduengo, A. J. *Acc. Chem. Res.* **1999**, *32*, 913.

(15) http://www.chm.bris.ac.uk/webprojects2002/grant/webcomp/non-crossing.html.

(16) Arduengo, A. J.; Gamper, S. F.; Tamm, M.; Calabrese, J. C.; Davidson, F.; Craig, H. A. *Structure* **1995**, *117*, 572-573.

(17) Wanzlick, H. W.; Schönherr, H. J. *Angew. Chem.* **1968**, *80*, 154-154.

(18) Ofele, K. *Angew. Chem., Int. Ed.* **1968**, *12*, 950.

(19) Arduengo III, A. J.; Dias, H. V. R.; Harlow, R. L.; Kline, M. *J. Am. Chem. Soc.* **1992**, *114*, 5530-5534.

(20) Jean-Baptiste Dit Dominique, F.; Gornitzka, H.; Hemmert, C. *Organometallics* **2010**, *29*, 2868-2873.

(21) Lappert, M. F. *J. Organomet. Chem.* **1988**, *358*, 185-213.

(22) Lin, T.-S.; Luo, M.-Z.; Liu, M.-C. *Tetrahedron* **1995**, *51*, 1055-1068.

(23) Liu, B.; Liu, X.; Chen, C.; Chen, C.; Chen, W. *Organometallics* **2012**, *31*, 282-288.

(24) Lin, I. J. B.; Vasam, C. S. *Coord. Chem. Rev.* **2007**, *251*, 642-670.

(25) Liu, B.; Xia, Q.; Chen, W. *Angew. Chem., Int. Ed.* **2009**, *48*, 5513-6.

(26) Green, J. C.; Scurr, R. G.; Arnold, P. L.; Cloke, G. N. *Chem. Commun.* **1997**, 1963-1964.

(27) Mercs, L.; Labat, G.; Neels, A.; Ehlers, A.; Albrecht, M. *Organometallics* **2006**, *25*, 5648-5656.

(28) Garrison, J. C.; Youngs, W. J. *Chem. Rev.* **2005**, *105*, 3978-4008.

(29) Kandepi, V. V. K. M.; Cardoso, J. M. S.; Peris, E.; Royo, B. *Organometallics* **2010**, *29*, 2777-2782.

(30) Chianese, A. R.; Li, X.; Janzen, M. C.; Faller, J. W.; Crabtree, R. H.; Organomet, W. A. J. *Organometallics* **2003**, *22*, 1663-1667.

(31) Wang, H. M. J.; Lin, I. J. B. *Organometallics* **1998**, *17*, 972-975.

(32) Cardoso, J. M. S.; Royo, B. *Chem. Commun.* **2012**, *48*, 4944-4946.

(33) Corbera, R.; Sanau, M.; Peris, E. *Organometallics* **2006**, *25*, 4002-4008.

(34) Scott, N. M.; Dorta, R.; Stevens, E. D.; Correa, A.; Cavallo, L.; Nolan, S. P. *J. Am. Chem. Soc.* **2005**, *127*, 3516-26.

(35) Bringmann, G.; Price Mortimer, A. J.; Keller, P. A.; Gresser, M. J.; Garner, J.; Breuning, M. *Angew. Chem., Int. Ed.* **2005**, *44*, 5384-5427.

(36) Crabtree, R. *J. Organomet. Chem.* **2005**, *690*, 5451-5457.

(37) Díez-González, S.; Marion, N.; Nolan, S. P. *Chem. Rev.* **2009**, *109*, 3612-76.

(38) Herrmann, W. A.; Öfele, K.; Elison, M.; Kuhn, F. E.; Roesky, P. W. *J. Organomet. Chem. 480*, C7-C9.

(39) Imlinger, N.; Wurst, K.; Buchmeiser, M. R. *J. Organomet. Chem.* **2005**, *690*, 4433-4440.

(40) Jiménez, M. V.; Pérez-Torrente, J. J.; Bartolomé, M. I.; Gierz, V.; Lahoz, F. J.; Oro, L. A. *Organometallics* **2008**, *27*, 224-234.

(41) Patil, S.; Deally, A.; Gleeson, B.; Helge, M.; Paradisi, F.; Tacke, M. *Appl.Organometal.Chem.* **2010**, *24*, 781-793.

(42) Moret, M.-etienne; Chaplin, A. B.; Lawrence, A. K.; Scopelliti, R.; Dyson, P. J. *Organometallics* **2005**, *24*, 4039-4048.

(43) Patil, S.; Claffey, J.; Deally, A.; Hogan, M.; Gleeson, B.; Miguel, L.; Méndez, M.; Müller-bunz, H.; Paradisi, F.; Tacke, M. *Eur. J. Inorg. Chem.* **2010**, 1020-1031.

(44) http://www.personal.psu.edu/the1/sn1ande.htm.

(45) Elango, K.; Srirambalaji, R.; Anantharaman, G. *Tetrahedron Lett.* **2007**, *48*, 9059-9062.

(46) Sauerbrey, S.; Majhi, P. K.; Daniels, J.; Schnakenburg, G.; Brändle, G. M.; Scherer, K.; Streubel, R. *Inorg. Chem.* **2011**, *50*, 793-9.

(47) Fre, P. D.; Scott, N. M.; Stevens, E. D.; Ramnial, T.; Lightbody, O. C.; Macdonald, C. L. B.; Clyburne, J. A. C.; Abernethy, C. D.; Nolan, S. P. *Organometallics* **2005**, *24*, 6301-6309.

(48) Busetto, L.; Cristina Cassani, M.; Femoni, C.; Macchioni, A.; Mazzoni, R.; Zuccaccia, D. *J. Organomet. Chem.* **2008**, *693*, 2579-2591.

(49) Abraham, R. J.; Byrne, J. J.; Griffiths, L.; Perez, M. *Magn. Reson. Chem.* **2006**, *44*, 491-509.

(50) Newman, C. P.; Clarkson, G. J.; Rourke, J. P. *J. Organomet. Chem.* **2007**, *692*, 4962-4968.

(51) Kline, M.; Harlow, R. L. *J. Am. Chem. Soc.* **1991**, *113*, 363-365.

(52) Kuhn, H.; Woodgate, G. K. *Nature* **1950**, *166*, 906.

(53) Gaillard, S.; Slawin, A. M. Z.; Nolan, S. P. *Chem. Commun.* **2010**, *46*, 2742-2744.

(54) Casarini, D.; Lunazzi, L.; Mazzanti, A. *Eur. J. Org. Chem.* **2010**, *2010*, 2035-2056.

(55) Enders, D.; Gielen, H.; Runsink, J.; Breuer, K.; Brode, S.; Boehn, K. *Eur. J. Inorg. Chem.* **1998**, 913-919.

(56) Enders, D.; Gielen, H. *J. Organomet. Chem.* **2001**, *618*, 70-80.

(57) Sabbah, M.; Soulère, L.; Reverchon, S.; Queneau, Y.; Doutheau, A. *Bioorg. Med. Chem.* **2011**, *19*, 4868-75.

(58) Hirtenlehner, C.; Krims, C.; Hölbling, J.; List, M.; Zabel, M.; Fleck, M.; Berger, R. J. F.; Schoefberger, W.; Monkowius, U. *Dalton Trans.* **2011**, *40*, 9899-9910.

(59) Sheldrick, G. M. *SADABS Program for Absorption Correction Using Area Detector Data* **1996**.

5 Table of Figures

6 List of Schemes

7 List of Tables